OPTIMISATION AND PROPERTIES OF GAMETE TRANSPORT

by

PAUL WILLIAM WAKELEY

A thesis submitted to
The University of Birmingham
for the degree of
DOCTOR OF PHILOSOPHY

School of Mathematics
University of Birmingham
April 2008

ABSTRACT

We consider a series of problems from the field of biological fluid mechanics, in particular the properties and optimisation of human sperm motility, and the fluid flow in the oviduct.

Recent experimental data shows a modulation in the beat pattern of human sperm given a change in the viscosity of the medium. As an initial approach, we consider and refine a sinusoidal planar model by introducing a new envelope function with parameters to specify the distal component of the beat pattern and to account for non-constant wavenumber; we investigate the properties of beat pattern configurations such as predicted cell velocity, power consumption and efficiency. The modelling of self-propelled flagellated micro-organisms at low Reynolds number is achieved using the powerful singularity method and slender-body theory.

Results using the modified envelope parameter model agree qualitatively with experimental data to show that a balance between velocity, drag and power consumption is a factor in determining a beat pattern configuration. Limitations of the model are discussed including the underlying assumption that the beat pattern is a modified sinusoidal wave which limits the range of permissible patterns.

A new method for specifying beat pattern configurations is developed arising from analysis of experimental data using the shear-angle. The resulting two parameter model encompasses a wide range of beat pattern observed in human sperm *in vitro*. The two parameter model is considered and various modes of efficient beating are illustrated. By considering the bending moment density (which scales with viscosity) we offer an explanation for the viscosity-dependent modulation of human sperm beat. Further extensions and applications of the new model are proposed.

We also consider the flow in the oviduct as a result of peristaltic pumping and ciliary activity. A general method for considering peristaltic flows is presented and a number of novel features are observed through an asymptotic and dynamical systems analysis. The approach adopted is to consider the underlying muscular peristalsis with the ciliary activity as a small perturbation. Analysis includes the use of local Lyapunov exponents to quantify the levels of mixing. Biological implications of the results are discussed.

ACKNOWLEDGEMENTS

Firstly and foremost, I should like to thank my Supervision team: Professor John Blake, Dr Dave Smith, Dr Daniel Loghin, Dr Jackson Kirkman-Brown and Dr Eamonn Gaffney. Without their insight, enthusiasm and encouragement this thesis would have been impossible to complete.

Secondly, I thank all my colleagues and friends in the School of Mathematics and beyond, who are too numerous to mention individually. I have had the pleasure of meeting, working and sharing cake with many wonderful people and I thank everyone for making my time at Birmingham so rewarding, both scientifically and otherwise. I do however, offer particularly special thanks to James Sprittles who, despite some occasional banter, offered invaluable advice and an eagle-eye when I was assembling this thesis.

I should also like to thank my Parents for their continual and steadfast support in what ever I have chosen to do.

I would like to thank my examiners for their very valuable comments.

Finally I acknowledge the financial support of EPSRC, for allowing me to continue my studies and enable me to live in a manner to which I have become accustomed.

CONTENTS

List of Figures

List of Tables

CHAPTER 1

INTRODUCTION

1.1 Motivation

The application of fluid dynamics' theory to physiological and biological problems is an interesting and broad area of research owing to the large diversity of possible systems. Fluid dynamics, combined with kinematics and experimental work enables us to understand and model biological and physiological systems across a broad range of scales – from the movement of animals and the flight of birds to the motion of micro-organisms (see Lighthill (1975))

The effective motility of human sperm is a key factor in human reproduction; the largest causes of infertility in couples (24%) is attributed to deficiencies or abnormal functionality of sperm (Hull et al., 1985). One in seven couples will have difficulty conceiving naturally (Templeton et al., 1990). To understand sperm motility we can study sperm experimentally *in vitro* – the resulting experimental data can then be studied in its own right or, as in this thesis, be combined with kinematics and fluid dynamics enabling further investigations to take place to gain an insight into the physics.

The applications of manipulating sperm motility in the laboratory are important in assisted conception (such as in *in vitro fertilisation*), in 'sperm sorting' (distinguishing those sperm carrying the male chromosome from those carrying the female one) and, if sperm motility could be artificially stopped in a temporary and reversible manner, male contraception.

Katz et al. (1978) and Ho and Saurez (2001) found experimentally that for human sperm swimming in cervical mucus the bending of the flagellum was confined to the distal portion of the flagellum and had a lower amplitude and wavelength compared to those swimming in a Newtonian medium. Moreover Ishijima et al. (1986) and Smith et al. (2008b,c) illustrate that in different viscosities of Newtonian media, different beat patterns can be observed *in vitro* – this is our key motivation. Figure 1.1 illustrates two photographs taken from experimental data (Smith et al., 2008b): (a) taken at (approximate) $10^{-3}\text{Pa}\cdot\text{s}$ viscosity in Earle's balanced salt solution where the flagellum exhibits high amplitude 'whip-like' beating with long wavelength, whilst (b) at higher viscosity, (approximate) $1.3\text{Pa}\cdot\text{s}$, the wavelength is shorter, the amplitude is lower and the beat pattern takes on a meandering form, with the majority of the beating in the distal portion of the flagellum. The beat patterns observed by Smith et al. (2008c) for high viscosity Newtonian media correspond to the finding of Katz et al. (1978), Ishijima et al. (1986) and Ho and Saurez (2001) in cervical mucus. A number of different viscosities are encountered by human sperm during the natural conception process and in *in vitro* situations and thus it is important to understand the variation in beat pattern observed (Suarez and Pacey, 2006).

The motivation for the first part of this thesis is the modulation in beat pattern observed by changing the viscosity of the fluid medium in which the sperm are swimming. By combining experimental data with new mechanisms for specifying the beat pattern and utilising the powerful technique of singularity modelling we shall discuss the difference between beat patterns observed *in vitro* and illustrate mechanisms that might cause modulation between beat patterns.

Another area of interest is the flow in the female reproductive tract. Much work has been carried out on physiological peristaltic flows (see literature review §1.4.2); however, recent work relating to the non pregnant uterus and oviduct (such as Eytan and Elad

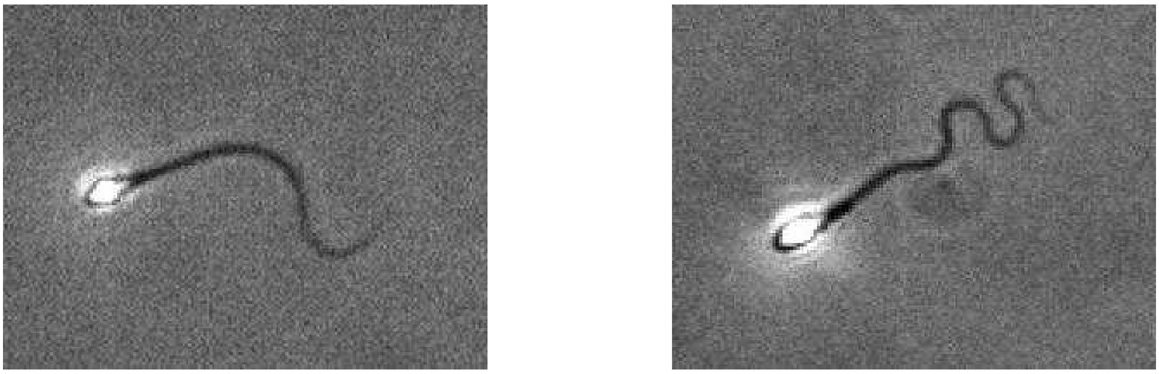

(a) Watery Medium
approximately $10^{-3}\text{Pa}\cdot\text{s}$

(b) More Viscous Medium
approximately $1.3\text{Pa}\cdot\text{s}$

Figure 1.1: Typical human sperm beat patterns observed at different viscosities: (a) approximate viscosity of $10^{-3}\text{Pa}\cdot\text{s}$ in Earle's balanced salt solution (b) Earle's medium with methylcellulose (sigma MO512, nominal viscosity 4000cp at 20°C) to give an approximate viscosity of $1.3\text{Pa}\cdot\text{s}$. Notice that at the lower viscosity (a) there is a high amplitude whip-like beat with long wavelength, whilst (b) at the higher viscosity the beat pattern is meandering, with lower amplitude and shorter wavelength.

(1999); Eytan et al. (1999)) has often neglected the role of the cilia despite the fact that Blake et al. (1982) showed that they alone were sufficient to drive a fluid flow in an oviduct. We shall therefore consider a model which accounts for both the underlying peristalsis flow and a small perturbation designed to model the ciliary flow.

In the remainder of this chapter we outline the underlying physiology of sperm cells, the ovum and cilia and then discuss experimental and data processing methods. We complete the chapter with an overview of the fundamental fluid dynamics experienced at low Reynolds numbers and conduct a literature review of previous studies in the areas of interest.

1.2 Physiology and *in vivo* processes

Fauci and Dillon (2006) describe the human reproductive system as a 'complex fluid-structure interaction' which relies on a intricate interplay of co-ordinated muscular contractions, ciliary beating, chemical signalling and the motion of sperm. A failure of just one of these processes can result in the inability of a couple to conceive. Some of the mechanisms that are involved in conception include the active swimming of motile sperm and the passive motion of sperm cells and ova by the muscular contraction and ciliary beating of the uterus and the oviduct. Each of the different mechanisms, through the forces produced, causes a fluid flow. Many of the surfaces in question are elastic and so will respond to the forces applied.

We shall now briefly outline some of the important physiology and *in vivo* processes involved in human reproduction.

1.2.1 The sperm cell

Following copulation between 50 and 400 million mature sperm cells maybe found in semen, in the female reproductive tract at the top of vagina near the cervix; the figure varies significantly in an individual and between individuals and is dependent on a large number of factors (de Jonge and Barratt, 2006; Chen et al., 2006). Compared to the fact that only one cell is required for successful fertilisation, the number of cells in an ejaculation might sound high, however, there is considerable debate in the biological community about the normality of sperm cells: Chen et al. (2006) recorded (figures in brackets are standard deviations) in a sample of 23 men, an average sperm concentration of 125.5 (92.3) million cells per millilitre; 45.6% (22.2) of which were motile, 28.4% (15.2) displayed progressive motility and only 8.0% (4.6) displayed normal morphology. Notice that the standard deviations are large, highlighting the variation across the population.

The definition of what is a normal sperm is somewhat subjective. Kruger et al. (1988) set strict guidelines (which were used by Chen et al. (2006)) defining an abnormal sperm cell to be one which has a head, midpiece or tail defect. A sperm cell is considered normal if the head has a smooth oval configuration with a well-defined acrosome over 40%-70% of the sperm head and a midpiece and tail without abnormality. The length of the normal head is 5 to 6μm, with a diameter of 2.5 to 3.5μm. Midpiece defects include debris in the

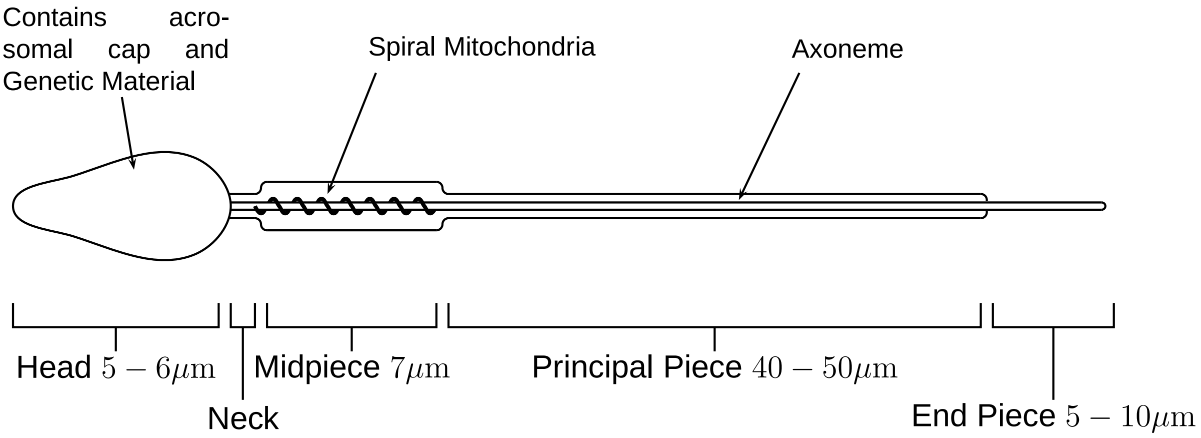

Figure 1.2: Microstructure of a mature human sperm. Lengths are not shown to scale. Based upon a diagram in Debuse (1998)

neck or a midpiece of more than 30% of the total length. Other abnormalities include heads which are round, small, large, tapered or cells with two heads and/or tails. A normal flagellum is around 50-60μm. The micro-structure of a normal human sperm cell is illustrated in Figure 1.2.

The World Health Organisation (1999), state that greater than or equal to 30% of sperm must display normal morphology for the sample to be considered fertile.

During spermatogenesis, the transport of the immature sperm has many distinct phases in which different mechanisms are seen to play important roles (Kay and Robertston, 1998). From the creation of a sperm cell, the still immotile cells are transported through the *efferent ductules* by a combination of pressure gradient, ciliary activity and peristalsis. The sperm reach the epididymis where after 12 days they achieve maturity and then become motile.

1.2.2 The ovum

A human ovum is 200μm in diameter and is initially encapsulated in a cumulus consisting of follicular fluid and granulosa cells. The size of the cumulus can be as much as 700μm (Debuse, 1998), and this means that in some areas of the oviduct the ovum is close to,

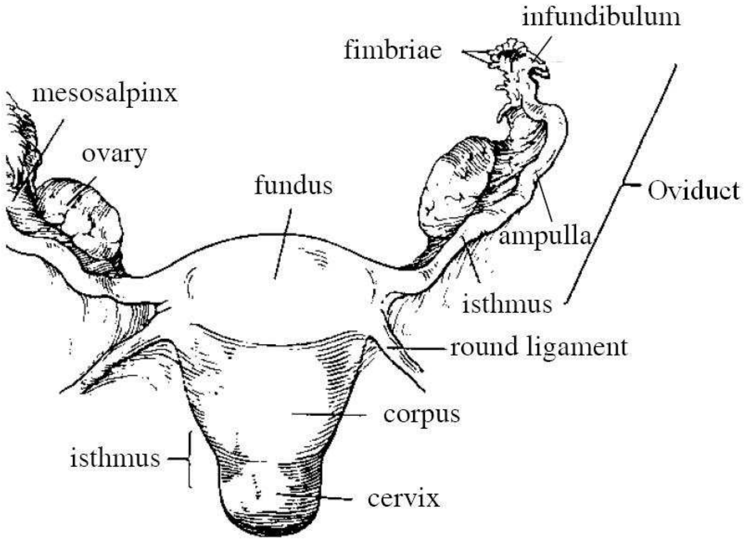

Figure 1.3: Anterior view of the uterus. The oviduct consists of three sections, from nearest the uterus, the intramural, isthmic and ampullary regions. Taken from Eytan and Elad (1999).

or in contact with, the ciliated surfaces of the oviduct. The inner layer around the egg is known as the zona pellucida. The zona is a membrane which surrounds the ovum through which the capacitated sperm must pass to reach the centre of the egg. It is thought that a variety of chemical and mechanical mechanisms combine to breakdown the cumulus and the zona pellucida to allow the sperm to penetrate the ovum (Baltz et al., 1988).

1.2.3 Anatomy of the oviduct

The oviducts, or fallopian tubes, are muscular tubes which extend from the cornua of the uterus curving to the ovaries (Debuse, 1998). From the uterus, the oviduct consists of the uterine-tubular junction (which may be closed, or occluded with mucus (Jansen, 1980)), the isthmus, the ampulla, and the infundibulum. Figure 1.3 illustrates the oviducts in relation to the uterus. The isthmus of the oviduct, in cross-section, is a highly convoluted structure as illustrated in a cross section in Figure 1.4.

The mucosa of the oviduct is a ciliated surface which secretes mucus into the lumen of the oviduct. This mucus serves to nourish the fertilised ovum as it is carried towards the

Figure 1.4: Typical cross section of the human oviduct in the Isthmic region. The bar is 250μm in length. Taken from University of Kansas Medical Center (2006).

uterus by the action of the cilia and peristalsis (Eytan et al., 2001b). Unlike sperm cells, the ovum has no self-propulsion mechanism and thus it is dependent on external factors to move it through the female tract.

An interesting study by Sjösten et al. (2004) found that patients, after clinical examination with powdered gloves, were found to have accumulations of starch powder particles at the ovarian end of the oviduct, following removal of the genital tract twenty-four hours later as part of a hysterectomy. As we noted previously, ciliary and peristaltic effects move the mucus towards the uterus; these findings suggest there is also a flow from the cervix towards the ovaries.

It is also worth noting that the ‘text-book’ image of the female reproductive system suggests open spaces which are filled with fluid. This image is a result of the need for clarity in the representation, however, in reality most surfaces are close to one another; Eytan et al. (2001b) gives the passive width of the uterus from anterior to posterior as 0.488 ± 0.187mm. An analogy of the fluid forming the filling of a sandwich is more appropriate.

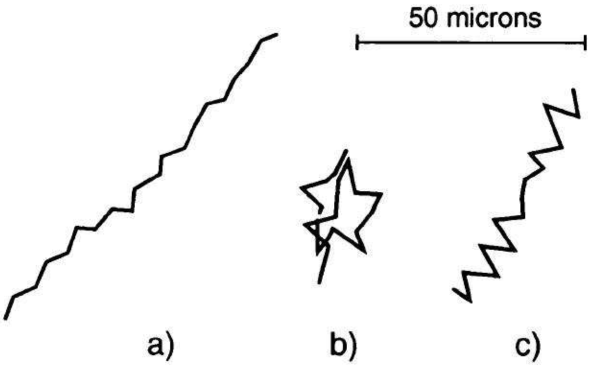

Figure 1.5: Sperm motility patterns. (a) Forward progressive; (b) hyperactivated; (c) transitional. From Kay and Robertston (1998).

1.2.4 Beat patterns and internal structure

Three general types of sperm motility have been observed *in vitro* (Kay and Robertston, 1998). Figure 1.5(a) demonstrates the so-called normal forward progressive motility associated with uniform, symmetric, low-amplitude flagellar beating. Figure 1.5(b) shows a star shaped trajectory displayed by non-progressive hyperactivated sperm with a larger amplitude, asymmetric beat pattern. The third type (Figure 1.5(c)) can be thought of as being in between the normal pattern and the hyperactivated pattern and is characterised by high frequency, high amplitude flagellar beating that does result in forward motion. Suarez et al. (1991) suggest that hyperactivation can confer a mechanical advantage upon sperm in the oviduct, where they encounter viscous oviductal fluid or viscoelastic cumulus. However, Kay and Robertston (1998) observed hyperactivation as being a non progressive motility pattern; thus the true mechanism and function of hyperactivation is not known.

We have already observed that modulation of beat pattern based on viscosity (Smith et al., 2008c) and have noted a similar result in non-Newtonian cervical mucus (Ho and Saurez, 2001; Katz et al., 1978).

One early model for sperm motion was proposed by Machin (1958), who considered the propulsion of sperm by a mechanism of waves being propagated along a (passive) elastic flagellum. This elastic beam model was shown to be insufficient for the description

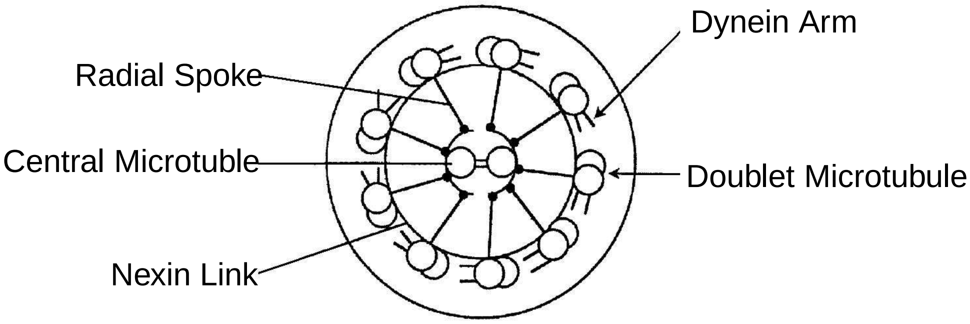

Figure 1.6: The internal structure of the axoneme - part of the flagellum. Illustrating the '9 + 2' structure of microtubules. Taken from Dillion et al. (2006).

of the beat patterns which were observed *in vitro*, and thus it was postulated that an internal mechanisms was required to propel the sperm's flagellum. It is now understood that the flagellum of sperm has an internal mechanical structure that drives the motion: the mechanism consists of nine outer dense fibres which lie between the $9 + 2$ axoneme and the mitochondrial sheath. This arrangement is illustrated in Figure 1.6.

1.2.5 Sperm travelling through the female tract

The sperm traverse the female reproductive tract to reach the ovum in the oviduct. The first obstacle encountered by the sperm is cervical mucus, which forms a plug between the vagina and the uterus, partly to protect the uterus from bacterial infection. Cervical mucus is composed of fibrillar sub-units which normally arrange so that the fibrils are aligned parallel to the direction of travel from the vagina to the uterus (Ceric et al., 2005). However, cervical mucus is a non-Newtonian fluid (Wolf et al., 1977a) which, dependent on the stage of the female menstrual cycle, varies in viscosity and fibril alignment; oestrogen promotes watery mucus which facilitates sperm transport, whereas progesterone results in a mucus which is hostile to sperm motility (Wolf et al., 1977b). Oestrogen levels peak at the time of ovulation making sperm penetration easier at this time. Around 10% of sperm deposited in the vagina pass into the uterus through the cervical mucus (Eisenbach, 2004; Scott, 2000). The cervix is typically 3cm in length (Sherwood, 2003).

After penetrating the cervical mucus, the sperm travel through the uterus toward one of the two oviducts - a distance of approximately 6cm (Sherwood, 2003); the oviducts are lined with mucus producing cells, called mucosa and are ciliated; mucus flows towards the uterus through a combination of ciliary and peristaltic actions (Eytan et al., 2001b). Therefore the sperm may need to 'swim' against this fluid flow in order to reach the ovum. Katz et al. (1989) highlight the different mechanisms that a sperm has to use to traverse the female tract, and suggest that sperm move along the oviduct walls to reach the ovum.

Mucus in the oviduct and the uterus both carries and nourishes the fertilised ovum, and may play a role in the capacitation of sperm before fertilisation (Zaneveld et al., 1991). (Capacitation is a process sperm undergo to enable them to penetrate the zona pellucida and thus fertilise the ovum (Cohen-Dayag et al., 1995)). Uterine fluid is less viscous than cervical mucus (Eytan and Elad, 1999; Karni et al., 1971), however there is evidence that the isthmuses are occluded with mucus plugs during certain stages of the reproductive cycle (Jansen, 1980). It is clear therefore that a successful sperm will need to be motile in fluids of differing viscosities. Figure 1.7 demonstrates the different stages of sperm motility through the female reproductive tract.

The precise mechanism by which sperm reach the ovum is an open question – although Fauci and Dillon (2006) attribute it mainly to fluid dynamics as opposed to chemotaxis or chemokinesis (discussed in Ralt et al. (1994); Eisenbach (1999, 2004); Spehr et al. (2003)). The concept of a number of genetically best sperm was devised by Cohen and Werrett (1975). In their experiments it was demonstrated, through the breeding of rabbits, that sperm which naturally reached the oviduct in a first animal would disproportionately reach the ovum in a second animal when they were mixed back with a normal ejaculate. The reason Cohen and Werrett (1975) suggest for such a mechanism in which certain sperm are favoured, is that in the total sperm population the majority will have a genetic error which

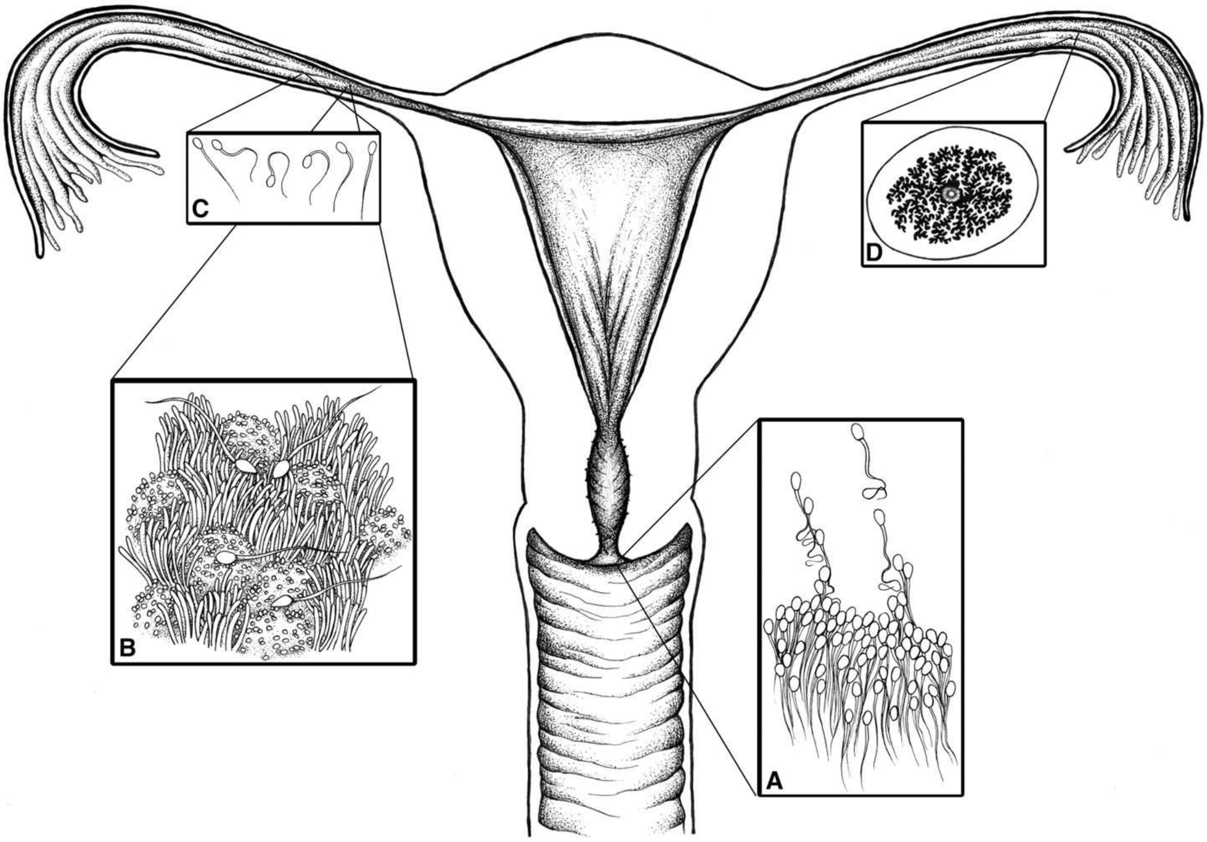

Figure 1.7: Diagram showing the different stages of sperm transport through the female reproductive system: (A) Sperm are deposited in the vagina and some ($\sim 10\%$) travel through the cervical mucus. (B) Sperm move along the ciliated surfaces of the oviduct. (C) Only a few sperm will reach the upper range of the tract where fertilisation occurs. (D) The geometry of the oviduct is convoluted and ciliated. From Suarez and Pacey (2006).

has occurred during meiosis and only those genetically competent sperm should fertilise the ova (and these are the ones with the swimming advantage). There is no data for such behaviour in human sperm; on the contrary the success of ICSI (Intro-Cytoplasmic Sperm Injection) suggests that the majority of sperm are genetically viable. In ICSI a sperm is selected *in vitro* from the ejaculate without knowledge of its genetic makeup and the sperm's head is injected directly in to the ova; the sperm need not be motile (HFEA, 2007).

Clinical data suggests that there are about a dozen sperm in the vicinity of the ovum at

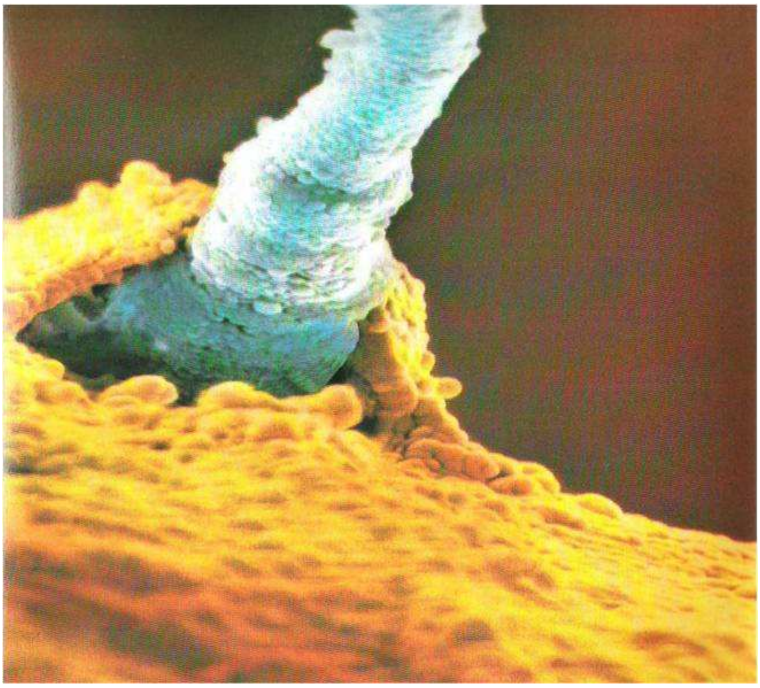

Figure 1.8: A pseudo-coloured electron microscope picture of a sperm cell penetrating the zona pellucida of an ovum, taken from Nilsson (1990)

the time of fertilisation (de Jonge and Barratt, 2006; Suarez and Pacey, 2006). Figure 1.8 shows an electron microscope picture of a sperm cell penetrating the zona pellucida.

1.2.6 Physiology of cilia

An individual cilium can be thought of as a hair-like projection from the surface of a cell, which performs whiplash like movements by which fluid is propelled (Blake, 1971; Blake and Sleigh, 1974). If a surface is covered in many cilia, their collective action can be used to maintain a flow past the surface or to propel a micro-organism through a fluid medium. The movement of cilia can be thought of as having two distinct parts. There is the effective stroke, where the cilium moves in the direction of the flow of the fluid, and the recovery stroke where it returns to its original state. Existing models of the effective stroke have the cilia in a rigid state, fully extended in a near vertical orientation to the surface, a flexure at the base causes the cilia to swing away from the cell's surface (Blake

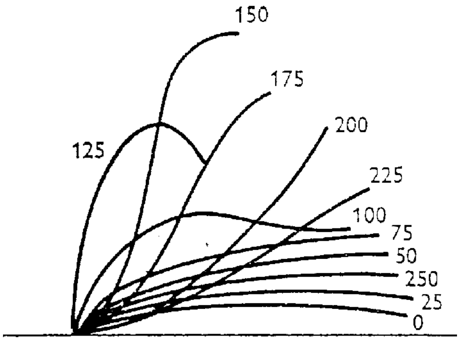

Figure 1.9: The effective stroke 0-125, and recovery stroke 125-250, of a cilium on the surface of the protozoon *Opalina.* Taken From Blake and Sleigh (1974).

and Sleigh, 1974). This is followed by a sharp movement back to the other side of the base, while the upper portion of the cilium continues to move in the effective direction. The bend in the cilium caused by these two swings is propagated toward the tip of the cilium during the recovery stroke so that cilium moves back close to the cell surface in preparation for the beginning of the next effective stroke. See Figure 1.9 for an example of the effective and recovery stroke in the cilia of the protozoon *Opalina.* The effective stroke occurs in a much shorter time than the recovery stroke. Such a mechanism is required due to the reversibility of Stokes flow.

Within the human body, the mechanisms for the motion of cilia in the lungs has been studied, where the cilia propel a thin mucus layer which lines the surfaces of the airways (Smith et al., 2007a,b). Less study, however, has been made of cilia in the reproductive system. Uterine and oviductal cilia are similar in dimension to those in the respiratory system, being typically 0.25μm in diameter and 6μm in length. It is also worth noting that the covering of cilia in the reproductive system is not as uniform as that observed in the respiratory system, however, a suitable analogy is a forest with clearing, rather than isolated clumps of cilia (see Figure 1.7(B) (Suarez and Pacey, 2006)).

1.3 Experimental methods and *in vitro* processes

An interest in human sperm motility in the modern sense started in the 1950s. A particularly interesting early work is that of Rothschild (1963) who observed that bull semen were not uniformly distributed throughout a droplet of semen but tended to accumulate near surfaces. Winet et al. (1984) observed a similar result for human sperm, and also concluded that gravity has no significant effect on human sperm. As an aside, Smith et al. (2008a) have since implemented a hybrid boundary integral/slender-body theory method which predicts that human sperm cells are attracted towards boundaries under certain initial conditions.

The two main experimental techniques we shall consider are *Computer-assisted semen analysis* (CASA) and the acquisition of photographic data using high speed microphotography. These are discussed in more detail in Appendix A.

1.4 Literature review

We consider the existing literature relating to the two problems which we shall study; the mathematical models of flagellar propulsion and the modelling of peristaltic flows.

1.4.1 Development of mathematical models of flagellar propulsion

The mechanism that drives eukaryotic cilia and flagella, such as those found on sperm, is different from that used to drive bacterial flagella. Sperm flagella and cilia are driven by a complex underlying structure internal to the flagella, whereas bacterial flagella are rotated by a single ‘motor’ in the cell wall (DiLuzio et al., 2005). Eukaryotic flagella do not rotate relative to the cell body (Debuse, 1998).

The study of the theoretic motion of sperm has been considered over many years. The low Reynolds numbers encountered in these situations, leads to the assumption of reversible Stokes flow. Taylor (1951) first considered the motion of an infinite sheet undergoing small amplitude oscillation in a very viscous fluid. He demonstrated that a travelling wave can cause the kind of non-reversible motion which is required to drive propulsion at low Reynolds numbers. Taylor also presented one of the principles underlying self-propulsion in a viscous regime, being that the total resultant force which the fluid exerts on to the body must be zero. Chwang and Wu (1971) provide the other defining principle, that of zero resultant torque: these two assumptions underlie all theoretical studies of flagellar motion including computational-fluid-dynamics simulations. Taylor (1952) extended the analysis to three-dimensional flow around a cylindrical body undergoing planar small amplitude beating and produced a model sperm, which swam by using a propagating spiral wave.

Hancock (1953) introduced the term *Stokeslet* for the singularity solution due to a point-force in Stokes flow. He used a distribution of Stokeslets and potential-dipoles with varying strength to model the flow due to finite amplitude beats of a flagellum – this method later is refined to become *slender-body theory*. Slender-body theory provides a more efficient method for modelling cell movement and fluid flow in a 3D domain than by solving the Stokes equations directly.

A slender-body falling in viscous flow has twice as much resistance to motion perpendicular to the long-axis to the slender-body, as to that parallel to it (Hancock, 1953). Thus a slender-body falling longitudinally will fall twice as quickly as the same body falling transversely (the force applied in this case is assumed constant and equal to the body's weight). In this context it means that for a certain force, it may be advantageous for the flagellum to be moved perpendicular to the direction of flow. This highlights a hydrodynamic advantage to certain types of flagellar beating. The ratio of normal to tangential resistance being larger than one is a defining feature of swimming at low Reynolds numbers.

A local approximation to slender-body theory is *resistive-force theory* which was developed by Gray and Hancock (1955) to model the sinusoidal planar beating of the flagellum of sea-urchin sperm. The flagellum is considered as a series of small cylinders; on each cylinder the force is calculated using estimated 'resistance coefficients' which suppose the force on an element of the flagellum is proportional to the relative velocity of the segment and the fluid. Additional progress was made by Batchelor (1970) who placed a series of Stokeslets along the centreline of a long thin, but arbitrarily cross-sectioned body and Cox who considered similar slender-bodies asymptotically in an undisturbed medium and shear flows (Cox, 1970, 1971).

Machin (1958) considered the motion of a flagellum as an elastic beam attached to the head, from where all the motion was derived; the inability of the model to accurately predict observed beat patterns demonstrated that an internal mechanism was required. Machin (1963) also demonstrated that nearby flagella will tend to synchronise. Sperm flagella have a '9 + 2' axoneme structure, which provides the motive power along the length of the flagellum (Debuse, 1998). Pironneau and Katz (1974) utilised resistive-force theory, in the case of small amplitude flagellar beating to obtain an optimally efficient beat pattern.

Katz et al. (1975), whilst considering the motion of a slender-body near to and parallel to a surface using resistive-force theory, noted that resistive-force theory was only strictly valid for small amplitude motions and suggested that a new approach was needed. Improving computing ability enables numerical solutions of the slender-body theory integral equations for the force distribution required on the flagellum to be taken easily. There are two approaches: (1) applying surface-velocity collocation directly to Hancock's slender-body theory, as in Higdon (1979a,c); Liron and Mochon (1976), or (2) to approximate Hancock's representation based on 'integrating out' the local Stokeslet/dipole contribution, as used by Lighthill (1976) and subsequently by Dresdner et al. (1980); Gueron and Liron (1992); Fulford et al. (1998); Gueron and Levit-Gurevich (2001).

Dresdner et al. (1980) developed a theory which extracted the local contributions due to the normal and tangential motions, and allowed an iterative approach to solving for the unknown force distribution using an initial estimate gained through using resistive-force theory. The cell-body was modelled as spherical, and the concept of the *effective radius* was introduced: that is to model the sperm's head as a sphere with the same volume as a real head. Typically, for human sperm, the effective radius is 1.25μm. This technique was used in a number of papers to investigate forces, torques and power consumptions of sperm in physiological scenarios (Dresdner and Katz, 1981; Baltz et al., 1988; Drobnis et al., 1988).

The application of the surface-velocity collocation method was used by Liron and Mochon (1976); the flagellum was divided in to sections over which the force was assumed constant. This discretisation leads to a matrix equation, whose entries are the Stokeslet/dipole integral equations, which must be solved to find the force coefficients. The integrals were approximated using a 'midpoint' value of the Stokeslet on each segment. Higdon (1979a) utilised the same technique, but evaluated the integrals directly using a change of co-ordinate system. An iterative solution scheme was used. With modern technology, the accurate evaluation of Stokeslet integrals is achieved using Gauss Quadrature (Stroud and Secrest, 1966), and the resulting matrix equations can be solved either directly or iteratively. The method of modelling finite amplitude flagellar motion devised by Higdon (1979a,c) is accurate and modifiable, and shall be exploited extensively in this study.

A boundary-integral method for modelling non-spherical heads was developed by Phan-Thien et al. (1987) who modelled a spheroid cell body propelled by a helical tail. His results agreed with the slender-body theory of Higdon (1979c). A combined boundary-integral slender-body model has been devised by Smith et al. (2008a) (based on work by Pozrikidis (1992, 2002)) which utilised a more physiologically realistic spade-shaped head.

Ramia et al. (1993) developed the technique to model three-dimensional helical swimming near a circular plate; efficient computational methods were developed for solving the time-dependent problem which arises once the rotational symmetry of the problem is broken due to the presence of a boundary.

One of the over-riding factors of many of the studies is the focus on helical beat patterns. In reality, this type of beat pattern is rarely observed in sperm: an exception being sea-urchin sperm which can be induced to swim with a helical pattern at high viscosities (Woolley and Vernon, 2001). Physically the observed beat pattern is a result of the driving mechanisms of the flagellum and the external fluid dynamics – the systems are inherently coupled (Fauci and Dillon, 2006). From the computational standpoint, Fauci and McDonald (1995) devised an approach using an immersed boundary method for a 2D sperm moving near a boundary or two other sperm cells, where the waveform becomes an emergent property of the coupled fluid-structure problem, influenced by the internal mechanics and the rheology. Dillon et al. (2007) developed a coupled model of the internal generation of force, the passive elastic mechanics of microtubules and forces due to the nexin link with a surrounding incompressible fluid. The results are considered for both viscous and viscoelastic fluids. The internal mechanism that produces the modes of beating is not fully understood and is an area of ongoing study; two models for the internal generation of bending are Lindemann's geometric control model (Lindemann, 2007) and Brokaw's curvature history control model (Brokaw, 2002), which we shall discuss further in Chapter 5.

1.4.2 Development of mathematical models of peristaltic flows

The study of peristaltic flows can be traced back to Taylor (1951), who considered them whilst discussing the motion of microscopic organisms illustrating how a self-contained 'waving sheet' is sufficient to drive fluid motion. Later study was motivated by an interest in fluid transport and the use of peristaltic pumps in biomedical and industrial settings where contact of the fluid with a physical blade or impeller needs to be avoided. Burns and Parkes (1967), Hanin (1968), Fung and Yih (1968) and Shapiro et al. (1969) produced a series of papers which considered the solution for two-dimensional geometries, with analytic progress being made for axisymmetric geometries by Burns & Parkes and Shapiro et al. Solutions were presented for zero Reynolds number by Burns & Parkes and Shapiro et al, whilst Hanin and Fung & Yih presented solutions for arbitrary Reynolds numbers; other authors such as Zien and Ostrach (1970) required small, but not necessarily zero, Reynolds numbers. All, except Shapiro et al., assumed that the amplitude ratio, the ratio of wave amplitude to unperturbed height, was small. All the models considered were for Newtonian fluids. A review of this early work was published by Jaffrin and Shapiro (1971), who compared existing experimental work with asymptotic solutions and demonstrated good agreement.

Two interesting phenomena were predicted and observed experimentally by Shapiro et al. (1969), those of reflux and trapping. Their experimental setup consisted of a quasi two-dimensional channel (wide enough to ignore 3D effects in the centre) formed with a PVC tube and adjustable finger to mimic the peristaltic wave. Reflux is a situation where there is fluid flow in the opposite direction to that of the travelling peristaltic wave, and trapping is a situation where a circulating bolus of fluid is transported at the wave speed, as if it were trapped by the wave. Yin and Fung (1971) produced experimental data to support the theory of reflux; they observed channel flow in a rectangular cross section with fixed side and top walls and a travelling wave along the bottom, using injected dyes. Particle transport in two-dimensional peristaltic flow was studied experimentally by Hung and Brown (1976) who demonstrated the reflux and trapping phenomena, and also the effect of the Reynolds number on the particle's trajectory. Non-Newtonian characteristics were studied by Böhme and Friedrich (1983) by considering a low Reynolds number linear Maxwell viscoelastic fluid. They found that the optimal wave speed corresponds to the memory of the fluid particles extending over several periods of the wave; however, maximum efficiency (defined as the ratio of useful power to applied power) corresponds to the Newtonian limit, that is as the Maxwell 'memory' term tends to zero.

Mittra and Prasad (1974) presented solutions for the effect of Poiseuille flow, due to a pressure gradient, on peristaltic transport using a two-wall sinusoidal model; it was found that the mean flow reversal is strongly dependent on the Poiseuille flow, and that the position of reversal can vary significantly from the centre of the channel to the boundaries.

The study of Srivastava and Srivastava (1985) considered peristaltic flow applied to the male reproductive system and the motion of a 'power-law' fluid in the *vas deferens* using a zero Reynolds number and long-wavelength approximation. The theoretical flow rates compare favourably with experimental data from fluid flow in the *vas deferens* of rhesus monkeys and flow in the human small intestine. Pozrikidis (1987) considered the motion of flow in a two-dimensional channel with sinusoidal waves applied through the use of boundary integral methods for Stokes flow and results achieved agreed with earlier analytic solutions (Burns and Parkes, 1967; Shapiro et al., 1969; Yin and Fung, 1971).

Brasseur et al. (1987) conducted a detailed analysis of the effect of the peripheral layer; that is a thin layer of a different fluid near the boundary, on the bulk fluid motion, and conclude that a more viscous layer near the boundary improves pumping performance while a less-viscous boundary-layer impairs pumping. The assumption of an infinite wave train was relaxed by Li and Brasseur (1993), who considered an arbitrary wave shape and wavenumber for tubes of finite length, meaning the problem could not be reduced to a steady problem in the wave frame. In particular, they studied the effect of a single peristaltic wave against a 'wave train' and offer evidence to suggest that greater reflux is observed in the case of a single wave compared to a wave train, under the lubrication approximation, with zero Reynolds numbers in an axi-symmetric geometry.

The majority of models prescribe the position of the peristaltic walls, however, Nicosia and Brasseur (2002) consider a model of the muscular wall mechanics and from this they derive the peristaltic motion of the wall of the oesophagus whilst moving a bolus of food. The model proposed decomposes the oesophageal muscular movement into longitudinal and circular components and after solving these equations, with suitable constitutive equations, considered the motion of an elastic bolus of food.

There are a number of reasons for neglecting feedback and thus prescribing the position of, in this case, the walls. Firstly, by making this assumption of neglecting feedback the complexity of the problem is greatly reduced. It is also the case that often we do not understand entirely the complexities of the underlying physiology, and moreover, even in situations where the mechanism is understood physically, we may not be able to model the problem accurately mathematically. It is worth noting that when we observed the system *in vivo*, the experimental data we observed is already the result of the coupled processes including the feedback.

The problem of a long-wavelength, low-Reynolds number approximation is revisited for Newtonian flow by Mishra and Rao (2003) using an infinite wave train, as a solution in powers of the wavenumber. They demonstrate that the phenomena of reflux and trapping are at a maximum when the channel is symmetric. The same authors also consider the same problem by utilising a domain transformation, (Rao and Mishra, 2004a), which maps the channel into a domain of uniform cross section where higher order analysis is more tractable. The authors also note that the effects of the Reynolds number and asymmetry may play an important role in the development of mixing, but do not suggest any particular biological applications.

Rao and Mishra (2004b) consider peristaltic flow under the long-wavelength, low-Reynolds number approximation, with a power law fluid in an axi-symmetric tube. The Beavers-Joseph and Saffman type slip boundary conditions (Beavers and Joseph, 1967; Saffman, 1971) are applied on the surface of the tube which is assumed to be porous.

Peristalsis works as a pump against the increased pressure observed with a shear thickening fluid and the opposite for shear thinning fluid. The trapping phenomena is observed to decrease as the ‘behaviour index’ is reduced from shear thickening to shear thinning fluids.

In the area of reproductive biology, Eytan and Elad (1999) and Eytan et al. (1999) have considered the flow of fluid in the uterus as a result of the peristaltic contraction of the uterine walls with experimentally derived parameters for the spacing of the walls, the amplitude, frequency and phase shift of the waves. The lubrication approximation is used, and the motion is considered as channel flow between two walls with sinusoidal travelling waves which are not necessarily in phase. In Eytan et al. (2001b) clinical ultrasound data was processed to obtain new characteristic features of the intrauterine fluid-wall interface such as the existence of both downward (toward the cervix) and smaller upward (toward the ovaries) propagating waves.

Hydrosalpinx is a condition whereby one, or both, oviducts become blocked, and become substantially distended and filled with fluid. The condition of hydrosalphinx has a known effect on the success rate of IVF treatment; Strandell et al. (1994, 1999, 2001) found that the pregnancy rate for patients with persistent hydrosalpinx was only half that of patients with other types of oviductal damage. Using the model of uterine peristalsis, Eytan et al. (2001a) considered uterine fluid dynamics to model problems associated with IVF embryo implantation for women with hydrosalphinx. They found that the existence of areas of reflux may cause an embryo to be swept away from ideal site of fertilisation, which may lead to a failure of implantation or an ectopic pregnancy (implantation of the embryo in the lining of the oviduct, rather than uterus)

In Eytan et al. (2001c) the authors adopt a tapered two-dimensional geometry for the wall, and show that the transport phenomena are strongly dependent on the phase shift of wall displacement and the phase angle between the walls. Yaniv et al. (2003) uses a finite element code to simulate the effect of embryo transfer in to the fluid-filled uterus, modelled as two-dimensional channel with oscillating walls, and conclude that, at normal injection rates, the presence of a catheter in the uterus only affects the nature of the flow within around 1mm of the catheter (catheter has diameter 0.3mm). The speed at which the embryo is introduced from the catheter into the uterus is the main factor in determining its eventual location. If the embryo is introduced at the same order of magnitude as the peristaltic wave (0.5mm/s), then the eventual position is determined by the natural peristaltic wave. If the embryo is introduced at an ‘excessively high injection speed’ (8 times the peristaltic wavespeed) then an ectopic pregnancy may develop.

The work of Eytan et al, does not consider the effect of the cilia which line uterine and oviductal surfaces; their rationale is that cilia are much smaller than the size of the ovum and thus will not be effective in moving the ovum. However, work by Blake et al. (1982), shows that the fluid flow caused by the cilia is sufficient to provide a mechanism for the motion of the ovum in the oviduct. This is also shown in the mathematical models of Anand and Guhal (1978) where using anatomical data for flow in the oviduct, ciliary beating may lead to ovum movement at near normal rates in the absence of peristalsis.

1.4.3 Methods for modelling ciliary driven flows

The modelling of the fluid motion due to cilia draws on the combined studies of flagellar and peristaltic propulsion. In particular, we could consider an array of cilia under the singularity and slender-body theory method (Blake, 1972) or we could suppose that the overall effect of the cilia could be modelled using an envelope placed on the ciliary tips (Ross and Corrsin, 1974).

The advantage of the singularity method is obvious in terms of details, however, as we require a large array of cilia the computational power required to solve such problems becomes a limiting factor. A continuous approximation to the singularity method is the traction-layer method (Keller et al., 1975). The approximation is valid provided the cilia density is sufficiently high, however, in making this approximating any information relating to the motion of an individual cilium is lost. Blake et al. (1982) applied the traction-layer method for flow in the human oviduct along with a single non-travelling wave model of peristalsis and illustrated that the ciliary component of the flow was important as it could drive flow in the oviduct.

In this thesis we shall adopt the envelope model as this can be seen to be very similar to our modelling approach adopted for peristaltic flows and hence adding ciliary effects to peristaltic flows is an achievable extension.

1.5 Fluid mechanics

In this section we outline the fundamental fluid dynamics which is relevant to this study. In preparation for the application of slender-body theory and singularity methods to the problem of sperm propulsion and the subsequent optimisation which follows, we discuss the fundamental singularity of Stokes flow, otherwise known as the Stokes flow Green's function or more commonly the *Stokeslet*.

1.5.1 Equations of fluid motion

The governing equations of fluid dynamics are derived from the principles of the conservation of momentum and the conservation of mass applied to a fluid particle under the continuum hypothesis. Adopting the standard index notation and the summation convention the basic equations for fluid flow are

$$\rho\left(\frac{\partial u_i}{\partial t}+u_j\frac{\partial u_i}{\partial x_j}\right)=\frac{\partial \sigma_{ij}}{\partial x_j}+\rho F_i, \tag{1.1a}$$

$$\frac{\partial \rho}{\partial t}+\frac{\partial\left(\rho u_k\right)}{\partial x_k}=0. \tag{1.1b}$$

where the parameters are defined as follows: velocity $\boldsymbol{u}=(u_1,u_2,u_3)$, density ρ, the stress tensor $\boldsymbol{\sigma}$ and body force $\boldsymbol{F}$.

1.5.2 Constitutive relation

Fluid behaviour can be categorised by the variation in shear stress on the rate of strain; mathematically this is embedded through a constitutive relation between the rate of strain and the shear stress.

The simplest relationship for the constitutive relation is linear and fluids which follow this model are termed *Newtonian*. Many fluids, including water, obey this simple linear relationship and it is these types of fluids which we shall consider in this thesis. If, however, the relationship is non-linear then the fluid is termed *non-Newtonian*. Mucus and blood are examples of biological fluid which are non-Newtonian (Wolf et al., 1977a; Quemada, 1993).

1.5.3 Navier-Stokes equations

The constitutive equation for an incompressible Newtonian fluid is

$$\sigma_{ij} = -p\delta_{ij} + \mu e_{ij}, \tag{1.2}$$

with $e_{ij} = \partial u_i/\partial x_j + \partial u_j/\partial x_i$. By combining this equation with the statements of conservation of mass and momentum (Equation (1.1)) we gain the following famous *Navier-Stokes equations* viz.

$$\rho\left(\frac{\partial u_i}{\partial t} + u_j\frac{\partial u_i}{\partial x_j}\right) = -\frac{\partial p}{\partial x_i} + \mu\frac{\partial^2 u_i}{\partial {x_j}^2} + \rho F_i \tag{1.3a}$$

$$\frac{\partial u_k}{\partial x_k} = 0. \tag{1.3b}$$

Equation (1.3a) is the momentum balance equation and Equation (1.3b) is the mass conservation equation, or simply, the continuity equation.

1.5.4 Non-dimensionalisation of the Navier-Stokes equations

The Navier-Stokes equations can be non-dimensionalised by scaling lengths by a typical length scale L, velocities by a typical velocity U, and time by a typical frequency ω. Upon rescaling two non-dimensional groups of parameters are derived; the Womersley parameter α and the Reynolds number Re defined as

$$\alpha^2 = \frac{\omega L^2}{\nu} \quad \text{and} \quad \mathrm{Re} = \frac{UL}{\nu}, \tag{1.4}$$

where $\nu = \mu/\rho$ is the kinematic viscosity. The Reynolds number is a measure of the ratio of inertial to viscous effects in the flow. Flows where the Reynolds number is small ($\ll 1$) are dominated by viscous forces and are discussed in depth below.

The dimensionless Navier-Stokes equations are

$$\alpha^2 \frac{\partial \widehat{u}_i}{\partial \widehat{t}} + \mathrm{Re}\, \widehat{u}_j \frac{\partial \widehat{u}_i}{\partial \widehat{x}_j} = -\frac{\partial \widehat{p}}{\partial \widehat{x}_i} + \frac{\partial^2 \widehat{u}_i}{\partial \widehat{x}_j^2} + \widehat{F}_i, \qquad \frac{\partial \widehat{u}_k}{\partial \widehat{x}_k} = 0. \tag{1.5}$$

One should notice that the velocity, pressure and force are now non-dimensional quantities identified with 'hats'.

1.5.5 Re $\ll 1$: The Stokes equations

As an example of why it is appropriate to consider the zero Reynolds number limit of the Navier-Stokes equations we shall consider some typical values for the length scale, velocity scale and viscosities associated with sperm motility, a situation which we shall discuss later. For the case of a single sperm swimming, a typical length scale is its length which is O(10^{-4}m), and a sperm will typically swim no more than a body length per second, hence typical velocities are O(10^{-4}ms^{-1}). Kinematic viscosities range from 'watery media' at O(10^{-6}m^{2}s^{-1}) to 'viscous media' at O(10^{-3}m^{2}s^{-1}). The upper-bound for the Reynolds number is therefore O(10^{-2}).

Taking the limit as Re → 0 gives the equations of *unsteady Stokes Flow*,

$$\alpha^2 \frac{\partial \widehat{u}_i}{\partial \widehat{t}} = -\frac{\partial \widehat{p}}{\partial \widehat{x}_i} + \frac{\partial^2 \widehat{u}_i}{\partial \widehat{x}_j^2} + \widehat{F}_i, \qquad \frac{\partial \widehat{u}_k}{\partial \widehat{x}_k} = 0. \tag{1.6}$$

One should notice that in this limit of zero Reynolds number the flow is driven by viscous effects and the non-linearity of the Navier-Stokes equations is removed.

The Womersley parameter α^2, can be estimated in a similar fashion and provided that frequencies are no larger than $O(10^2\text{Hz})$, then $\alpha^2 \ll 1$. Typical beat frequencies of the flagellum in sperm are of the order of $10 - 20\text{Hz}$, which ensures that $\alpha^2 \ll 1$ is a valid assumption, thus allowing us to take the limit of $\alpha^2 = 0$ resulting in the reduction of Equation (1.6) to the equations of quasi-steady *Stokes Flow*:

$$\frac{\partial \widehat{p}}{\partial \widehat{x}_i} = \frac{\partial^2 \widehat{u}_i}{\partial \widehat{x}_j^2} + \widehat{F}_i \qquad \frac{\partial \widehat{u}_k}{\partial \widehat{x}_k} = 0. \tag{1.7}$$

That is to say the pressure gradient and body forces are balanced by viscous effects subject to the continuity equation.

1.5.6 Fundamental singularity of Stokes flow: The Stokeslet

The Stokeslet is the Green's function of Stokes flow with a point force as the only body force $\boldsymbol{F}(\boldsymbol{x}) = \boldsymbol{f}\delta(\boldsymbol{x})$ ($\boldsymbol{f} \in \mathbb{R}^3$) at the point $\boldsymbol{x} = \boldsymbol{0}$. The governing (dimensional) Stokes equations are

$$0 = -\nabla p + \mu \nabla^2 \boldsymbol{u} + \boldsymbol{F}, \qquad \nabla \cdot \boldsymbol{u} = 0, \tag{1.8}$$

where $\boldsymbol{u} \in \mathbb{R}^3$ and $p \in \mathbb{R}$, with the far-field conditions $|\boldsymbol{u}| \to 0$ as $|\boldsymbol{x}| \to \infty$.

The solution for u_j and p to Equation 1.8 is

$$u_j = \frac{f_k}{8\pi\mu}\left(\frac{\delta_{jk}}{|\boldsymbol{x}|} + \frac{x_j x_k}{|\boldsymbol{x}|^3}\right), \tag{1.9a}$$

$$p = -\frac{f_k x_k}{4\pi|\boldsymbol{x}|} \tag{1.9b}$$

The equation for u_j (Equation 1.9a) is often written as $u_j = S_{jk} f_k$, where S_{jk} is the fundamental solution of the Stokes Equations, often known as the *Stokeslet*

$$S_{jk} = \frac{1}{8\pi\mu}\left(\frac{\delta_{jk}}{|\boldsymbol{x}|} + \frac{x_j x_k}{|\boldsymbol{x}|^3}\right). \tag{1.10}$$

The derivation of this result can be found in Appendix B.

Physically, Equations (1.9) represents the velocity field $\boldsymbol{u}$ and pressure field p, due to a point force $\boldsymbol{f}$ at the origin in an unbounded fluid. Mathematically, the Stokeslet is the free-space Green's function for Stokes equations (1.8). Green's Theorem enables us to conclude that the flow about a collection of finite bodies may be represented by a distribution of Stokeslets, and their normal derivatives over body surfaces; these derivatives are known as *higher-order singularities* and some are discussed below. This is the basis of the very powerful boundary-integral method. In connection with slender-body theory and the centre-line theory which we shall employ, in principle it is possible to use a Green's function approach to provide a method for solving many problems posed in Stokes flow (Higdon, 1979c).

1.5.7 Higher-order singularities

Due to the linearity of the Stokes flow equations, any derivative of the fundamental solution the Stokeslet will, in infinite space, be a solution to the original problem. A number of other singularities can be derived in this fashion and here we outline some of them

The first derivative of the Stokeslet is known as the *Stokes-doublet* and is expressed, using the summation convention, as

$$
\begin{aligned}
u_i &= \frac{d_{jk}}{8\pi\mu}\left[\frac{\delta_{ij}x_k}{|\boldsymbol{x}|^3} - \frac{\delta_{ik}x_j}{|\boldsymbol{x}|^3} - \frac{\delta_{jk}x_i}{|\boldsymbol{x}|^3} + \frac{3x_ix_jx_k}{|\boldsymbol{x}|^5}\right],\\
p &= \frac{d_{jk}}{4\pi}\left[-\frac{\delta_{jk}}{|\boldsymbol{x}|^3} + \frac{3x_jx_k}{|\boldsymbol{x}|^5}\right],
\end{aligned}
$$

where d_{jk} is defined as the strength of the Stokes-doublet, which may be interpreted as the negative value of the gradient in the k-direction of a Stokeslet orientated in the j direction. We notice that the Stokes-doublet terms may be split into symmetric and anti-symmetric terms as follows (Blake and Chwang, 1974)

$$
u_i^S = \frac{d_{jk}}{8\pi\mu}\left[-\frac{\delta_{jk}x_i}{|\boldsymbol{x}|^3} + \frac{3x_ix_jx_k}{|\boldsymbol{x}|^5}\right], \qquad p^S = \frac{d_{jk}}{4\pi}\left[-\frac{\delta_{jk}}{|\boldsymbol{x}|^3} + \frac{3x_jx_k}{|\boldsymbol{x}|^5}\right]. \tag{1.11a}
$$

$$
u_i^A = \frac{d_{jk}}{8\pi\mu}\left[\frac{\delta_{ij}x_k - \delta_{ik}x_j}{|\boldsymbol{x}|^3}\right], \qquad p^A = 0. \tag{1.11b}
$$

Equation (1.11a) is defined as a *stresslet* and corresponds to straining motion. The anti-symmetric term, Equation (1.11b), corresponds to rotational motion and is called a *rotlet* or a *couplet*. Alternatively the rotlet may be defined as

$$
u_i^A = \frac{\varepsilon_{ijk}\Omega_j x_k}{8\pi\mu|\boldsymbol{x}|^3},
$$

where Ω_j is the rotation vector, and $d_{jk}(\delta_{ij} - \delta_{ik}\delta_{jk}) = \varepsilon_{ijk}\Omega_j$, where ε_{ijk} is the permutation symbol. The *permutation symbol* or *Levi-Civita symbol* ε_{ijk} is defined as follows

$$
\varepsilon_{ijk} = \begin{cases} +1 & \text{if } (i,j,k) \in \{(1,2,3),(2,3,1),(3,1,2)\},\\ -1 & \text{if } (i,j,k) \in \{(3,2,1),(1,3,2),(2,1,3)\},\\ 0 & \text{otherwise.} \end{cases}
$$

A force diagram, such as that shown in Figure 1.10, can be used to demonstrate the

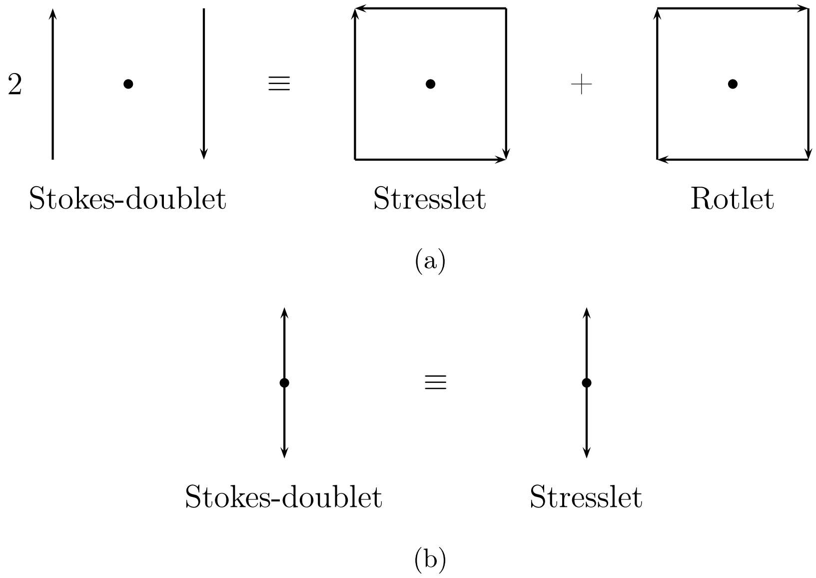

Figure 1.10: (a) Decomposition of the Stokes-doublet into a symmetric stresslet term and the antisymmetric rotlet term. (b) A symmetric Stokes-doublet is identical to a stresslet. Redrawn from Blake and Chwang (1974).

decomposition of a Stokeslet-doublet into component parts.

The process may be continued and the second-derivative of the Stokeslet is known as the *Stokes-quadrupole.*

1.5.8 Image systems

The theory derived thus far has considered the flow due to a point source in an infinite domain. Clearly most physical flows have boundaries where the standard no-slip boundary condition needs to be applied. The no-slip boundary conditions asserts that a fluid particle on a boundary will move with the boundary; ie, the velocity of the boundary will be equal to the fluid velocity on the boundary.

One of the situations we shall encounter is flow due to a point force in the presence of a sphere, the point force being external to the sphere. The required image system was derived by Oseen (1927).

Image system for a sphere

The velocity at a point $\boldsymbol{x}$ due to a point force $\boldsymbol{f}$ at the point $\boldsymbol{X}$ in the presence of a sphere of radius A centred at the origin is given by

$$u_j(\boldsymbol{x}) = \left[S_{jk}(\boldsymbol{x},\boldsymbol{X}) + S^{\star}_{jk}(\boldsymbol{x},\boldsymbol{X})\right] f_k, \tag{1.12}$$

for $|\boldsymbol{x}| > A$ and $|\boldsymbol{X}| > A$. S_{jk} is the standard expression for the Stokeslet and $S^{\star}_{jk}$ is the image system defined as follows:

$$\begin{aligned} S^{\star}_{jk}(\boldsymbol{x},\boldsymbol{X}) = \frac{1}{8\pi\mu}\Bigg(&-\frac{A}{|\boldsymbol{X}|}\frac{\delta_{jk}}{r^{\star}} - \frac{A^3}{|\boldsymbol{X}|^3}\frac{(x_j - X^{\star}_j)(x_k - X^{\star}_k)}{r^{\star 3}} \\ &- \frac{|\boldsymbol{X}|^2 - A^2}{|\boldsymbol{X}|}\Bigg\{\frac{X^{\star}_j X^{\star}_k}{A^3 r^{\star}} - \frac{A}{|\boldsymbol{X}|^2 r^{\star 3}}\left[X^{\star}_j(x_k - X^{\star}_k) + X^{\star}_k(x_j - X^{\star}_j)\right] \\ &+ \frac{2X^{\star}_j X^{\star}_k}{A^3}\frac{X^{\star}_l(x_l - X^{\star}_l)}{r^{\star 3}}\Bigg\} - (|\boldsymbol{x}|^2 - A^2)\frac{\partial\phi_k}{\partial x_j}\Bigg) \end{aligned} \tag{1.13a}$$

with

$$\begin{aligned} \frac{\partial\phi_k}{\partial x_j} = \frac{|\boldsymbol{X}|^2 - A^2}{2|\boldsymbol{X}|^3}\Bigg\{ &-\frac{3X_k(x_j - X^{\star}_j)}{Ar^{\star 3}} + \frac{A\delta_{jk}}{r^{\star 3}} - \frac{3A(x_j - X^{\star}_j)(x_k - X^{\star}_k)}{r^{\star 5}} \\ &- \frac{2X_k X^{\star}_j}{Ar^{\star 3}} + \frac{6X_k}{A^5}(x_j - X^{\star}_j)(x_l - X^{\star}_l)X^{\star}_l \\ &+ \frac{3A}{|\boldsymbol{X}^{\star}|}\left[\frac{X^{\star}_k(x_j - X^{\star}_j)r^{\star 2} + (x_j - X^{\star}_j)(x_k - X^{\star}_k)|\boldsymbol{X}^{\star}|^2 + (r^{\star} - |\boldsymbol{X}^{\star}|)r^{\star 2}|\boldsymbol{X}^{\star}|\delta_{jk}}{r^{\star 3}|\boldsymbol{X}^{\star}|(|\boldsymbol{X}^{\star}|r^{\star} + x_l X^{\star}_l - |\boldsymbol{X}^{\star}|^2)}\right] \\ &- \frac{3A}{|\boldsymbol{X}^{\star}|}\left[\frac{(|\boldsymbol{X}^{\star}|(x_k - X^{\star}_j) + r^{\star}x^{\star}_j)(X^{\star}_k r^{\star 2} - (x_k - X^{\star}_k)|\boldsymbol{X}^{\star}|^2 + (x_k - 2X^{\star}_k)r^{\star}|\boldsymbol{X}|)}{r^{\star 2}|\boldsymbol{X}^{\star}|(|\boldsymbol{X}^{\star}|r^{\star} + x_l X^{\star}_l - |\boldsymbol{X}^{\star}|^2)^2}\right] \\ &- \frac{3A}{|\boldsymbol{X}^{\star}|}\left[\frac{x_j X^{\star}_k + |\boldsymbol{x}||\boldsymbol{X}^{\star}|\delta_{jk}}{|x||\boldsymbol{X}^{\star}|(|\boldsymbol{x}||\boldsymbol{X}^{\star}| + x_l X^{\star}_l)}\right] + \frac{3A}{|\boldsymbol{X}^{\star}|}\left[\frac{(|\boldsymbol{X}^{\star}|x_j + |\boldsymbol{x}|X^{\star}_j)(|\boldsymbol{X}^{\star}|x_k + |\boldsymbol{x}|X_k)}{|x||\boldsymbol{X}^{\star}|(|\boldsymbol{x}||\boldsymbol{X}^{\star}| + x_l X^{\star}_l)^2}\right]\Bigg\} \end{aligned} \tag{1.13b}$$

where $\boldsymbol{X}^\star$ is the inverse point defined by

$$\boldsymbol{X}^\star = \frac{A^2}{|\boldsymbol{X}|^2}\boldsymbol{X}, \tag{1.13c}$$

and $r = |\boldsymbol{x} - \boldsymbol{X}|$ with $r^\star = |\boldsymbol{x} - \boldsymbol{X}^\star|$.

$S^\star_{jk}$ can be understood as those components necessary to provide the correct boundary condition of no-slip on the surface of the sphere. For the radial component of the Stokeslet, the images required are a Stokeslet, dipole and a stresslet at the inverse point. For the transverse component, the images are a line distribution of Stokeslets, dipoles and Stokes-doublets extending from the origin to the inverse point.

1.5.9 Advantages of the singularity method

The use of the singularity method for the solution of Stokes flow equations is tractable and the process, as we discuss later, involves writing down the velocity in the fluid as a sum (or integral) of a number (or distribution) of singularities; since the equations are linear hence solutions may be summed. The boundary conditions are typically no-slip on surfaces and no flow in the far field. The singularities need to have the correct strength in order to satisfy the no-slip boundary conditions and the determination of these coefficients is the unknown in the problem. Thus by using singularity methods the solution can be derived by solving a series of equations along a line rather than at each point in the bulk flow; ie, a three-dimensional problem is reduced to a one-dimensional one, which is a considerable simplification.

1.6 The structure of this thesis

The structure of this thesis is outlined below.

The first part of the thesis concentrates on modelling and optimising sperm beat patterns. In Chapter 2, we follow closely the classical model of slender-body theory for helical flagellar propulsion devised by Higdon (1979c), making adaptations where necessary (such as allowing planar beating) to allow for the work in the following chapters. Chapters 3 and 4 are two studies which are carried out using a novel modified envelope function and wavenumber specification for the beat pattern based on a planar sinusoidal beat pattern – in order to account for some of the variation observed in the experimental work which is discussed in this thesis.

In Chapter 5, a new model for modelling sperm beat patterns is developed. Using analysis of experimental data, a new specification for the beat pattern is made using the shear-angle with only a small number of parameters. Despite the small number of parameters, a large spectrum of beat patterns observed *in vitro* is encompassed by the new model. The new kinematic model is then studied using slender-body theory in the optimisation frame work and we offer an explanation for the modulation in beat pattern observed in experiments.

In Chapter 6 we consider a mathematical model for flow in a general two dimensional peristaltic channel, and discuss some special cases using analysis of pathlines, flowrates and Lyapunov exponents. We consider the system using the envelope model for cilia as a small perturbation on top of a larger peristaltic wave.

Finally in Chapter 7, we present conclusions of the work in this thesis and indicate some further developments which could follow; in particular we highlight future uses of the new model from Chapter 5.

In the Appendices we present background information relating to our problems; specifically, the experimental methods and data processing (Appendix A), the derivation of the Stokeslet (B), details of the numerical implementation of the slender-body theory code (C.1), finite difference scheme (C.2) and the calculation of the local Lyapunov exponents (C.3).

Appendix D is a copy of a paper cowritten with JR Blake and EO Tuck regarding the S-transform, its properties and use in slender-body theory in Stokes flow. Originally intended as a method to transform integrals into linear equations for use in slender-body theory modelling, it was later decided that the numerical approach which we shall adopt is more adaptable.

Supporting movies and videos of experimental and theoretic work can be found at `http://web.mat.bham.ac.uk/∼wakeleyp`.

CHAPTER 2

SLENDER-BODY THEORY FOR A FLAGELLATED CELL

2.1 Introduction

In this chapter we develop the application of slender-body theory to the motion of a single flagellated cell in an infinite Newtonian fluid following the concepts of Higdon (1979a,b,c). The underlying mathematical model uses slender-body theory and singularity methods to determine the solution for the induced fluid flow as a combination of the effects of the head and the flagellum.

Higdon's original papers considered the problem for a three-dimensional helical beat pattern. Using his concept we develop a computer code capable of handling a greater variety of beat patterns such as planar beat patterns, which we shall utilise later in this thesis. Further details of the computational code are highlighted in Appendix C.1.

2.2 Geometry

Consider a sphere of radius A centered at the origin, attached to a flagellum of constant radius a and length L. The position of the flagellum is known for all values of time and is assumed as known *a priori*. We define a co-ordinate system (X, Y, Z) to have the origin at, and moving with, the centre of the head. It is supposed that relative to a laboratory or 'rest frame' $\mathcal{R}$, the body frame moves with velocity $\boldsymbol{U_0}$ and has angular velocity $\boldsymbol{\Omega_0}$; both of which are to be determined. The original model of Higdon specifies a helical flagellum,

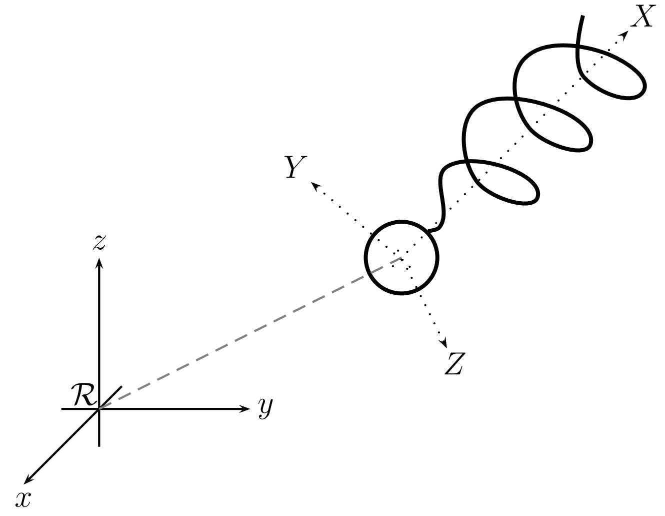

Figure 2.1: The geometry of the problem with a body reference frame centred at the midpoint of the sphere, moving relative to the fixed frame $\mathcal{R}$.

which is coiled around the X axis, as shown in Figure 2.1; we shall discuss this in depth below.

2.3 Slender-body theory

The concept of slender-body theory is that we represent the fluid velocity at a point in a 3D field due to the presence of a slender-body. To model the motion of a flagellum we place a distribution of singularities of Stokes flow along the centreline of the flagellum. The specification of the distribution function, which is equivalent to the force coefficients, is the unknown in the problem. We make the assumption that the distribution function is piecewise constant over small sections of the flagellum. By applying the no-slip boundary condition on the surface of the slender-body, we obtain a series of equations for the values of unknown distribution; this is the collocation method.

When the distribution is found, the velocity of any point in the flow can be calculated by performing the integration along the centre-line using the now known distribution function. An early example of the method, which also has an analytic solution, can be found in the work of Chwang and Wu (1975), where the solution for flow past a pinned prolate-spheroid was considered.

2.3.1 The velocity induced by a flagellum

The velocity induced by the motion of a flagellum is written as a distribution of Stokeslets and dipoles along the centre-line of the flagellum. The choice of Stokeslets and dipoles to model the motion is used as these correspond to translational velocities and have been shown to provide a constant velocity over each cross-section of the flagellum (Higdon, 1979a).

The definitions of the Stokeslet and the dipole are

$$S_{jk}(\boldsymbol{x}, \boldsymbol{X}) = \frac{\delta_{jk}}{r} + \frac{(x_j - X_j)(x_k - X_k)}{r^3}, \tag{2.1a}$$

and

$$D_{jk}(\boldsymbol{x}, \boldsymbol{X}) = -\frac{\delta_{jk}}{r^3} + \frac{3(x_j - X_j)(x_k - X_k)}{r^5}, \tag{2.1b}$$

where these are the free-space Green's functions for a point $\boldsymbol{x}$ due to a force singularity at $\boldsymbol{X}$, with $r = |\boldsymbol{x} - \boldsymbol{X}|$.

The reader should be aware that the definition of the Stokeslet is subtly different from that derived in Section 1.5.6, where our definitions included a divisor of $8\pi\mu$. The reason for the different notation used here is so that this chapter maintain consistency with Higdon who defines his Stokeslets as in Equation (2.1a) (ie, without the divisor of $8\pi\mu$), so that the velocity induced by Higdon's stokeslet is $u_j = S_{jk}f_k/8\pi\mu$ as opposed to our derivation in Section 1.5.6 which gives velocity $u_j = S_{jk}f_k$ as the $1/8\pi\mu$ is already included in the definition of the Stokeslet.

This definition of the Stokeslet and dipole enables us to say that the velocity induced at a point $\boldsymbol{x}$ due to a distribution of Stokeslets and dipoles situated along the centre-line of the flagellum, with force distributions $\boldsymbol{f}$ and $\boldsymbol{d}$ respectively, is given by

$$u_j(\boldsymbol{x}) = \int_0^L \left[S_{jk}(\boldsymbol{x}, \boldsymbol{X}(s)) \frac{f_k(s)}{8\pi\mu} + D_{jk}(\boldsymbol{x}, \boldsymbol{X}(s)) \frac{d_k(s)}{4\pi} \right] \mathrm{d}s. \tag{2.2}$$

where s parameterises the arc-length of the flagellum, measured from the head/tail junction.

It was shown by Lighthill (1976), that the dipole strength $\boldsymbol{d}$ required to ensure that the induced velocity is approximately constant around the flagellar cross section, is determined by the component of the Stokeslet strength normal to the centre-line;

$$d_k = -\frac{a^2}{4\mu}(\delta_{kl} - t_k t_l) f_l \tag{2.3}$$

where $\boldsymbol{t}$ is the unit vector tangent to the flagellum. Recall that a is the radius of the flagellum. This relationship allows us to cast Equation (2.2) as

$$u_j(\boldsymbol{x}) = \int_0^L \left[S_{jk}(\boldsymbol{x}, \boldsymbol{X}(s)) - D_{jl}(\boldsymbol{x}, \boldsymbol{X}(s)) \frac{a^2}{2}(\delta_{lk} - t_l t_k) \right] \frac{f_k(s)}{8\pi\mu} \mathrm{d}s. \tag{2.4}$$

We do not consider the effects of the end of the flagellum here, except to make reference to Tuck (1964) in which the effect of the blunt end is considered; the effect of the blunt end on the rest of the body is shown to be at worst $\mathrm{O}(a/L)$, which with $a = 300$nm and $L = 60\mu$m is $\mathrm{O}(a/L) = 10^{-3}$.

2.3.2 Image system for the head

We need to satisfy the no-slip boundary condition on the surface of the sphere centred at the origin. This can be accomplished in two ways; firstly we could consider a distribution of Stokeslets inside the sphere and solve the integral equation which results from applying the no-slip boundary condition (like for the flagellum); however, this greatly complicates the solution of the problem as we are required to solve an integral equation in two independent variables.

The second method, the method we shall adopt herein, is to utilise Green's functions for the flow external to a sphere in the presence of a point force; this implements the boundary condition without introducing any additional unknowns. The Stokeslets in Equation (2.2) needs to be replaced by a Green's function of the form

$$G_{jk}(\boldsymbol{x}, \boldsymbol{X}) = S_{jk}(\boldsymbol{x}, \boldsymbol{X}) + S^{\star}_{jk}(\boldsymbol{x}, \boldsymbol{X}), \tag{2.5}$$

where S_{jk} is the Stokeslet given in Equation (2.1a) and $S^{\star}_{jk}$ is the image system for the sphere. The expression for $S^{\star}_{jk}$ was derived in Oseen (1927) and is presented in Equation[1] (1.13). The induced fluid velocity due to the point force at $\boldsymbol{X}$ and a sphere of radius A located at the origin is given by

$$u_j(\boldsymbol{x}) = \left[S_{jk}(\boldsymbol{x}, \boldsymbol{X}) + S^{\star}_{jk}(\boldsymbol{x}, \boldsymbol{X})\right] \frac{f_k}{8\pi\mu}.$$

We conclude the velocity induced by the flagellum, with the correction for the boundary condition on the surface of the sphere has the form

$$u_j(\boldsymbol{x}) = \int_0^L \left[S_{jk}(\boldsymbol{x}, \boldsymbol{X}(s)) + S^{\star}_{jk}(\boldsymbol{x}, \boldsymbol{X}(s)) - D_{jl}(\boldsymbol{x}, \boldsymbol{X}(s))\frac{a^2}{2}(\delta_{lk} - t_l t_k)\right] \frac{f_k(s)}{8\pi\mu}\,\mathrm{d}s. \tag{2.6}$$

We have not included the image systems for the dipole in a sphere (the same as Higdon (1979c)) as it is of higher order than the Stokeslet images system and as we shall see later (Section 2.9) the Stokeslet image has negligible effect, therefore the higher order dipole singularity is also negligible.

---

[1] The definition of the Oseen singularity in Section 1.5.8 already contains the factor of $1/8\pi\mu$, however, to maintain consistency in this chapter with Higdon the $S^{\star}_{jk}$ used does not contain this factor and thus it must be re-introduced (as is the case for the way Higdon defined the Stokeslet above).

2.3.3 Evaluating the integrals

In order to evaluate the integral in Equation (2.6), we suppose that the flagellum is split up into N intervals, of not necessarily uniform length. We assume that over each of these intervals the value of $\boldsymbol{f}$ is constant, and equal to $\boldsymbol{f}(s_n)$, where $n = 1, \ldots, N$. It is noted that none of the functions to be integrated are singular within the domains in which we shall be evaluating them; in particular notice that $S^{\star}_{jk}$ is singular inside the sphere, but as integration extends along the flagellum the singularities are avoided.

This 'meshing' allows us to approximate Equation (2.6) as

$$u_j(\boldsymbol{x}) = \sum_{n=1}^{N} K_{jk}(\boldsymbol{x}, \boldsymbol{X}(s_n)) f_k(s_n) \tag{2.7a}$$

where

$$\begin{aligned} &K_{jk}(\boldsymbol{x}, \boldsymbol{X}(s_n)) \\ &\quad = \int_{s_n-\delta s_n}^{s_n+\delta s_n} \left[S_{jk}(\boldsymbol{x}, \boldsymbol{X}(s)) + S^{\star}_{jk}(\boldsymbol{x}, \boldsymbol{X}(s)) - D_{jl}(\boldsymbol{x}, \boldsymbol{X}(s)) \frac{a^2}{2}(\delta_{lk} - t_l t_k) \right] \frac{\mathrm{d}s}{8\pi\mu}. \end{aligned} \tag{2.7b}$$

It is understood that '$2\delta s_n$' is the width of the nth interval, centred at $\boldsymbol{X}(s_n)$.

2.3.4 Evaluating the kernel K_{jk}

In a break from Higdon's method, we shall integrate the expression in Equation (2.7a) numerically. This has a number of advantages over the analytic method which Higdon used. Firstly, it does not require the analytic evaluation of the integral for the Stokeslet and dipoles, which has to be constructed through the movement to a local co-ordinate system centred at each of the N points along the flagellum and the computational power required to evaluate the integrals numerically is no longer a limiting factor.

To evaluate the integrals we use the Gauss-Legendre quadrature method (Stroud and Secrest, 1966). In order to approximate integrating along the centre-line of the flagellum,

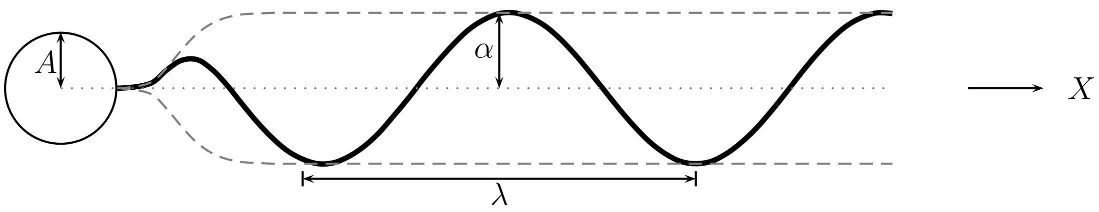

Figure 2.2: Model of a sperm with a spherical head and helical flagellum. The circle represents the head, the solid line the helical beat of the flagellum and the dashed grey line the flagellar envelope.

we use a set of Gauss nodes placed along a straight line parallel to the tangent centred at each of the $\boldsymbol{X}(s_n)$. The standard Gauss nodes and weights are constructed for a domain of $[-1, 1]$ and these are transformed onto a domain of length $2\delta s_n$ in our specified geometry. Typically integration routines will use 8 gauss points.

2.4 Classical helical model

The centre-line of the flagellum is defined as $\boldsymbol{X}(X, t)$. The analysis of Higdon assumed that the flagellum took a helical form of constant arc-length L, parameterised by a fully developed amplitude of α and linear wavelength λ as shown in Figure 2.2.

We continue with the analysis as Higdon did, however, we make appropriate extensions to allow for more general beat patterns in the work that is too follow.

We suppose that the flagellum attaches to the cell body radially at the point $(A, 0, 0)$, that is the intersection of the sphere and the centre-line of the helix – the X-axis. We define the helical wave, as Higdon did, by

$$\boldsymbol{X}(X, t) = (X, \mathcal{E}(X - A)\alpha \cos(k(X - A) - \omega t), \mathcal{E}(X - A)\alpha \sin(k(X - A) - \omega t)) \quad (2.8a)$$

where

$$\mathcal{E}(x) = 1 - \exp\left\{-(k_E x)^2\right\}. \quad (2.8b)$$

The wavenumber of the helix is k, ω is the frequency of the helical beat and k_E determining how quickly the helix grows to the asymptotic amplitude. We also note that $\mathcal{E}(0) = 0$ and $\mathcal{E}'(0) = 0$ meaning that the flagellum is attached to the head at the fixed point $(A, 0, 0)$ with the tangent vector at this point parallel to the X-axis and $\mathcal{E}(x)$ grows to its asymptotic value $\lim_{x\to\infty} \mathcal{E}(x) = 1$, at a rate dependent on k_E.

When the position of a point on the inextensible flagellum is given by $\boldsymbol{X}(s, t)$, where s is the arc-length measured from $X = A$, the velocity of the point (with respect to the body frame) is given by

$$\boldsymbol{u}(s, t) = \frac{\partial}{\partial t}\boldsymbol{X}(s, t).$$

The arc-length parameter s can be expressed as

$$s = \int_A^X \left[1 + \left(\frac{\partial Y(X, t)}{\partial X}\right)^2 + \left(\frac{\partial Z(X, t)}{\partial X}\right)^2\right]^{\frac{1}{2}} \mathrm{d}X,$$

which in the case of a helical wave specified above gives

$$s = \int_A^X \left[1 + (\alpha k \mathcal{E}(X - A))^2 + (\alpha \mathcal{E}'(X - A))^2\right]^{\frac{1}{2}} \mathrm{d}X. \tag{2.9}$$

Notice that this expression for s is a function of X only and it is independent of time and therefore

$$\frac{\partial}{\partial t}\boldsymbol{X}(s, t) = \frac{\partial}{\partial t}\boldsymbol{X}(X, t),$$

which in turn means the velocity of the centre-line of the flagellum can be found by differentiating Equation (2.8a) to give

$$\boldsymbol{u}(X, t) = (0, \alpha\omega\mathcal{E}(X - A)\sin(k(X - A) - \omega t), -\alpha\omega\mathcal{E}(X - A)\cos(k(X - A) - \omega t)) \tag{2.10}$$

It is noted that Equation (2.10) can be written as

$$\boldsymbol{u}(X,t) = (-\omega, 0, 0) \times \boldsymbol{X}. \tag{2.11}$$

The length of the flagellum L, in the helical case, can be defined in terms of the number of wavelengths N_λ and the linear wavelength λ of the helical wave to give

$$L = \int_0^{\lambda N_\lambda} \left\{1 + [\alpha k \mathcal{E}(x)]^2 + [\alpha \mathcal{E}'(x)]^2\right\}^{\frac{1}{2}} \,\mathrm{d}x.$$

An analytic form of the velocity is not necessarily available; the expression for the velocity $\boldsymbol{u}(X,t)$ in general can be derived numerically using finite differences. It is also worth noting that the condition (2.9), which for the helical case demonstrates a constant arc-length, in general does not hold and thus we must ensure that this condition is applied in our code.

2.5 System of equations

2.5.1 Boundary conditions

We have so far computed the velocity of the flagellum with regard to the body frame (Equation (2.11)). By the rotating axis theorem, the velocity relative to the rest frame is

$$\boldsymbol{u}_R(\boldsymbol{x}) = \boldsymbol{U}_0 + \boldsymbol{\Omega}_0 \times \boldsymbol{x} + \boldsymbol{u}(s,t), \tag{2.12a}$$

or in the case of the helical wave

$$\boldsymbol{u}_R(\boldsymbol{x}) = \boldsymbol{U}_0 + \boldsymbol{\Omega}_0 \times \boldsymbol{x} + (-\omega, 0, 0) \times \boldsymbol{x}, \tag{2.12b}$$

where the body frame has velocity $\boldsymbol{U}_0$ and angular velocity $\boldsymbol{\Omega}_0$. The singularities needed to match the velocity on the surface of the sphere are a Stokeslet and dipole for translation, and a rotlet for rotation. The resulting velocity field produced is

$$u_{H_j}(\boldsymbol{x}) = \frac{3}{4}A\left(S_{jk}(\boldsymbol{x},0) - \frac{A^2}{3}D_{jk}(\boldsymbol{x},0)\right)U_{0_k} + \frac{A^3}{|\boldsymbol{x}|^3}\varepsilon_{jkl}x_l\Omega_{0_k}. \tag{2.13}$$

Thus the boundary condition for a point on the surface of the flagellum, must match the velocity due to the singularity distributions (2.7a) and due to the rotation and translation of the spherical head (2.13) with that due to the rotation of the body frame (2.12a/2.12b); for the helical case we have,

$$\begin{aligned} &U_{0j} + \varepsilon_{jkl}\Omega_{0k}x_l + \varepsilon_{jkl}[(-\omega,0,0)]_k x_l \\ &\quad = \frac{3}{4}A\left(S_{jk}(\boldsymbol{x},0) - \frac{A^2}{3}D_{jk}(\boldsymbol{x},0)\right)U_{0_k} + \frac{A^3}{|\boldsymbol{x}|^3}\varepsilon_{jkl}x_l\Omega_{0_k} + \sum_{n=1}^{N}K_{jk}(\boldsymbol{x},\boldsymbol{X}(s_n))f_k(s_n). \end{aligned} \tag{2.14}$$

By evaluating Equation (2.14) at N collocation points along the boundary of the flagellum, $\boldsymbol{x} = \boldsymbol{X}(s_n)$, we obtain $3N$ equations for the $3N+6$ unknowns $\boldsymbol{f}(s_n)$, $\boldsymbol{U}_0$ and $\boldsymbol{\Omega}_0$. The six remaining equations are derived from the force and moment balances.

2.5.2 Force and moment balances

The sperm is self propelled and so is not subject to any net force. Thus, we have that the total force and total moment is zero. Recall that a Stokeslet corresponds to a point force, so in this case we require the total Stokeslet strength, including the cell head and tail, to be zero. To calculate the total Stokeslet strength we consider the contributions of the Stokeslets along the flagellum, their images within the sphere and the Stokeslets due to the translation of the sphere.

The strength of the images is found by considering the radial and transverse components of a Stokeslet on the flagellum. Suppose $\boldsymbol{F}$ is a Stokeslet on the flagellum, then we can write $\boldsymbol{F}$ as a sum of a radial component and a transverse component, relative to the sphere:

$$F_k = \left(F_j \frac{X_j X_k}{|\boldsymbol{X}|^2}\right) + \left(F_k - F_j \frac{X_j X_k}{|\boldsymbol{X}|^2}\right).$$

The total force on the sperm due to the Stokeslet $\boldsymbol{F}$ and its image is

$$F_k(1 + C_T) + F_j \left(\frac{X_j X_k}{|\boldsymbol{X}|^2}\right)(C_R - C_T)$$

where

$$C_R = -\frac{3}{2}\frac{A}{|\boldsymbol{X}|} + \frac{1}{2}\frac{A^3}{|\boldsymbol{X}|^3} \quad \text{and} \quad C_T = -\frac{3}{4}\frac{A}{|\boldsymbol{X}|} - \frac{1}{4}\frac{A^3}{|\boldsymbol{X}|^3}.$$

As the flagellum has a distribution of Stokeslets with force density $\boldsymbol{f}$, we obtain the force balance by considering the sum of the Stokeslets along the flagellum, the images and the force due to translations; which in total is zero. This yields

$$\sum_{n=1}^{N} \left\{ \left[(1 + C_T(s_n))\delta_{jk} + \left(\frac{X_j(s_n) X_k(s_n)}{|\boldsymbol{X}(s_n)|^2}\right)(C_R(s_n) - C_T(s_n)) \right] f_j(s_n) 2\delta s_n \right\} + 6\pi\mu A U_{0_k} = 0 \tag{2.15}$$

where $2\delta s_n$ is the length of the nth interval. The drag of a sphere of radius A, in a fluid of viscosity μ and speed $\boldsymbol{U}_0$ has the classical result of $6\pi\mu A\boldsymbol{U}_0$ (Stokes, 1851).

For the moment balance (relative to the centre of the head, the contribution of the radial image Stokeslets is zero. The strength of the image rotlet in the sphere is

$$\boldsymbol{M} = -\frac{A^3}{|\boldsymbol{X}|^3}\boldsymbol{X} \times \boldsymbol{F},$$

and the moment about the centre of a sphere due to a Stokeslet $\boldsymbol{F}$ at the point $\boldsymbol{X}$ and its image is

$$\varepsilon_{ijk} X_j F_k \left(1 - \frac{A^3}{|\boldsymbol{X}|^3}\right)$$

The moment about the origin due to the rotation of the sphere is given as $8\pi\mu A^3\boldsymbol{\Omega}_0$. Once again summing over all the Stokeslets on the flagellum, the moment balance becomes

$$\sum_{n=1}^{N}\left\{\varepsilon_{ijk}X_j(s_n)f_k(s_n)\left(1-\frac{A^3}{|\boldsymbol{X}(s_n)|^3}\right)2\delta s_n\right\}+8\pi\mu A^3\Omega_{0_i}=0 \tag{2.16}$$

2.6 Solution method

2.6.1 Computational scheme

Mathematically, the linear system derived has $3N+6$ unknowns $f_k(s_n)$, U_{0k}, Ω_{0k} for $k=1,2,3$, $n=1,..,N$, and $3N+6$ equations; $3N$ equations from applying the boundary condition at N collocation points on the flagellum (Equation 2.14), three equations from evaluating the force balance (Equation 2.15) and 3 equations from evaluating the moment balance (Equation 2.16).

These equations form a matrix system which can be coded using a MATLAB routine. Throughout the computational slender-body theory code, where required, integration is performed using Gauss-Legendre quadrature and differentiation (such as finding velocities of the flagellum, or tangent and normal vectors) using second order central difference methods. Occasionally forward or backward differences are required due to the geometry of the problem, such as at the end points.

Appendix C.1 contains details of the numerical implementation of the code including an outline of the code.

2.6.2 Coordinate systems for the helical case

There are a couple of points to note regarding the co-ordinate systems. The solution of the system discussed above defines the motion of a sperm for a single point in time; thus in general to obtain 'average' swimming velocities it is necessary to consider several time instances within the cycle, however, the rotational symmetry of a helically prescribed beat pattern enables an analytic simplification. In general that is not the case and we must evaluate the system at a number of time points within an time period to obtain average values

Recall that we have a body frame in which the helix rotates, where the body frame is fixed at the centre of the sperm's head. If we consider a 'phase frame' which is rotating at angular velocity $(-\omega, 0, 0)$ with respect to the body frame, then the flagellum will be stationary in this frame; thus meaning the motion is identical for all values of time due to the spherical nature of the head; thus solutions in the phase frame are time independent.

The velocity of the phase frame with respect to the rest frame is $\boldsymbol{U}_0$, and the angular velocity of the phase frame with respect to the rest frame is $\boldsymbol{\Omega}_p = \boldsymbol{\Omega}_0 + (-\omega, 0, 0)$. Thus, the phrase frame rotates with constant angular velocity $\boldsymbol{\Omega}_p$, and translates at constant velocity $\boldsymbol{U}_0$, where $\boldsymbol{U}_0$ is with respect to the rest frame. These conditions imply that the origin of the phrase frame moves along a helical path with the helical axis parallel to the rotation vector $\boldsymbol{\Omega}_p$. Thus the average swimming speed $\bar{U}$ is the component of $\boldsymbol{U}_0$ parallel to $\boldsymbol{\Omega}_p$;

$$\bar{U} = \frac{(\boldsymbol{U}_0 \cdot \boldsymbol{\Omega}_p)}{|\boldsymbol{\Omega}_p|} \tag{2.17}$$

Higdon non-dimensionalises this average swimming speed using the parameter $V = \omega/k$.

2.7 Power and efficiency: towards optimisation

In order to consider how efficient a particular configuration of the flagellum is we shall consider the power consumption of the organism. The power consumption is the product of the force and velocity integrated over the surface of the organism, which in this case yields the simple relation

$$P = \sum_{n=1}^{N} \left(\boldsymbol{u}(s_n) \cdot \boldsymbol{f}(s_n)\right) 2\delta s_n \tag{2.18a}$$

where $\boldsymbol{u}$ is given by Equation (2.11).

In order to quantity an efficient beat pattern, Lighthill (1952) defines the quantity *inverse efficiency* as a balance of average power consumption $\bar{P}$ to average velocity $\bar{U}$ and drag and is equal to

$$\eta^{-1} = \bar{P}/(6\pi\mu A\bar{U}^2), \tag{2.18b}$$

where recall A is the head radius. It is worth noting that $6\pi\mu A\bar{U}^2$ is the power which has to be applied externally to keep a rigid sphere in uniform motion with velocity $\bar{U}$, thus we are comparing each type of beating with a fixed measure the power required to move the head.

The term 'inverse efficiency' is used to distinguish from the normal concept of mechanical efficiency which scales on $[0, 1]$ with 1 being the most efficient. η^{-1} is minimal for the most efficient beating pattern; physically this represents the beat pattern with a high velocity output for a given power consumption.

2.8 Validating the computational code against existing results

In order to ensure the correct functioning of the code, the components of the code have been tested against 'test cases' and the whole code was tested against the benchmark values in Higdon (1979c).

2.8.1 Integration routines and singularities

The integration routines for the Stokeslets and dipoles were validated using the Chwang and Wu (1975) solution for uniform flow past a prolate spheroid; where the result of the numerically integrated Stokeslets and dipoles was compared with the analytic solution. The solution of the boundary condition on the surface of the spheroid was verified and a relative error for the force calculations was 2.0811×10^{-6} compared to the analytic solution. This integration routine, like others we employ, used Gauss-Legendre quadrature with 8 points.

In order to check the correct encoding of the Oseen image system, the value of $S_{jk}+S^{\star}_{jk}$ has also been verified to be zero on the surface of the sphere in a separate test program.

2.8.2 Grid density and convergence

Validating $\boldsymbol{U}_0$ and $\boldsymbol{\Omega}_0$

In order to test for the convergence for the value of $\boldsymbol{U}_0$ and $\boldsymbol{\Omega}_0$ we consider the results of the convergence of $\bar{U}/V$ as this encompasses both components and can be compared directly with results of Higdon.

Our investigations show that around 20 points are required for each wavelength on the flagellum: In Figures 2.3 and 2.4 the values of the average swimming speed and the power consumption for a fixed set of parameters and varying N are shown. In this case $N_\lambda = 3$, and we notice convergence to within 1% when $N \geqslant 50$ for $\bar{U}/V$ and $N \geqslant 60$ for η^{-1}.

The additional variation experienced in η^{-1} can be attributed to the fact that it utilises the square of $\bar{U}$ in its calculation thus compounding any numerical error.

2.8.3 Force distribution

The calculated terms from the slender-body theory code are the components of the force distribution, $\boldsymbol{f}$, at each of the N sections of the flagellum. In Figure 2.5, the components of the force vector $\boldsymbol{f}(s_n)$ are plotted as a function of the X co-ordinate, for different values of N, specifically $N = 50$ and $N = 100$. In this case the other parameters are $N_\lambda = 1$, $\alpha k = 1$, $k/k_E = 1$, with $L/A = 5$ and $a/A = 0.02$.

The discrepancy on the end values of the force is due to the end effects of the singularity method, as is discussed in details in Tuck (1964). Part of the problem arises because we are modelling a cylinder of constant radius (the flagellum), using the solution to flow

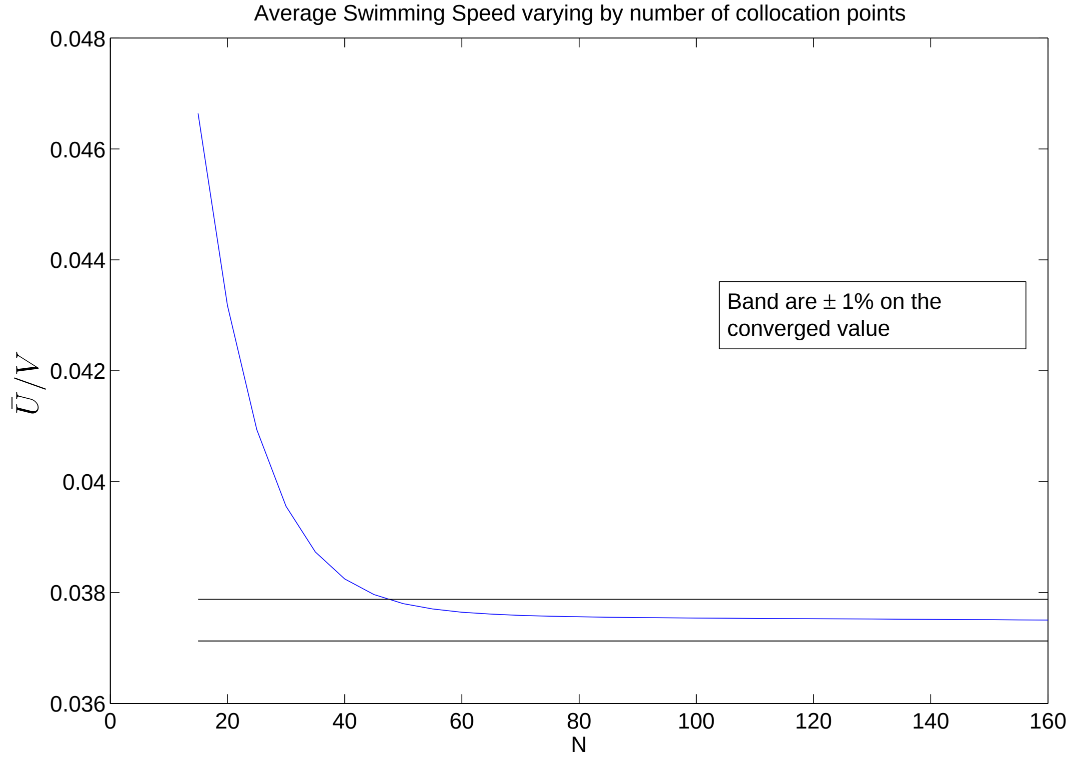

Figure 2.3: Example of the calculation of the velocity for different values of N. Notice convergence within 1% of the asymptote for $N \geqslant 50$

around an prolate spheroid, without regard for the ends. The code is however, verified to ensure that the total force and total moment balances are correct in all cases.

Due to the nature of the construction of the solution, and the piecewise constant nature of the calculated force distribution, it is not easy to make a direct comparison numerically between the two data sets for $N = 50$ and $N = 100$, however, we can verify the solution qualitatively through Figure 2.5 and by considering the 'peak force' values shown in Table 2.1, which also shows excellent agreement.

2.8.4 Optimal N_λ

In the following sections we repeat the analysis of Higdon (1979c) and show agreement between his model and our implementation of it.

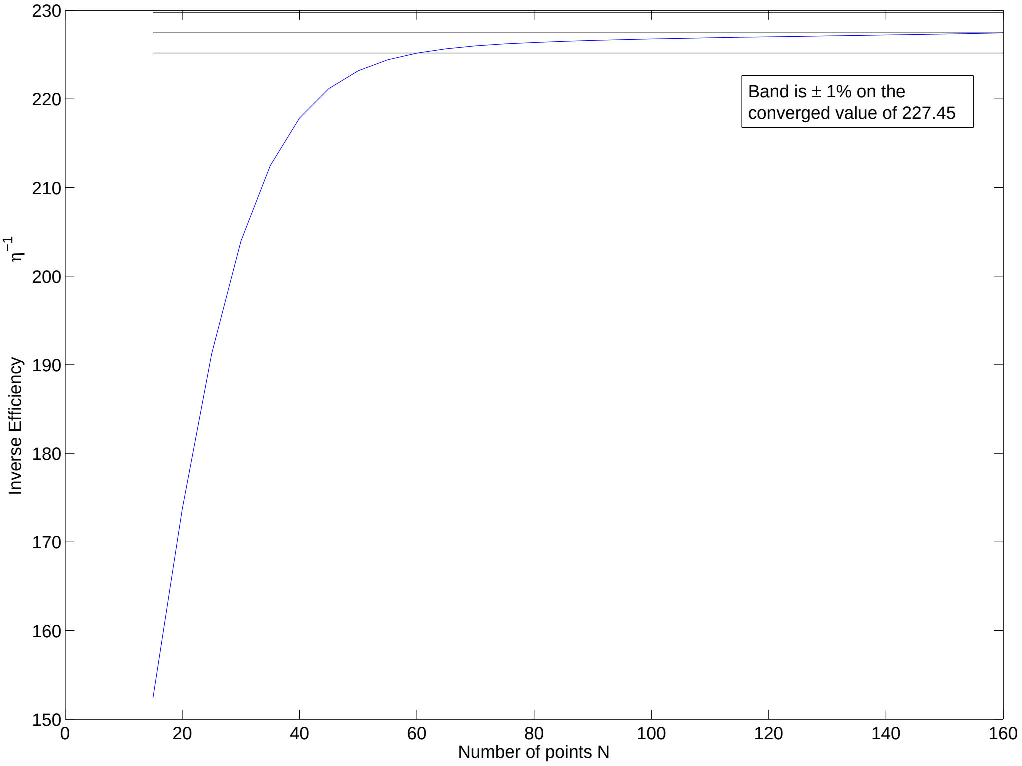

Figure 2.4: Example of the calculation of η^{-1} for different values of N. Notice convergence within 1% of the asymptote for $N \geqslant 60$

Maximum	f_1	f_2	f_3
$N = 100$	0.5297	2.1035	1.9724
$N = 50$	0.5322	2.1101	1.9720
Relative Error	0.0047	0.0032	0.0002

Table 2.1: Comparison of the 'peak' force values for $N = 100$ and $N = 50$ nodes used in evaluating the solution. (Parameters are $N_\lambda = 1$, $a/A = 0.02$, $\alpha k = 1$ and $k/k_E = 1$, with $L/A = 5$, as in Figure 2.5)

We are interested in five parameter groupings to consider optimal power usage; three wave parameters N_λ, αk, k/k_E and two body parameters a/A and L/A. In general we shall consider the effect of the parameters on the inverse efficiency η^{-1}.

Firstly, we wish to consider the optimal motion achieved by varying the parameter N_λ, that is the number of wavelengths along the flagellum. In Figure 2.6 we plotted $\bar{U}/V$

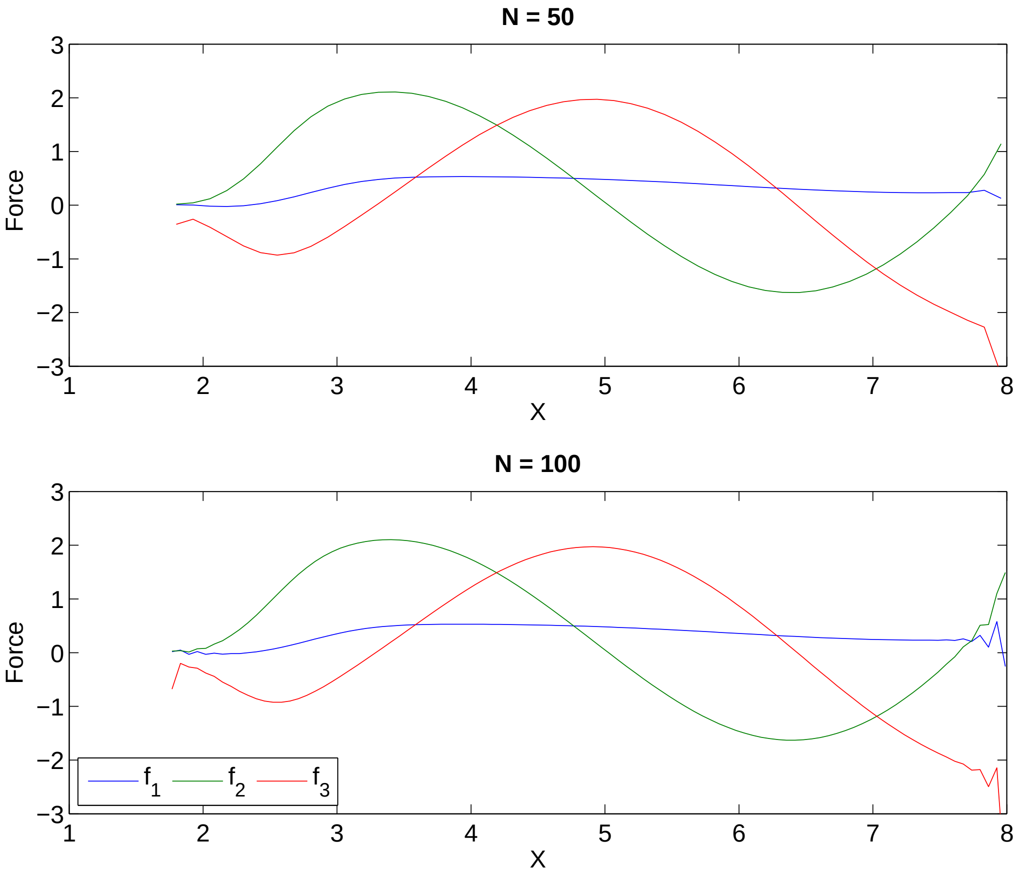

Figure 2.5: The components of the force $\boldsymbol{f} = (f_1, f_2, f_3)$ for values along the curve parameterised by their X co-ordinate. The two test values are $N = 50$ and $N = 100$.

for a variety of different length flagella as a function of N_λ. In each case we notice that velocity increases to a maximum and then falls off less steeply after the maximum value of η^{-1} has been achieved; in the case of $L/A = 20$, the maximum swimming speed is for $N_\lambda > 6$.

The explanation for this behaviour arises from considering the geometry of the problem; as the number of wavelengths N_λ increases, the amplitude and the wavelength reduce. The torque on the flagellum is proportional to the length times the amplitude squared. Thus, increasing the number of waves reduces the torque.

The slow decay of the velocity after a peak value, can be explained hydrodynamically.

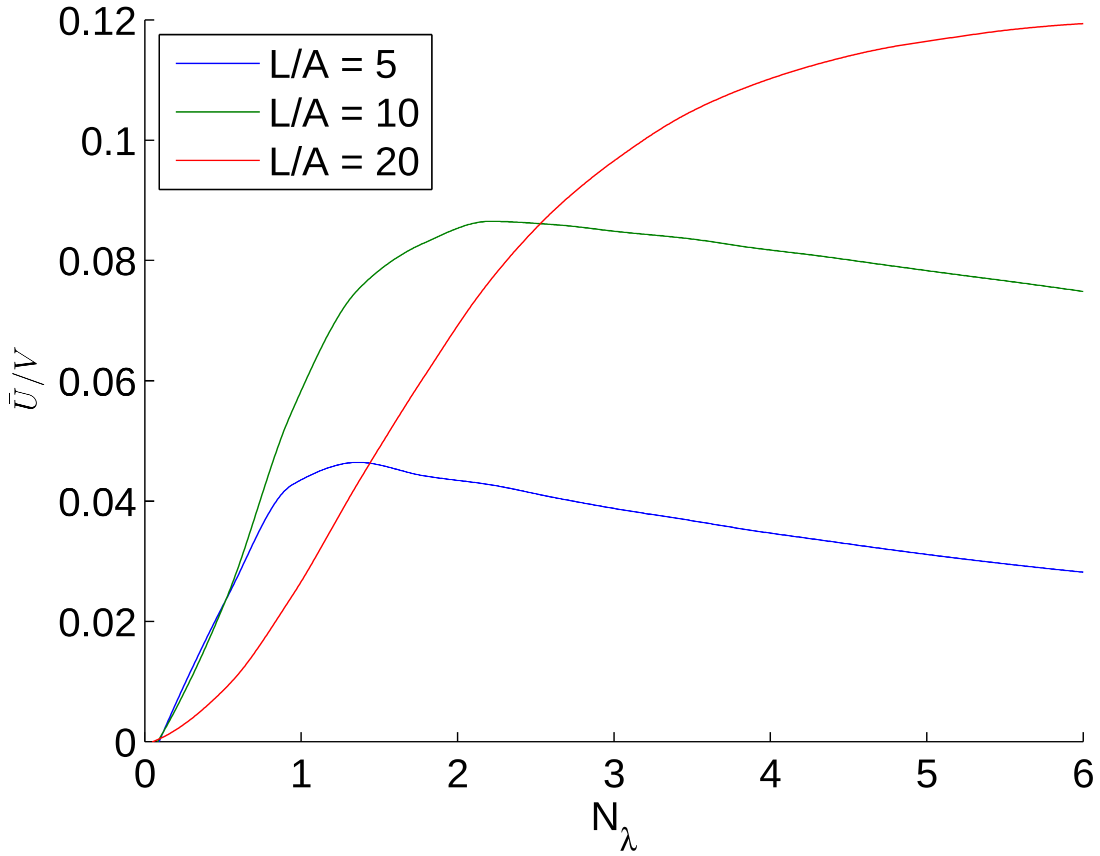

Figure 2.6: Average swimming speed $\bar{U}/V$ for a variety of the number of wavelength N_λ, for different length flagella. Other parameters are $a/A = 0.02$, $\alpha k = 1$ and $k/k_E = 1$.

We noted earlier that the basis of flagellar propulsion is the fact that the resistance of a long slender-body is much greater for normal motion as opposed to tangential motion. In the case of waves travelling on a flagellum, the significant parameter is the logarithm of the ratio of the wavelength to flagellar diameters, and as above, as N_λ increases, the wavenumber will decrease as will the slenderness ratio - and thus this mechanism of propulsion becomes less effective.

It is the interplay of these two mechanisms (exploiting the '2:1' ratio, and torque balance) that leads to the shape of curve. It is when the two mechanisms are balanced that the maximum swimming speed occurs - and varying N_λ will causes a penalty in terms of average speed.

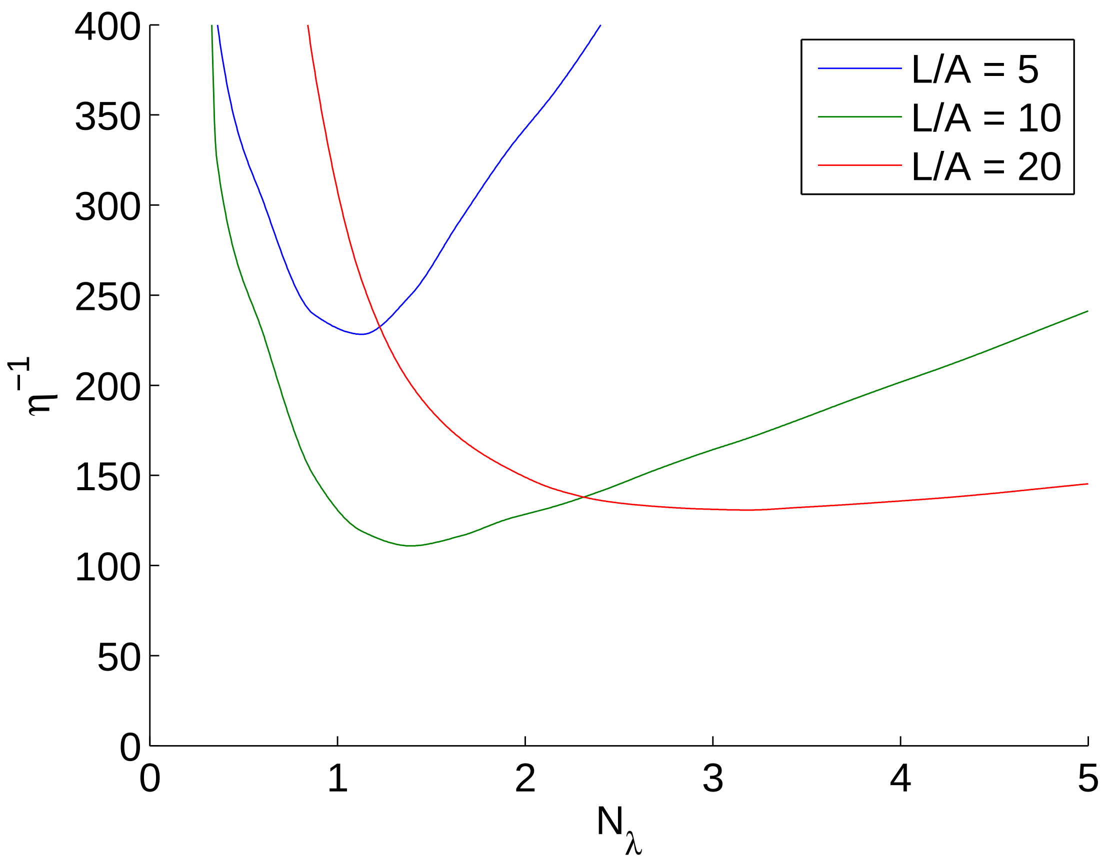

Figure 2.7: Inverse efficiency η^{-1}, for a variety of number of wavelengths N_λ, for different length flagella. Other parameters are $a/A = 0.02$, $\alpha k = 1$ and $k/k_E = 1$.

For the same set of parameters, we plot the inverse efficiency η^{-1}, as shown in Figure (2.7). Optimal efficiency ($\propto P/\bar{U}^2$) occurs when $N_\lambda = 1$ for $L/A = 5$; $N_\lambda = 2$ for $L/A = 10$, and $N_\lambda = 4.5$ for $L/A = 20$.

2.8.5 Optimal αk

The variation in average swimming speed and inverse efficiency for changing the parameter αk can be seen in Figure 2.8 and 2.9 respectively. The optimal values of αk for inverse efficiency vary only slightly from $\alpha k = 1$ and Higdon uses this for his optimal parameter in all cases. The parameter $\alpha k = 1$ corresponds to the segments of the flagellum making an angle of 45° with the helical axis; when $\alpha k < 1$ the angle is smaller and each segment

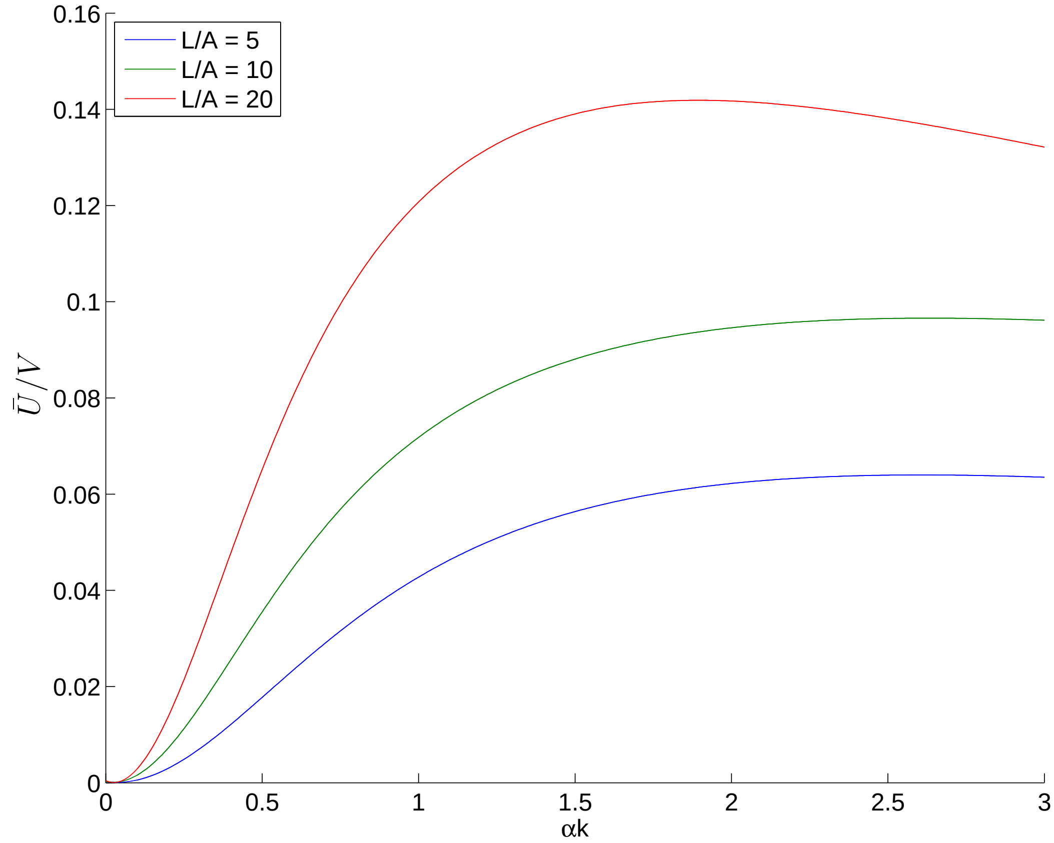

Figure 2.8: Average swimming speed $\bar{U}/V$ as a function of αk, for different length flagella with $a/A = 0.02$, optimal N_λ and $k/k_E = 1$.

contributes less thrust per unit length.

Once again we observe that the maximum swimming speed (Figure 2.8) occurs at $\alpha k \approx 2$; but once again in reaching the maximum swimming speed (which for shorter flagellum levels plateau for $\alpha k > 2$) the amount of power required, due to the orientation of the flagellum, is disproportionately high.

2.8.6 Optimal k/k_E

The final wave parameter is k/k_E, the ratio of the wavenumber to the 'factor' determining how the wave grows to its maximum amplitude, with smaller values of k/k_E being

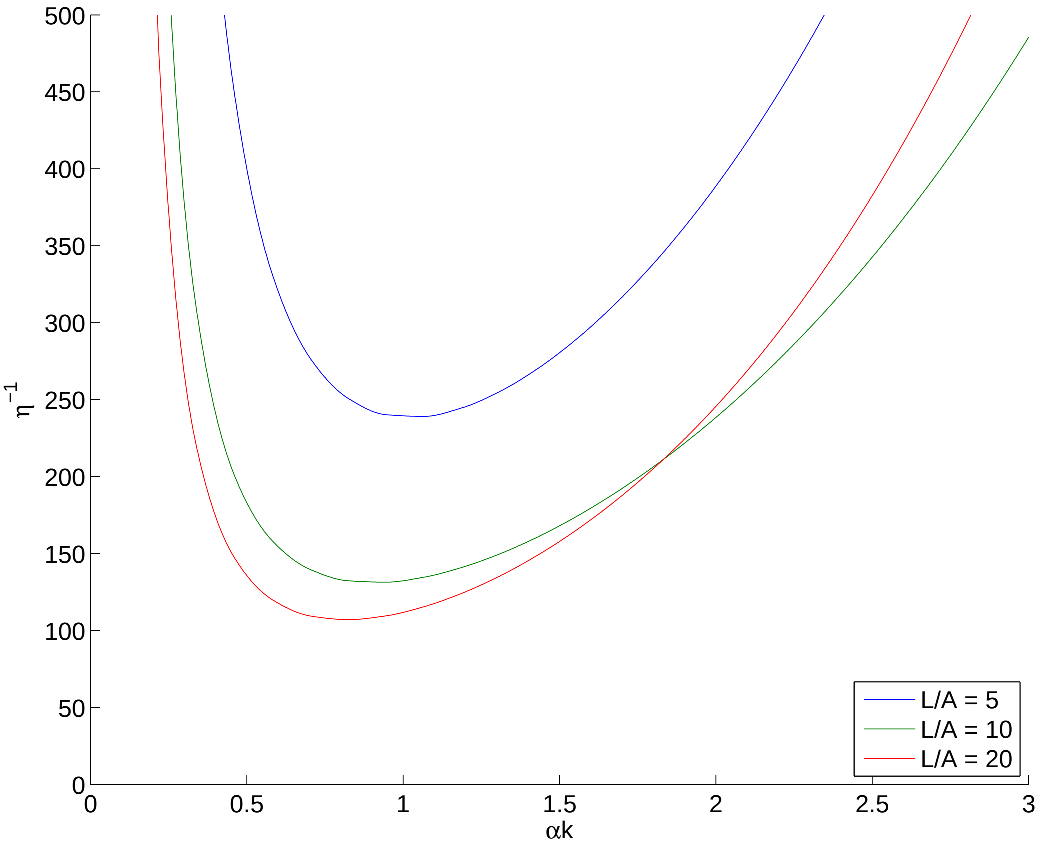

Figure 2.9: Inverse efficiency η^{-1} as a function of αk, for different length flagella with $a/A = 0.02$, optimal N_λ and $k/k_E = 1$.

associated with a fast transition to the maximum amplitude.

From Figure 2.10, we can see that variation in power consumption with k/k_E is low for $L/A = 5$, $k/k_E < 3$; $L/A = 10$, $k/k_E < 5$ and for all values of k/k_E with $L/A = 20$. The conclusion we draw from this is that as long as the flagellum is long enough for the amplitude variation to occupy a small proportion of the total length, its effect is negligible. It is important to note that the parameter set studied by Higdon misses parameters we may be interested in for sperm motility, where, as we observed in Figure 1.1, the beat pattern is often confined to the distal end of the flagellum.

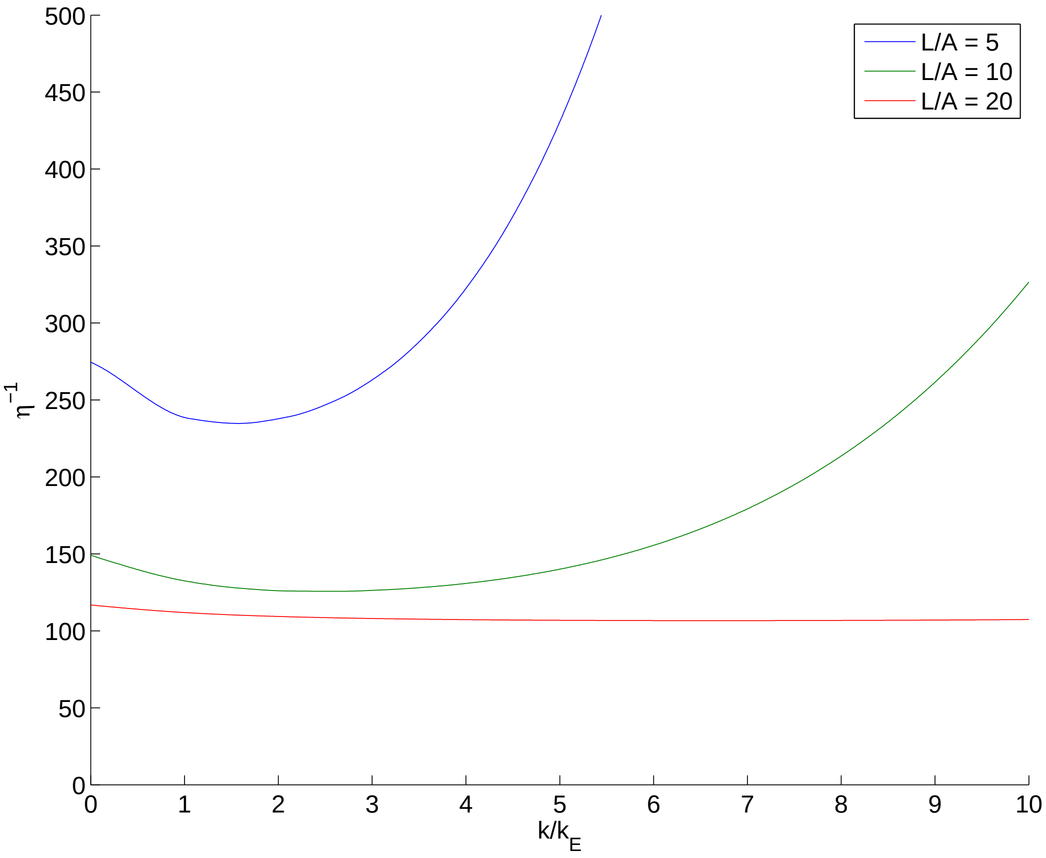

Figure 2.10: Inverse efficiency η^{-1} as a function of αk, for different length flagellum with $a/A = 0.02$, optimal N_λ and $k/k_E = 1$.

	N_λ	αk	k/k_E
$L/A = 5$	1	≈ 1	< 3
$L/A = 10$	1.5	≈ 1	< 5
$L/A = 20$	4.5	≈ 1	no limit

Table 2.2: Summary of the optimal wave parameters for Higdon's helical model.

2.8.7 Higdon's optimal helically flagellated micro-organism

Higdon's optimal helically flagellated micro-organism is summarised in terms of parameters in Table 2.2. An example micro-organism is plotted in Figure 2.11 for $L/A = 20$.

2.9 Biologically relevant parameters for sperm and the effect of $S^{\star}_{jk}$

The definition of $S^{\star}_{jk}$ in Equation (1.13), by design, results in the no-slip boundary condition being satisfied on the surface of the sphere since $S_{jk} + S^{\star}_{jk} \equiv 0$ for all points on the surface of the sphere. We have verified this numerically in §2.8.1. However, the calculation and integration of the $S^{\star}_{jk}$ image system presents several difficulties; firstly it is costly in terms of computational time and secondly it does not ensure the boundary condition on the sphere is satisfied for singularities other than the Stokeslet(For example, the viscoelastic or Brinkman analogues of the Stokeslet will have a different image system to the Oseen singularity)

As a precursor to the optimisation routines in future chapters, we shall briefly consider the effect of the image system on the resultant average swimming speed of a biologically realistic sperm cell.

Within the Higdon framework which has been constructed, we are able to vary the parameters to those expected in real human sperm cells. Although we have noted that human sperm do not have spherical heads, following the lead from Dresdner et al. (1980), we can account for the effect of the head, by utilising a sphere of an effective radius $A = 1.25\mu$m, so that the volume of the physiological head and the spherical representation are the same. An example set of parameters for a more biologically correct sperm with a whip-like pattern is $\lambda = 50$; $N_\lambda = 1$; $\alpha = 5$, $A = 1.25$, $a = 0.002$.

Figure 2.12 shows the average swimming speed $\bar{U}/V$ and Figure 2.13 the power consumption η^{-1} for a variety of N_λ for the solution including the full image system $S^{\star}_{jk}$, and that without $S^{\star}_{jk}$. One should notice that except for $N_\lambda < 1$, there is excellent agreement between the solutions for average swimming speed and power consumption. The relative error is calculate as the difference between the results with and without the image system, divided by the result with the image system.

From this one concludes that when ‘biologically relevant’ parameters, and in particular a small sphere radius, are used, the effect of the Oseen image system $S^{\star}_{jk}$ can be neglected, provided that N_λ is bigger than 1.25.

2.10 Conclusions

In this chapter we have implemented a numerical code based on Higdon’s model for a flagellated cell using slender-body theory and singularities, to model a single flagellated micro-organism in an infinite viscous fluid. The resulting system of equations has been coded using MATLAB, and results presented compare favourably with the results Higdon (1979c) presented. The model has been validated using a number of numerical checks.

The parameter search undertaken by Higdon, and repeated here, yields an optimal set of parameters for a helically propelled micro-organism. It is important to notice here that the parameters and helical model adopted by Higdon does not adequately capture the scales and range of beat patterns associated with human sperm motility. We have illustrated that for biologically relevant parameters (small heads) the effect of the Oseen image system is negligible.

The extensions written in to the code allow for non-helical specification of beat patterns including time-sequenced experimental data. The slender-body theory code will now be utilised in subsequent chapters using new models of specifying the beat pattern. By investigating the effect of the parameters of the new model on the outputs of the slender-body theory code we consider the concept of an optimal beat pattern for human sperm, in relation to our experimental observations.

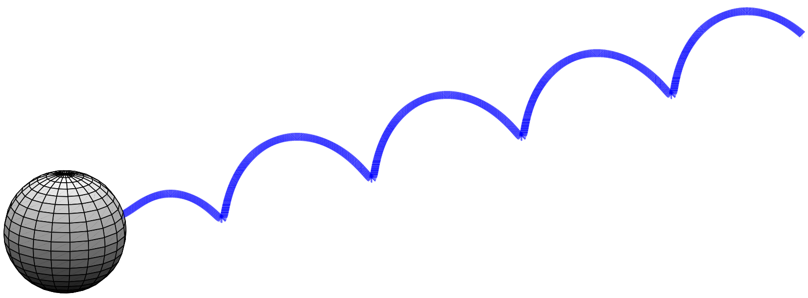

Figure 2.11: An example of Higdon's 'optimal' helically propelled organism, for $L/A = 20$ with $N_\lambda = 4.5$, $\alpha k = 1$, $k/k_E = 2.5$ and $a/A = 0.02$.

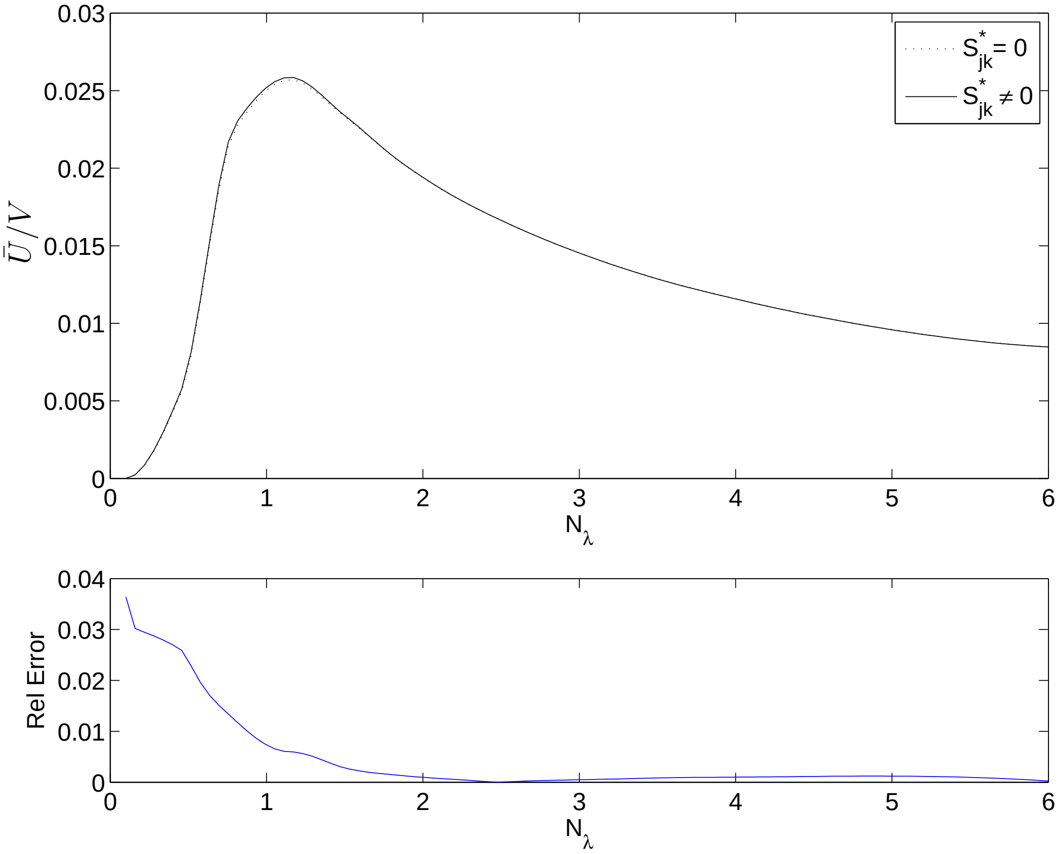

Figure 2.12: Solution for $\bar{U}/V$ for varying values of N_λ for a biologically 'realistic' sperm, with $S^\star_{jk} = 0$ and $S^\star_{jk} \neq 0$. The lower subplot shows the relative error, with is less than 1% for $N_\lambda > 0.75$.

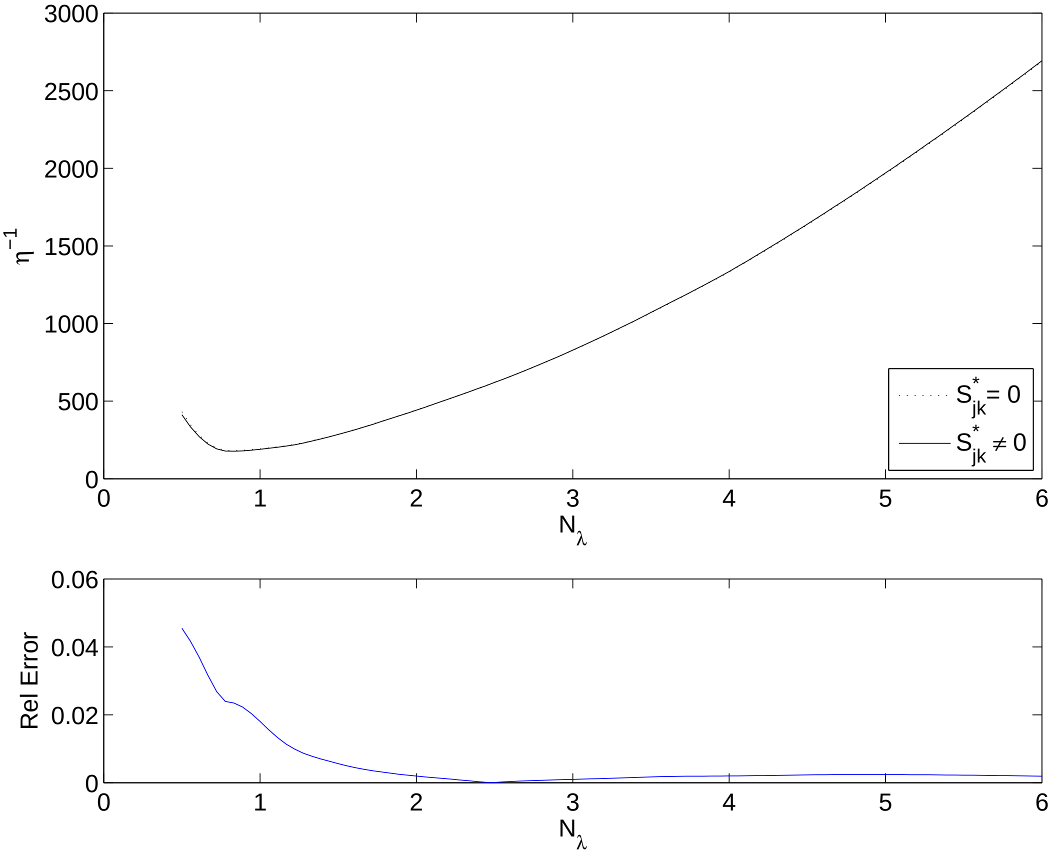

Figure 2.13: Solution for η^{-1} for varying values of N_λ for a biological 'realistic' sperm, with $S^\star_{jk} = 0$ and $S^\star_{jk} \neq 0$. The lower subplot shows the relative error, with is less than 1% for $N_\lambda > 1.25$.

CHAPTER 3

OPTIMISATION OF A PARAMETERISED SPERM BEAT PATTERN: HYBRID ENVELOPE MODEL

3.1 Introduction

In this chapter we consider the optimisation of a new beat pattern parameterisation as a model for human sperm. The sperm cell is assumed to have a prescribed planar beat pattern based on a sinusoidal wave modulated by an envelope function. The choice of a planar beat is twofold; firstly, reliable experimental data is currently only two-dimensional and, in certain cases, shows little variation in overall tail length and secondly, the existence of a longitudinal thickening of the fibrous sheath on the sperm tail running along opposite sides of the tail, is interpreted as ribs or struts which may restrict motion in certain directions (Fawcett, 1958). The specification of the beat pattern is such that it allows variation in amplitude, position of the development of the beat and the wavenumber. The introduction of a mechanism to control how distal the development of the beat pattern is, is a novel addition to the previous studies.

Experimental evidence, such as Figure 1.1, illustrates that a helix is not an appropriate model. The motivation for this chapter is that the section of the flagellum nearest the head of the sperm is often inactive in beating, a feature not replicated using Higdon's helical model.

In order to allow for the types of beat patterns observed experimentally, in our modelling, we will utilise a hybrid exponential-arctan envelope. Motivation is drawn from Dresdner et al. (1980), who used an arctan function to represent the non-constant wavenumber; however, we adopt a hybrid version to provide a novel model for the envelope function. We interpret the effect of the parameters by using information about velocity, efficiency, power consumption and energy usage, derived using the slender-body theory code developed in the previous chapter.

3.2 Novel specification of the flagellar envelope

We shall adopt the refined slender-body theory of Higdon (1979b) and consider the motion of a single sperm cell in an infinite domain, where the physical dimensions of the sperm are taken from experimental data and assumed constant. We specify a flagellum of length $L = 56\mu$m and radius $a = 0.05\mu$m, and a spherical head of $A = 1.25\mu$m, using the concept of *effective radius* from Dresdner et al. (1980) and discussed earlier. We have also shown (Section 2.9) that removing the Oseen correction for the slip on the head has negligible effect on the overall result for such small head sizes, and this is confirmed by the uses of a hybrid boundary-element slender-body theory method (Smith et al., 2008a).

Higdon specified the position of the flagellum as $\boldsymbol{X}(X, t)$ (Equation 2.8a) in the body frame as a helical wave modified by an envelope function $\mathcal{E}$ (Equation 2.8b). We specify the beat pattern as a sinusoidal planar wave affected by a modified envelope function, where A is the head radius, as follows

$$\boldsymbol{X}(X, t) = (X, \mathcal{E}(X - A)\cos(k(X - A) - \omega t), 0) \tag{3.1a}$$

where

$$\mathcal{E}(x) = \alpha \left(1 - \exp(-x^2)\right) \left(\tan^{-1}\left(\sigma(x - \delta x_{\max})\right)\pi^{-1} + 0.5\right) \tag{3.1b}$$

With the added condition that the total arc-length is fixed in time with $L = 56\mu$m. The reasons for specifying a modified exponential-arctan envelope is that it allows a parametrisation which adjusts how near the posterior of the tail the beat pattern develops - or in other words how much of portion of the tail nearest the head is not active in high amplitude beating.

The model parameters and their interpretations are as follows

- *Fixed parameters:* ω is fixed so that the frequency of the beat pattern is 18Hz. The frequency of the beat does vary with viscosity (Pate and Brokaw, 1980; Ishijima et al., 1986), however, 18Hz is a typical value observed and by fixing it we reduce the complexity of the problem; we know that as power scales to the square of frequency and linearly with viscosity, inverse efficiency is unaffected by frequency. The parameter σ is considered to be fixed and equal to 1.5; σ is responsible for the rate of transfer from the zero- to the large-amplitude state and this assumption of fixing its value is discussed in detail in Section 3.4.1.

- *Variable parameters:* α is the amplitude of the fully developed wave pattern, and $\delta \in (0,1)$ adjusts how far along the flagellum the beat pattern switch changes from the zero to α amplitude state. The wavenumber $k = 2\pi/(x_{\max}/k_v)$, is chosen so that the parameter k_v is a measure of how many wavelengths occur along the length of the flagellum.

The effect of the model parameters is shown in Figure 3.1. We have three parameters that we shall optimise for: α, δ and k_v.

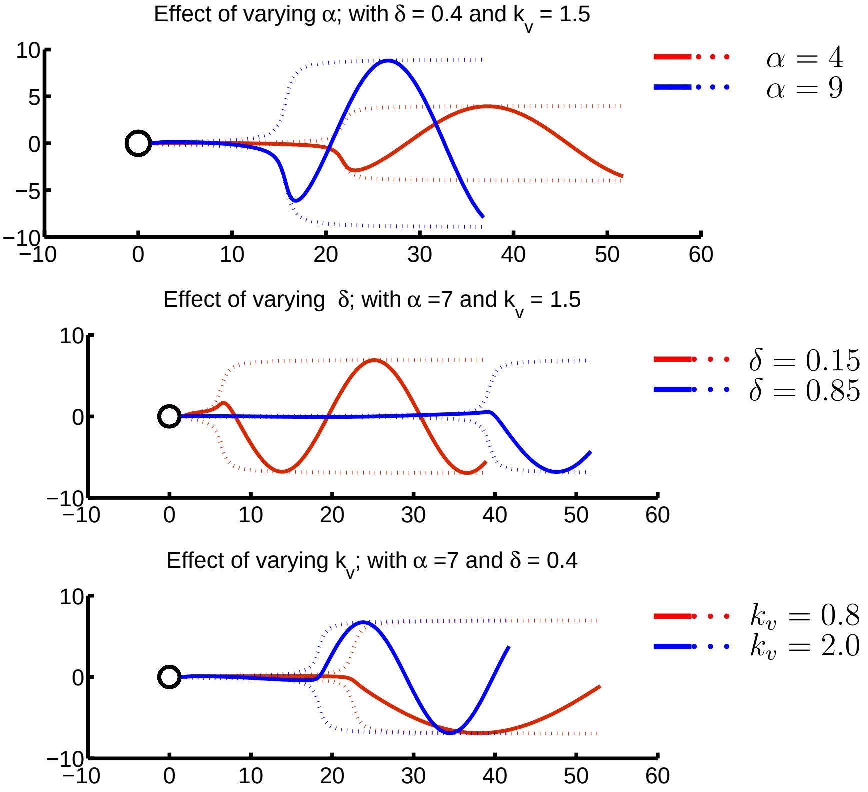

Figure 3.1: Effect of the parameters α (top), δ (middle) and k_v (bottom) on the beat patten and envelope. The solid blue and red lines represent an instantaneous flagellar position for a set of parameters, which is associated with the matching colour envelope function. In each case the total length of the flagellum is a fixed parameter $L = 56\mu$m.

3.3 Optimisation method

3.3.1 Optimisation functionals

The raw outputs of the slender-body theory code are the force distribution, the velocity of the sperm cell and the angular velocity of the sperm cell. From these outputs we are able to calculate certain measures which are used in assessing the optimality of a particular beat pattern.

Compared to Higdon's helical wave model, our specification is no longer time invariant, therefore, we need to calculate the average of the outputs over a series of time points within the period of the beat pattern. It is important that we ensure that the total arc-length of the flagellum is fixed.

From the outputs we construct four functionals for comparison

- average swimming speed $\bar{U}$,
- average power consumption $\bar{P}$,
- average inverse efficiency η^{-1},
- average energy consumption $\propto \bar{P}/\bar{U}$.

The instantaneous power consumption can be calculated as

$$P(t) = \sum_{n=1}^{N} (\boldsymbol{u}(s_n) \cdot \boldsymbol{f}(s_n))\, 2\delta s_n,$$

and thus the average power consumption is the time average of this quantity.

In order to quantify an efficient beat pattern we utilise the inverse efficiency

$$\eta^{-1} = P/(6\pi\mu A\bar{U}^2) \tag{3.2}$$

The inverse efficiency is a balance of power consumption to velocity and drag. Due to the construction of η^{-1}, we seek the lowest value of η^{-1} which corresponds to the most efficient parameter set.

3.3.2 Newton's method and descent methods

Finding the stationary points of a function corresponds to finding the zeros of the derivative of the function and as such we can utilise root finding methods such as the Newton-Raphson approach, which in higher dimensions is simply known as *Newton's method.*

In order to find a maximum or a minimum of a function f, we need to calculate its derivative and second derivative. We do not necessarily need analytic forms for these derivatives, as we shall shortly consider using a finite difference approach to calculate them. To find a zero for the one-dimensional function f, we use an iterative Newton-Raphson scheme, whereby the next solution x_{k+1}, can be found from the current value x_k as follows

$$x_{k+1} = x_k - f(x_k)/f'(x_k). \tag{3.3}$$

A natural extension to Equation (3.3), in order to find the stationary/turning points of f (that is where the derivative is zero), we utilise the formula

$$x_{k+1} = x_k - f'(x_k)/f''(x_k). \tag{3.4}$$

Newton's method can be extended into higher, say, m-dimensions, in order to find extrema of a multi-dimensional surface. Considering the situation of finding the maximum or minimum of an function $f : \mathbb{R}^m \longrightarrow \mathbb{R}$, as we shall in this chapter, the first derivative is replaced by the gradient vector $\boldsymbol{d} = -\nabla f$ (dimension $m \times 1$) and the second derivatives form the Hessian matrix (dimension $m \times m$) which is defined as

$$[\boldsymbol{H}]_{ij} = \frac{\partial^2 f}{\partial x_i \partial x_j}. \tag{3.5}$$

The iterative algorithm now becomes

$$\boldsymbol{x}_{k+1} = \boldsymbol{x}_k + \boldsymbol{H}_k^{-1}\boldsymbol{d}_k. \tag{3.6}$$

where $\boldsymbol{H}_k$ and $\boldsymbol{d}_k$ are the values of the Hessian matrix and the gradient vector calculated at the point $\boldsymbol{x}_k$ respectively.

An alternative to Newton's method is the *(steepest) descent method.* Newton's method is a fast algorithm for determining the zeros of a function, which converges quadratically, however, the quality of the initial starting guess is very important, and a poor starting method can cause Newton's method to fail to converge (Süli and Mayer, 2003). In the descent method, iterations are always performed in the direction of maximum decrease of the function, parallel to the gradient vector $\boldsymbol{d} = -\nabla f$; with a to-be-determined multiplier τ_k

$$\boldsymbol{x}_{k+1} = \boldsymbol{x}_k + \tau_k \boldsymbol{d}_k. \tag{3.7}$$

The value of τ_k is chosen as follows (for the steepest descent method)

$$\tau_k = \frac{\|\boldsymbol{d}_k\|^2}{\boldsymbol{d}_k^T \boldsymbol{H}_k \boldsymbol{d}_k}. \tag{3.8}$$

The descent method converges more slowly than Newton's method and still requires the calculation of the gradient vector and the Hessian matrix, but despite this, in the initial stages of the root search, it has been found to be more robust than Newton's method (Süli and Mayer, 2003). Therefore, we adopt a combined scheme that utilises the slower descent method for the first few, say 3 or 4, iterations, and then the faster Newton's method afterwards.

Details of implementing the calculation of the required derivatives using finite difference is presented in Appendix C.2

3.3.3 Pseudo-code diagram

In this section we outline how the optimisation code, the slender-body theory code and the parameters are linked in our scheme. Figure 3.2 shows a 'black-box' diagram for the solution of our problem.

In our situation the slender-body theory code developed earlier plays the role of the function and for a set of parameters returns a set of useful measures such as the inverse efficiency, which can then be used to optimise over. Specifically, for a given set of parameters, the slender-body code needs to be run a number of times, for a very small alteration in parameters in order to calculate the gradient vector and the Hessian matrix; this is

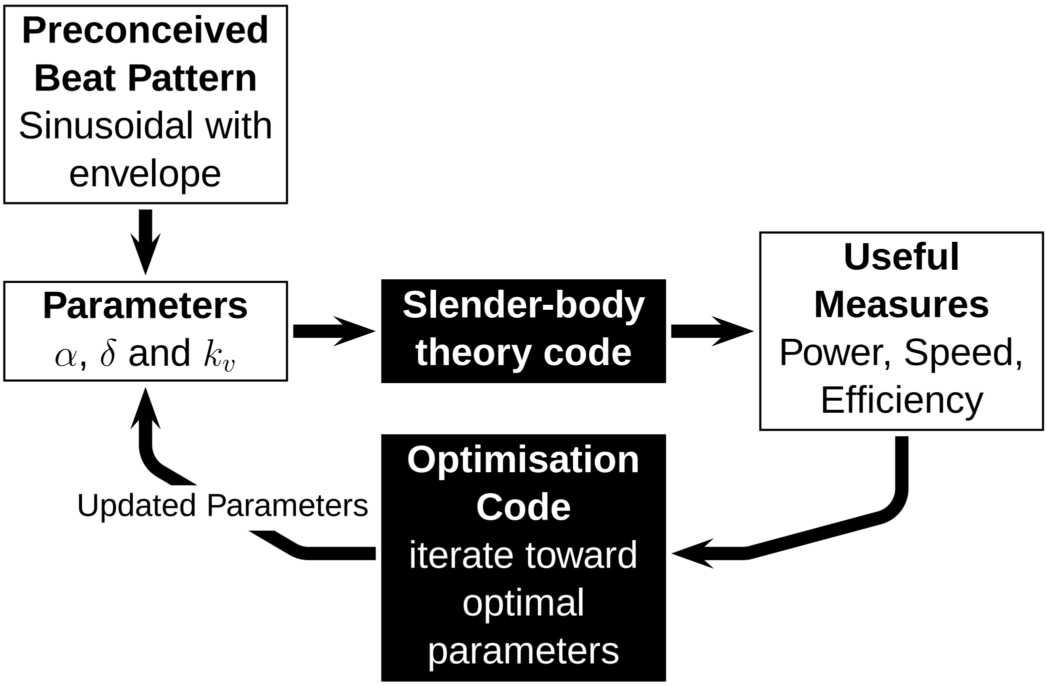

Figure 3.2: Black-box diagram, illustrating the pseudo-code, showing the relationship of the optimisation code, the slender-body theory code and the model parameters.

the time consuming step of the process. The updated parameter set is then calculated using Newton's method and the process is then repeated by calculating the Hessian and gradient vectors based on the new parameters. Convergence is determined by considering the value of the gradient vector and the difference in each successive set of parameters through the iteration.

3.4 Results

3.4.1 Effect of σ

Firstly, we shall explore the effect of the parameter σ on inverse efficiency, thus setting $f = \eta^{-1}$. The aim of this preliminary study is to fix the value of σ for future work, and thus reduce the dimension of the optimisation problem. Intuitively, it is the parameter which is likely to heave least affect on the overall result since it controls the gradient of the flagellum as it transfers from the zero-amplitude state to the fully-developed state

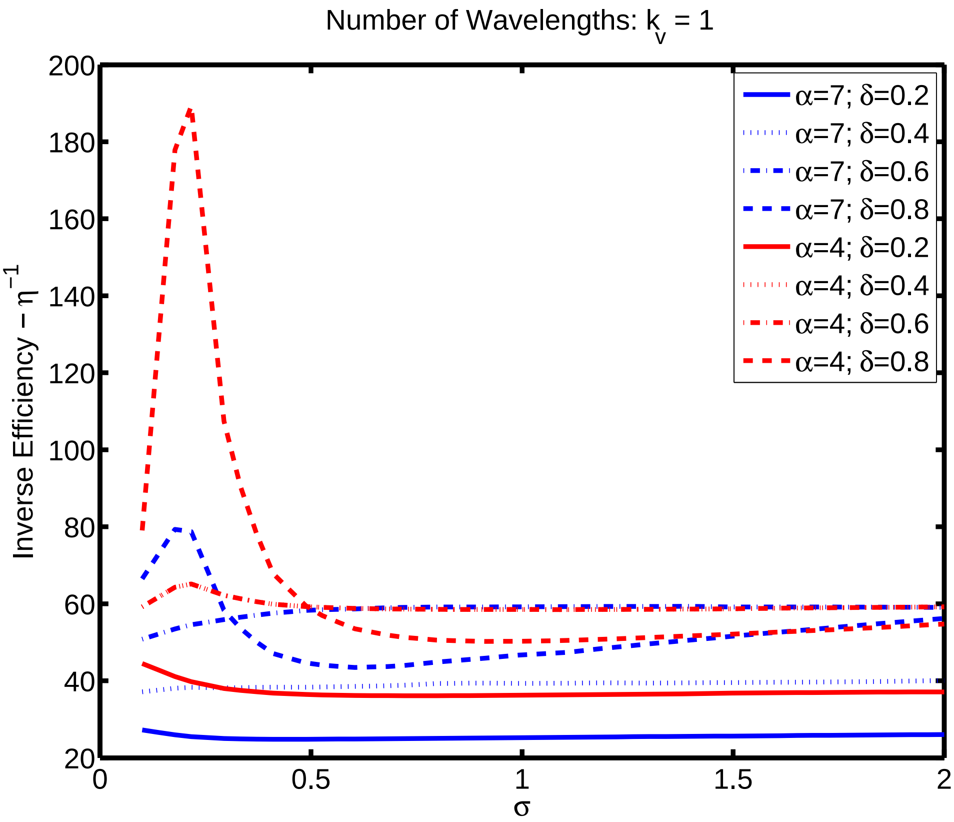

Figure 3.3: Inverse efficiency η^{-1} versus σ. Different combinations of α and δ are given, for fixed $k_v = 1$.

and we require σ to stay small enough so the curvature of the flagellum does not go too high.

Figures 3.3–3.5, show the variation in the inverse efficiency as a function of σ for values of $k_v = 1, 1.5$ and 2 respectively and for different pairing of α and δ. Recall α corresponds to the amplitude and δ corresponds to how far along the flagellum the beat pattern develops; thus $\delta = 0.2$ corresponds to beating along the majority of the flagellum, whereas $\delta = 0.8$ corresponds to beating on the distal one-fifth of the flagellum.

In Figure 3.3 we see that when one wavelength is observed on the tail ($k_v = 1$), then once σ is above a critical value of around 1 the behaviour for all the values of (α, δ) is similar – that is the curves have reached a plateau, or grow only slightly, with little variation. The pattern is even more striking in Figure 3.4 where $k_v = 1.5$. Here, as in the

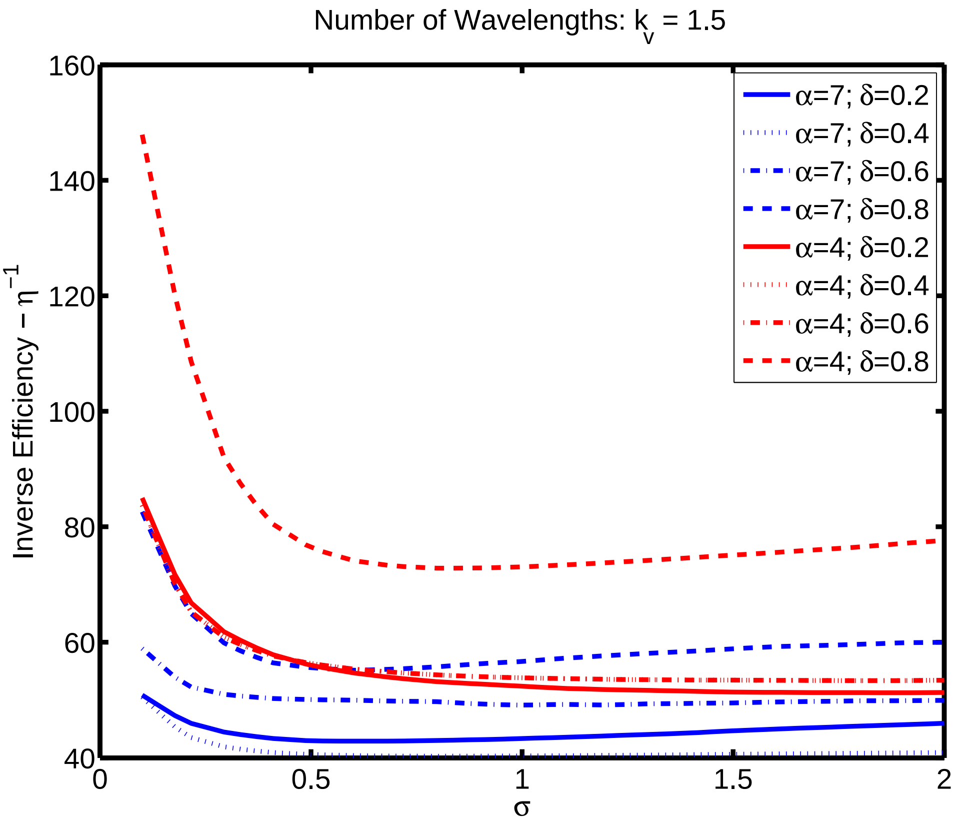

Figure 3.4: Inverse efficiency η^{-1} versus σ. Different combinations of α and δ are given, for fixed $k_v = 1.5$.

previous figure, once past a similar critical value, the behaviour is very similar.

Figure 3.5 illustrates the situation whereby for some combinations of (α, δ), the minimum inverse efficiency is observed for very small values of σ, whereas others display the plateau or slow growth behaviour. Although a critical value is less obvious here, following from the previous two diagrams, choosing a value of $\sigma > 1$, but not too large will ensure we are near-optimal in most cases. It is important to notice that if we push σ too high, say $\sigma > 4$, although mathematically the equations are still tractable, the shapes generated for the flagellum are too 'sharp', the curvature is too high and thus unphysical (see Figure 3.6).

Based on the evidence presented in this section, we make the assumption that we can fix the value of $\sigma = 1.5$ for all subsequent calculations.

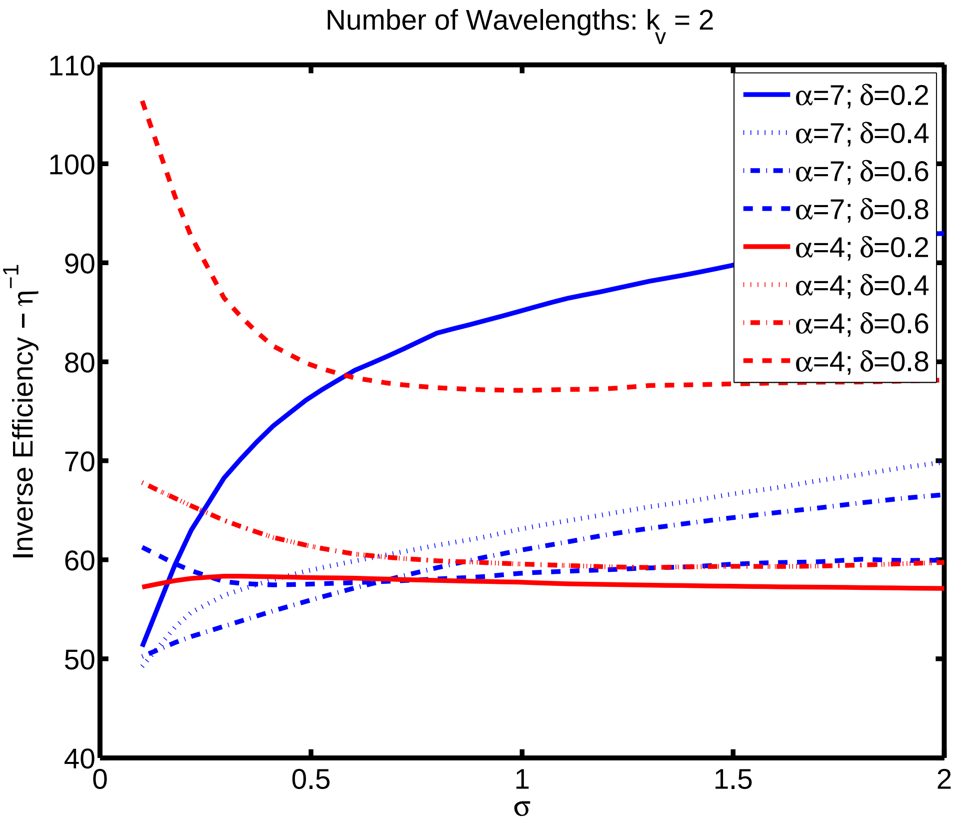

Figure 3.5: Inverse efficiency η^{-1} versus σ. Different combinations of α and δ are given, for fixed $k_v = 2$.

3.4.2 Two-dimensional optimisation - α and δ

We consider the case of two-dimensional optimisation for the two parameters α and δ, whilst leaving $\sigma = 1.5$ as before, and also fixing the value of $k_v = 1.5$. This will enable us to gain some insight into interaction of the two parameters α and δ.

Figures 3.7-3.10 illustrate the variation in average speed, average power consumption, inverse efficiency and measure of energy usage, for varying values of α and δ.

Figure 3.7 illustrates that the maximum average speed of the cell occurs when the amplitude α is large, and when δ is small, that is physically the situation of a large amplitude beat pattern which is fully developed along most of the flagellum; this is not a counter-intuitive result as it corresponds to most of the flagellum being involved in

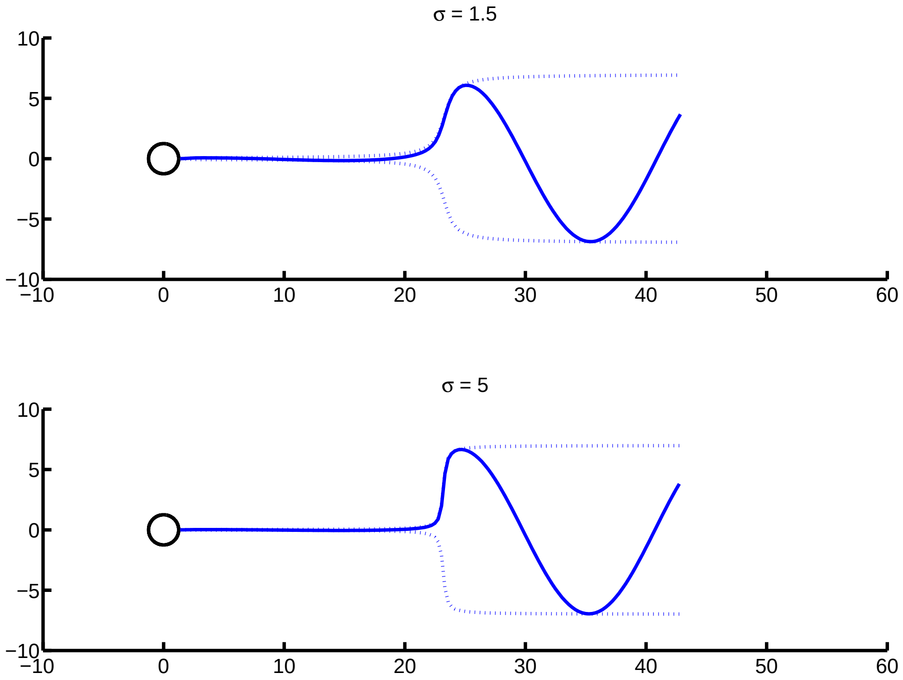

Figure 3.6: The effect of setting σ too high is demonstrated in the second plot; with $\alpha = 7$, $\delta = 0.5$ and $k_v = 2$. The combined exponential-arctan envelope is given by the dashed blue lines. The first plot has $\sigma = 1.5$, whereas in he second plot is $\sigma = 5$ and we see that the flagellum, whilst mathematically acceptable, is physically unrealistic due to the high curvature. The dashed lines represent the flagellar envelope.

beating. However, compared with Figure 3.8, we see that this extra speed comes at a cost – a much higher power consumption, however, we immediately notice that the maxima of these two graphs do not coincide.

The combination of power consumption and average swimming velocity discussed in Section 3.3.1 as inverse efficiency, gives us a measure of whether the increase in velocity occurs at disproportionate cost to an organism's power consumption. Figure 3.9 illustrates the variation in the inverse efficiency for different values of α and δ.

There are a number of important points to notice in Figure 3.9 and in particular its relation to Figures 3.7 and 3.8 from which it is derived. Firstly notice the existence of two minima in our parameter region of interest; a minimum at $(\alpha, \delta) = (6.8, 0.30)$ and another

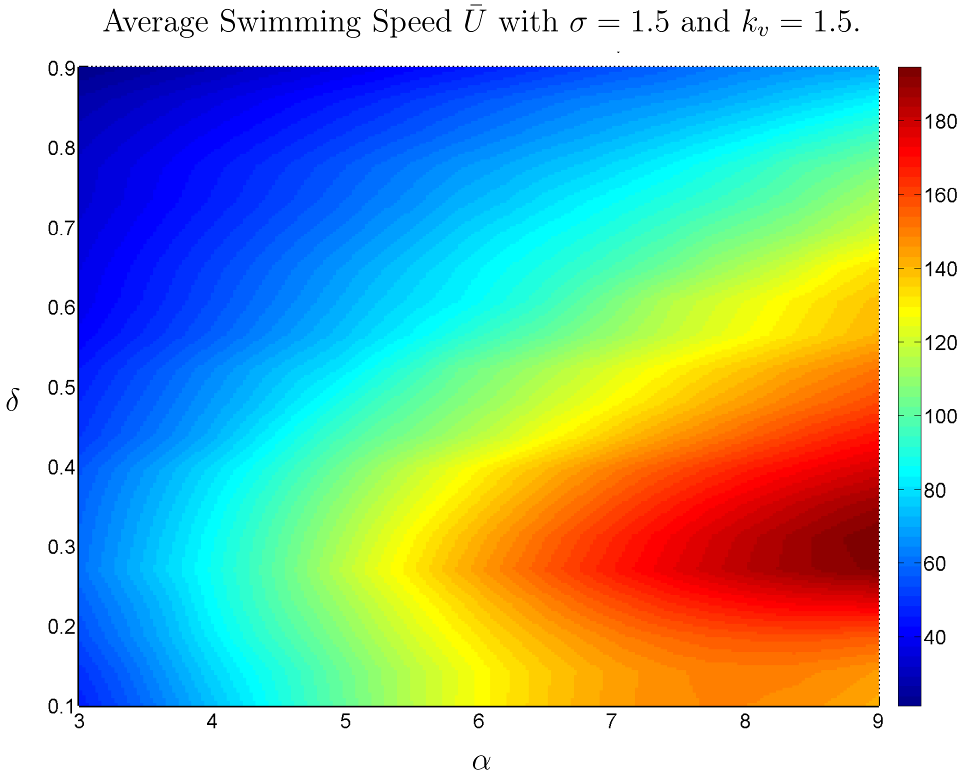

Figure 3.7: Plot of average swimming speed $\bar{U}$ for varying α and δ for $\sigma = 1.5$ and $k_v = 1.5$.

region, for high-posterior beating with large amplitude – the point marked is $(8.5, 0.82)$. Although the first value is the global minimum, the existence of another region of low inverse efficiency is interesting. Firstly it should be noted that this region has a lower swimming velocity and power consumption, but the organism is still motile.

The existence of two regions of minimal inverse efficiency suggests that there may be some other mechanisms which means that beat pattern opts for one choice over another. We shall explore this by considering the average energy consumption of the sperm.

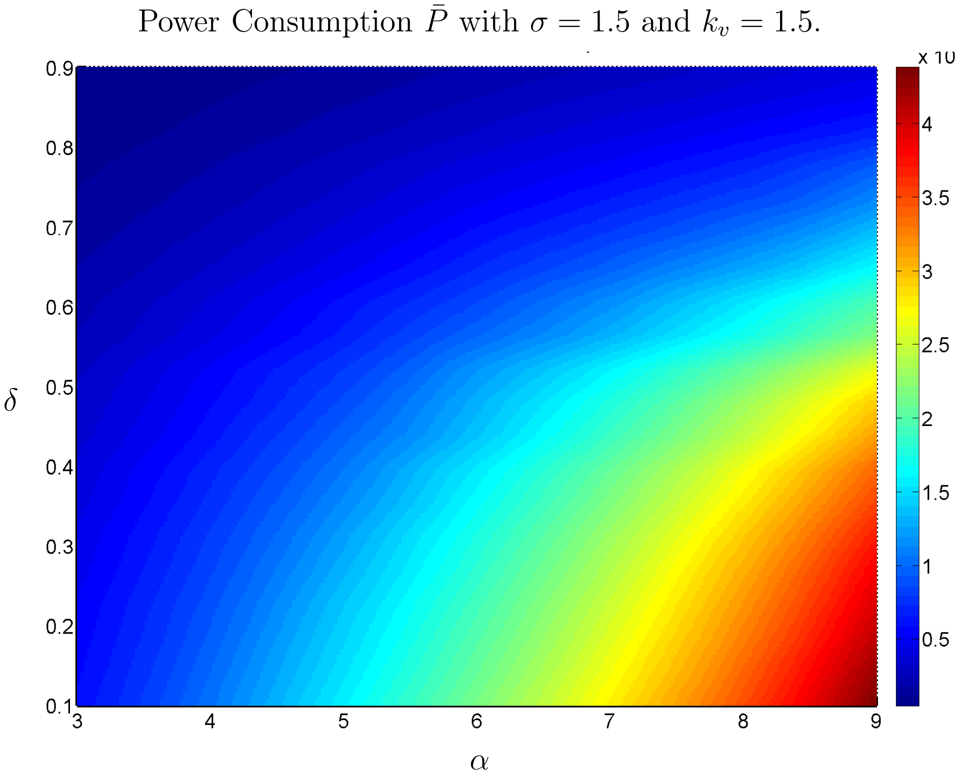

Figure 3.8: Plot of average power consumption $\bar{P}$ for varying α and δ for $\sigma = 1.5$ and $k_v = 1.5$.

The average energy consumption $\propto \bar{P}/\bar{U}$ is given in Figure 3.10, and once again demonstrates that, as expected, large amplitude, well developed beat patterns require the most energy. We consider the energy consumption of the two regions of minimum inverse efficiency. We notice that the energy consumption of the local minimum $(8.5, 0.82)$ is much lower than that of the global minimum $(6.8, 0.3)$; which suggests that if energy is a physical constraint then it may cause a switch to another, although slower, still efficient but more energy saving mode of beating.

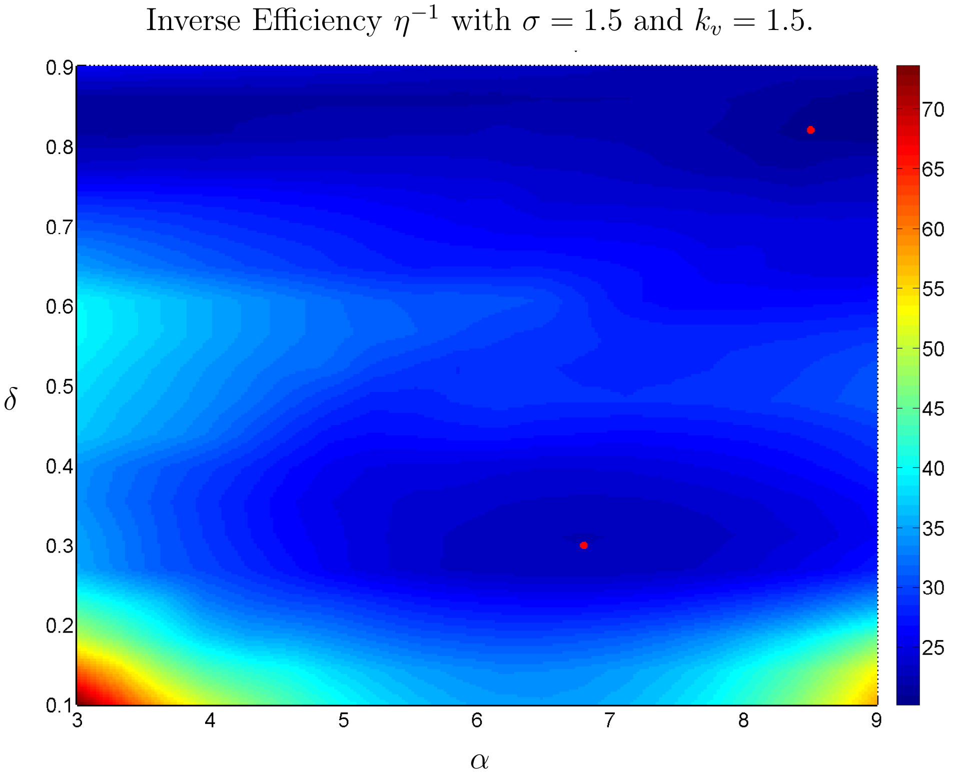

Figure 3.9: Plot of average inverse efficiency η^{-1} for varying α and δ for $\sigma = 1.5$ and $k_v = 1.5$. Marked, in red, are the two minima of the inverse.

3.4.3 Two-dimensional optimisation - δ and k_v

In this section we explore the link between the parameters δ and k_v; that is we explore the relationship between how posterior the beat pattern is and the wavenumber.

Firstly, in Figure 3.11 we observe that the highest swimming speeds are achieved for beating which occurs across the majority of the tail and with a low number of wavelengths, however, as one would expect this comes at a cost with fully developed beat patterns have high power consumption for a wide range of k_v, as shown in Figure 3.12.

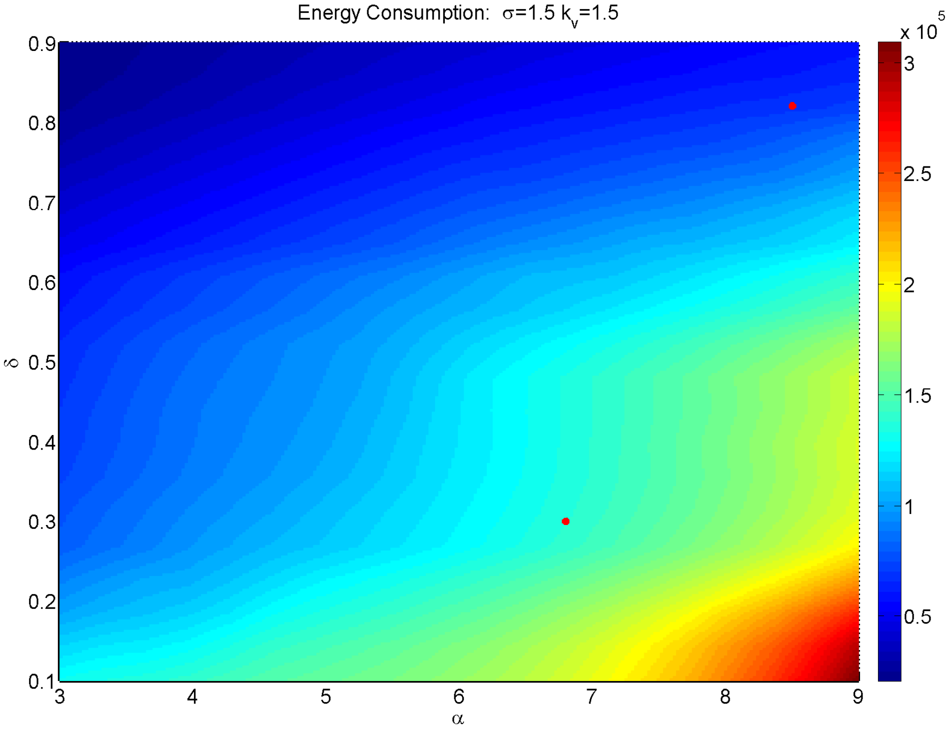

Figure 3.10: Plot of average energy consumption for varying α and δ for $\sigma = 1.5$ and $k_v = 1.5$. Marked on are the two minima of the inverse efficiency functional.

Shown in Figure 3.13 is the calculated inverse efficiency for this data. Firstly we notice that the most efficient beat patterns coincide with those of the highest velocity. It is also worth noting, that the ‘band’ of efficient beating patterns then extends out in to the (k_v, δ) space, suggesting that in order to maintain an efficient beat pattern, that for a fixed amplitude, if a beat pattern is more proximal, then the number of wavelengths on the tail should increase, and vice-versa. The trend is illustrated by a white line on Figures 3.13 and 3.14.

There is a second mode of very efficient, but slower beating around $\delta = 0.8$ for small k_v; this is similar to the secondary region found in the first optimisation.

Figure 3.14 illustrates that moving along the general path highlighted in Figure 3.13 is moving in the direction of increasing energy consumption; and thus this mechanism may not be advantageous compared to switching to the alternative mode of beating highlighted

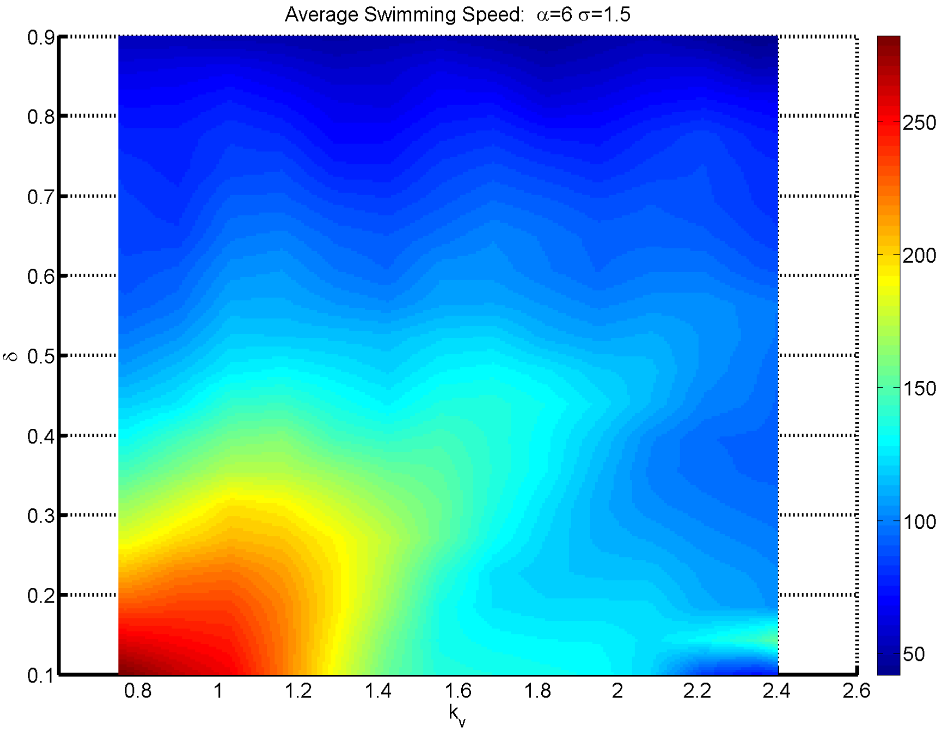

Figure 3.11: Plot of average swimming speed $\bar{U}$ for varying k_v and δ for $\sigma = 1.5$ and $\alpha = 6$.

earlier. However, it is still interesting to consider this region, as the swimming speeds are still high here compared to the second region.

3.5 Discussion

3.5.1 (α, δ) optimisation

The results for the two-dimensional optimisation of the amplitude and the measure of how posterior the beat pattern forms (α, δ), has illustrated several key points. We have highlighted that there are two regions of optimal beating for inverse efficiency. Figure 3.15 illustrates these two optimal beat patterns identified; recall at this stage the wavenumber is fixed. Figure 3.15(a) shows beating which is developed along the majority of the tail and at a lower amplitude, compared to the beating which is confined to the posterior of

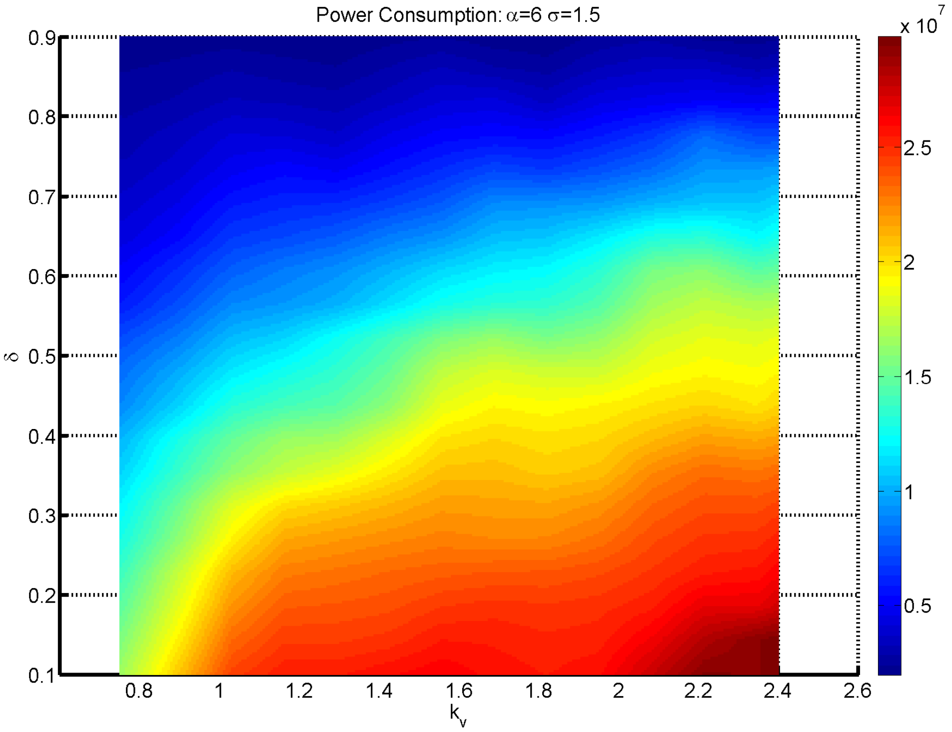

Figure 3.12: Plot of power consumption $\bar{P}$ for varying k_v and δ for $\sigma = 1.5$ and $\alpha = 6$

the tail and occurs at a larger amplitude.

We have demonstrated that we have an alternative optimal solution, which has a lower overall speed, but at an appropriate power reduction. We have also seen that despite the reduction in velocity of the local minimum over the global minimum, there is a saving to be made in energy consumption. The reason why a sperm cell may opt between these two minima is an open question and the answer is unlikely to be found by studying the fluid dynamics alone. Combining fluid dynamics with an understanding of the physical process which occur in the cells such as how quickly ATP (*Adenosine triphosphate* – the energy currency of cells) can be transported along the flagellum, should provide a better insight. However, at present intracellular processes are not fully understood.

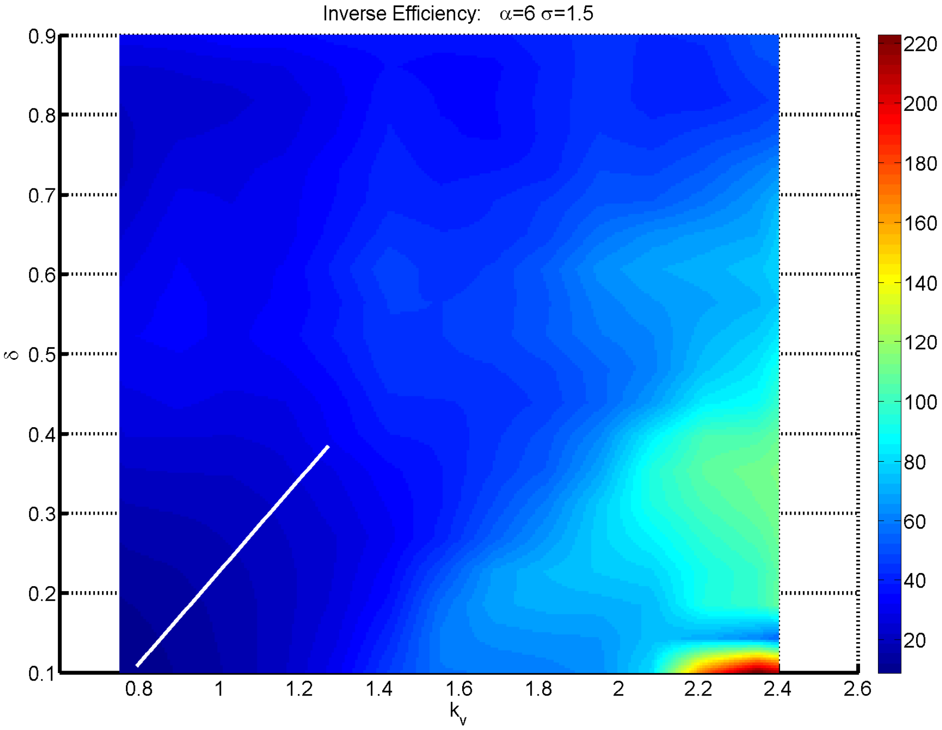

Figure 3.13: Plot of average inverse efficiency η^{-1} for varying k_v and δ for $\sigma = 1.5$ and $\alpha = 6$. The white line highlights a path through the parameter space, which seeks to minimise inverse efficiency.

3.5.2 (δ, k_v) optimisation

The results of the optimisation of k_v and δ demonstrate that in order to maintain an efficient beat pattern, it is necessary to increase the number of wavelengths on the flagellum if the posteriority of the beat pattern is increased, and vice-versa.

So far in the considering the optimisation of (δ, k_v), we have had a fixed amplitude α, however, we have seen previously that amplitude and δ linked. Figure 3.16 illustrates the variation in the inverse efficiency for values of α, when we use the values of δ and k_v lying within our optimal region on the inverse efficiency plot (values along the white line). We observe the optimal value for the amplitude parameter α is about constant and equal to 7 for all the different parameters sets along the optimal region.

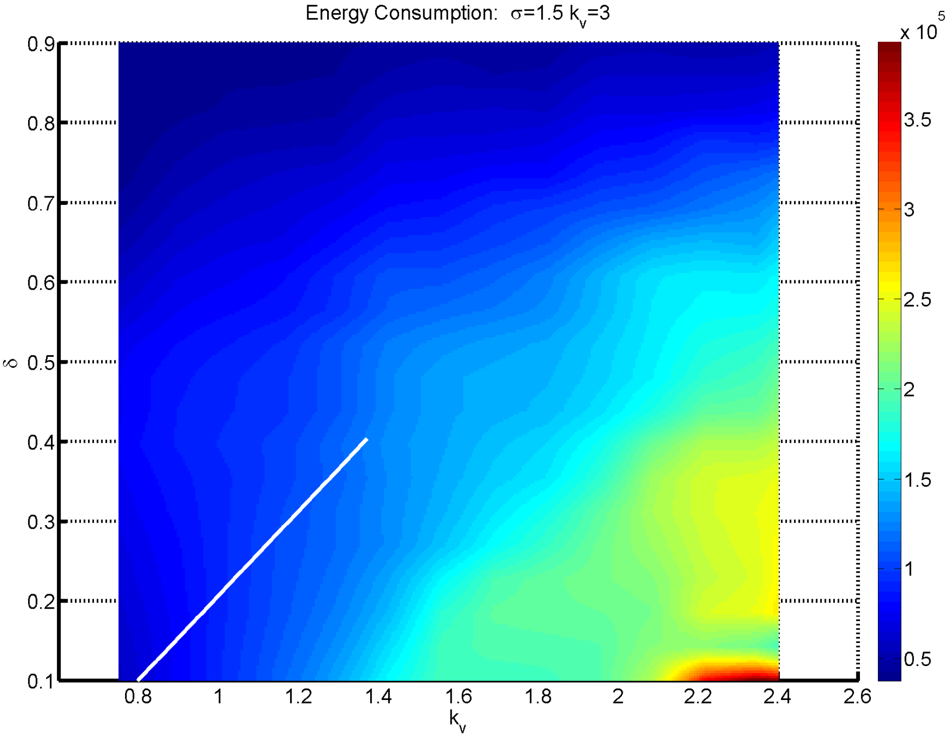

Figure 3.14: Plot of average energy consumption $\bar{P}/\bar{U}$ for varying k_v and δ for $\sigma = 1.5$ and $\alpha = 6$

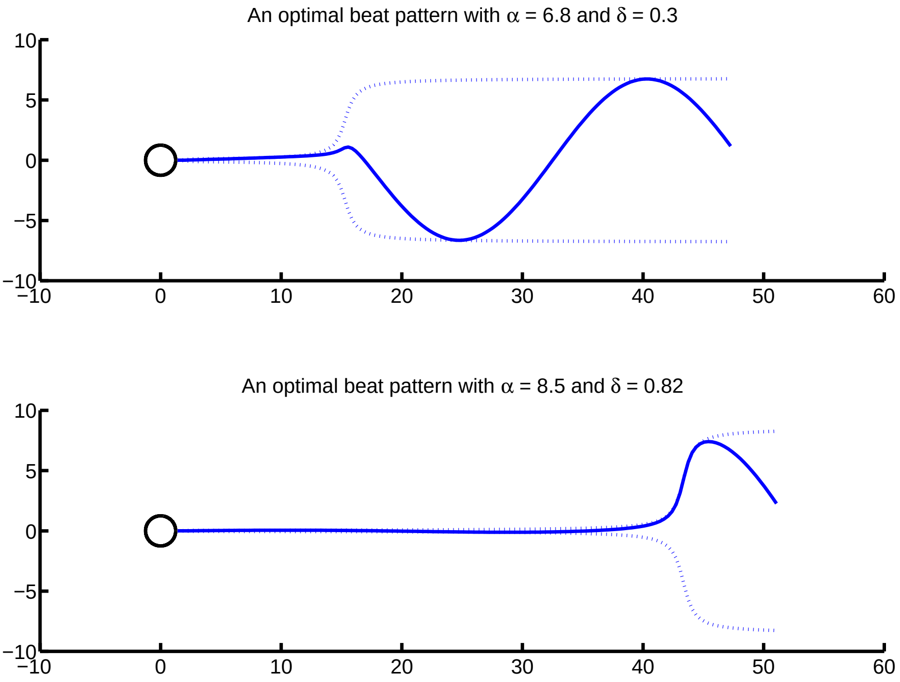

Figure 3.15: Plot of the two optimal sperm cells with (top) $\alpha = 6.8$, $\delta = 0.3$, and (bottom) $\alpha = 8.5$, $\delta = 0.82$. The dashed line represents the flagellar envelope.

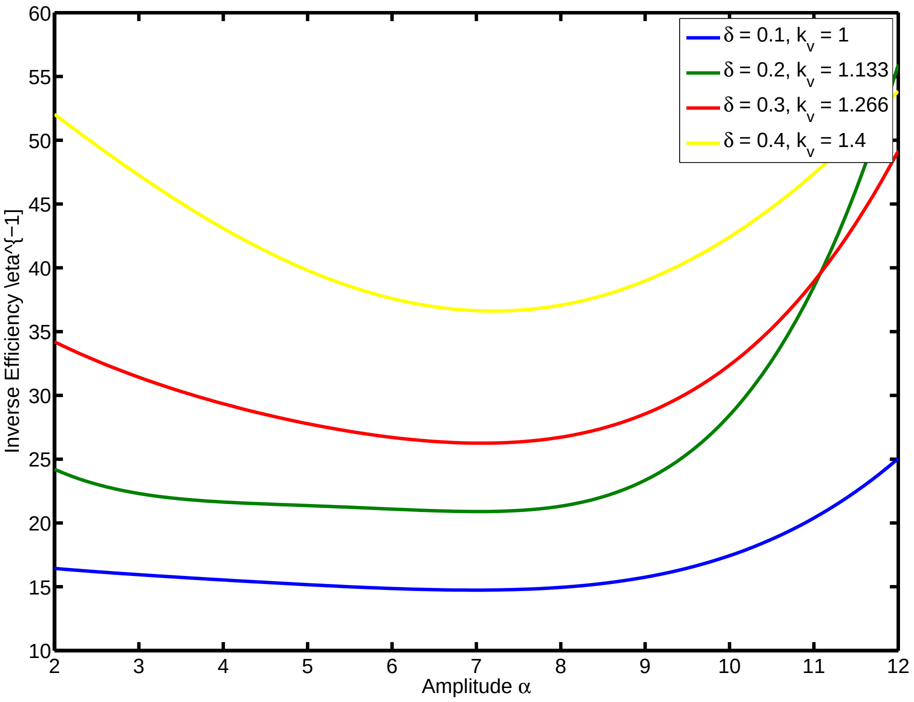

Figure 3.16: Variation in inverse efficiency as a function of α for a series of values of (k_v, δ) lying with the optimal band of parameter space. Notice that an amplitude of $\alpha \approx 7$ maintains efficiency in most cases.

3.6 Conclusions

In this chapter we have considered the optimisation of a parameterised sperm beat pattern using a new parametrisation which enables us to consider how posterior a beat pattern is. The mathematical model used is that of slender-body theory based upon the ideas of Higdon (1979c), modified to use a planar sinusoidal beat pattern with a combined exponential-arctan envelope.

By considering the three-parameter space, we have demonstrated that the three parameters – amplitude, posteriority of the beat pattern, and wavenumber are intrinsically linked with regard to minimising inverse efficiency. In particular we have shown that there are two different modes of optimal beatings for a given amplitude - with a reduction in overall velocity being compensated by a reduction in energy consumption. We have also illustrated that wavenumber and the posteriority of the beat pattern are linked – the more posterior the beat pattern, the more wavelengths are required on the flagellum to maintain a level of optimality, whilst the amplitude is fixed.

We have illustrated that in determining the optimal solution, all three parameters we have explored are linked in their effect on the velocity and power consumption and have qualitatively illustrated that the linking of parameters is consistent with experimental observations, such as those beat patterns seen in Figure 1.1.

One of the limitations of this model is that the wavenumber is assumed constant. In the next chapter, we relax this assumption to allow for a wavenumber which increases with the arc-length.

Chapter 4

Optimisation of a Parameterised Sperm Beat Pattern: Non-constant Wavenumber model

4.1 Introduction

In the previous chapter we investigated, as a model for human sperm, a sinusoidal planar wave modified with a combined exponential-arctan envelope. This specification previously adopted however, like the helical model of Higdon (1979c), did not allow for non-constant wavenumber. It is not obvious that the wavenumber should be assumed constant and experimental data (Smith et al., 2008b) suggests that the wavenumber is not constant along the flagellum and tends to increase towards the posterior of the flagellum; this can be observed in our motivating figures (Figure 1.1(b)). In order to account for this mathematically, we adapt our hybrid exponential-arctan model introduced in the previous chapter, to allow for an underlying sinusoidal planar wave with a non-constant wavenumber. Similarly to the previous chapter we shall explore, using the slender-body theory code, the relationship between the model parameters and the useful measures such as power and inverse efficiency.

4.2 Specification of the flagellum

We suppose that the position of the flagellum in the (X, Y, Z) space $\boldsymbol{X}(X, t)$, is given as follows

$$\boldsymbol{X}(X, t) = (X, \mathcal{E}(X - A)\cos([\Lambda(X - A)]\,(X - A) - \omega t), 0), \tag{4.1a}$$

with the envelope function

$$\mathcal{E}(x) = \alpha\left(1 - \exp(-x^2)\right)\left(\tan^{-1}\left(\sigma(x - \delta x_{\max})\right)\pi^{-1} + 0.5\right). \tag{4.1b}$$

These equations should be compared with those in the previous chapter; the expression for the envelope function is the same, however, the constant wavenumber k in Equation (3.1a) is replaced by a function Λ in Equation (4.1a).

The form of Λ is

$$\Lambda(x) = \left[\frac{2\pi k_v}{x_{\max}}\right]\left(\frac{x}{x_{\max}}\right)^{\theta - 1}. \tag{4.1c}$$

The reason for this choice of Λ is so that in the case $\theta = 1$, then $\Lambda(x)$ reduces to $\Lambda(x) = 2\pi k_v/x_{\max}$ which is the same as the expression for constant wavelength, and that k_v plays the role of the number of wavelengths as in the previous chapter. If $\theta > 1$ the number of wavelengths increasing towards the posterior of the tail, whilst for $\theta < 1$ it decreases; as illustrated in Figure 4.1.

The model parameters are the same as those in the previous chapter, except with the addition of θ, as discussed above, and the slightly modified interpretation of k_v.

As in Chapter 3, we consider the effect of changing the parameters on the useful measures which are derived from the outcome of the slender-body theory code developed in Chapter 2.

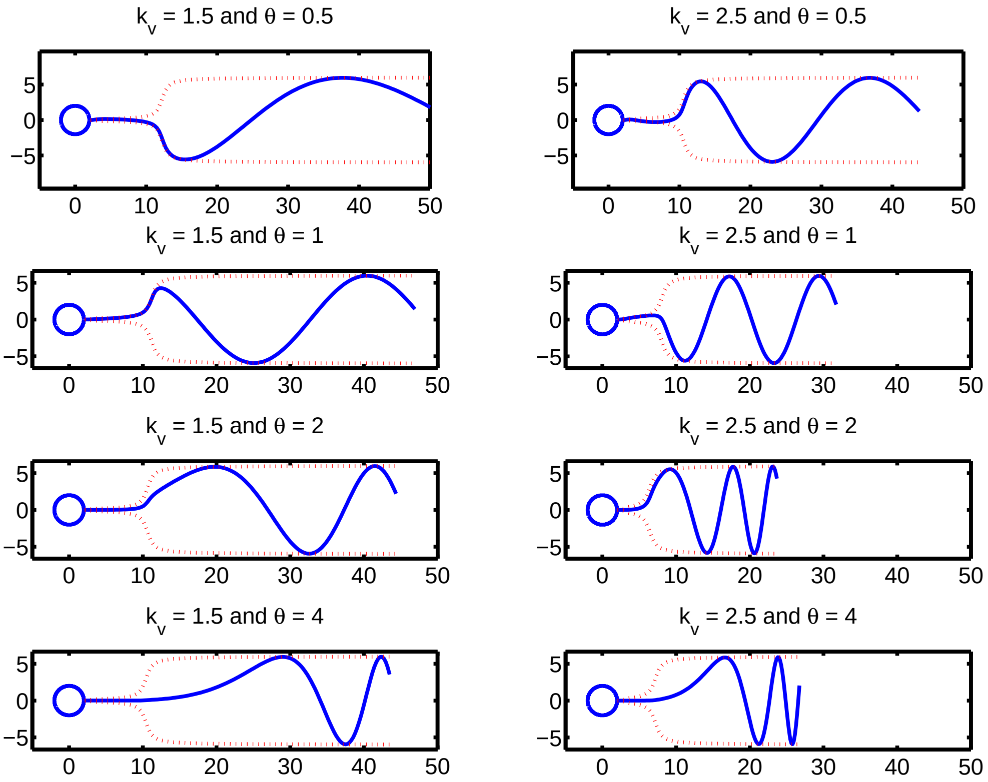

Figure 4.1: The effect of the parameters k_v (fixed in columns) and θ (fixed in rows). k_v has a similar role as in Chapter 3 (the number of wavelengths), and θ affects the effective wavenumber along the flagellum.

4.3 Results and discussion

4.3.1 Optimisation of (α, θ)

In this section we explore the relationship between the amplitude parameter α and the new parameter θ which provides the non-constant wavenumber. The other parameters are fixed as $\sigma = 1.5$, $\delta = 0.3$ and $k_v = 1.5$, which are the optimal parameters derived in the previous chapter.

Figure 4.2 illustrates the effect on the average swimming speed for a sperm cell for a varying values of α and θ. The fastest speeds occur for the higher amplitude beat patterns, which is consistent with our previous finding. Moreover, we find that the fast

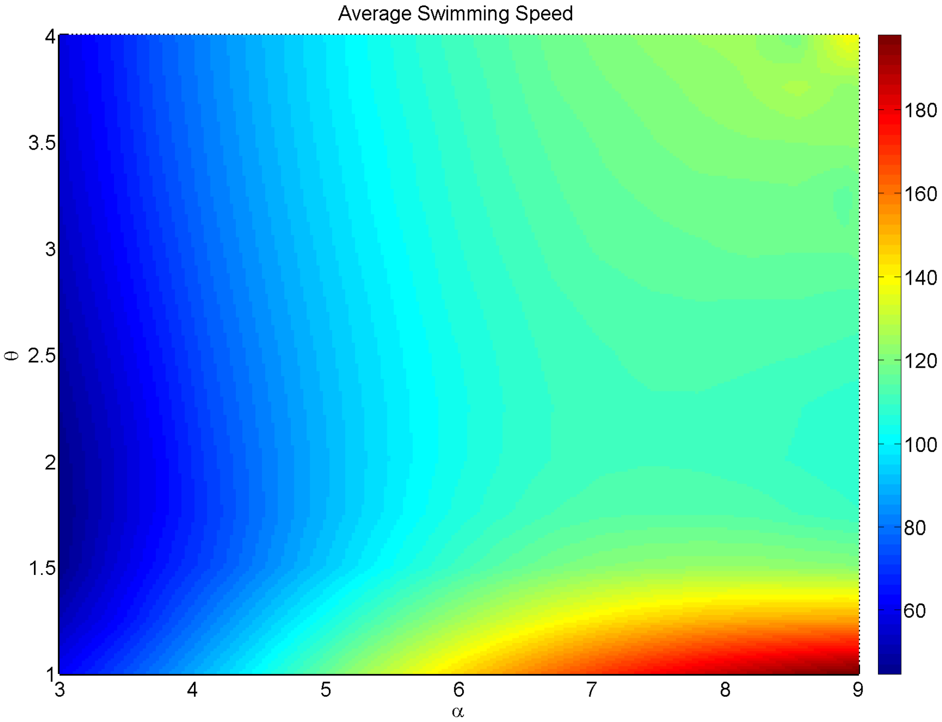

Figure 4.2: Average swimming speed $\bar{U}$ against α and θ, for the non-constant wavenumber envelope model.

speeds occurs when $\theta = 1$, that is to say that the wavenumber is constant along the flagellum.

Considering power consumption in Figure 4.3, we observe that as θ increases for a fixed value of α the power consumption increases. Combining these quantities of speed and power consumption generates the inverse efficiency, which is what we are seeking to minimise. Figure 4.4 illustrates that the minimum inverse efficiency has a 'saddle point' type structure with two optimal regions. There is a region for $\theta = 1$ with between $\alpha = 6$ and 7 which corresponds to a near maximum swimming speed. There is also a secondary region of optimal efficiency, for smaller amplitudes between $\alpha = 3$ and 5, but for increasing wavenumber, in particular for $\theta > 3$. The speed of this second region is however much slower than the most optimal region with $\theta = 1$. Figure 4.5 illustrates typical configurations from the two optimal regions.

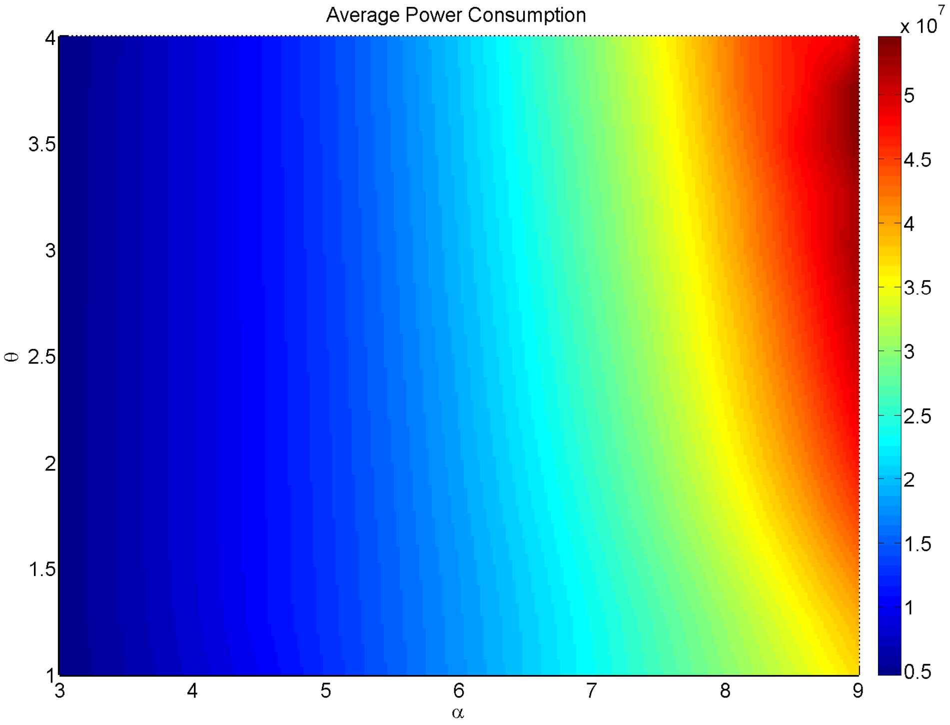

Figure 4.3: Average power consumption $\bar{P}$ against α and θ.

4.3.2 Optimisation of (k_v, θ)

In this section we present the result for the optimisation of the parameter combination k_v and θ. These parameters both form part of the specification of the variable wavenumber formulation Λ.

Figure 4.6 illustrates that the maximum average cell speeds occur when $k_v = 0.5$ and $\theta > 2$, which corresponds to increasing wavenumber towards the rear of the flagellum, however with a small multiplier k_v, meaning even at the end the wavenumber will still only be 0.5. Figure 4.7 illustrates a beat pattern configuration with these parameters, which corresponds to a whip-like configuration.

There is a second region of high average swimming speed when $\theta = 1$ with $k = 1.3$; this corresponds to the results found in the previous chapter.

In terms of the inverse efficiency, Figure 4.9 illustrates that for any given value of k_v

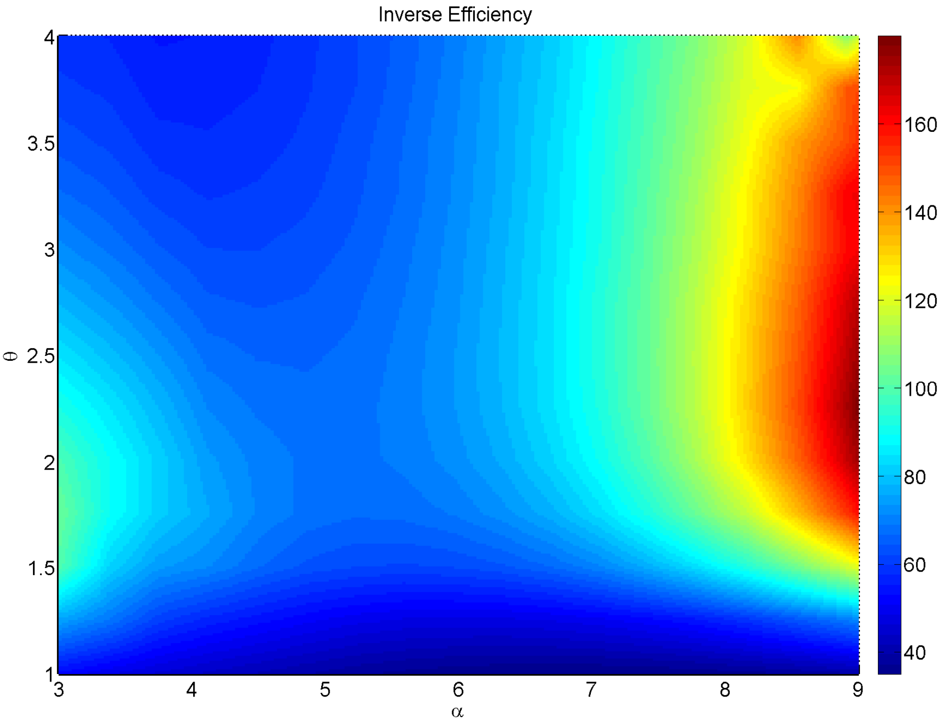

Figure 4.4: Average inverse efficiency η^{-1} against α and θ.

then setting $\theta = 1$ is the most efficient configuration. Overall, $\theta = 1$ and $k_v = 0.5$ is the most efficient configuration, however, in this case this does not correspond to the fastest swimming pattern but in fact a very efficient slow swimmer with low power consumption as shown in Figure 4.8. The region corresponding to the highest speeds (as discussed earlier) are near optimal.

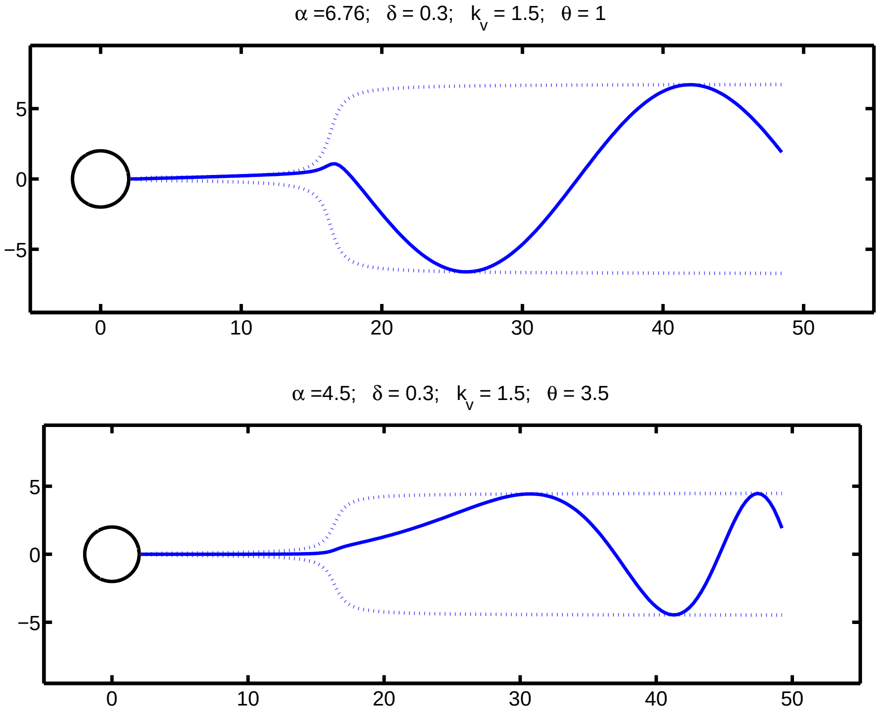

Figure 4.5: Two optimal sperm configurations found by optimising k_v and θ. The first sperm has a larger amplitude but constant wavenumber; for the second slower configuration the amplitude is lower but the wavenumber is not constant and increasing towards the posterior of the tail.

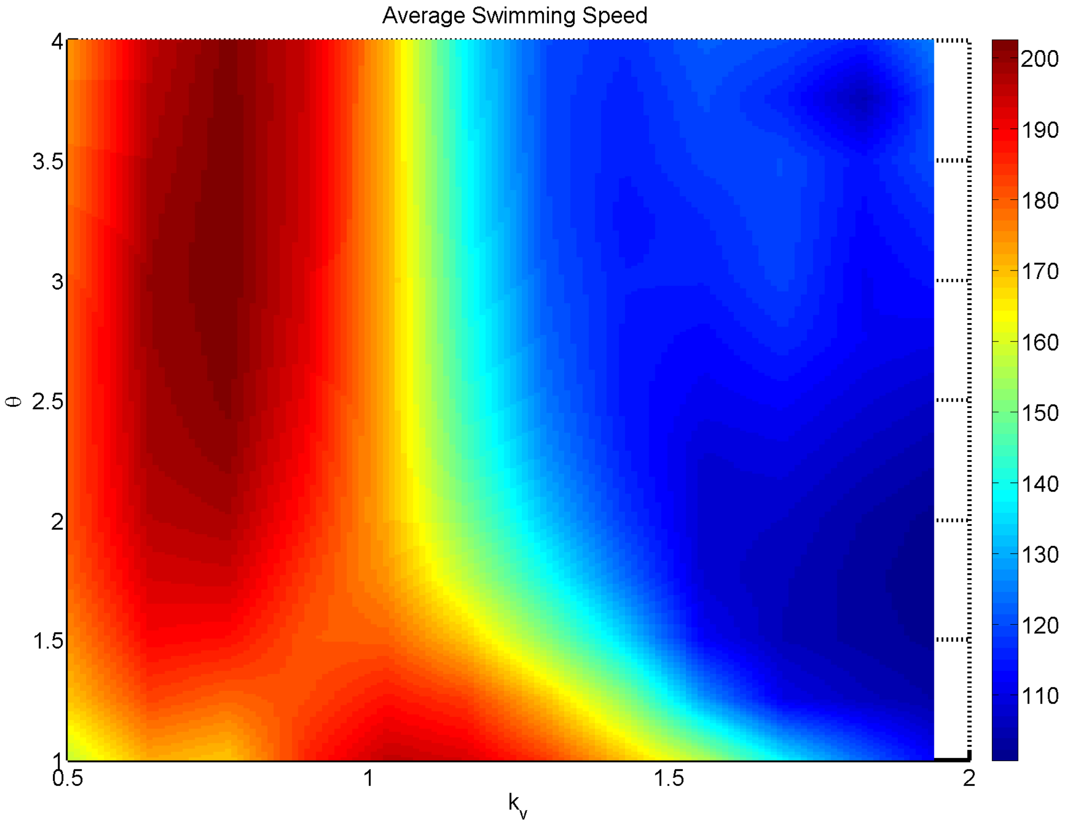

Figure 4.6: Average swimming speed $\bar{U}$ against k_v and θ.

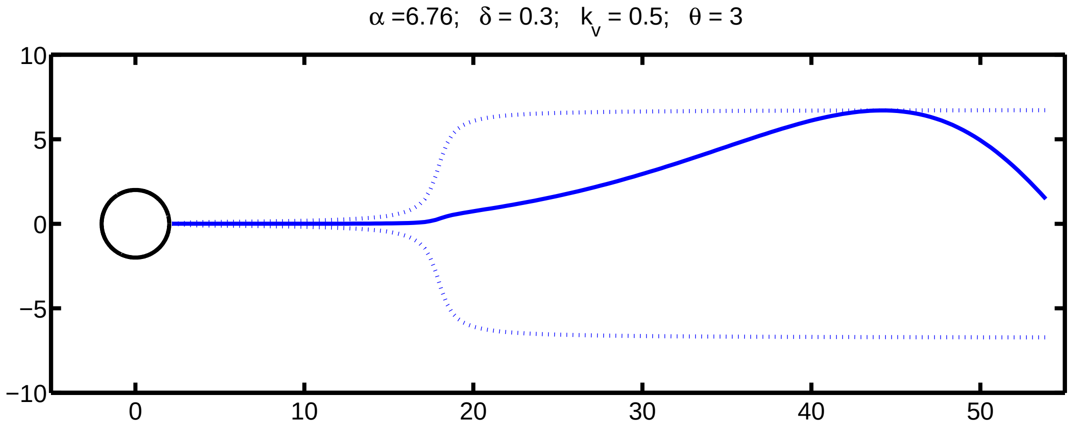

Figure 4.7: An example of a maximum swimming speed beat pattern, with $\alpha = 6.76$, $\delta = 0.3$, $k_v = 0.5$ and $\theta = 3$. Notice the whip-like beat pattern configuration.

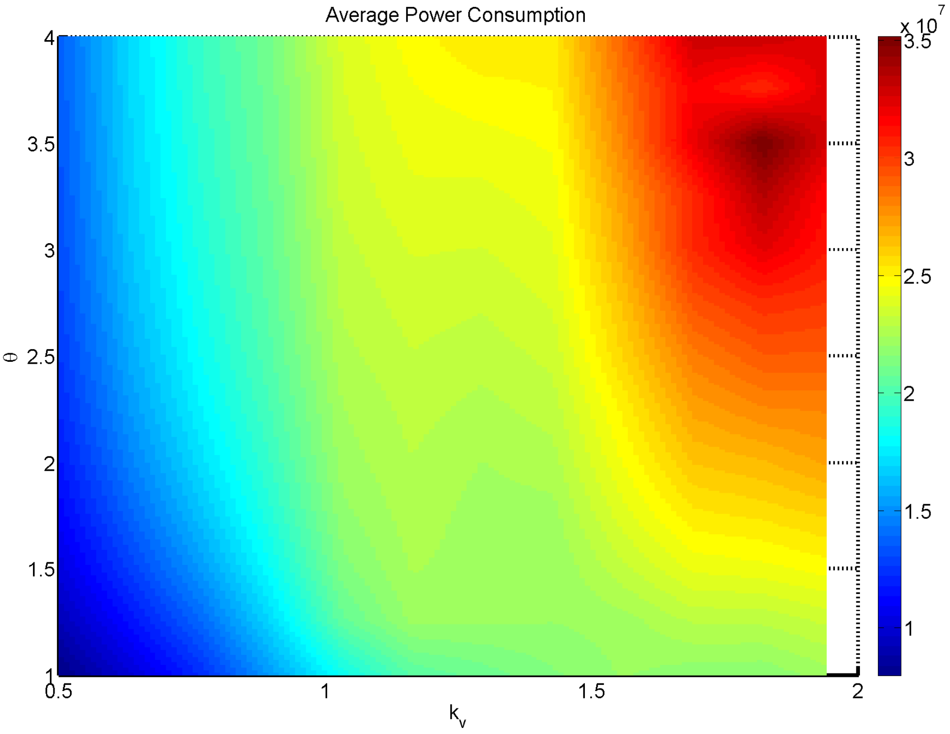

Figure 4.8: Average power consumption $\bar{P}$ against k_v and θ.

4.3.3 Optimisation of (δ, θ)

In this section we present the results for the optimisation of the posteriority of the wave δ and parameter associated with causing the non-constant wavenumber θ.

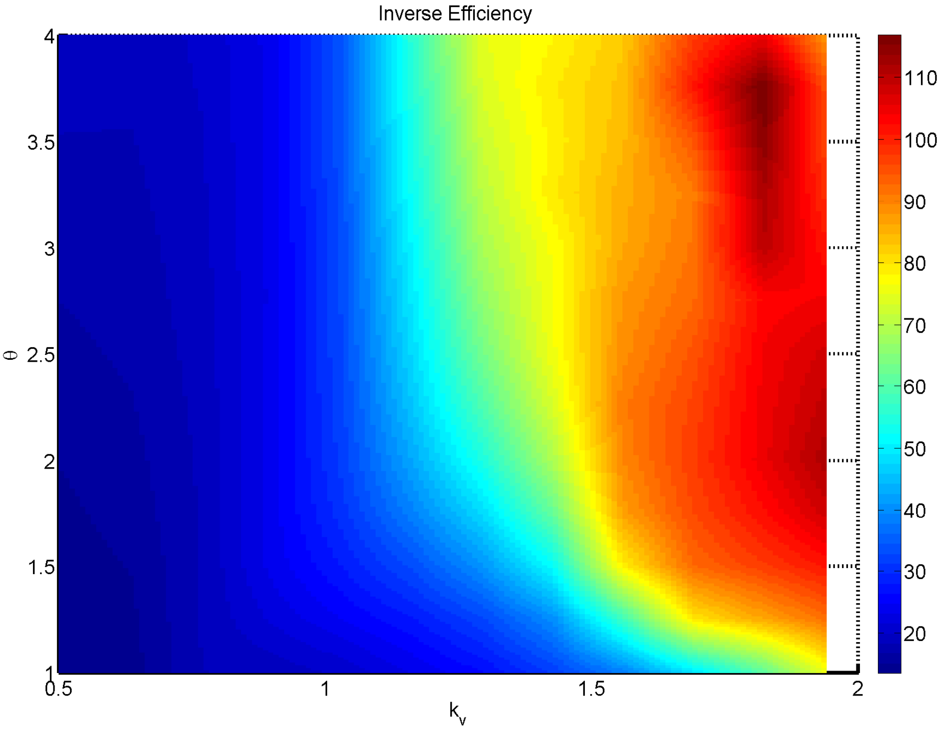

Figure 4.9: Average inverse efficiency η^{-1} against k_v and θ.

Figure 4.10 illustrates the average swimming velocity for different combinations of δ and θ. The first thing to notice are two modes of high velocity swimming for $\delta = 0.3$ and $\theta = 1$ (constant wavenumber) and importantly, for $\delta = 0.1$ and $\theta = 4$. These two modes are illustrated in Figure 4.11.

The inverse efficiency plot (Figure 4.12) illustrates a region of parameter space which results in configurations with similar inverse efficiencies. For $\delta < 0.3$, all values of θ are permissible and display near optimal efficiency. This region, labelled 1, encompasses our two previous modes of fastest swimming, and all the region of fast swimming illustrated in Figure 4.10. We also notice that this region coincides with the area of medium energy consumption as shown in green in Figure 4.13 (onto which the regions have been marked). The second region, with $0.4 < \delta < 0.65$ and $1 < \theta < 2$, is a region in which the inverse efficiency is low, however we notice that as δ increases the speed decreases, but so does

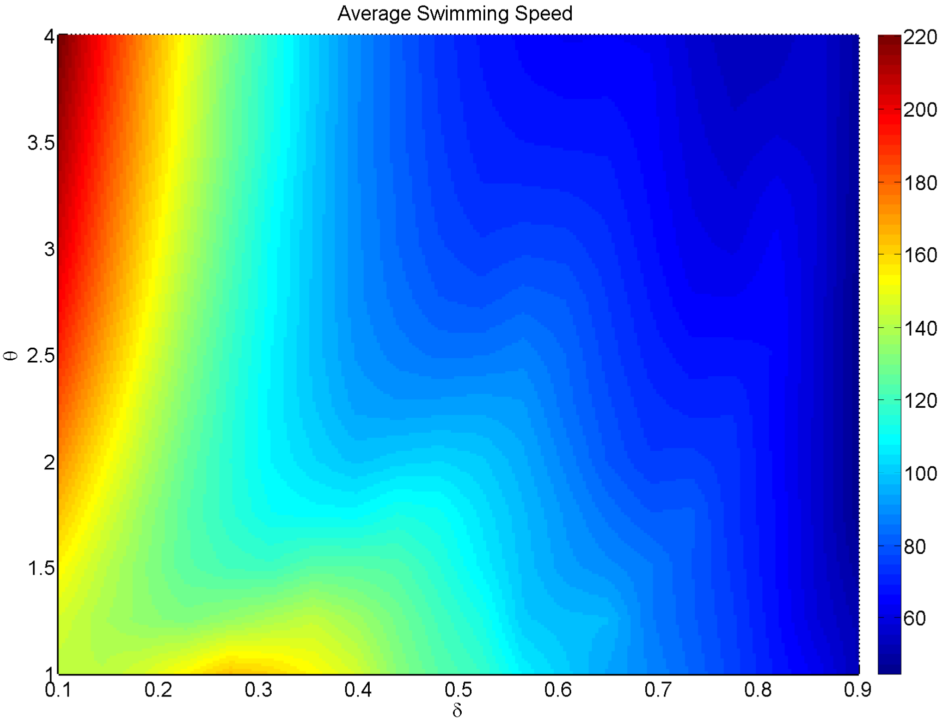

Figure 4.10: Average swimming speed $\bar{U}$ against δ and θ

the energy consumption. The final region occupies a triangle for $0.75 < \delta < 0.9$ and for increasing values of k_v from 2 towards 4; this region has the slowest swimming speed, however, it also has the lowest power consumption. This region 3 corresponds to proximal beating and an increasing wavenumber. Example configurations from each region are shown in Figure 4.14.

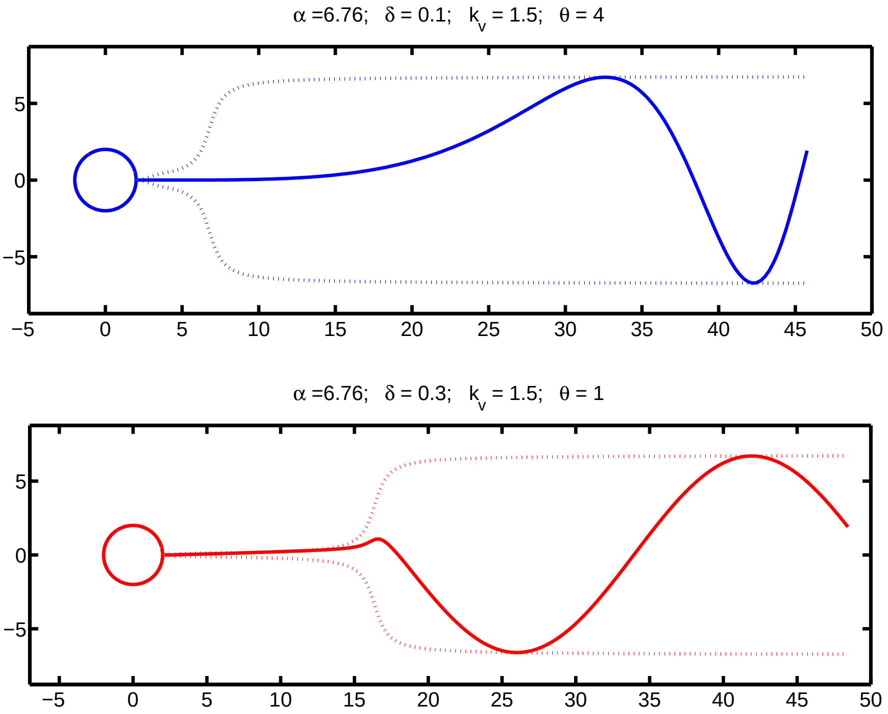

Figure 4.11: Examples of the maximum swimming speed beat patterns for (δ, θ).

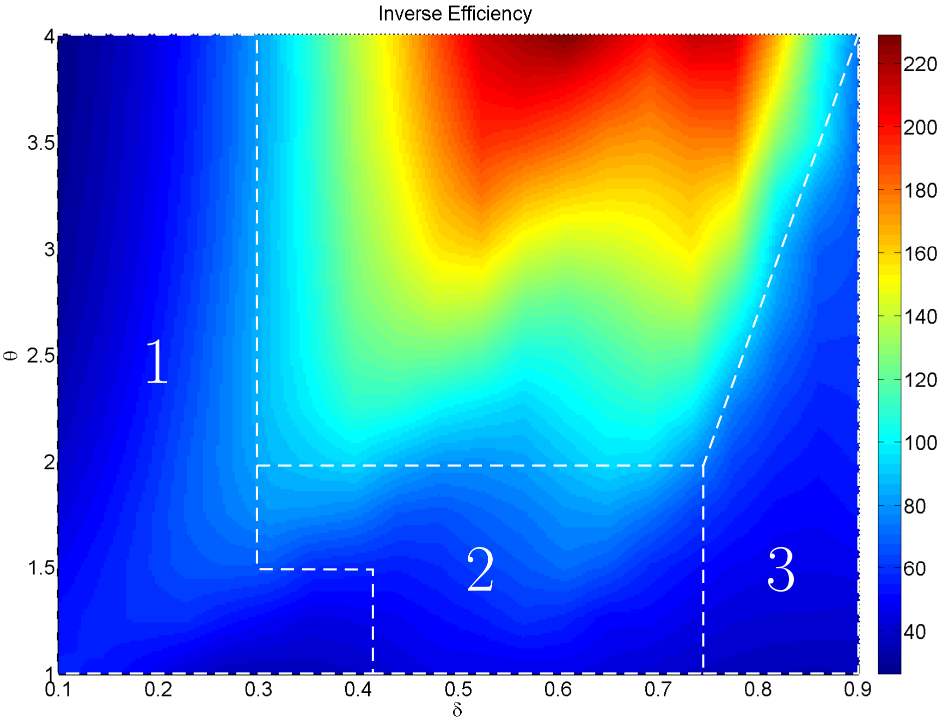

Figure 4.12: Average inverse efficiency η^{-1} against δ and θ. Marked on the graph are the three regions discussed in the text.

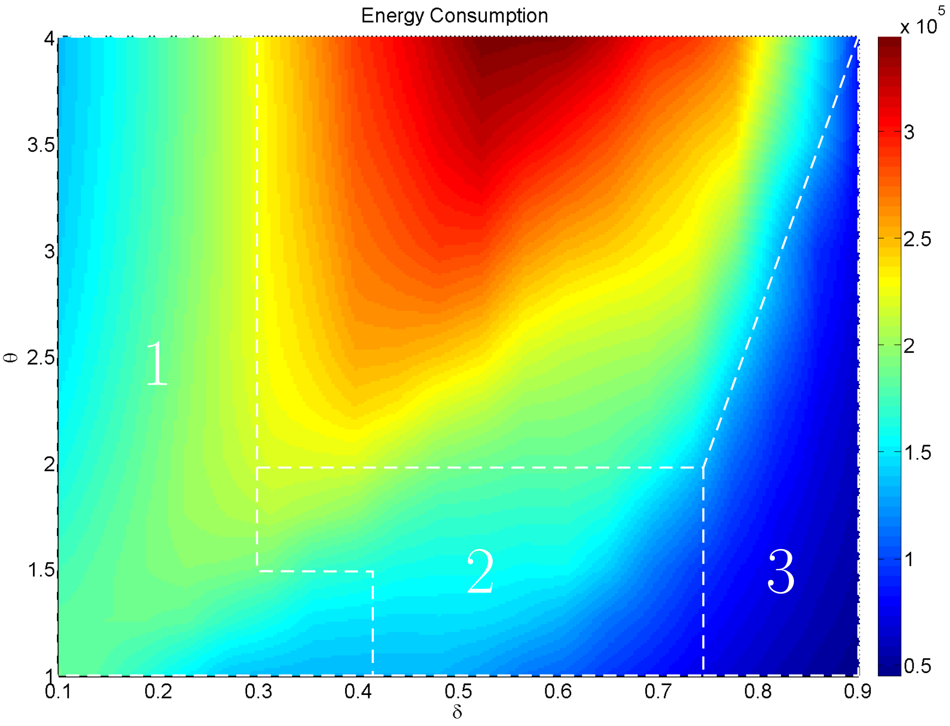

Figure 4.13: Average energy consumption $\bar{P}/\bar{U}$ against δ and θ; the regions of similar inverse efficiency from Figure 4.12 are marked on for comparison.

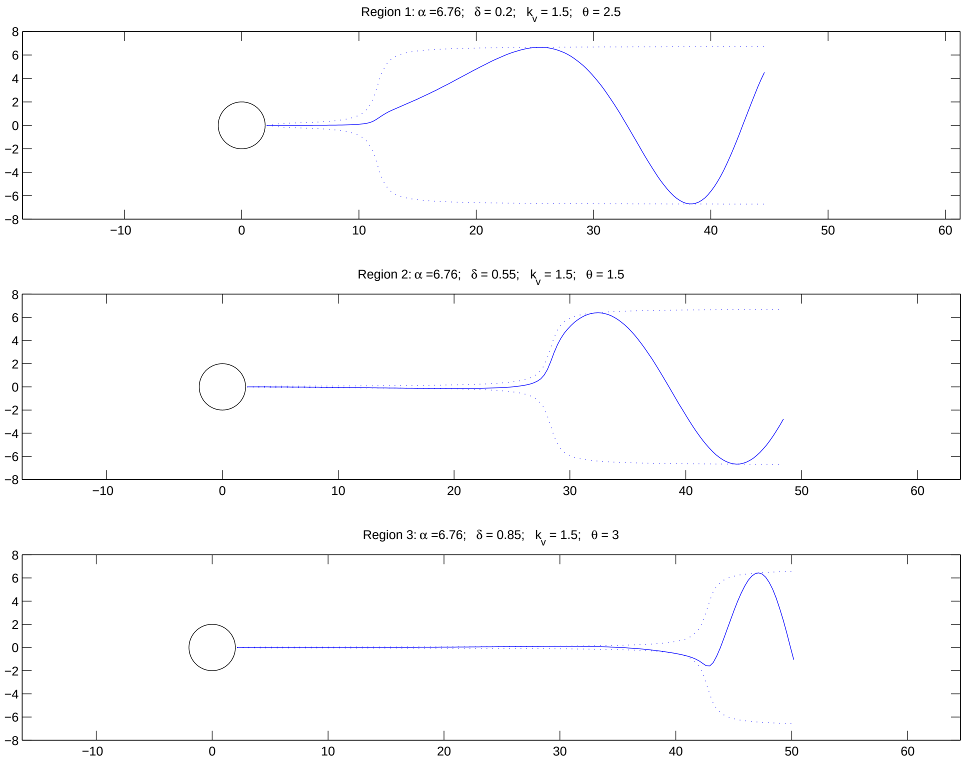

Figure 4.14: Example configurations from (top) region 1 with $(\delta, \theta) = (0.2, 2.5)$; (middle) region 2 with $(0.55, 1.5)$ and (bottom) region 3 with $(0.85, 3)$. In each case $\alpha = 6.76$ and $k_v = 1.5$.

4.4 Conclusions

In this Chapter we have developed a variable wavenumber extension of the model developed in Chapter 3. We have demonstrated the existence of optimal beat configurations which could not be adequately described using a fixed wavenumber model. In particular we have illustrated that the combination of the posteriority of the development of the beat pattern and an increasing wavenumber can be used to stay within optimal regions of the beat pattern. We have observed a whip-like configuration for the beat pattern and found two regions of optimality corresponding to varying the amplitude and the parameter controlling the non-constant wavenumber of the beat pattern.

In this chapter and the preceding chapter, we have used the concept of an underlying beat pattern – a planar sinusoidal wave – modified by an envelope function with a number of parameters. This specification, however, does not admit configuration such as the meandering patterns observed *in vitro*, as seen in Figure 1.1. In both chapters the results have agreed qualitatively with the experimental observation discussed earlier, however, in order to match the experimental data more accurately the number of parameters required is approaching a limit of what can be reasonably explored. In the next section, we devise and adopt a new method for specificating the beat pattern of a flagellum by considering the angle that the flagellum makes with the horizontal, parameterised by arc-length. This *shear-angle* method is devised based on experimental observation and is discussed in detail in the next chapter.

Chapter 5

Experimentally Based Parametrisation of Beat Kinematics using Shear-Angle

5.1 Introduction

In this chapter we formulate a new model for the specification of a flagellar beat pattern by specifying the angle which the flagellum makes with the horizontal (in the body frame) as a function of arc-length and time. The concept of applying this technique to flagellar beat patterns was used by Hines and Blum (1978) and Dresdner et al. (1980). The advantage of specifying an angle as a function of arc-length rather than the Y position as a function of the X position, allows configurations which are not expressible when $Y = Y(X)$, such as a 'meandering' type pattern where the angle to the horizontal may increase above 90°. By considering experimental data we are able to make certain generalisation upon which our model is based. The resultant model benefits from having only a small number of parameters.

Following the development of the new model, the second part of this chapter considers the application of this new model under our optimisation regime, using the slender-body theory code. We provide an explanation for the initial motivating experimental data.

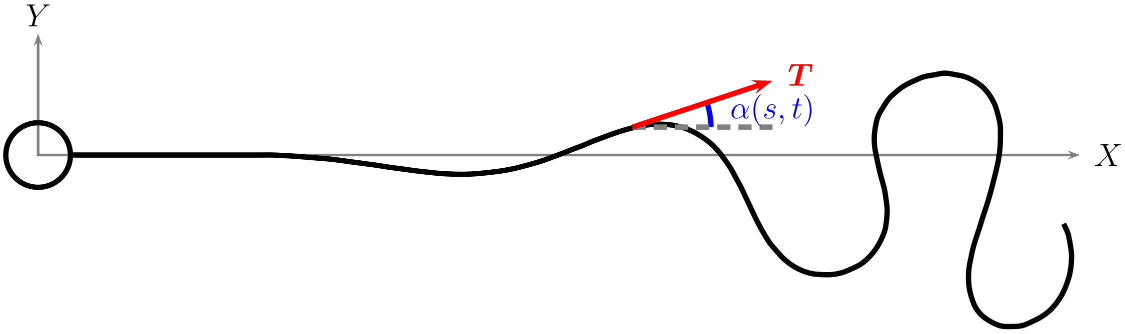

Figure 5.1: An example plot of a hyperactivated sperm beat recovered from experimental data (Smith et al., 2008b). The red arrow represents the tangent vector and $\alpha(s,t)$ is the angle which the tangent vector makes with the X-axis.

5.2 Beat pattern specification

Formally, we specify the position of a planar flagellum in the X, Y body frame as

$$X(s,t) = \int_0^s \cos(\alpha(s',t))\mathrm{d}s', \tag{5.1a}$$

$$Y(s,t) = \int_0^s \sin(\alpha(s',t))\mathrm{d}s', \tag{5.1b}$$

where $s \in [0,1]$ parameterises the arc-length and $\alpha(s,t)$ is the angle that the flagellum makes with the horizontal at arc-length s and time t. Figure 5.1 illustrates an example beat pattern, taken from experimental data of human sperm in Earle's medium with Methylcellulose 4000 at 2% concentration, with viscosity approximately 1.3Pa·s. The relationship between the bend angle α, the horizontal and the tangent vector $\boldsymbol{T}$ is highlighted in Figure 5.1.

In general the problem arises in determining the form of $\alpha(s,t)$. The aim is to devise a specification for $\alpha(s,t)$ which is not based on a parameterised function which must be assumed *a priori*. In the next section we consider experimental data for different types of sperm motility and from these make assumptions upon which our model is developed.

5.3 Experimental data

Using data from Smith et al. (2008b,c) we are able to obtain MATLAB data for the flagellum position of a human motile sperm in time sequenced frames. The data are first manipulated so that the data are all considered in the body frame such that the origin is located at the centre of the (assumed) spherical head and the tangent vector of the head/flagellar junction is parallel to the X-axis (as in Figure 5.1). The Y axis is right-hand perpendicular to the X-axis and thus the unused Z axis points out of the page.

In Figures 5.2 and 5.3 are two example sperm beat patterns with their associated bend angle as a function of arc-length taken from experimental data for a human sperm in a high viscosity medium (Figure 5.2 – Earle's medium with methylcellulose 4000 at 2%) and in a watery media (Figure 5.3 – Earle's medium only).

Notice that whilst the two physical beat flagellar beat patterns have many differences, the plots of their shear-angle (as a function of arc-length) have similarities; it is these similarities that we shall exploit in order to determine an appropriate model. The aim is to represent the shear angle as a function of space and time, through the use of a small number of knot points to form the basis of a cubic interpolation to complete the full specification of the angle profile in space with the time dependence arising from changing the amplitudes of the knots in time. Recall that the shear-angle is a two variable function having a dependence on arc-length s and time t. Our first approach is to consider fixing a set of knots at fixed values of $s_i^\star$ and then considering how these evolve in time using Fourier analysis of the experimental data.

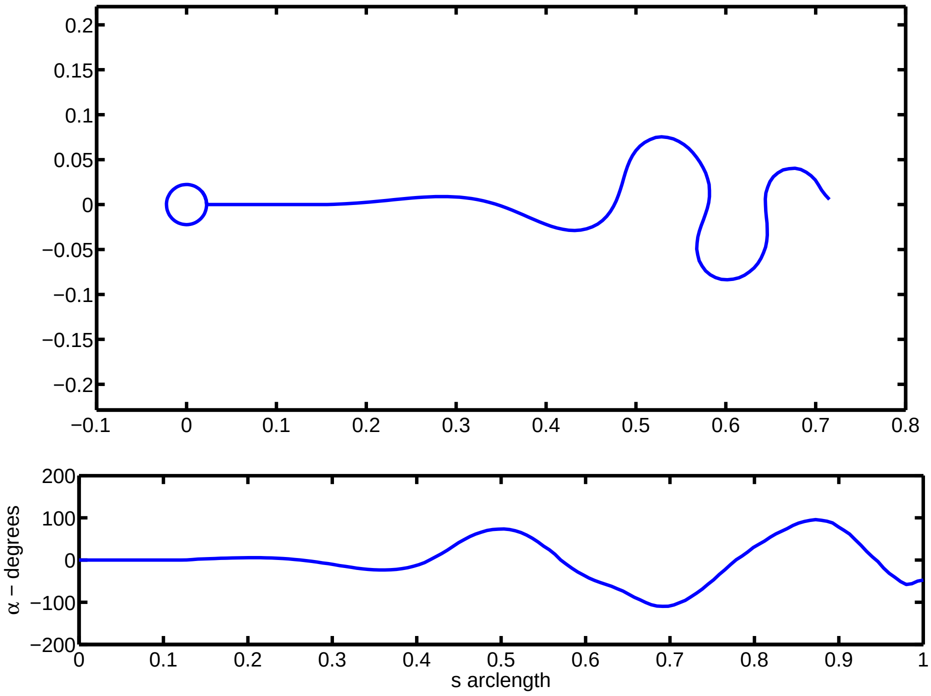

Figure 5.2: An example of a plot of a sperm beat pattern from experimental data and associated shear-angle. This sperm has a ‘meandering’ beat pattern; notice that the largest angles are near the posterior and that the first portion of the flagellum is not involved in bending. The experimental data has been scaled so that the total arc-length of the flagellum is 1.

5.4 Mathematical model

5.4.1 Fixed knots

We suppose that the knots are fixed at set values $s_i^\star$ in s space; the choice of the location of the knots is however, free. By taking the fast-Fourier transform of the experimental shear-angle at each of these knots over time and using Fourier analysis we are able to derive an expression for the value of $\alpha(s_i^\star, t)$ at each of the fixed knot points as a Fourier series. Each knot requires, as a minimum, an amplitude, a phase shift and a frequency which we found to be constant over all the knots. The number of parameters is thus quite high given we need at least five or more knots to adequate capture even the basic form

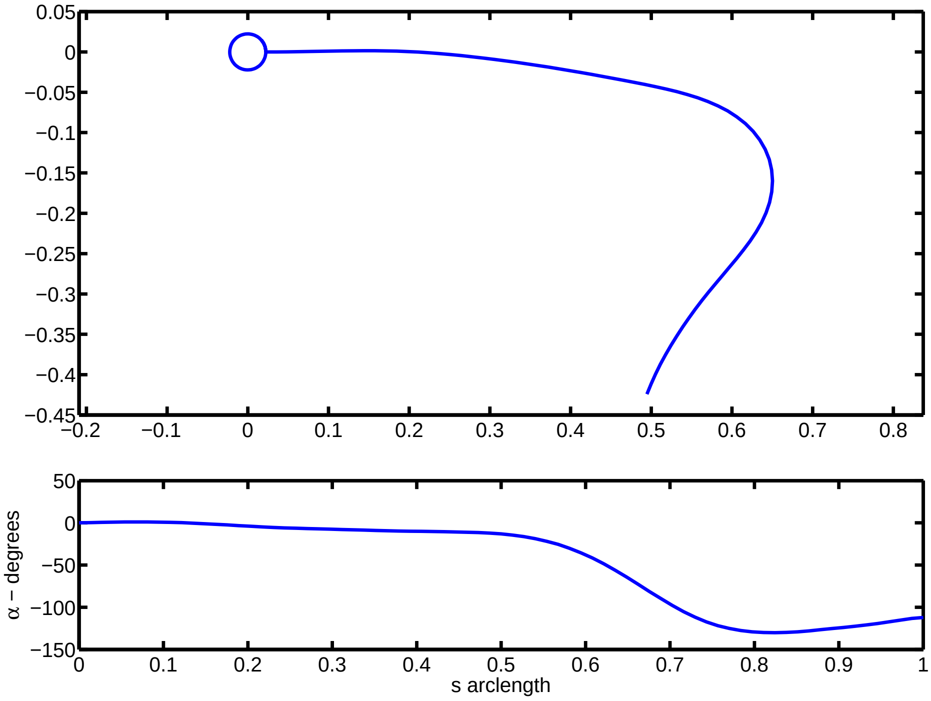

Figure 5.3: An example of a plot of a sperm beat pattern from experimental data and associated shear-angle. This sperm has a 'whip-like' beat pattern. In common with Figure 5.2, notice that the largest angle occurs near the posterior and the first portion of the flagellum is not involved in beating.

of the data. Our preliminary investigations however, highlighted no obvious relationship between the remaining parameters.

Additionally and moreover, the method was found to be unsatisfactory at modelling the variety of beat patterns we could expect and the prediction of the model would often lose many of the important features of the experimental data. One of the problems of the fixed knot model is that despite fitting certain periods of the data well, for certain time values all the knots may have very low amplitudes, and thus the cubic interpolation fitted to recover the continuous form of α is a poor match to the actual data, losing many of the important features. As an example consider the data used in Figure 5.2, if we fix knots *a priori*, as say evenly, there are instances in time when the Fourier series representation is

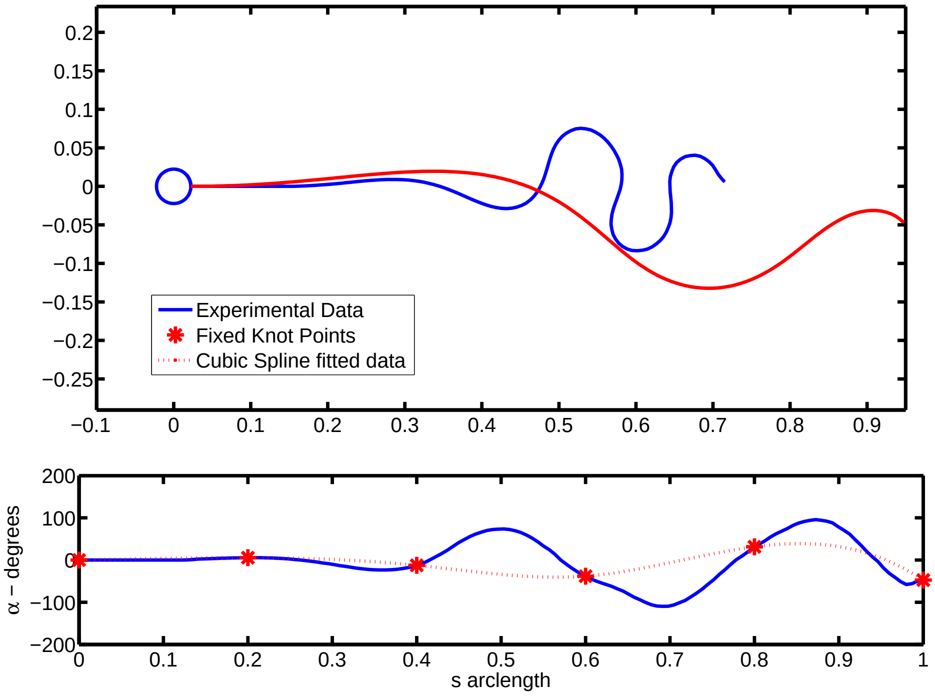

Figure 5.4: Experimental data of a meandering sperm beat pattern shown in blue. The red stars are the fixed knot points with amplitude predicted using Fourier series analysis. The dashed red line is the cubic interpolation which is calculated from the knot points. The red tail pattern is the predicted pattern from the interpolated shear-angle. Notice that the match is very poor and the features of the beat pattern are lost.

very good, whilst for other times, such as that illustrated in Figure 5.4, the match is very poor.

The reason for the poor match is that the important features of the shear-angle namely the extrema are often missed by the knot fixed points; resulting in a loss of structure. Clearly the problem can be circumvented by increasing the number of knots points – this is true of many kinds of data fitting procedures, however, in this case extra knots bring additional parameters. Our aim is to have a model parameterised in such as way as the parameter space can be studied in detail. A mechanism for capturing the extrema of the shear-angle is thus required; a solution lies in smartly moving the knots.

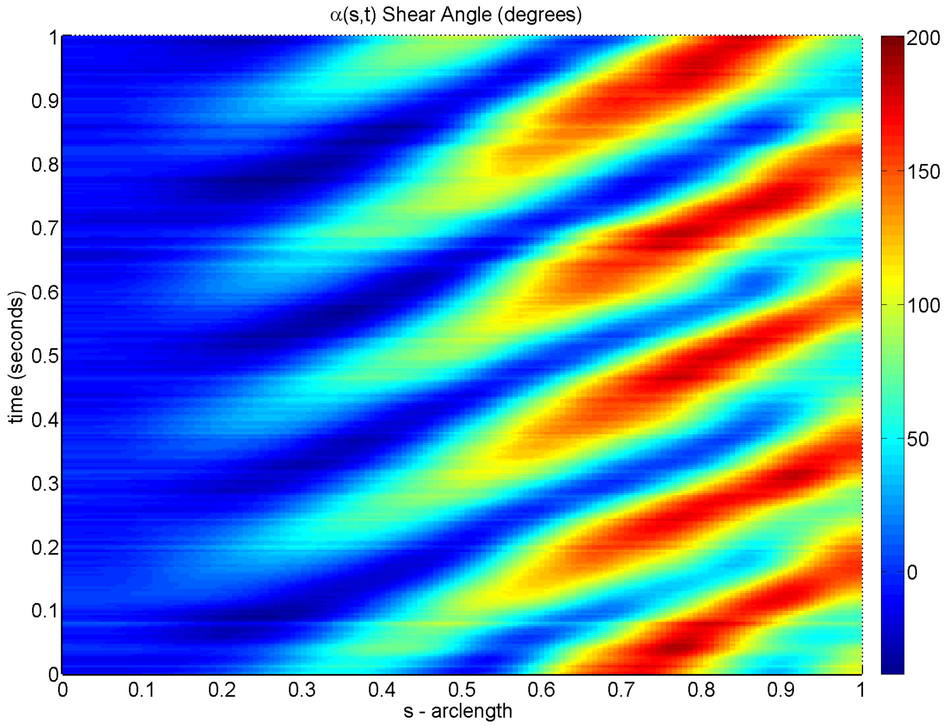

Figure 5.5: The variation in the shear bend angle as a function of arc-length and time. Notice the bands of maximum bending (red) and minimum bending (blue) which move towards the posterior of the flagellum with near constant speed and spacing. (Processing of the data by Mr Hermes Gadêlha (Oxford), using techniques in Smith et al. (2008b))

5.4.2 Moving knots

The important points in determining the nature of a curve, when approximating it with cubic interpolation, are the extrema - these are the maxima and minima of the curve. In order to consider this in detail we present experimental data of how the shear-angle changes with time. Figure 5.5 illustrates the change in bend angle as a function of arc-length and time for the sperm with a meandering beat pattern (such as that in Figure 5.2). The data are for a human sperm swimming in methylcellulose 4000 at 1%; notice that the beat pattern for this particular sperm is not symmetric about the X axis.

The extrema, shown as red (maximum) and blue (minimum) bands, move towards the posterior of the tail as time increases. There is only negligible deviation from $\alpha = 0$ in the region when $s \leqslant 0.2$ and we shall adopt this as a modelling assumption – backed-up by the fact that this region contains the 'midpiece' containing the mitochondria (see Figure 1.2). From this data we can extract, assuming that the extrema progress linearly, a speed of progression of the extrema against arclength as traversing from $s = 0.2$ to $s = 1$ in around 0.5 seconds, giving a speed of $8/5\,\mathrm{s}^{-1}$. We shall discuss the speed parameter in detail below. We must also make an assumption about how the amplitude of the shear-angle varies with the knots' position; we make the assumption that the amplitude increases linearly from zero at $s = 0.2$ to some maximum value a_1 which is the (positive) value an extremum will take if it occurs at $s = 1$. We shall shortly consider an upper limit on the value of a_1, which turns out to be dependent on the other parameters, to avoid self-intersecting beat patterns.

We wish to parameterise the distance between the extrema; we use a parameter N_e, analogous to N_λ in Chapter 2, so that when N_e is an integer it denotes the number of extrema in $s \in [0.2, 1]$, however, it can take any positive value, as $0.8/N_e$ is the knot spacing.

From Figure 5.5, we see that the spacing of the extrema are approximately constant and uniform; we shall adopt this as a modelling assumption.

A summary of the modelling assumptions is as follows

- There is no deviation in the range $s < 0.2$, and consequently $\alpha(s < 0.2, t) \equiv 0$, for all t.
- Extrema are uniformly spaced between $s = 0.2$ and $s = 1$, and there are N_e in this range.
- Extrema move linearly in time with a known speed.
- Amplitude of the knots increases linearly from zero at $s = 0.2$ to a maximum absolute value of a_1 at $s = 1$.

- The shear-angle is ‘symmetric’ – the absolute value of the amplitude of an extremum at $s = 1$ is the same for maxima and minima.

As an example of the method, consider applying it to the example where the fixed knot scheme failed above (Figure 5.4). Using the moving knot model with $N_e = 4.7$ and $a_1 = 120°$, the results, which show a much better level of agreement than the fixed knot model, are illustrated in Figure 5.6. It is worth noting that although the new model does not match the experimental data exactly we have developed a scheme which, with a very small number of parameters, captures the important features of a beat pattern seen *in vitro*. The model for devising the beat pattern allows the beat pattern to be easily scaled back onto a realistic sized sperm with a flagellum length of $L = 56\mu$m

It is worth noting at this point that we have just three parameters, one of which, the speed, we shall discuss below in more detail below. Compare this with the number of parameters in the fixed knot model considered in Section 5.4.1, where as a result of the Fourier analysis, we had for the 5 fixed knots, 11 parameters which were poorly defined and required direct Fourier analysis of the experimental data – moreover, the 11 parameter model was a poor fit to the data, especially compared to our moving knot model.

5.4.3 The speed parameter and time period

We currently have three free parameters; the number of extrema N_e, the maximum bend angle a_1 and the speed of the knots v. We have a number of derived parameters - firstly the spacing of the knots which is $= 0.8/N_e$ and a *fundamental time period* T defined to be the time between the ‘generation’ (at $s = 0.2$) of successive maxima. As the extrema are spaced uniformly and travel with speed v, subsequent maximum will be generated every $T = 2(0.8/N_e)/v$ – the need for the multiplier of 2 is that generation of extrema alternatives between maxima and minima. Outside the fundamental time period T, the beat pattern simply repeats due to the progression of the extrema.

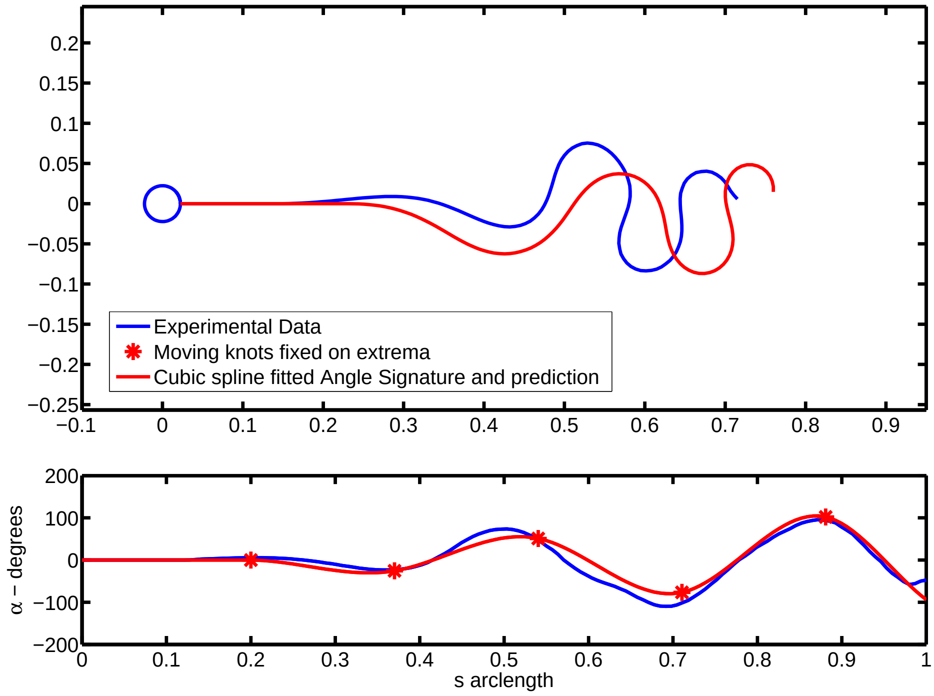

Figure 5.6: Experimental data of a meandering sperm beat pattern shown in blue. The red stars are the moving knot points which form the extrema of the fitted cubic interpolation. The red line is the cubic interpolation which is calculated from the knot points and is then converted into the representation of the tail in the top portion of the figure. Notice that the match is much better, especially as we have fitted it using only two parameters. The important features of the beat pattern are captured in this model. The model parameters are $N_e = 4.7$ and $a_1 = 120°$.

Assuming nothing at present about the form of v, we can see that T is inversely proportional to N_e; that is, as the number of extrema increases the time period T will decrease, increasing the frequency – this contradicts experimental results of Ishijima et al. (1986) who, for human sperm, observe a whip-like beat pattern in Hank's solution (with viscosity 1cp) with frequency $11.8 \pm 2.2\,\text{Hz}$; and a ‘meandering’ distal beat pattern in Methylcellulose at 4000cp of $7.0 \pm 1.2\,\text{Hz}$, and $12.3 \pm 1.8\,\text{Hz}$ in cervical mucus at 4360cp. A reasonable assumption is that the frequency can be therefore be assumed to not depend on the type of beat pattern.

We shall shortly consider the beat kinematics, through the bending rate $\partial\alpha/\partial t$, as a function of our model parameters. We observe that the bending rate is proportional to a_1, N_e and v. The rate at which a flagellum can bend is a physical limitation and we propose the assumption that the bending rate should not be dependent on the number of extrema, but just the maximum bend angle. This can be achieved by choosing v such that $v \propto 1/N_e$. This choice has the added benefit that the fundamental time period, and hence the frequency, is now fixed for all beat pattern configurations.

We have observed that in the motivating experimental data (Figure 5.5) with $N_e = 5$, the extrema traverse the final four-fifths of the flagellum length in 0.5 seconds. For other data with a symmetric pattern and $N_e \approx 5$ we have observed that the final four-fifths of the flagellum length are traversed in 0.7 seconds. As we have made the modelling assumption that v is inversely proportional to N_e, based on experimental data we set $v = 5.33/N_e$ flagellum lengths per second which yields a time period of $T = 0.3$s.

5.4.4 Computational implementation

The computational code is devised in two parts: a program to calculate the bend angle $\alpha(s,t)$ as a function of s and t and a program which calculates the coordinates of the flagellum in (X,Y) space. The second program outputs for a given t the coordinates of the N points used to represent the tail in the body frame, (X_n, Y_n) (for $1 < n < N$). The integration required to calculate (X_n, Y_n) from $\alpha(s,t)$ in Equations 5.1 is performed using Gauss-Legendre quadrature.

The first program is used to calculate the value of α for a given value of s and t. Recall, that the underlying model is that we specify the movement of the knots from which the continuous function of $\alpha(s,t)$ is determined using cubic interpolation.

Pseudo-code for determining $\alpha(s,t)$

In order to successfully encode the mathematical model and ensure that the cubic interpolation is 'well behaved' in the region of interest $s \in [0,1]$ we need to implement two small procedures in the computational scheme for $\alpha(s,t)$. Firstly, to ensure that the predicted angle is well behaved in the region between the last knot and $s = 1$, we need to place 'ghost knots' in the region $s > 1$ to ensure that the resultant cubic interpolation is bounded in our region of interest. Secondly, in order to ensure smooth derivatives of the angle with respect to time, the propagation of the knots in the region near to $s = 0.2$ needs to be modified slightly. In particular to ensure that $\partial\alpha/\partial s|_{s=0.2} \approx 0$ for all values of t, we place a series of ghost knots in $[0.1, 0.2)$ with zero coefficient. Moreover, the knots in the region near to $s = 0.2$ with $s > 0.2$, have their amplitudes by an exponential envelope $1 - \exp\{-100(s-0.2)^2\}$ to ensure that the required derivatives are smooth.

The pseudo-code for determining $\alpha(s,t)$, give the number of extrema N_e and maximum amplitude a_1 is as follows

- You will have need a total of $\lceil N_e \rceil$ knots.
- These are spaced a distance $0.8/N_e$ apart.
- The knots progress forward in s space in time at speed v.
- The coefficients of the knots take alternating positive and negative values.
- The coefficients of the knots are determined based on the linearly increasing assumption, with the exponential envelope modification near $s = 0.2$.
- The continuous form of the data is derived using cubic interpolation using the MATLAB function `pchip` (piecewise cubic Hermite interpolating polynomial), which has the advantage over standard cubic splines that the resultant (spatial) interpolation will have a continuous second derivative.
- Any knots with $s \leqslant 0.2$ are set to have amplitude zero.

Figure 5.7 illustrates the construction of α, including the ghost-knots, the exponential envelope modification and the cubic spline.

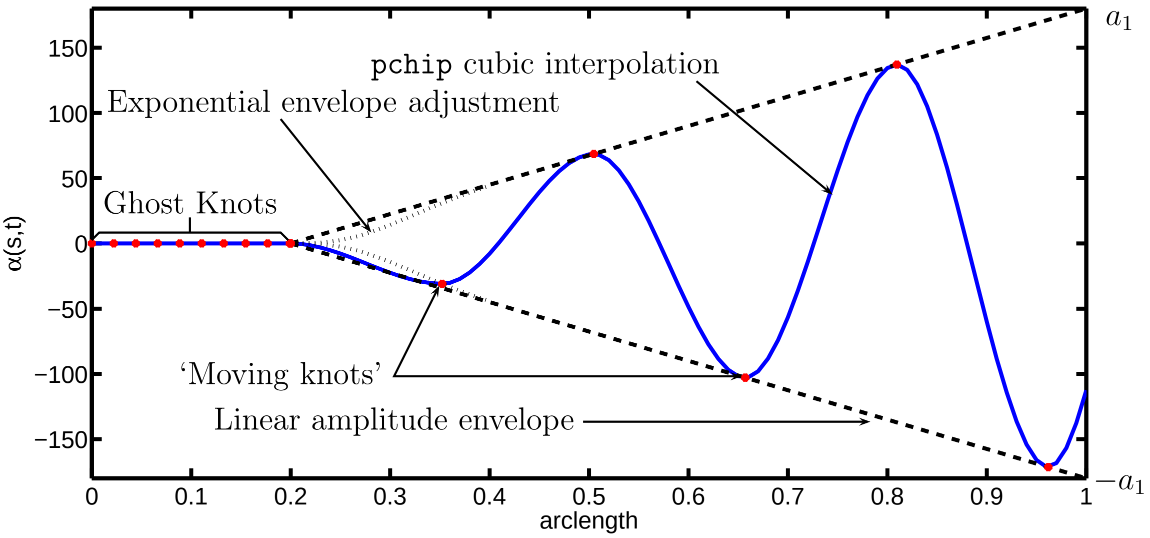

Figure 5.7: An example of a shear angle plot illustrating the important points in the computational scheme, with parameters are $N_e = 5.25$ and $a_1 = 180°$.

5.4.5 Self-intersection

As we are concerned with planar wave forms, it is necessary to ensure that we do not consider any regions of parameter space which, for any time, admit self-intersecting forms of the beat pattern. Figure 5.8, illustrates the permissible region of parameter space, derived from a numerical experiment.

5.4.6 Range of beat patterns

In the section we shall look at the possible beat pattern configurations available by ranging over the parameter space of N_e and a_1. Both parameters are encoded in such a way as to be continuous, with the understanding that $N_e \geqslant 1$ and that $a_1 > 0$, and small enough that the sperm's tail does not intersect (this is discussed above). In Figure 5.9 we illustrate

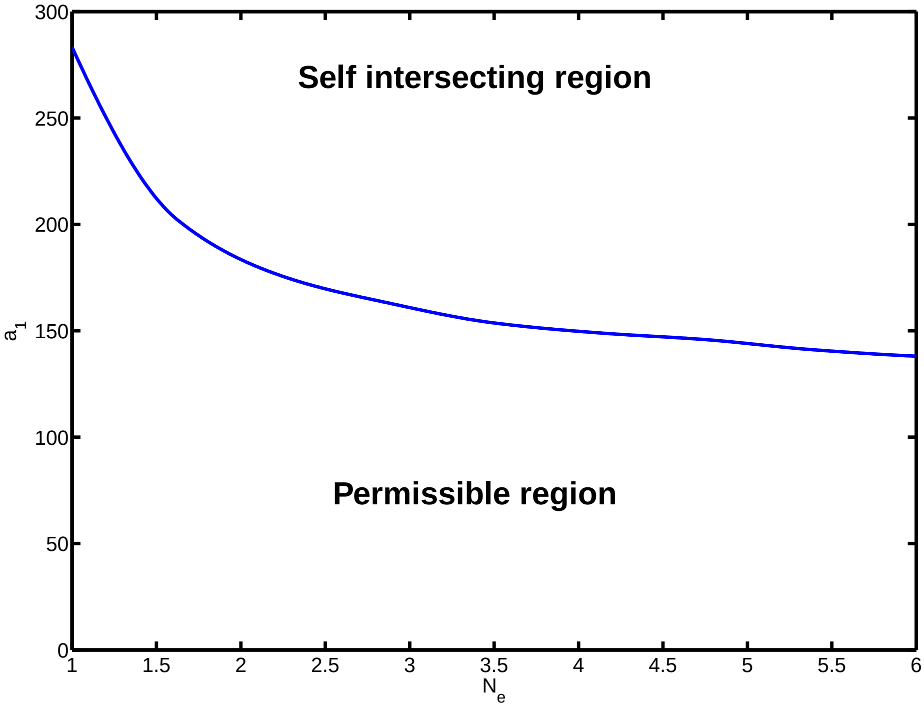

Figure 5.8: The parameter space (N_e, a_1) divided into regions which admit permissible beat patterns and those with self-intersecting patterns which are not permissible under our implementation.

the possible beat pattern configuration for values of the parameters N_e and a_1; figure 5.10 is the corresponding shear-angle against arc-length for the previous figure. For necessity of presentation, the beat patterns are shown as discrete points in the parameter space the representation is continuous.

5.4.7 Experimental example

As an example of the application of the new model to experimental data, consider the photographs used as motivation for this study in Chapter 1 (Figure 1.1). The photographs are reproduced in Figure 5.11 along with their representations under the new model.

It is worth noting that the moving knot model, with just two parameters, enables experimental data to be fitted to the model by eye rather than requiring detailed image

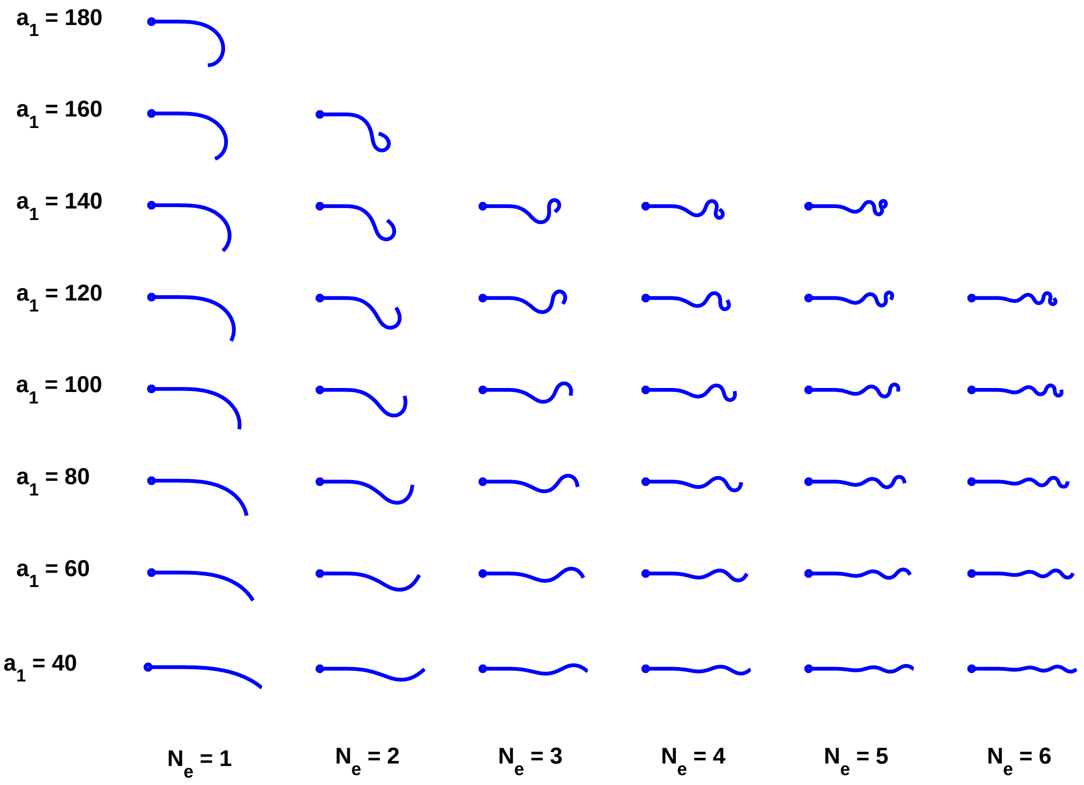

Figure 5.9: Examples of the different well specified beat patterns available by traversing the (N_e, a_1) parameter space for an instance in time. Notice that both 'whip-like' and 'meandering' beat pattern configuration are available using this parametrisation. Figure 5.10 illustrates the corresponding shear-angles as a function of arc-length.

processing and Fourier analysis of the data to obtain the relevant coefficients. A data fitting routine could be introduced to determine exact values of the parameters.

5.4.8 An extension to the model – asymmetric beat patterns

At present the model only permits symmetric beat patterns; this was a modelling assumption. As a tool for understanding the beat dynamics this is a reasonable assumption as it reduces the dimensions of parameter space. However, many beat patterns observed in reality are not symmetric and it is worth noting the steps required to modified our proposed model for asymmetric beat patterns.

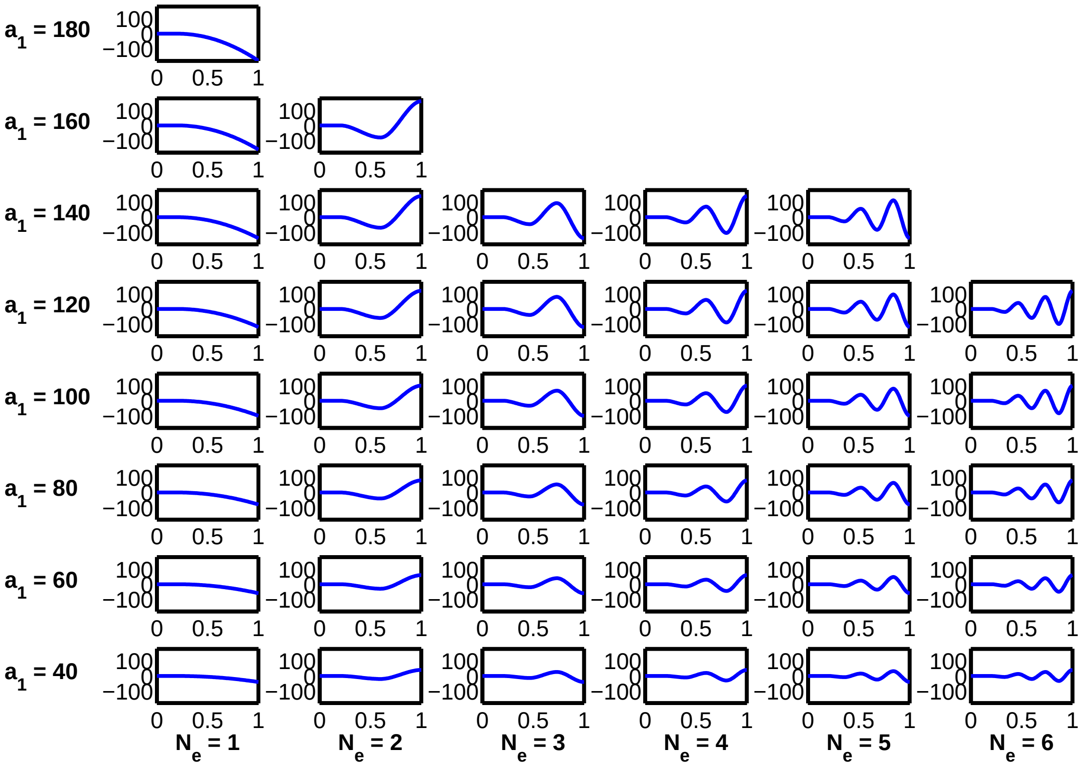

Figure 5.10: The model predicted shear-angles versus arc-length – corresponding to the beat patterns shown in Figure 5.9. The horizontal axis is arc-length s and the vertical axis shear-angle α in each of the subplot (the labels were excluded for clarity)

Firstly, the assumption that needs to be relaxed is that maxima and minima occurring at $s = 1$ take the same (absolute) value for the angle a_1. By making the assumption that a maximum occurring at $s = 1$ will take the value $a_{\max}$ and that a minimum will take the value $-a_{\min}$, we have introduced one new parameter, however, the type of beat patterns achievable greatly increased. There is no formal specification for the ranges of the parameters $a_{\max}$ and $a_{\min}$, however, the caveat is that the beat patterns do not self-intersect. The values of the parameters need not necessarily be positive; the value of the parameters form a 'wedge' in angle-space which the cubic interpolation is within. This wedge can become too small for reasonable beat pattern configurations if the values of the parameters are too small, or if the parameters have opposite signs and are of similar

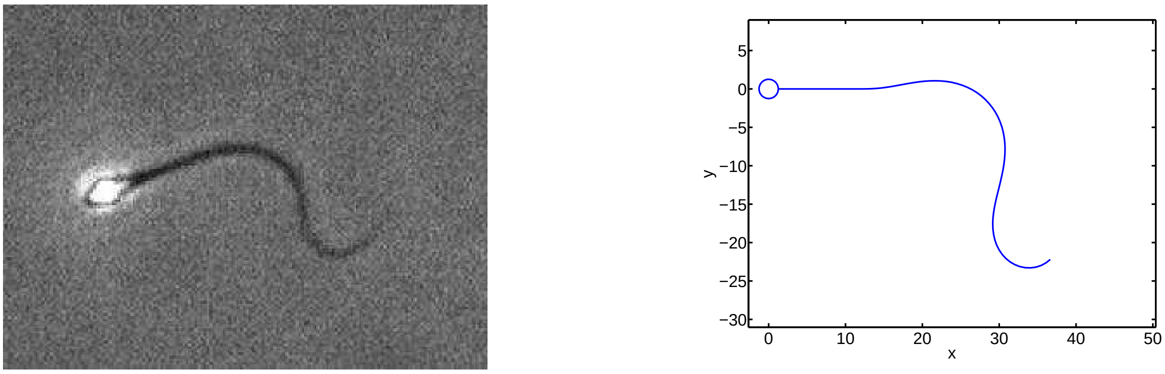

(a) whip-like pattern with approximate viscosity $10^{-3}\mathrm{Pa}\cdot\mathrm{s}$.

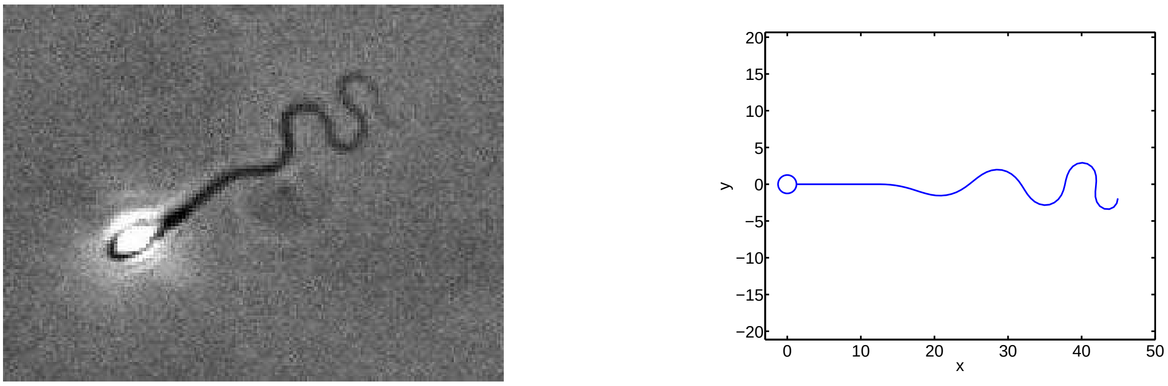

(b) meandering pattern with approximate viscosity $1.3\mathrm{Pa}\cdot\mathrm{s}$.

Figure 5.11: Photographs of human sperm taken at different viscosities and their configuration using the new model. The parameters are (a) $N_e = 1.5$ and $a_1 = 130°$ and (b) $N_e = 5.5$ and $a_1 = 110°$.

magnitude.

Figure 5.12 illustrates an example of applying the asymmetric model to an example configuration with the a fixed $a_{\max} = 120°$ and a variable $a_{\min} \in [0, 160°]$. Notice the case when $a_{\min} = 120°$ which corresponds to the symmetric case. In each case the corresponding shear-angle as a function of arclength is plotted, along with the envelope. One particular interesting case is where $a_{\min} = 0$; in which case you develop a completely one-sided beat pattern, where the bend angle is always positive.

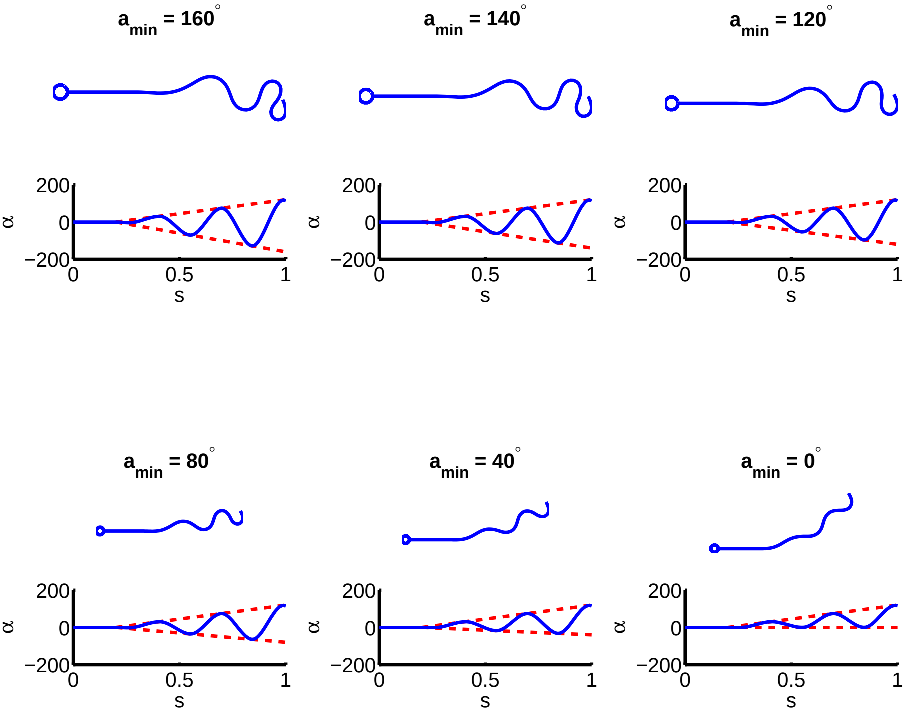

Figure 5.12: An example of the asymmetric beat pattern available by introducing one additional parameter. In all cases $N_e = 5.5$ and $a_{\max} = 120°$.

5.5 Analysis of the model

In the following sections we assume that the head radius is $A = 1.25\mu\text{m}$ and the flagellum has length $L = 56\mu\text{m}$ and radius $a = 0.05\mu\text{m}$.

5.5.1 Beat kinematics – bending rates

Firstly, we shall consider the bending rate, and particulary, the peak bending rate of a flagellum configuration using our new model; by design we have removed a linear dependence on N_e through v, but still expect a dependence on a_1.

The bending rate is defined at $\partial\alpha(s,t)/\partial t$, and is illustrated for an example fixed time along the flagellum in Figures 5.13 and 5.14 for a meandering and whip-like beat pattern respectively using the parameters from the matched experimental data in Figure 5.11. Notice that the maximum bending rate occurs at the maximum curvature of the flagellum. The time series equivalent of Figures 5.13 and 5.14 are shown in Figure 5.15 and 5.16 over a fundamental time period; notice that the peak bending rates move linearly in s and strengthen with time.

In Figure 5.17 we have considered the peak bending rate predicted at each configuration in our parameter space. That is to say, for each N_e and a_1, plotted is

$$\max_{s\in[0,1]} \max_{t\in[0,T]} \frac{\partial\alpha(s,t)}{\partial t}.$$

Notice that the maximum bend rates occur for the very whip-like beat patterns with high values of a_1. We notice a difference between our two experimental examples in that the meander configuration has a lower peak bending rate than the whip-like structure; this is interesting as the whip-like structure occur at lower viscosity.

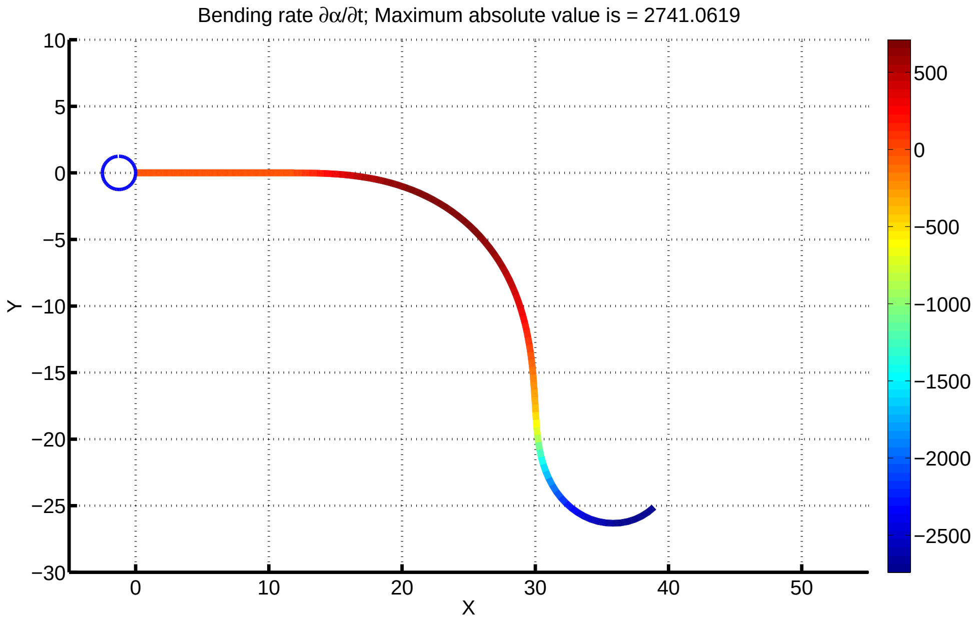

Figure 5.13: The bending rate plotted along the flagellum for an example beat whip-like configuration with $N_e = 1.5$ and $a_1 = 130°$.

5.5.2 Optimisation – speed and efficiency

In this section we explore the properties, such as speed and efficiency, of the different beat pattern configurations permissible under the new model which we have developed.

In Figure 5.18, we illustrate the swimming speed of a sperm cell with the beat pattern as specified by the model parameters a_1 and N_e. Interestingly the fastest beat pattern configurations are those with a small number of extrema and the highest bend angle – the region of parameter space which we would identify as whip-like patterns. The cell speed drops off significantly for small values of a_1 and large values of N_e; however, the cells are still motile.

Figure 5.19 illustrates the power consumption of the cells with beat pattern configurations using our two parameters. Importantly notice that the configurations which

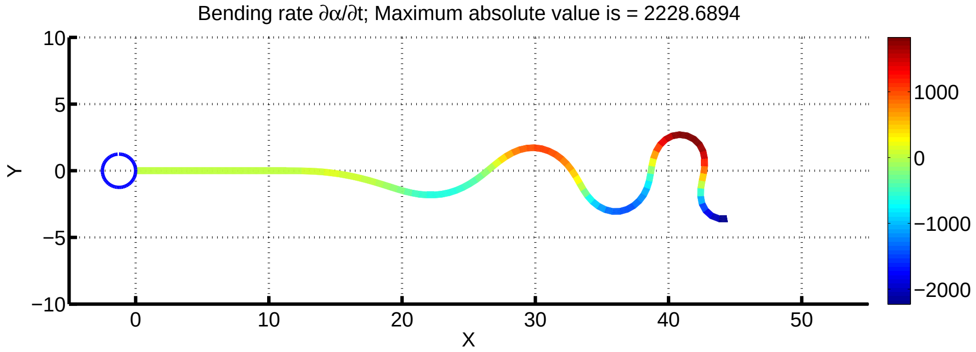

Figure 5.14: The bending rate plotted along the flagellum for an example beat meandering configuration with $N_e = 5.5$ and $a_1 = 110°$.

corresponded to the fastest swimming speeds also correspond to those with the highest power consumption. The relationship of these two parameters, power and speed, manifests itself through the inverse efficiency. Figure 5.20 illustrates the inverse efficiency as a function of the model parameters. The fastest swimming configurations of whip-like beat patterns also correspond to the most efficient beat patterns; if a balance of power to velocity was the only concern of the cell, then a whip-like pattern should be adopted. Notice, however, that the decay of the inverse efficiency is not uniform; there are regions are region of high and low inverse efficiency. The region with $N_e \in (3, 4)$ is poor, in terms of efficiency, in comparison to its neighbour regions. Moreover, the region with $N_e \in (4, 5.5)$ for values of $a_1 \in (60, 110°)$, is a local minimum of the inverse efficiency.

Notice that our example cells (Figure 5.11) fall within the two regions we have highlighted; firstly the whip-like configuration is a (interestingly) near optimal swimmer with

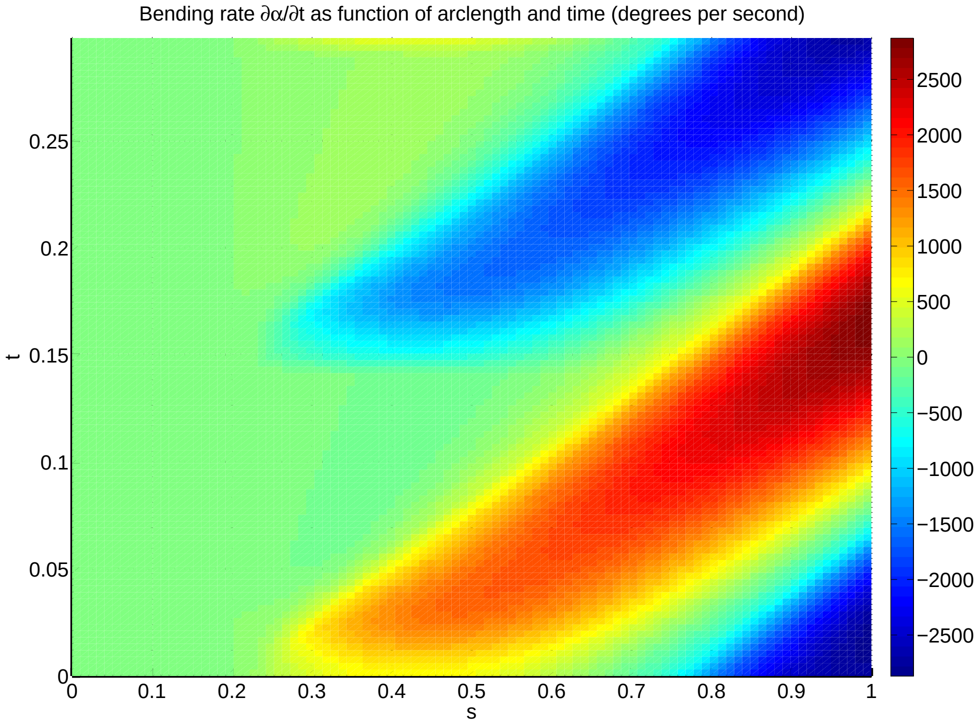

Figure 5.15: The bending rate $\partial\alpha/\partial t$ as a function of s and t, for the whip-like beat pattern in Figure 5.13. Notice that the maximum and minimum bands moves towards the posterior of the flagellum and strengthen.

a fast efficient beat pattern, whilst the meandering configuration is near the local minimum for slower, but yet still locally efficient beating. The reason for switching between one beat and another is not clear from this analysis alone.

We have already noted that the whip-like beat patterns which are the fastest, have the highest bending rates. We shall now proceed to consider the bending moment density; a quantity which has a physical interpretation as it is the result of the active bending of the flagellum due to the dynein plus the elastic bending moment due to the ultrastructure.

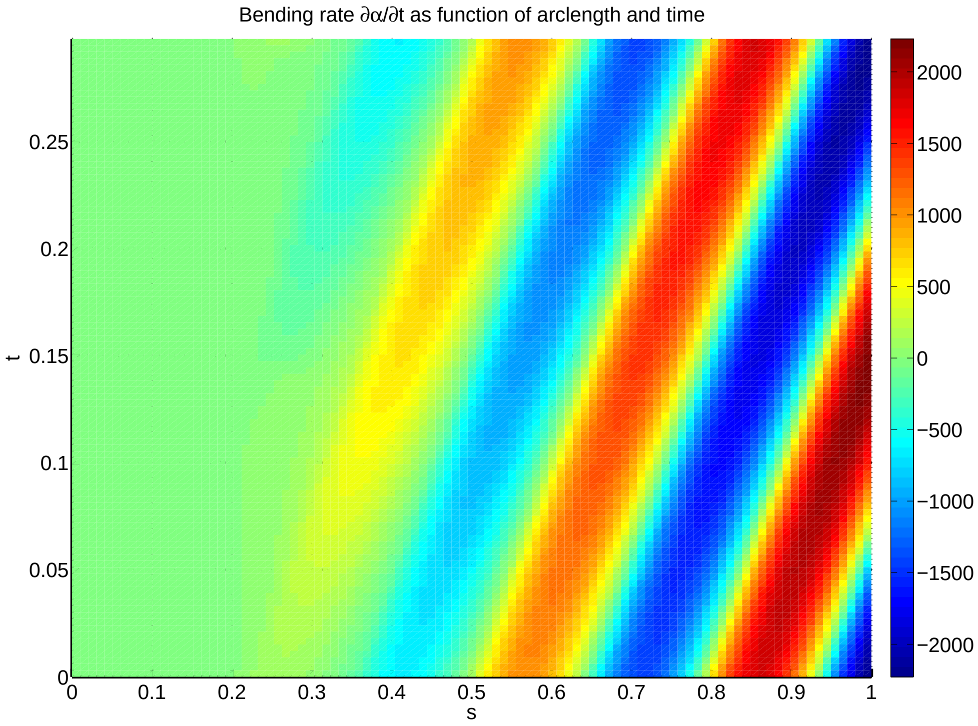

Figure 5.16: The bending rate $\partial\alpha/\partial t$ as a function of s and t, for the meandering beat pattern in Figure 5.14.

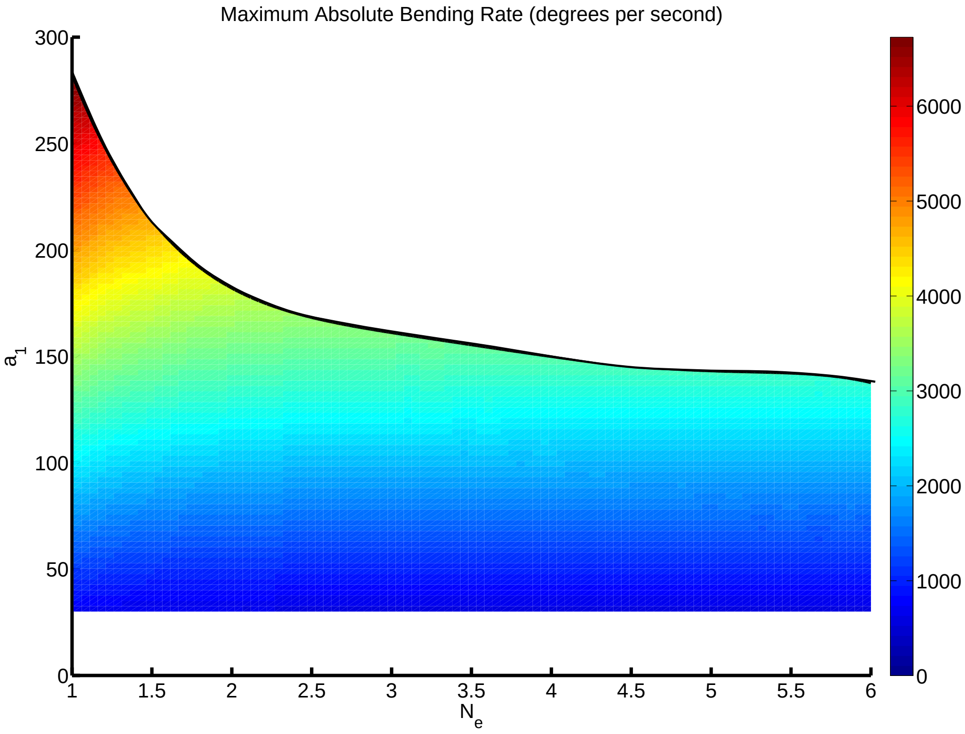

Figure 5.17: The maximum bending rate as a function N_e and a_1.

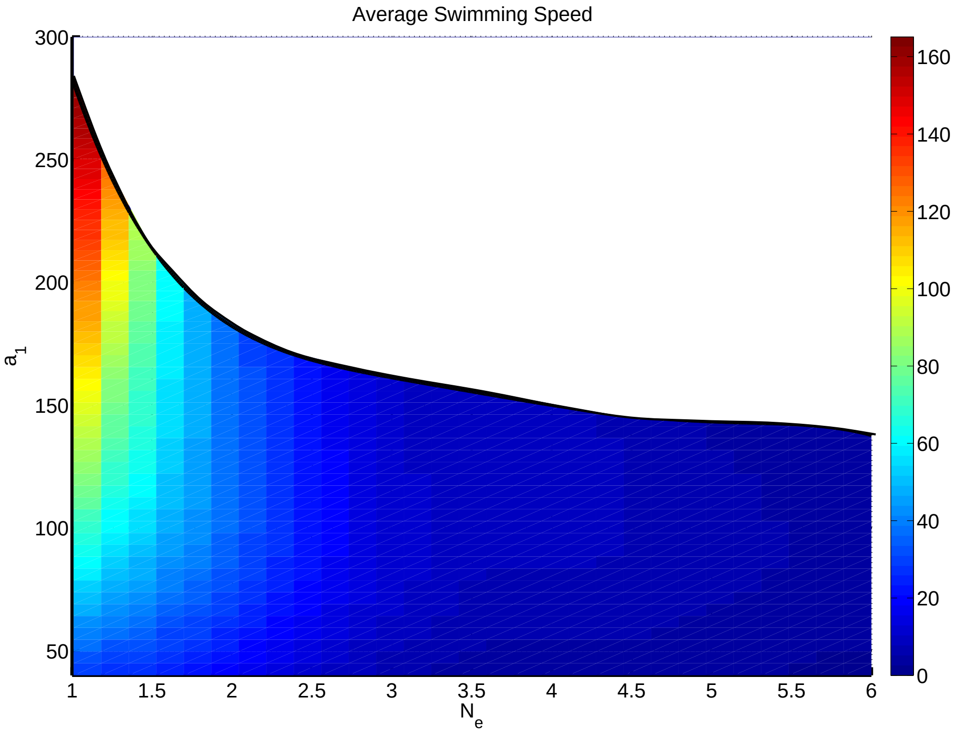

Figure 5.18: Average swimming speed as a function of the model parameters N_e and a_1. The fastest configurations are the whip-like patterns with high final angle a_1.

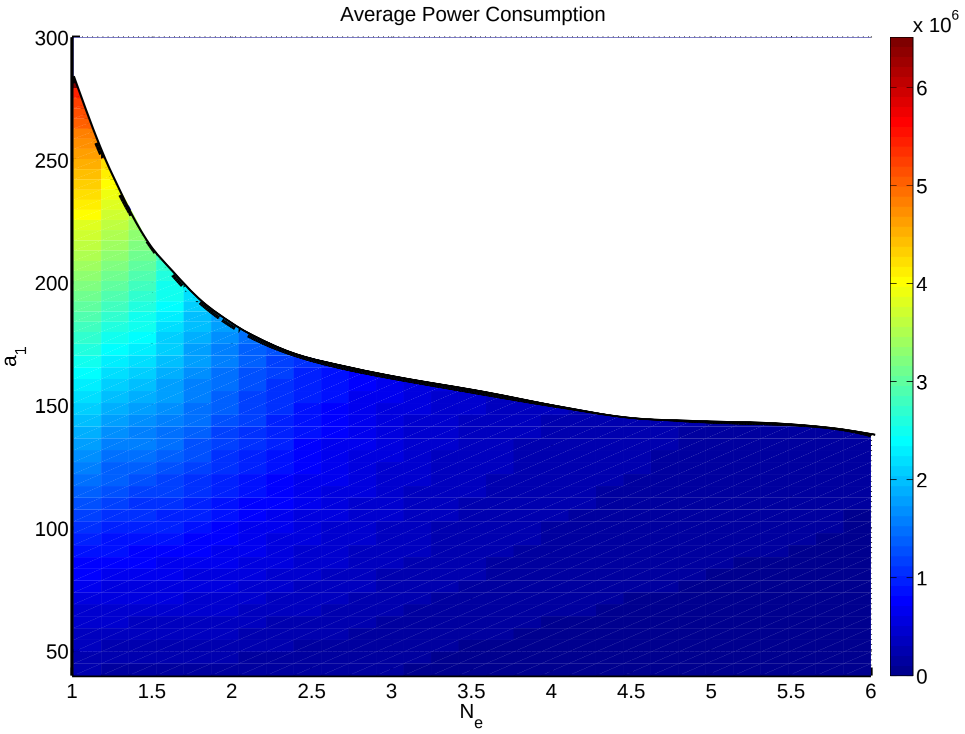

Figure 5.19: Average power consumption as a function of the model parameters. The configuration with the highest power consumption correspond to the cells with the highest speed.

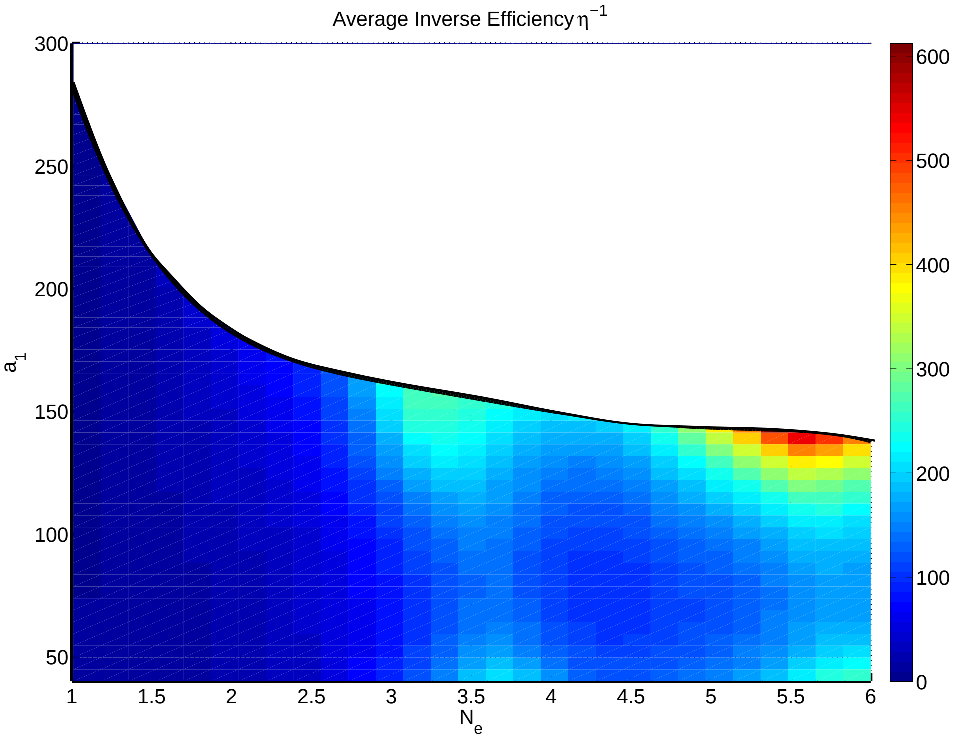

Figure 5.20: Average inverse efficiency as a function of the model parameters.

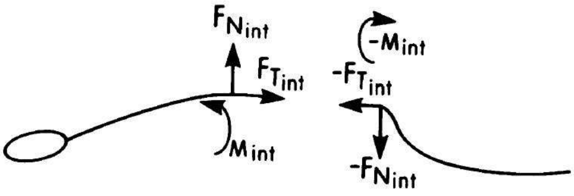

Figure 5.21: The bending moments (M_{int}) and shear forces ($F_{N_{\text{int}}}$ and $F_{T_{\text{int}}}$) that must be applied to the cut ends of a flagellum to preserve its motion. Reproduced from Hines and Blum (1978).

5.5.3 Bending moment density

The viscous *bending moment density* (Hines and Blum, 1978) is the component of the integral force $\boldsymbol{F}$ in the direction normal to the flagellum,

$$m_v(s) = \boldsymbol{F}(s) \cdot \boldsymbol{n}(s),$$

where $\boldsymbol{n}(s)$ is the normal vector to the flagellum at arc-length s. The integral force is given by

$$\boldsymbol{F}(s) = 6\pi\mu A\boldsymbol{U}_0 + \int_0^s \boldsymbol{f}(s')\,\mathrm{d}s', \tag{5.2}$$

where $\boldsymbol{f}(s)$ is the force distribution along the flagellum, calculated using the slender-body theory code.

The understanding of the integral force (Equation 5.2) is given in Hines and Blum (1978) and illustrated in Figure 5.21. If, during beating, a flagellum were to be suddenly cut at some point s, two internal forces $\boldsymbol{F}_{\text{int}}$ and a bending moment M_{int}, would be needed at the cut end to retain the original motion of that point. Consequently, the sum of the external force due to the head, the force produced up to the cut at s and the internal force $\boldsymbol{F}_{\text{int}}$ must be zero (to ensure that the flagellum does not accelerate); therefore the expression for $\boldsymbol{F}$ in Equation (5.2) is a measure of the internal force generated.

The total moment is a sum of that due to the dynein activity, the viscous moment and

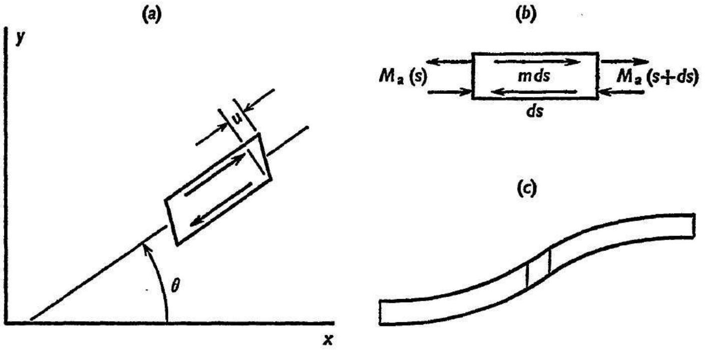

Figure 5.22: Bending moment density in a sliding filament model of the flagellum (a) An element along the length of the flagellum, subject to shear u between the filaments, θ denotes the shear angle, which in our study is denoted α. (b) Active moment M_a along a short length of flagellum ds. The bending moment density m produced by dynein activity is given by $m \approx (M_a(s+ds) - M_a(s))/ds$. (c) Flagellar bending caused by positive active shear in a small length of flagellum. Reproduced from Brokaw (1971).

the elastic moment, and the total of these is zero. In general during bending the active moment will be greater than the viscous moment $|m| \geqslant |m_v|$. Therefore, by considering the viscous moment (which we can calculate) we place a bound on the value of the active moment - which is a result of the active bending within the flagellum.

The technique of bending moment density has been used by Hines and Blum (1978) and Brokaw (1970, 1971) to formulate model of flagellar internal mechanics, including Brokaw's curvature control model (Brokaw, 2001, 2002). Figure 5.22 (from Brokaw (1971)) illustrates how a bending moment within a short section of flagellum can generate a curvature of the flagellum.

Schmitz et al. (2000) estimates from experimental observations that each dynein arm produces a maximum force of 10 pN. Recall that the internal structure of the flagellum has 9+2 microtubules (Figures 1.6 and 5.23). The spacing of the microtubules is 3.25×10^{-7}m, and they have a density along the flagellum of 70 dynein arms per micrometre (Schmitz et al., 2000). For a bend in a given direction, only half of the dynein arms will be involved in producing this bend (See Figure 5.23). It is worth noting that this method will over estimate the bending moment density as not all 4 dyneins on the sides which is bending

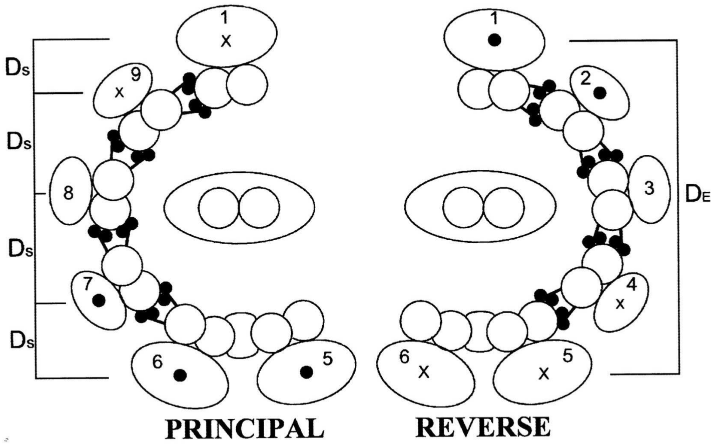

Figure 5.23: Functional schematic of the mammalian sperm axoneme, illustrating the sliding induced by the microtubules. Notice that for a thrust into the page on those marked • are active and × for thrust out of the page. Reproduced from Schmitz et al. (2000).

will contribute equally as they are not all perpendicular to the bend direction.

The estimate of bending moment density is the product of the spacing of the dyneins, the force per dynein arm, the density of the dyneins and the number of dyneins involved in bending. This gives $(3.25 \times 10^{-7}) \times (10 \times 10^{-12}) \times (70 \times 10^{6}) \times 4 \approx 1\,\mathrm{nN}$.

As the dyneins can only produce a given force, and this relates to the moment that can be generated it can be seen that there is a limit to the bending moment density that a sperm flagellum can generated.

The bending moment density for a given beat pattern configuration scales linearly with viscosity. In our modelling regime the beat patterns are generated without prior knowledge of the bending moment density and thus a beat pattern can be specified which may have too high a bending moment density to exist in reality. Therefore studying the predicted bending moment densities of the different types of beat patterns which can be generated, in combination with our velocity/power efficiency measure, may provide a mechanism to explain why certain beat pattern are observed at given viscosities

The bending moment and bending moment density can be calculated from the viscous forces acting on a moving flagellum from data describing the bending behaviour of the

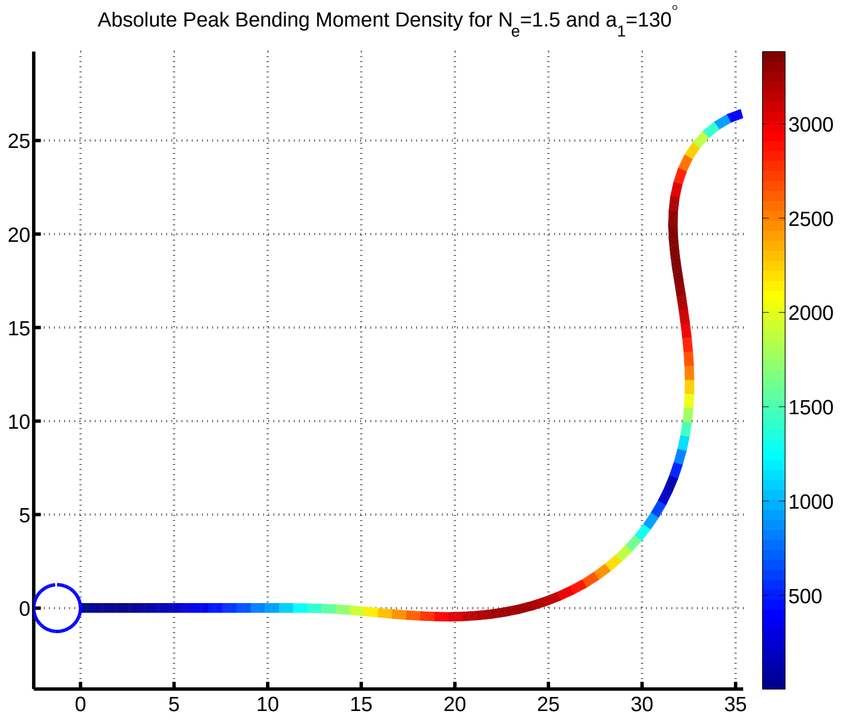

Figure 5.24: Bending moment density for a given time period, as a function of arc-length for a whip-like beat pattern configuration with $N_e = 1.5$ and $a_1 = 130°$.

flagellum, using concepts discussed in Brokaw (1970).

As noted, the bending moment density is a function of arclength and will vary depending on time, therefore to compare individual beat pattern configurations, we shall consider the peak value for the bending moment density for a given configurations taken over arclength and a time period. The rationale for considering the peak value, rather than an average or cumulative total, is that the peak value highlights the maximum force to be generated by a cell – if this is more than a cell can generate then the beat pattern is unphysical.

Figures 5.24 and 5.25 illustrate the (absolute) bending moment density of two example beat pattern configurations as a function of arc-length. The figures relate to the experimental whip-like sperm and the meandering sperm. Notice that the highest bending moment densities are found in the whip-like configuration.

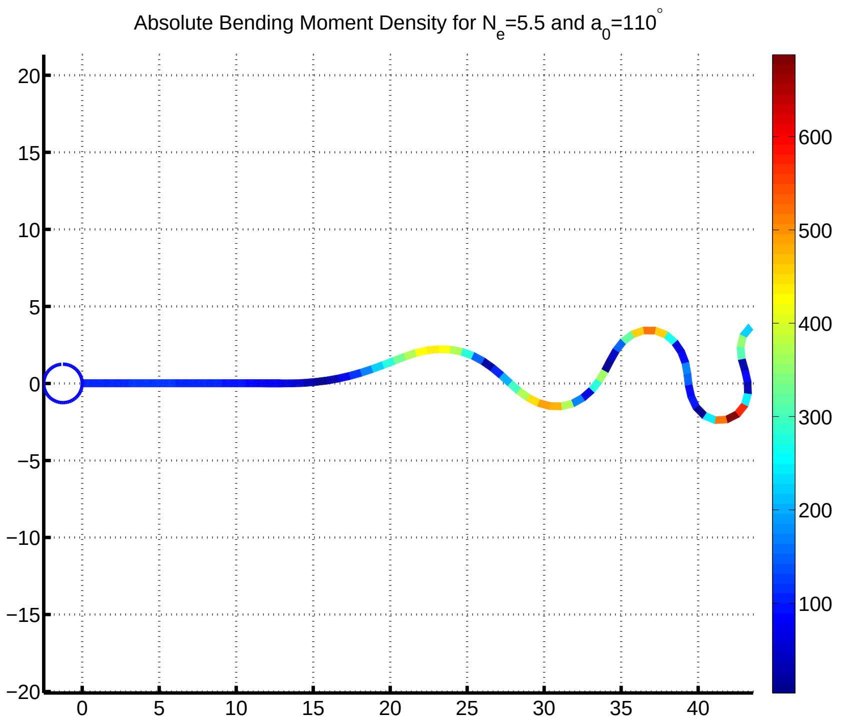

Figure 5.25: Bending moment density for a given time period, as a function of arc-length for a meandering beat pattern configuration with $N_e = 5.5$ and $a_1 = 110°$

Figures 5.26 and 5.27 are the time-dependent equivalents of the example configurations shown in Figures 5.24 and 5.25 showing the variation in bending moment density as a function of the arc-length and time.

The peak absolute bending moment density of any given beat pattern configuration will indicate if a beat pattern configuration is physically permissible. This peak value can be found by taking the maximum value of the bending moment density over $s \in [0, 1]$ and $t \in [0, T]$. Figure 5.28 illustrates the log of the peak absolute bending moment density as a function of the model parameters. The peak bending moment density is highest for the whip-like beat pattern configuration.

From Figure 5.28 we notice that to move to a region (for a given viscosity) of lower peak bending moment density (or conversely to stay below an upper limit for bending moment density as viscosity is increased) we must reduce the maximum bend angle a_1

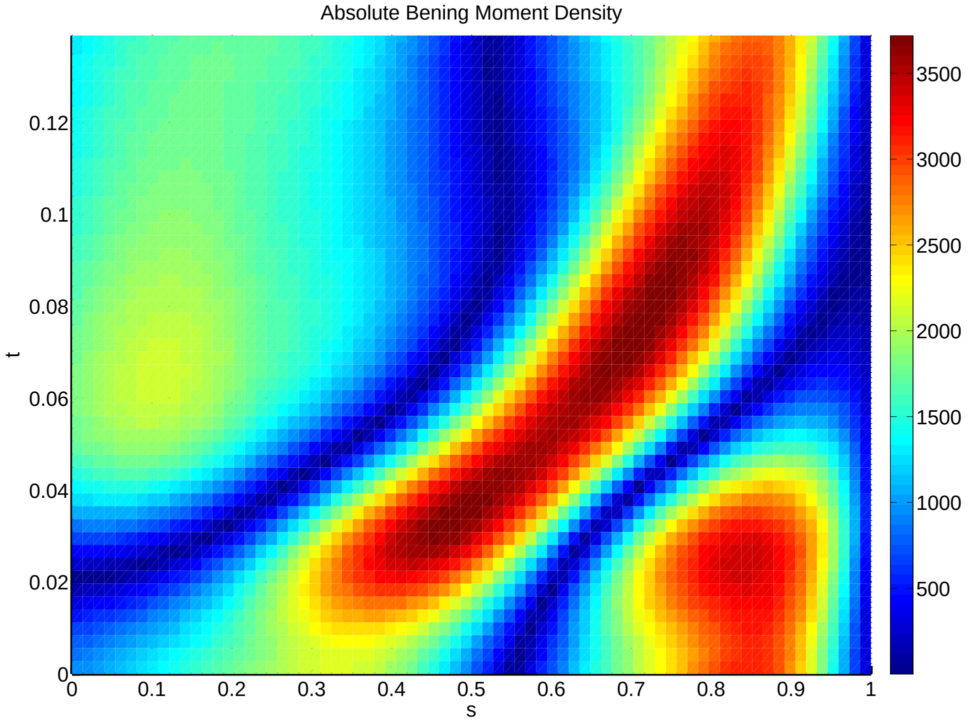

Figure 5.26: Absolute bending moment density as a function of arc-length and time for a whip-like beat pattern configuration with $N_e = 1.5$ and $a_1 = 130°$.

and increase the number of extrema N_e. Moreover, if we are interested in maintaining our measure of efficiency we have illustrated, that once N_e is above about 3, it is more efficient to have a beat pattern with $N_e \in (4, 5.5)$.

We observe that the whip-like beat pattern in our experimental data was near optimal in terms of speed and viscosity, however, these types of beating patterns also have the highest peak bending moment density. The peak bending moment density scales linearly with viscosity as highlighted in in Figure 5.29 for two beat pattern configurations. We have shown previously that there should be physical limit to bending moment density (due to the active bending of the dyneins). From Figure 5.29 we can see that if the whip-like beat pattern, for a given viscosity is unacceptable, then the locally efficient meandering type pattern always had a lower bending moment density.

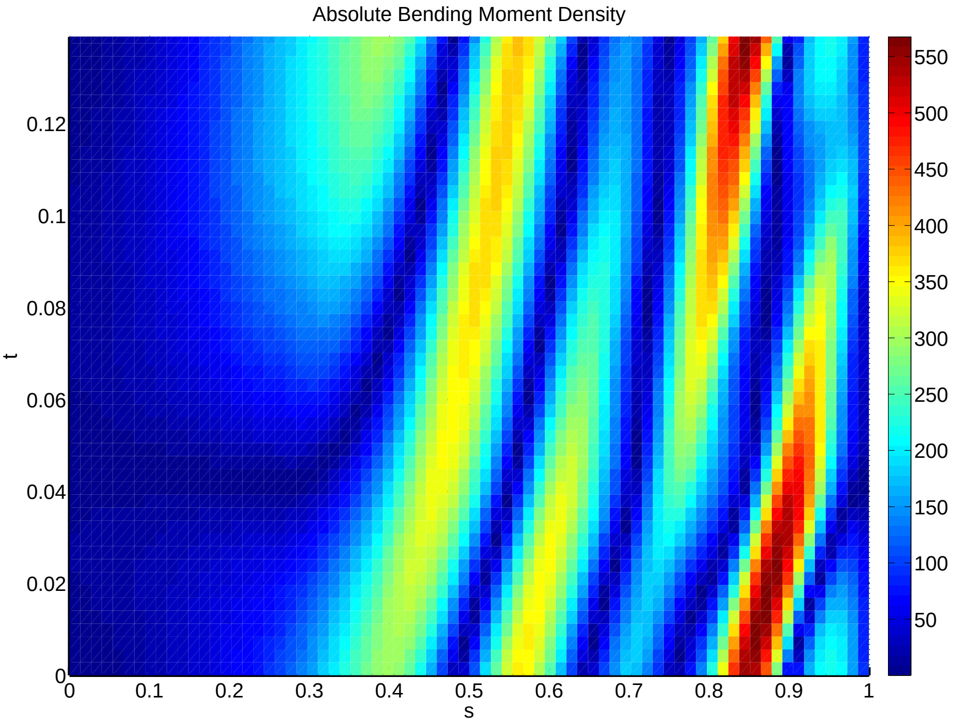

Figure 5.27: Absolute bending moment density as a function of arc-length and time for a meandering beat pattern configuration with $N_e = 5.5$ and $a_1 = 110°$.

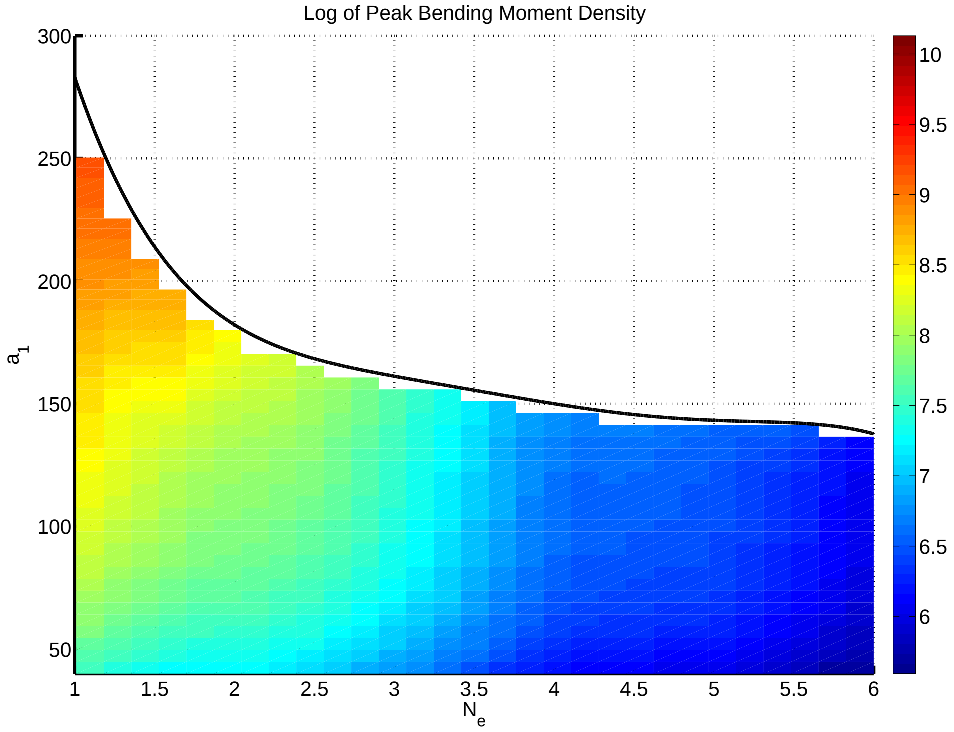

Figure 5.28: Log of the peak absolute bending moment density as a function of the model parameters a_1 and N_e. Notice that the whip-like beat patterns have the highest bending moment density; whilst meandering patterns have a much lower value (for a given viscosity).

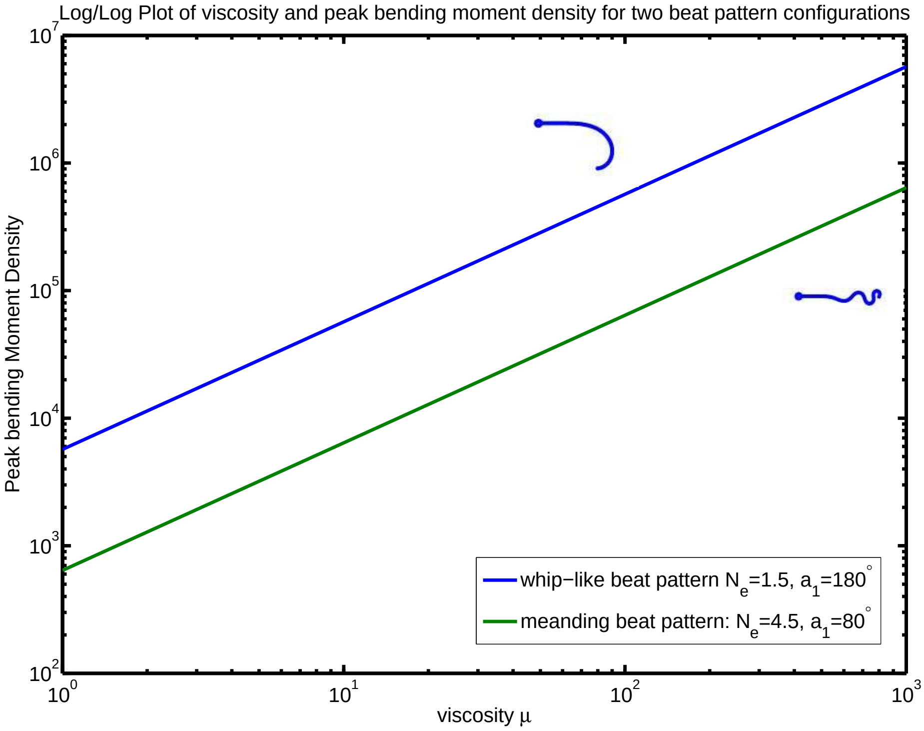

Figure 5.29: A log-log plot for peak bending moment density as a function of viscosity μ, for two different beat pattern configurations: A whip-like beating pattern $N_e = 1.5$ and $a_1 = 180°$ and a meandering beat pattern with $N_e = 4.5$ and $a_1 = 80°$. The whip-like pattern is near optimal in terms of inverse efficiency and the meandering pattern is in the second local optimum region for inverse efficiency.

5.6 Conclusions

In this section we have devised a new model for the specification of a sperm beat pattern configuration using the angle shear. Based upon experimental data a number of assumptions were devised and the resultant mathematical model has a very small number of parameters, but yet encompasses an array of beat patterns observed *in vitro*. A symmetric model was used for the future analysis, however, the model was extended for asymmetric beat patterns.

The mathematical model was used to fit parameters to our motivating experimental examples, with the added benefit that this can be done by eye, therefore not requiring detailed image processing or data analysis.

Analysis of the speed and power consumption of the cell with different beat pattern configurations was conducted. We found that there are a number of regions of efficient beating. By considering the bending moment density, which scales with viscosity, we were able to identify a mechanism which could cause the modulation of sperm beat pattern *in vitro*.

We conclude that the fastest and most efficient beat pattern is the ‘whip-like’ beat pattern observed in low viscosity medium; however, the value of the maximum bending moment density is high. If the viscosity is increased, thus increasing the bending moment density, then in order to maintain a physically acceptable beat configuration with a near maximum velocity, a suitable alternative beat pattern configuration is the meandering tail pattern, which is locally efficient.

It is worth noting that the region of near highest speed corresponds to the parameters fitted to the experimental data in watery medium (low viscosity) (Figure 5.11(a)) and the region of meandering patterns acceptable at high viscosities includes the parameters fitted to the experimental data in Figure 5.11(b).

Chapter 6

An Asymptotic Analysis of Peristaltic and Ciliary Flows: Mixing in the Oviduct

6.1 Introduction

The human oviduct is a complicated feature of the human reproductive system. Its main function is to transport the passive ovum from the ovaries at the time of ovulation to the uterus, where, if fertilisation has been successful, the ovum implants into the uterine wall to develop into a pregnancy.

The main mechanisms for the motion of a passive ovum are the peristaltic contractions of the oviduct and the uterus, and the action of the cilia which line the interior surfaces of the oviduct (Debuse, 1998). There are a number of other mechanisms in the human body that rely on peristaltic and/or ciliary activity; examples include: the alimentary system, where food is transported peristaltically through the digestive system; the lungs where cilia are responsible for the movement of mucus which lines the lung walls that protects the lungs by trapping pollutants and bacteria and removing them from the lungs. Other examples of peristaltically driven flows are the movement of immature sperm cells in the *vas deferens* of males, and the movement of urine from the kidneys to the bladder. Biomechanically, the 'heart-lung' machine and the kidney dialysis machine both use peristalsis to move blood.

The beat of a single cilium can be considered as having two distinct phases; firstly the fast 'effective stroke' in the direction of fluid motion and a slower 'recovery stroke' in which the cilium moves back to the initial position, whilst having minimal impact on the fluid motion. This particular type of motion is necessary due to the length scales and velocities experienced; typically the Reynolds number is very small, and thus viscosity dominates inertia, meaning that the motion of the cilium must be 'non-symmetric' to avoid the reversibility of Stokes flow (Blake and Sleigh, 1974).

The movements of adjacent cilia in one direction are out of phase, which is termed metachronism, and gives ciliated surfaces the appearance of a corn-field with wind blowing over it, as the motion of the cilia progresses like a wave over the surface.

This chapter aims to show, through mathematical analysis, that a combination of peristaltic and ciliary activity, can lead to flows in which mixing occurs.

The purpose of this chapter is to consider the fluid mechanics of flow in the oviduct; it is noted that peristaltic flows have been studied for many years (as illustrated in the literature review in Chapter 1), however, many of the recent studies have only limited applications to reproductive biology.

6.2 Peristaltic flow in a two-dimensional channel

We consider, as a model for flow in the oviduct/uterus, flow in a two-dimensional narrow channel with aspect ratio $\beta = d/l \ll 1 < 1$; with a typical longitudinal lengthscale of l and a typical transverse width of the channel d. The Navier-Stokes equations are non-dimensionalised as follows: $t = \frac{L}{U}t'$, $x = lx'$, $y = dy'$, $u = Uu'$ $v = \beta Uv'$ and $p = Pp'$, where dash denotes a dimensionless variable. The particular scaling for v coming from consideration of the continuity equation. The scaling for pressure, P, is to be determined.

For velocity components $\boldsymbol{u} = (u, v)$, the x- and y-momentum equations are

$$\beta\mathrm{Re}\left(\frac{\partial u'}{\partial t'} + u'\frac{\partial u'}{\partial x'} + v'\frac{\partial u'}{\partial y'}\right) = -\beta\frac{PL}{\mu U}\frac{\partial p'}{\partial x'} + \beta\frac{\partial^2 u'}{\partial x'^2} + \beta^{-1}\frac{\partial^2 v'}{\partial y'^2}, \tag{6.1a}$$

$$\beta\mathrm{Re}\left(\frac{\partial v'}{\partial t'} + v'\frac{\partial v'}{\partial x'} + v'\frac{\partial v'}{\partial y'}\right) = -\beta^{-1}\frac{PL}{\mu U}\frac{\partial p'}{\partial y'} + \beta\frac{\partial^2 v'}{\partial x'^2} + \beta^{-1}\frac{\partial^2 v'}{\partial y'^2}, \tag{6.1b}$$

Where $\mathrm{Re} = \rho UL/\mu$ is the Reynolds number. Data from Eytan et al. (2001a) estimates the aspect ratio $\beta \sim 0.01$ and the Reynolds number $\mathrm{Re} \sim 10^{-4}$ both to be small. In the lubrication approximation it is important that $\beta\mathrm{Re} \ll 1$ (Batchelor, 1967) and this is the case for the class of biological flows which we are going to consider (Vann and Blake, 1982; Eytan et al., 2001a; Fauci and Dillon, 2006).

To obtain a leading order balance in Equation 6.1a, we require that $PL/\mu U \sim O(\beta^{-2})$; thus we choose the viscous pressure scaling of $P = \beta^{-2}\mu U/L$. For the benefits of clarity, from herein we shall drop the dashes and all quantities are implied as dimensionless.

We shall assume that the wall of the channel are at $y = h_2(x, t)$ and $y = h_1(x, t)$ as illustrated in Figure 6.1, and that we have the boundary conditions of no-slip, so that a fluid particle on the boundary with the boundary. We assume also, that the boundaries only move perpendicular to the x-axis, giving the boundary conditions

$$\left.\begin{aligned} u &= 0, \\ v &= \frac{\partial h_i}{\partial t}, \end{aligned}\right\} \qquad \text{on} \qquad y = h_i, \quad i = 1, 2. \tag{6.2}$$

At leading order, equation 6.1a and 6.1b reduce to the following

$$-\frac{\partial p}{\partial x} + \frac{\partial^2 u}{\partial y^2} = 0 \tag{6.3a}$$

$$\frac{\partial p}{\partial y} = 0 \tag{6.3b}$$

$$\frac{\partial u}{\partial x} + \frac{\partial v}{\partial y} = 0 \tag{6.3c}$$

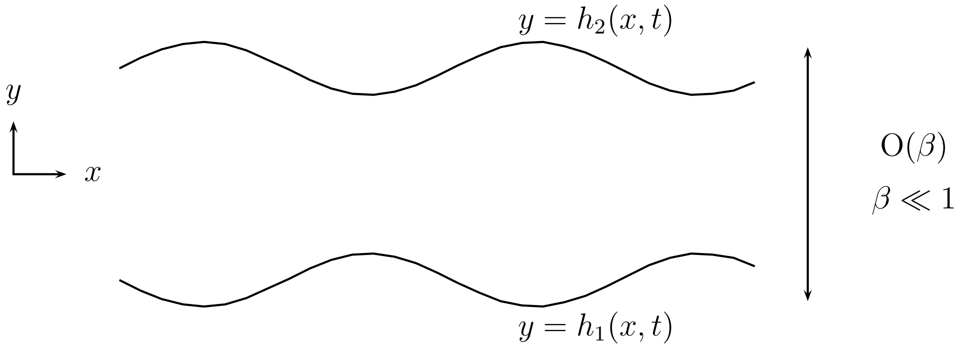

Figure 6.1: Schematic of the flow through a two-dimensional channel with flexible walls.

which we solve subject to the boundary conditions 6.2

The solution for the longitudinal velocity component u can be found by integrating Equation 6.3a in combination with the $u(y = h_i, t) = 0$ for $i = 1, 2$ boundary condition to yield

$$u = \frac{1}{2}\frac{\partial p}{\partial x}(y - h_1)(y - h_2). \tag{6.4a}$$

Utilising the Continuity Equation, we can determine the equation for v, up to a function $C_0(x,t)$ to be determined

$$\begin{aligned} v = -\frac{1}{2}\frac{\partial^2 p}{\partial x^2}\left(\frac{y^3}{3} - (h_1 + h_2)\frac{y^2}{2} + h_1 h_2 y\right) \\ - \frac{1}{2}\frac{\partial p}{\partial x}\left(-\frac{\partial}{\partial x}(h_1 + h_2)\frac{y^2}{2} + \frac{\partial}{\partial x}(h_1 h_2) y\right) + C_0(x,t), \end{aligned} \tag{6.4b}$$

To determine $C_0(x,t)$, we consider the application of the boundary condition for v, which results in two equations

$$\begin{aligned} \frac{\partial h_i}{\partial t} = -\frac{1}{2}\frac{\partial^2 p}{\partial x^2}\left(\frac{h_i^3}{3} - (h_1 + h_2)\frac{h_i^2}{2} + h_1 h_2 h_i\right) \\ - \frac{1}{2}\frac{\partial p}{\partial x}\left(-\frac{\partial}{\partial x}(h_1 + h_2)\frac{h_i^2}{2} + h_i\frac{\partial}{\partial x}(h_1 h_2)\right) + C_0(x,t), \qquad \text{for} \quad i = 1, 2. \end{aligned} \tag{6.5}$$

Subtracting the resulting equations, yields a partial differential equation for the pressure gradient,

$$\frac{\partial^2 p}{\partial x^2} + \frac{3(h_2^2 + h_1^2)}{(h_2 - h_1)^3}\frac{\partial}{\partial x}(h_2 - h_1)\frac{\partial p}{\partial x} + \frac{12}{(h_2 - h_1)^3}\frac{\partial (h_2 - h_1)}{\partial t} = 0, \tag{6.6}$$

which can be solved to yield

$$\frac{\partial p}{\partial x} = \frac{C(t)}{(h_2 - h_1)^3} + \frac{12}{(h_2 - h_1)^3}\int \frac{\partial (h_2 - h_1)}{\partial t}\,\mathrm{d}x \tag{6.7}$$

where $C(t)$ is a function related to time relating to the pressure at the end of the tube.

Thus, from Equation (6.5), we can specify $C_0(x,t)$ therefore specifying the solution of the problem to within a function of time,

$$\begin{aligned} C_0(x,t) = \frac{\partial h_1}{\partial t} + \frac{1}{2}\frac{\mathrm{d}^2 p}{\mathrm{d}x^2}\left(\frac{h_1^3}{3} - (h_1 + h_2)\frac{h_1^2}{2} + h_1^2 h_2\right) \\ + \frac{1}{2}\frac{\mathrm{d}p}{\mathrm{d}x}\left(-\frac{\partial}{\partial x}(h_1 + h_2)\frac{h_1^2}{2} + h_1\frac{\partial}{\partial x}(h_1 h_2)\right) \end{aligned} \tag{6.8}$$

Recall that for a two-dimensional flow field $\boldsymbol{u} = (u,v)$, if the streamfunction ψ exists then $u = \dfrac{\partial \psi}{\partial y}$ and $v = -\dfrac{\partial \psi}{\partial x}$. By using Equations (6.4a) and (6.4b) the form of the streamfunction can be derived as

$$\psi = \frac{1}{2}\frac{\mathrm{d}p}{\mathrm{d}x}\left(\frac{y^3}{3} - (h_1 + h_2)\frac{y^2}{2} + (h_1 h_2)y\right) - \int C_0\,\mathrm{d}x. \tag{6.9}$$

6.3 Measures of system dynamics

6.3.1 Particle tracking

It is possible to cast the two dimensional system derived above into standard dynamical systems form, by writing for position vector $\boldsymbol{x} = (x, y)$, the following expression

$$\frac{\mathrm{d}}{\mathrm{d}t}\begin{pmatrix} x \\ y \end{pmatrix} = \begin{pmatrix} u(x, y, t) \\ v(x, y, t) \end{pmatrix}, \tag{6.10}$$

where u and v are given in Equations (6.4a) and (6.4b) respectively.

By utilising the MATLAB function `ode45`, we are able to plot out particle paths for a variety of different starting positions. The advantage of using particle paths is that this allows us to track the motion of individual particles over time rather than taking a 'snap shot' of the global situation as one does at successive time when considering contours of the streamfunction.

6.3.2 Lyapunov exponents: a measure of mixing

A useful measure for the quantification of mixing is the *Lyapunov Exponent* (Ottino, 1989; Eckhardt and Yao, 1993; Otto et al., 2001); the basic principle behind the Lyapunov exponent is that it measures the divergence of trajectories from similar given initial conditions. The divergence of trajectories with similar but not identical initial conditions is a classical hallmark of chaos. Two initial particle positions, which vary only slightly, are evolved forward in time and the image length (the distance between the evolved points) is compared to the original length (the distance between the initial conditions). There is an infinite time and a finite time Lyapunov exponent which measures the overall dynamics of the system and that experienced at a point in the domain within a set period respectively. It is the latter that will be of more use in biological systems because effects maybe localised and biological systems operate on a finite time scale.

The definition of the Lyapunov Exponent is

$$\lambda_{LE} = \lim_{t \to 0} \left[\frac{1}{t} \log \left(\frac{||\delta \boldsymbol{x}(t)||}{||\delta \boldsymbol{x}(0)||} \right) \right] \tag{6.11}$$

where $||\delta \boldsymbol{x}||$ is the image length at time t (the distance between the evolved points). Owing to the infinite time limit required, this Lyapunov exponent is often termed the *infinite time Lyapunov exponent.* In practice the calculation of the infinite time limit is problematic, and at least for ‘real world’ biological systems as we are interested in mixing on a finite time scale, a finite alternative is required. For this purpose we define the finite time, or *local Lyapunov exponent* after Eckhardt and Yao (1993) as

$$\lambda_{LLE}(\boldsymbol{x}_0, t) = \frac{1}{t} \log \left(\frac{||\delta \boldsymbol{x}(t)||}{||\delta \boldsymbol{x}(0)||} \right) \tag{6.12}$$

One should notice now that the LLE depends on both time and the initial position.

The higher the (geometric) dimension of the problem, the greater the possible number of Lyapunov exponents there are; in theory it is possible to derive a different Lyapunov exponent for each of the linearly independent directions. The maximum Lyapunov exponent will correspond to the expansion which is aligned with the average direction of the most expansion of the system. Therefore the maximum Lyapunov exponent gives only a rate of stretching and not a direction.

We shall now briefly outline the structure used in calculating Lyapunov Exponents. Consider the image of two neighbouring points under the action of a map M. The points are initially situated a small known distance apart; after an action of the map this distance will either have expanded or contracted (or possibly not changed). In either case, by comparing the new separation distance with the separation of the initial points, we can quantify the expanding or contracting effect of the map. When the ratio of distances between the points is less than one, the distance is reducing and the map is decreasing. A small ratio (above but near 1) indicates the flow is mostly rotational in that region, showing little divergence from the initial conditions. If the ratio is significantly greater than one, then the distance between points after applying the map is greater than the initial distance and therefore the map is expanding. As λ_{LLE} is proportional to the log of the ratio, if the map is contracting then the ratio is < 1, and $\lambda_{LLE} < 0$; a static map will have $\lambda_{LLE} = 0$ and an expanding map will have $\lambda_{LLE} > 0$. A large amount of stretching after a certain fixed time scale indicates extensive mixing within a region under consideration. This would be characterised by a large Lyapunov exponent. Ottino (1989) comments that "positive Lyapunov exponent implies an exponential rate of stretching of material elements, and hence, good mixing". For biological systems we seek system which demonstrate mixing with a finite period of time.

Details of implementing the calculation of the local Lyapunov exponents can be founding Appendix C.3.

6.4 Analysis of two cases

To consider the dynamics of the system more fully, it is necessary to specify the wall shapes h_1 and h_2.

6.4.1 A wave propagating along the upper wall

We firstly consider the case where the lower wall is fixed and planar ($h_1 = 0$) and suppose that the upper wall is given by the expression

$$h_2(x,t) = 1 + g(x - ct) + \varepsilon h(\kappa(x - ct))f(t) \tag{6.13}$$

where $\varepsilon \ll 1$. This is a travelling wave with wave speed c plus a small time-dependent perturbation. The rationale behind this formulation is drawn from biological contexts, and in particular where the underlying muscular peristalsis can be thought of at $g(x-ct)$ and the effect of the tips of the cilia lining the surface can be viewed as a small perturbation $\varepsilon h(\kappa(x-ct))$, which does not necessarily occur at the same rate.

The leading order streamfunction is:

$$\psi = \frac{1}{2(1+g)^3}\left(C - 12cg\right)\left(\frac{y}{3} - \frac{1+g}{2}\right)y^2. \tag{6.14}$$

The method we adopt of using a travelling wave to model the net effect of a ciliated surface is called the 'envelope model' (Ross and Corrsin, 1974; Blake and Sleigh, 1974), and is based on the 'swimming sheet' method of Taylor (1951). We have already discussed this and other methods in detail in Section 1.4.3.

Moving to a travelling reference frame with

$$\widehat{x} = x - ct, \tag{6.15}$$

then we have the steam function

$$\bar{\psi} = \psi - cy, \tag{6.16}$$

then

$$\bar{\psi} = \bar{\psi}_0(\widehat{x}, y) + \varepsilon\bar{\psi}_1(\widehat{x}, y, t). \tag{6.17}$$

The unperturbed system ($\varepsilon = 0$) is integrable and the time periodic perturbation will introduce possible chaotic effects in the motion.

In the moving reference frame we seek stagnation points as these correspond to the centre of trapped regions which are moving with a velocity equal to the travelling wave velocity. For stagnation points in the reference frame, we require $u = v = 0$. The expression for the u velocity component is

$$u = \frac{C/2 - 6ch_2}{(1+g)^3} y(y - (1+g)) - c. \tag{6.18}$$

Considering $u = 0$ yields, from Equation (6.18), a quadratic in y which admits real solutions if the discriminant is positive

$$\Delta = (1+g)^2 \left(\frac{K + 4c - 2cg}{K - 6cg} \right) \geqslant 0, \tag{6.19}$$

where for brevity we have written $K = C/2$.

The condition in Equation (6.19) is equivalent to either

$$\textbf{Case A.} \qquad K - 2cg + 4c \geqslant 0 \text{ and } K - 6cg > 0, \tag{6.20a}$$

$$\text{or } \textbf{Case B.} \qquad K - 2cg + 4c \leqslant 0 \text{ and } K - 6cg < 0, \tag{6.20b}$$

and the y co-ordinate of the stagnation point is therefore

$$y_{\mathrm{st};1,2} = \frac{1 + g \pm \sqrt{\Delta}}{2}. \tag{6.21}$$

We are interested only in stagnation points which exist within the physical boundaries of the flow $0 < y_{\mathrm{st};1,2} < 1 + h_2$, and note this requires $c(1+g) \leqslant 0$.

We can recover the $v-$velocity component and find

$$v = \frac{y^2}{(1+g)^4} \frac{\mathrm{d}h_2}{\mathrm{d}\widehat{x}} \left[K\left(y - (1+g)\right) + c(1+g)\left(4y - 3(1+g)\right)\right]. \tag{6.22}$$

For the stagnation point we require $v = 0$, and this will occur, in general, at co-ordinates $(x_{\mathrm{st}}, y_{\mathrm{st}})$. In general the equation in the square parentheses does not admit real solutions. However, $v = 0$ when the derivative of h_2 (with respect to $\widehat{x}$) is zero. Thus stagnation points correspond to the maxima and minima of the unperturbed wall shape.

Thus, we conclude the existence of stagnation points at $(x_{\mathrm{st}}, y_{\mathrm{st}})$ such that x_{st} corresponds to maxima or minima of the upper wall shape, and y_{st} is given in Equation (6.21). To determine the stability of these stagnation points we consider the sign of the Hessian (King et al., 2003),

$$H = \left(\frac{\partial^2 \bar{\psi}}{\partial \widehat{x} \partial y}\right)^2 - \frac{\partial^2 \bar{\psi}}{\partial \widehat{x}^2} \frac{\partial^2 \bar{\psi}}{\partial y^2} \tag{6.23}$$

evaluated at the stagnation points. Under the conditions of Case A, for the class of points $(x_{\mathrm{st}}, y_{\mathrm{st};1,2})$ we find that

$$\operatorname{sign}(H) = \operatorname{sign}\left(\frac{\mathrm{d}^2 g}{\mathrm{d}\widehat{x}^2}\right) \tag{6.24}$$

thus maxima of the wall correspond to $\mathrm{d}^2 g/\mathrm{d}\widehat{x}^2 > 0$, and hence this class of stagnation points correspond to elliptic points, whereas the minima of the walls correspond to $\mathrm{d}^2 g/\mathrm{d}\widehat{x}^2 < 0$, and hence saddle points.

6.4.2 Two waves - the symmetric case

We shall consider the case where the upper and lower walls are symmetric wave forms; specificially where $h_1(x,t) \equiv -h_2(x,t)$. We define, the wall shape, as in the previous section as

$$h_2(x,t) = 1 + g(x - ct) + \varepsilon h(\kappa(x - ct)) f(t) \tag{6.25}$$

By moving to a a travelling reference frame, which is moving with the wave, with

$$\widehat{x} = x - ct, \qquad \bar{\psi} = \psi - cy, \qquad \bar{\psi} = \bar{\psi}_0(\widehat{x}, y) + \varepsilon \bar{\psi}_1(\widehat{x}, y, t). \tag{6.26}$$

We find the leading order streamfunction to be

$$\psi = \frac{(C + 24cg)(y^2 - 3(1+g)^2)y}{48(1+g)^3}. \tag{6.27}$$

We consider the existence of stagnation points at leading order. The $u-$velocity component at leading order is

$$u = \frac{1}{48(1+g)^3} (C - 24cg) (3y^2 - 3(1+g)^2) - c. \tag{6.28}$$

To determine the stagnation points, we equate (6.28) to be zero, which leads to a quadratic for y for the co-ordinates of the stagnation points, which admits real solutions if

$$\Delta = 4(1+g)^2 \frac{(C - 4cg + 8c)}{(C - 12cg)} \geqslant 0 \tag{6.29}$$

thus we require

$$\operatorname{sign}(C - 4cg + 4c) = \operatorname{sign}(C - 12cg), \tag{6.30}$$

which naturally leads to two cases

$$\textbf{Case A.} \qquad C - 4cg + 8c \geqslant 0 \text{ and } C - 12cg > 0, \tag{6.31a}$$

$$\text{or } \textbf{Case B.} \qquad C - 4cg + 8c \leqslant 0 \text{ and } C - 12cg < 0. \tag{6.31b}$$

Under the appropriate regime, we find that position of the stagnation points is given by

$$y_{\mathrm{st};1,2} = \pm(1+g)\sqrt{\frac{C - 4cg + 8c}{C - 12cg}} \tag{6.32}$$

We require both the stagnation points to be within the walls, and thus require

$$c(1+g) \leqslant 0, \tag{6.33}$$

or simply $c \leqslant 0$.

The vertical velocity component is recovered as

$$v = -\frac{1}{16(1+g^4)} y \frac{\mathrm{d}h_2}{\mathrm{d}\widehat{x}} \left[y^2(C - 16cg + 8c) - (C(1+g)^2 + 24c(1+g)^2) \right] \tag{6.34}$$

and again we consider the class of stagnation points with $\mathrm{d}g/\mathrm{d}\widehat{x}$.

The stability of these equilibrium points is determined by the sign of the Hessian which as in the one-wall case, is determined by the sign of the second derivative of the wall shape, $\mathrm{d}^2 g/\mathrm{d}\widehat{x}^2$, and thus maxima of the walls correspond to elliptic points and minima correspond to saddle points.

6.5 Results

In this section we shall discuss the observed dynamics of the one-wall and two-wall cases we have discussed previously, through the consideration of streamlines, particle paths, flow-rates and local Lyapunov exponents.

6.5.1 One-wall case

Unperturbed streamlines

We shall consider the upper wall to take the following form

$$h_2(x,t) = 1 + a\cos(x - ct) + \varepsilon a \cos(\kappa(x - ct))\sin(kt),$$

where $a = 0.1$. The statement is consistent with the general theory discussed previously.

The solution for the unperturbed streamlines ($\varepsilon = 0$) can be seen in Figures 6.2 and 6.3 where the two different structures of the solution are observed. Firstly, in Figure 6.2 we have the solution where the parameter set predicts the existence of elliptic orbits and saddle points. These stagnation points are identified with crosses (elliptic) and stars (saddles). The stable branches of the saddle point are those approaching from the ‘upper-

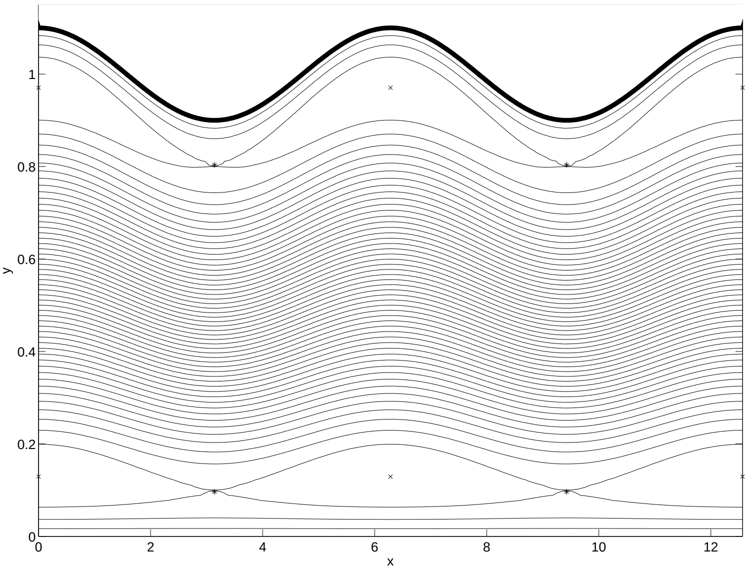

Figure 6.2: Streamlines of the unperturbed case with wall shape $1+0.1\cos(\widehat{x})$. Parameters are $c = -1$ and $C = 20$. Recall the c is the wave speed, and C is a constant dependent on the pressure gradient.

left' and the 'lower-right'. The vortex structure about the elliptic point therefore rotates clockwise.

Figure 6.3 demonstrates the regular streamlines predicted in the case when stagnation points are not predicted to exist within the boundaries of the flow.

Perturbed streamlines

We consider the case now when $\varepsilon \neq 0$ and consider the variation in the streamlines over time. Note this is a snap shot of the streamlines at a given instance and does not show particle trajectories. Figures 6.4, 6.5 and 6.6, all demonstrate the variation in streamlines over time for different wavespeed of the perturbation (varied by κ). Notice that by introducing a perturbation, the structure of the elliptic point and the heteroclinc orbits (Figure 6.2) is broken; this introduces mixing layers and provides a mechanism for mixing in a low Reynolds number flow. One should notice in particular when $\kappa = 2.5$ and $\kappa = 4$,

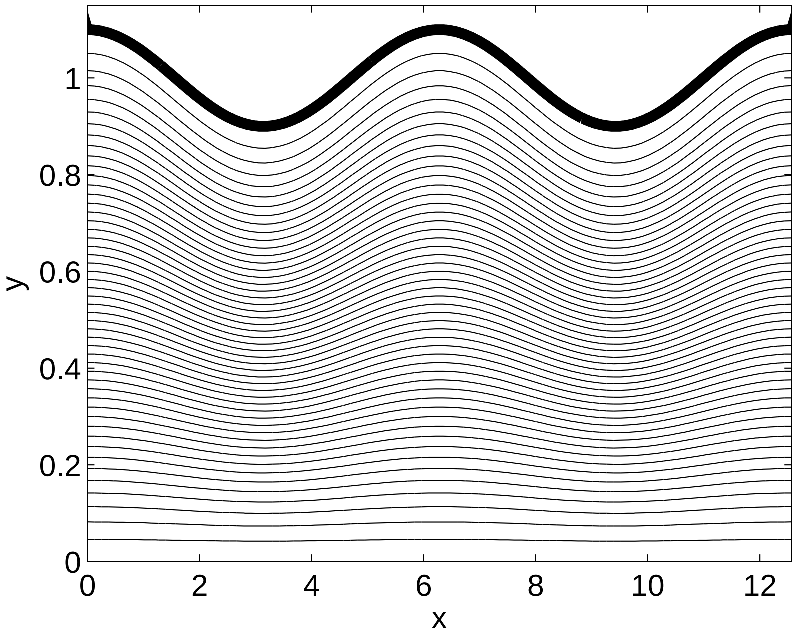

Figure 6.3: Streamlines of the unperturbed case with wall shape $1+0.1\cos(\widehat{x})$. Parameters are $c = 1$ and $C = 20$. Notice the absence of the vortex structure.

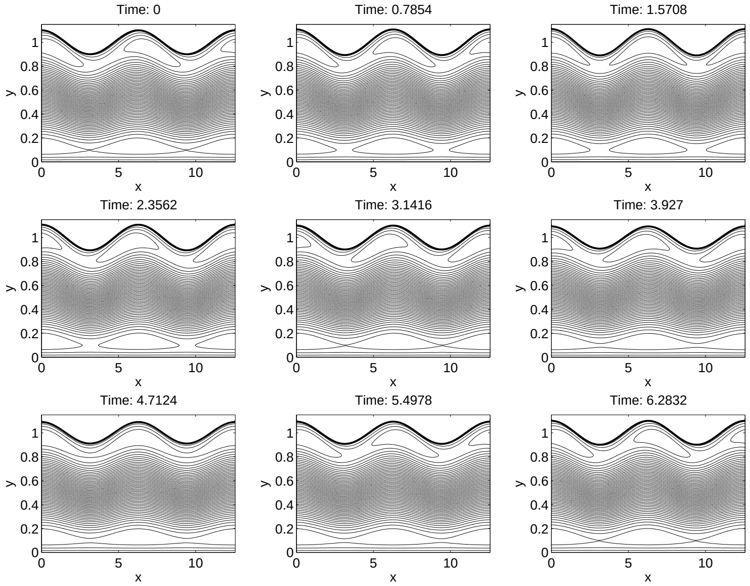

Figure 6.4: Time variation of the streamlines for the one-wall case as $t \in [0, 2\pi]$. Parameters are $C = 100$, $c = -5$, $\varepsilon = 0.01$, $\kappa = 1$ and $k = 1$.

the breaking of the vortex structure and the formation of daughter vortices.

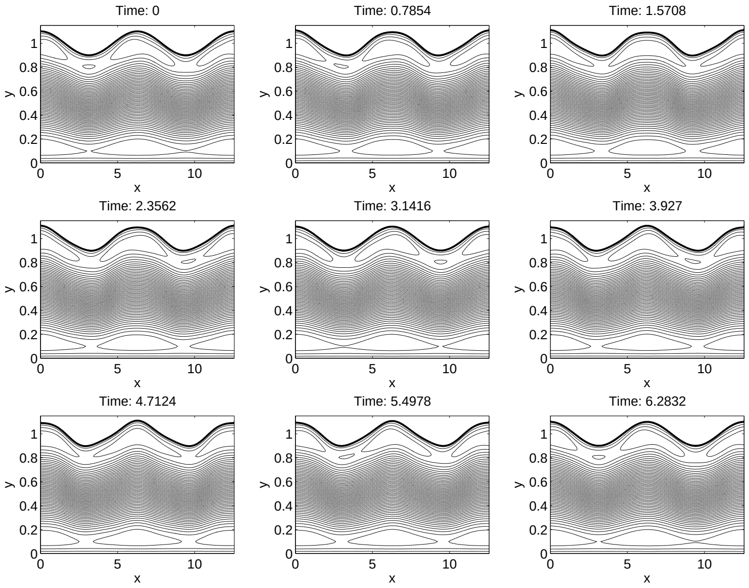

Figure 6.5: Time variation of the streamlines for the one-wall case as $t \in [0, 2\pi]$. Parameters as in Figure 6.4 except the speed of the perturbation is varied with $\kappa = 2.5$.

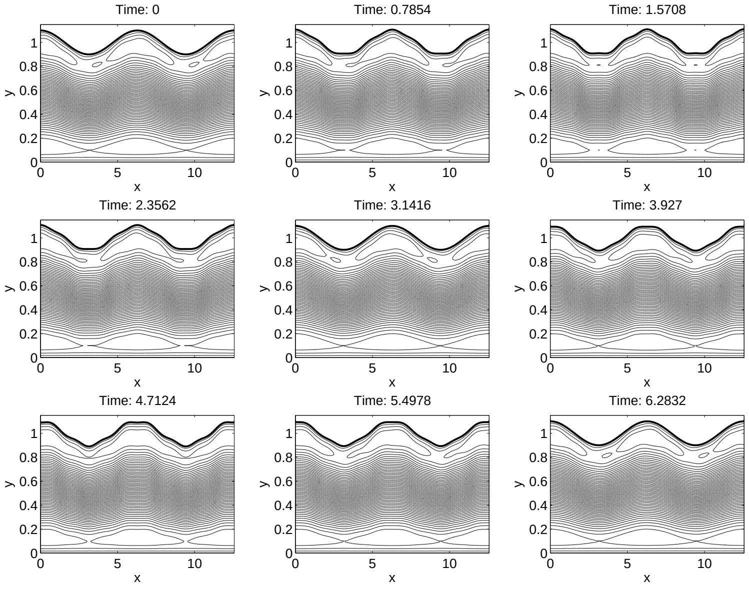

Figure 6.6: Time variation of the streamlines for the one-wall case as $t \in [0, 2\pi]$. Parameters as in Figure 6.6 except $\kappa = 4$.

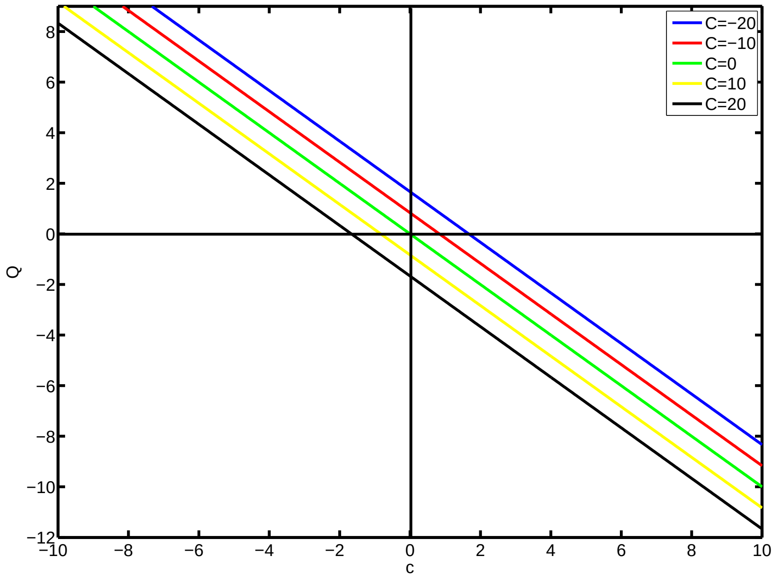

Figure 6.7: Plot of flow rate Q, as a function of c the wave speed, for various values of the pressure gradient C. Notice the existence of regions of reflux when $C \neq 0$.

Flow Rate

The flow rate, for the one-wall case, is defined as

$$Q = \int_0^{1+h_2(\widehat{x})} u(\widehat{x}, y)\mathrm{d}y,$$

and by the continuity equation is independent of the choice of x.

Figure 6.7 shows the calculated flow rate as a function of the wave speed parameter c. The essential features to notice is the flow rate changes sign depending on c, however except for $C = 0$, it does not pass through the origin. The regions where $c < 0$, $Q > 0$ and $c > 0$, $Q < 0$ correspond to non-reflux flow; the regions where c and Q are of the same sign correspond to the reflux phenomena, and regimes in which we observe the vortex structure. The existence of reflux is dependent on the pressure term C.

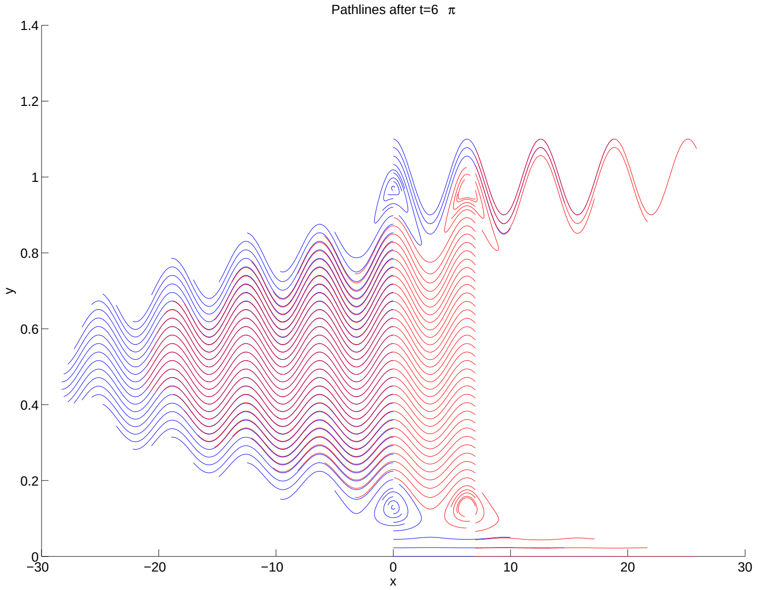

Figure 6.8: A series of particle paths starting from $x = 0$ (blue) and $x = 7$ (red). The system is unperturbed and the parameters are as follows $C = 1/0.04$ and $c = -1$

Particle Paths

Presented in Figures 6.8 and 6.9 are a set of particle paths for the unperturbed (6.8) and perturbed (6.9) cases. The blue particles were all started on the y-axis and the red particles were started on $x = 7$ (to deliberately avoid the stagnation points).

It is precisely the deviation of these particle paths which are of interest in calculating Lyapunov Exponents which we shall calculate for the two-wall case. Notice as time extends (moving away from the starting axes) that in the perturbed case some pathlines can be seen to cross.

6.5.2 Two-wall case

Unperturbed streamlines

Figure 6.10 is a plot of the streamlines for the unperturbed case when $h(x,t) = 1 + 0.1\cos(\widehat{x})$; notice the existence of the vortices and the saddle points marked with crosses

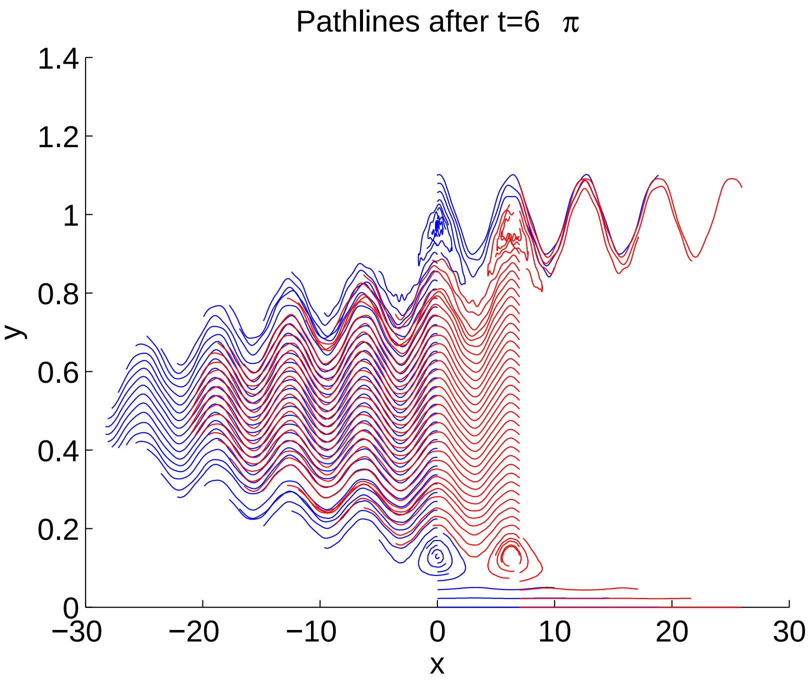

Figure 6.9: A series of particle paths (parameters as in Figure 6.8) for the perturbed system; $\varepsilon = 0.1$ and $\kappa = k = 2$.

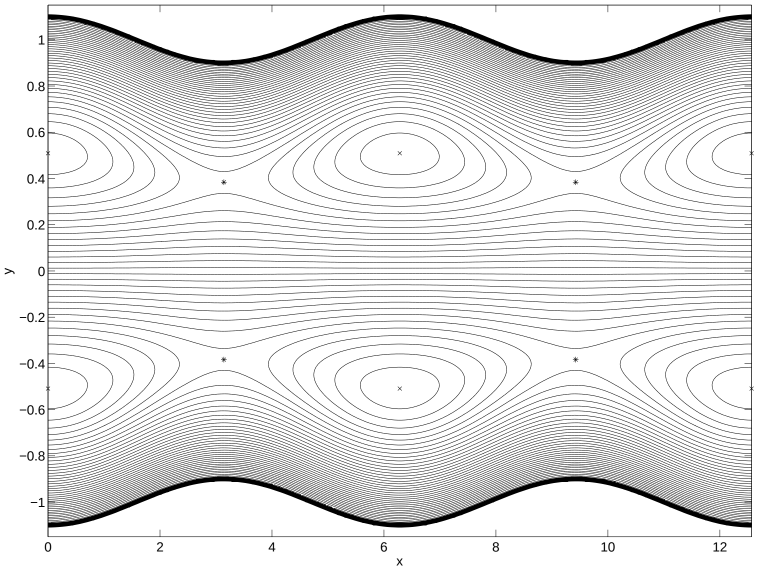

Figure 6.10: Streamlines of the unperturbed case with upper wall shape $1 + 0.1\cos(\widehat{x})$. Parameters are $c = -1$ and $C = 20$.

and stars respectively, as predicted and as observed also in the one-wall case.

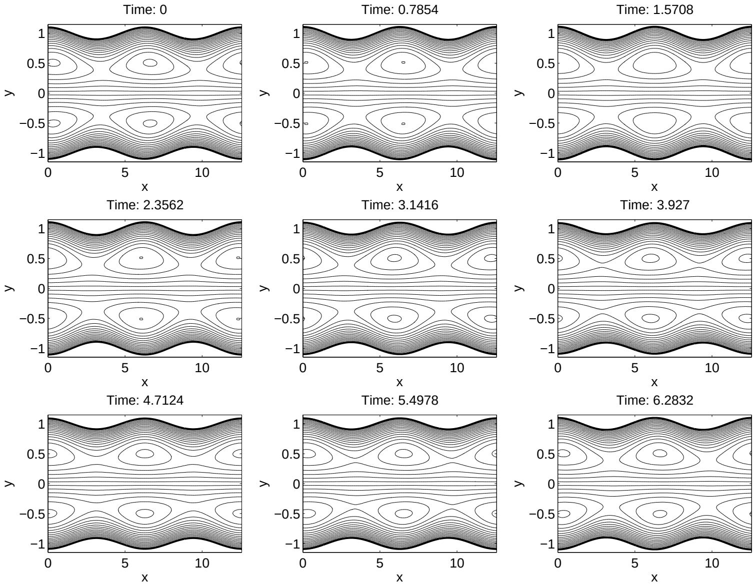

Figure 6.11: Time variation of the streamlines of the two wall shape with $c = -1$ and $C = 20$, $\varepsilon = 0.1$, $k = 2$ and $\kappa = 1$.

Perturbed streamlines

We consider the wall shapes to take the following form

$$h_2(x,t) = 1 + a\cos(x - ct) + \varepsilon a\cos(\kappa(x - ct))\sin(kt), \qquad h_1 = -h_2.$$

we once again observe the breakdown of the vortex structure and heteroclinic orbits are shown in Figures 6.11 and 6.12.

Flow Rate

Figure 6.13 shows the calculated flow rate for variation in the wave speed parameter c. As in the one-wall case, we observe the feature of reflux.

Particle Paths

Presented in Figures 6.14 and 6.15 are a set of particle paths for the unperturbed and perturbed cases, respectively. The blue particles were all started on the y-axis and the

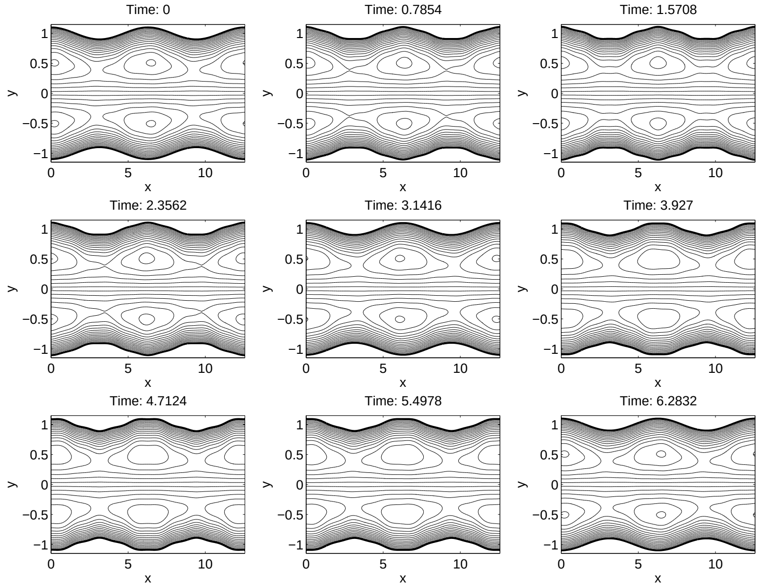

Figure 6.12: Time variation of the streamlines of the two wall shape with $c = -1$ and $C = 20$, $\varepsilon = 0.1$, $k = 2$ and $\kappa = 4$.

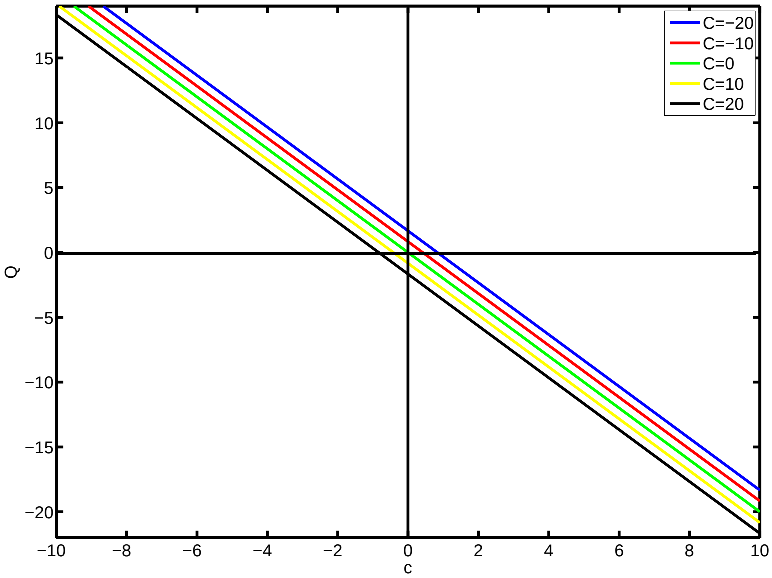

Figure 6.13: Plot of flow rate against varying values of c, for various values of C. Notice the line does not cross at the origin (except for $C = 0$), and thus provides evidence of reflux - associated with the vortex structure.

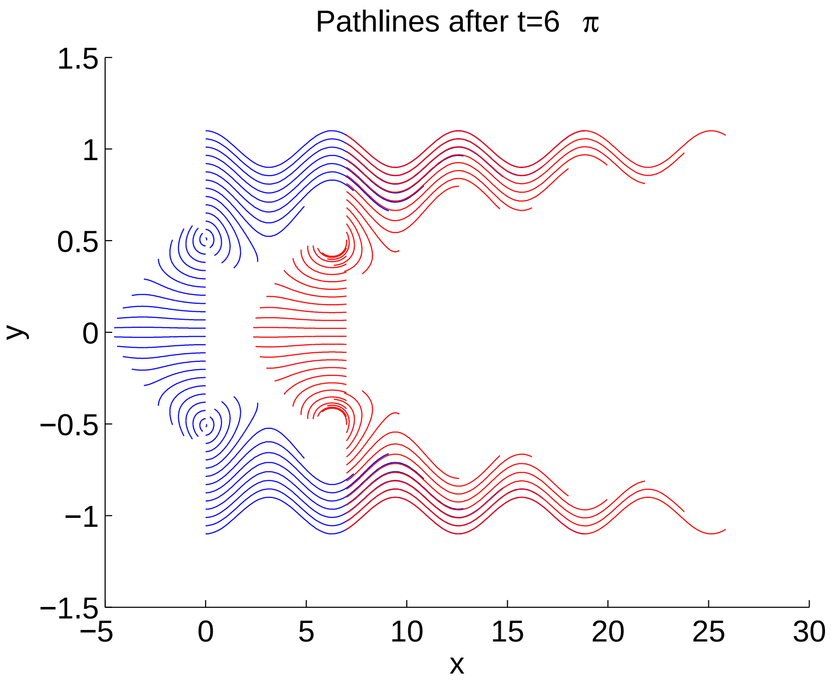

Figure 6.14: A series of particle paths starting from $x = 0$ (blue) and $x = 7$ (red). The system is unperturbed and the parameters are as follows $C = 1/0.04$ and $c = -1$

red particles were started on $x = 7$ (to deliberately avoid the stagnation points, located at $x = n\pi$ $(n \in \mathbb{Z})$).

Quantification of mixing: Lyapunov exponents

As discussed in Section 6.3.2, the Lyapunov exponent and in particular the local Lyapunov exponent is a useful measure of mixing and stretching within a system. Presented in Figures 6.16–6.18 are plots of the local Lyapunov exponents after 10, 50 and 99 periods of the wall motion.

Notice the existence of structured areas of the higher Lyapunov exponents in particular along the heteroclinc orbits which separate two regions of the flow (that in the vortices and that which lies above/below the vortices; it is in these areas that we expect to see the exchange of particles between the two regions. We also note in Figures 6.17 and 6.18 the formation of a structure mirroring the boundary just below it. In some sense this layer marks the edge of the particles which are directly affected by the perturbation of the wall.

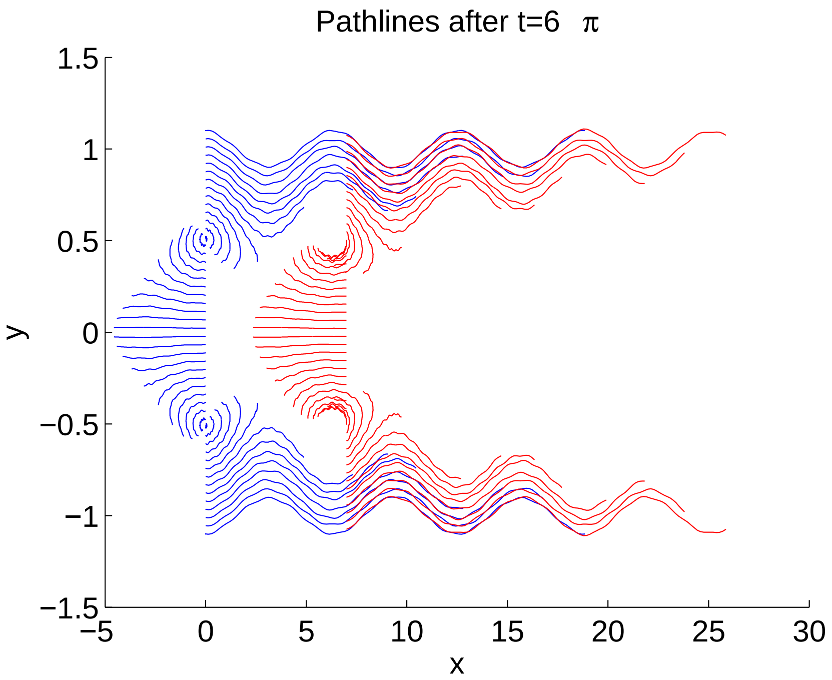

Figure 6.15: A series of particle paths (parameters as in Figure 6.8) for the perturbed system; $\varepsilon = 0.1$, $k = 2$ and $\kappa = 3.5$.

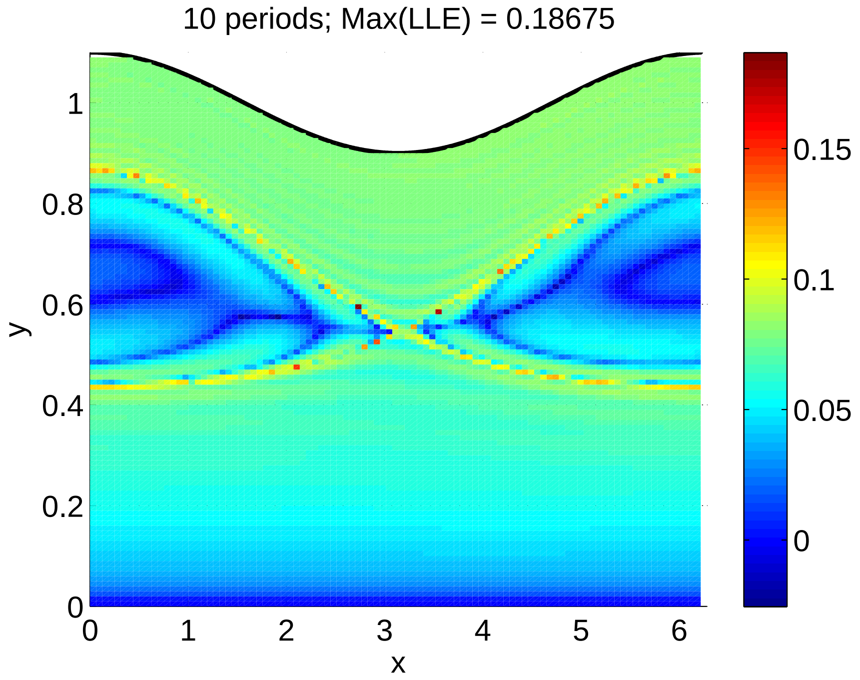

Figure 6.16: Local Lyapunov exponents for the two-wall case, after 10 periods. $C = 25$, $c = -1$, $k = 2$, $\kappa = 1$, $\varepsilon = 0.1$.

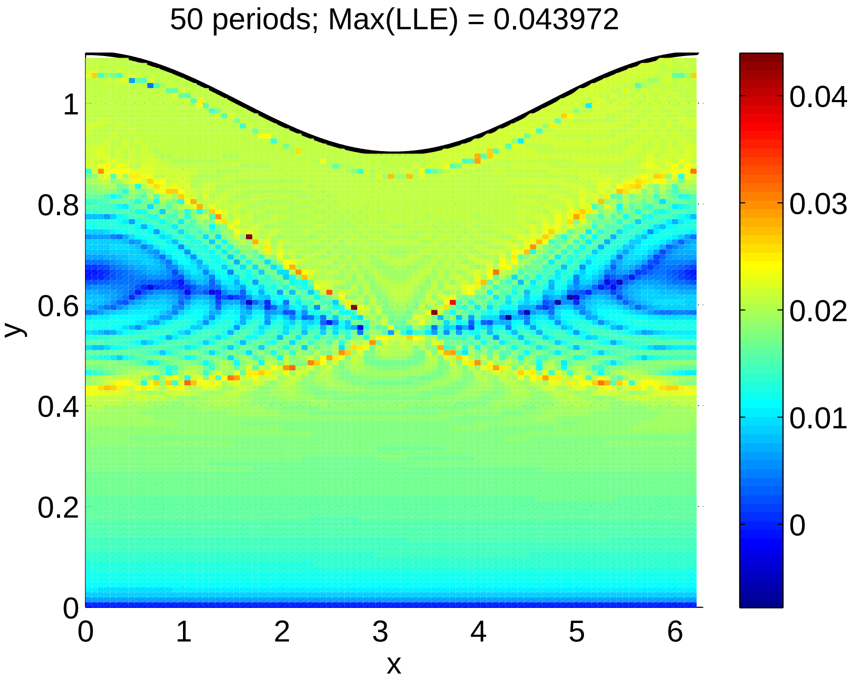

Figure 6.17: Local Lyapunov exponents after 50 periods. Parameters as in Figure 6.16.

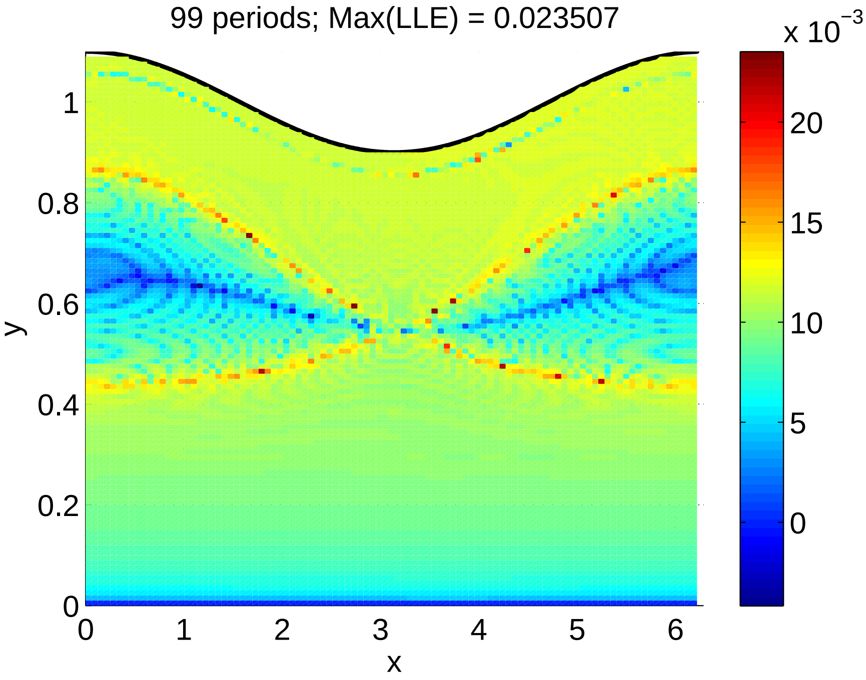

Figure 6.18: Local Lyapunov exponents after 99 periods. Parameters as in Figure 6.16.

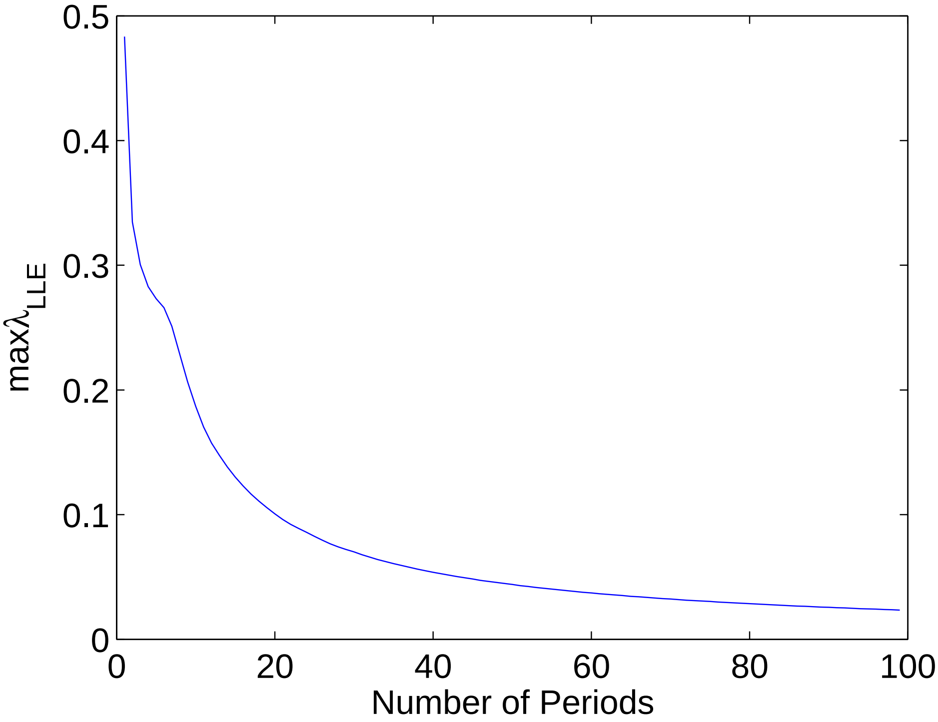

Figure 6.19: Plot of $\max \lambda_{LLE}$ against time periods, for the same parameters as in Figure 6.16. Notice that although a limit is not clear, the values of the maximum are small, but positive.

Figure 6.19 illustrates the change in the maximum local Lyapunov exponent as a function of time elapsed. We notice that the Maximum Lyapunov Exponent is always positive, it is small which indicates the existence of rotation, mixing and stretching of the fluid.

6.6 Biological implications

We have highlighted that the combined effect of peristaltic flow and ciliary beating is important in describing the fluid flow in the oviduct.

The transportation of the embryo to the correct site for implantation in the uterus is important; ideally the embryo should implant at the top of uterus (in the fundus). An embryo which implants too low in the uterus can lead to the placenta developing over

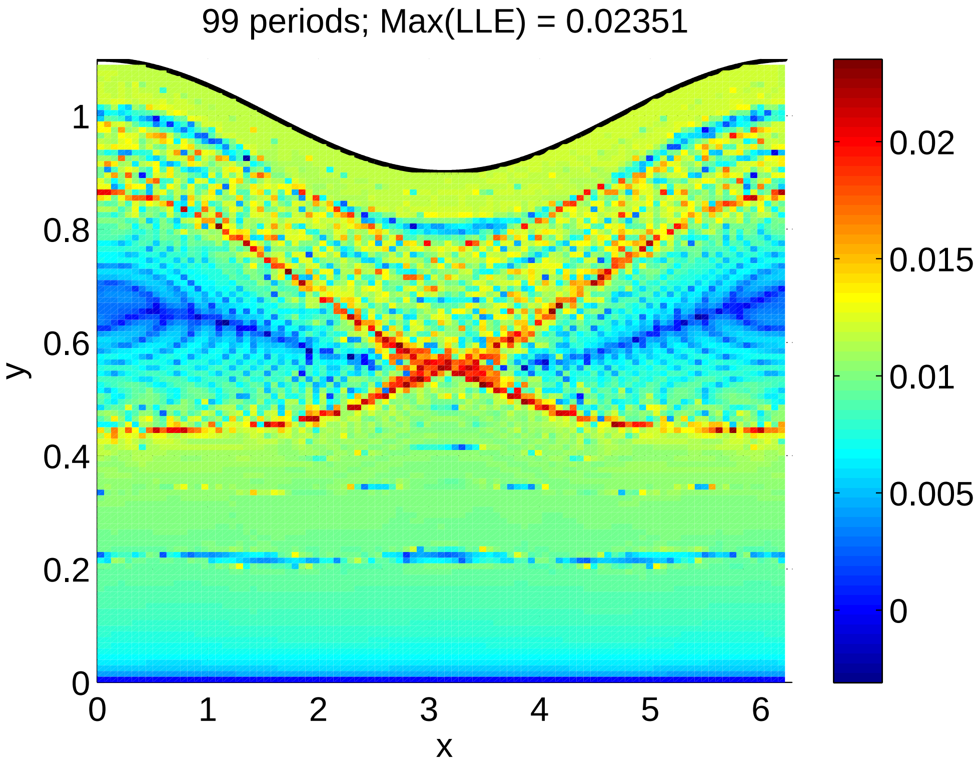

Figure 6.20: Local Lyapunov exponents for the two-wall case, after 99 periods with an increased rate of perturbation – $\kappa = 4$. Other parameters are $C = 25$, $c = -1$, $k = 2$, $\varepsilon = 0.1$.

the cervix (a condition called placenta previa), which can lead to a ruptured placenta (Eytan and Elad, 1999). The successful implantation of embryos is important in natural conception when the embryo has entered the uterus from the oviduct and in *in vitro* fertilisation, where embryos are transferred into the uterus a few days before implantation is expected. Laboratory fertilisation in IVF is 90% successful, however only 25% of cycles result in successful births – problems with implantation may explain some of this discrepancy (Yaniv et al., 2003). In both *in vitro* and *in vivo* situations the embryo will be present in the uterus for 3–4 days prior to implantation.

We have implemented a zero Reynolds number analysis of flow in the oviduct/uterus, in particular we have noted have noted the existence of reflux for certain values of the wave speed and pressure gradient and a mechanism to interchange fluid between regions of the channel. There is evidence to suggest that near to the ovum, there may be some short-range chemotactic effect (Bahat and Eisenbach, 2006), however, the effect of the mixing we have demonstrated compared to diffusion is difficult to quantify, as the Péclet number for such flows is often an open question – partly due to the uncertain nature of the precise chemotactic agents involved.

Sperm are known to accumulate near boundaries, and to 'crawl' along surfaces within the human reproductive system (Rothschild, 1963; Fauci and Dillon, 2006). The existence of a mechanism to move fluid (and particles) from nears the walls toward to the centre of the channel and towards the uterus may be important in the movement of sperm cells towards the site of fertilisation either directly by causing the sperm to be moved toward the site, or by allowing possible chemotactic agents to be transported to the sperm to act as a 'orientation mechanism'.

Our work highlights regions of flow within the channel which are in the opposite direction to the bulk flow. This lends theoretical evidence to the experiential observations of Sjösten et al. (2004) where starch particles are observed near the ovaries after their introduction at the cervix. This observation suggests some flow contrary to the direction of bulk flow, from the ovaries towards the uterus.

Implications of our work on the case of 'embryo/ovum present' situations are difficult to specify, especially as the diameter of the embryo (150 μm) may not be neglected compared to the width of the uterine channel ($\sim 1000\,\mu$m) (Eytan and Elad, 1999), meaning that to fully understand the interaction of the embryo/ovum and the structure driven fluid flow requires us to account for the non-zero volume of the embryo. Following ovulation the ovum is surrounded by a coating of cumulus cells, which need to be removed prior to fertilisation. The fluid flow generated, could be a potential mechanism to assist in the removal of these cumulus cells.

6.7 Conclusions

In this chapter, through an asymptotic analysis of flow in a channel with a small aspect ratio, we demonstrated that a small perturbation to a bulk peristaltic flow is important in the overall dynamics and mixing of the system.

We have demonstrated the motion of the fluid and particles in the channel, through the use of streamlines and pathlines, and demonstrated parameter ranges under which reflux occurs by considering the bulk flow rate. By utilising Lyapunov Exponents we have shown there are regions of mixing in the flow, typically around the edge of the observed vortex structure. This demonstrates that ciliary propulsion, although of a smaller amplitude than peristaltic waves, can be an important factor for motion - in particular with regards to mixing and exchanging fluids in Stokes flow.

Areas of future work should focus on adding additional biological features to the mathematical model, such as studying the motion in the oviduct with the ovum/embryo present, considering a axi-symmetric geometry for the oviduct, and considering non-Newtonian fluids such as power law fluids (where some asymptotic analysis should be possible)

CHAPTER 7

CONCLUSIONS

We conclude this thesis by summarising and commenting upon the results we have presented from a mathematical and biological context. We also provide an indication of future topics in this area, that warrant further investigation.

7.1 Summary

This thesis has considered the motion of human sperm and the flow in the human oviduct. The motility of human sperm has been modelled mathematically, using slender-body theory and the singularity methods for Stokes flow. The kinematic models have been devised and implemented based upon experimental observations. The outcome of the mathematical modelling is an insight into the physical properties of the modes of beating observed.

We have developed a slender-body theory code based on the work of Higdon (1979c), which is implemented computationally using numerical integration as to allow for future extensions - such as more complex fluid media and boundaries. We have extended existing mathematical models for planar sinusoidal propagation of the beat pattern to a hybrid 'exponential-arctan' envelope: We conclude that the parameters of amplitude, wavenumber and the position of the beat pattern are intrinsically linked, moreover, the more posterior the beat pattern is, the shorter the wavelength must be in order to maintain a level of optimality whilst the amplitude is fixed, which is consistent with our experimental observations

The model was extended to include the effect of a non-constant wavenumber and consequently we demonstrated that an optimally efficient beat pattern configuration could not be adequately described using a fixed wavenumber model. In particular we highlighted a link between an increasing wavenumber and the how posterior a beat pattern is. We also noted the optimality of whip-like beat pattern configurations.

These two initial models, assumed that the underlying beat pattern was a planar sinusoidal wave. By studying the experimental data, and considering the shear-angle, we derived a number of assumptions and, based upon these, devised a new model for the beat pattern configuration, with a small number of parameters. The new model removed the necessity to assume *a priori* a functional form of the beat pattern. This new model encompasses the broad range of beat patterns observed *in vitro* with the benefit of only needing two parameters and was extended to allow asymmetric beat patterns, by relaxing one of our modelling assumptions and the introduction of one new parameter.

Analysis of the speed and power consumption of the different configurations was conducted and it was found there are a number of groups of configurations with near optimal speed. By considering the bending moment density, which scales with viscosity, we were able to identify a mechanism which could explain the modulation of sperm beat pattern configurations. We conclude that the fastest beat pattern is the 'whip-like' beat pattern observed in low viscosity medium; however, the value of the maximum bending moment density is high. If the viscosity is increased, thus increasing the bending moment density, then in order to maintain a physically acceptable beat configuration with a near maximum velocity, a suitable alternative beat pattern configuration is the meandering tail pattern. The regions of optimal parameters show excellent agreement with the experimental data.

Through an asymptotic analysis of flow in a channel with a small aspect ratio, we demonstrated that a small perturbation to a bulk peristaltic flow is important in the overall dynamics and mixing of the system. The work also suggests regions of flow within the channel which are in the opposite direction to the bulk flow. This observation suggests some flow contrary to the direction of bulk flow, from the ovaries towards the uterus; which is consistent with experimental observations, such as Sjösten et al. (2004) where starch particles are observed near the ovaries after their introduction at the cervix. We have demonstrated that ciliary propulsion, although of a smaller amplitude than peristaltic waves, can be an important factor for motion - in particular with regards to mixing and exchanging fluids in Stokes flow.

7.2 Future developments

There are several ways that the new model devised for flagellar propulsion could be utilised. As a tool for modelling sperm beat patterns, the new model encompass a broad range of beat patterns observed *in vitro* with a small number of parameters meaning that the model is of valuable use in aspects of the modelling of planar sperm beating. Moreover, the model can be used to predict the properties of human sperm observed *in vitro* using the slender-body theory code. As the beat pattern parameters can be fitted by eye the model avoids the need for detailed image processing and data analysis, which is required if we are to calculate Fourier coefficients directly. Alternatively, accurate and less subjective parameters could determined through the use of a more sophisticated data fitting routine.

It would be beneficial to consider the motion of human sperm in a non-Newtonian fluid, such as a simple linear viscoelastic Maxwell fluid as a model for cervical mucus. A similar study could be undertaken as has been done in this thesis to consider the importance of the viscoelastic component of the flow on human sperm motility and the relation of the non-Newtonian component on the model parameters, for example the effect of the memory parameter in a linear Maxwell fluid or the effect of shear-thinning in a shear-dependent viscosity fluid.

The model could also be linked to a hybrid boundary-element slender-body theory code being devised by Smith et al. (2008a). The hybrid code seeks to model the 'correct' morphology of the human sperm head rather than using a sphere of 'effective radius'.

The motion of sperm could also be considered in a number of situations more complex than in isolation in a Newtonian fluid. For example, the model could be adopted to consider the effect of rheotaxis (an oncoming fluid flow) or by coupling with an appropriative advection/diffusion equation as a model for chemotaxis. The motion of sperm near boundaries – both planar, moving – and near the ovum could also be studied.

A current drawback of the model proposed is that it considers only planar beating. An extension to allow for three-dimensional beating should be considered, however, this is dependent on new experimental data regarding the motion of human sperm in the third-spatial dimension being available.

Future analysis of peristaltic flows in the oviduct may include the addition of a third-dimension or axi-symmetric flow with more realistic geometries and by considering non-Newtonian fluids such as power law fluids asymptotically. A particular area of interest should be the introduction in to the modelling the non-zero volume of the ovum and to consider the interactions of this on the fluid flow.

APPENDIX A

EXPERIMENTAL METHODS AND *in vitro* PROCESSES

There are a number of techniques for studying the motility of human sperm *in vitro*. In this section we shall briefly outline two of the techniques available and make a more detailed analysis of the particular method that was used to recover the data used and considered in this thesis.

A.1 Obtaining sperm cells for analysis

There are a variety of methods for obtaining sperm from semen for the use in experimentations. The preferred method by colleagues in the Birmingham Women's Hospital is a technique known as 'swim-up'. Upon ejaculation, semen coagulates into a gel which after around twenty minutes liquefies again. At this stage, 1ml of semen is placed in a test-tube, and then layered with 1ml of Earle's medium (Mortimer, 1991; World Health Organisation, 1999). The vessel is then incubated for 30 minutes at 37°C at 5% CO_2, after which time a small amount of the Earle's medium is removed, which now contains some motile sperm cells.

Some motile sperm will, during the incubation, swim-up from the semen at the bottom into the medium at the top. The advantage of the swim-up method is that the process easily differentiates between motile and non-motile cells, as the non-motile ones will not swim into the Earle's medium and hence will not be part of the study. Additionally, having sperm in medium allows us to control their environment and remove other molecules, such as proteins or bacteria from the sample, which may affect the result.

An alternative method that is available is to utilise a centrifuge, typically centrifuging semen at several hundred 'g's for ten to fifteen minutes (as used in Ishijima et al. (1986)); however, the physiological effects on the sperm, of such high forces for a prolonged period of time are not understood fully.

To study *in vitro* the motion of sperm in cervical mucus, requires extracting cervical mucus from a female and using this in the laboratory; however, this is difficult as the cervical mucus degrades very quickly. Substitute media are often used; firstly hyaluronic acid (Neuwinger et al., 1991), which is a component of natural cervical mucus or alternatively methylcellulose which has been shown to be an acceptable medium for clinical tests (Ivic et al., 2002).

Once prepared the cells can be studied using a number of methods, two of which are outlined below. In both cases the sperm will be contained in a chamber, microscope slide or capillary tube. The World Health Organisation (1999) manual states that "[coverslip] depths less than 20 microns may constrain the rotational movement of the sperm". For accurate focusing and clean imaging, a typical depth of coverslip used by colleagues is 20-40μm. As the head of a sperm is around 5μm in width in the broader direction, the use of a small coverslip ensures that most sperm swim in parallel horizontal plane which is beneficial for the purposes for imaging.

A.2 Computer assisted semen analysis

Computer Assisted Semen Analysis, can be undertaken using the Birmingham Women's Hospital's Hamilton Thorne IVOS system. The CASA process provides a variety of mean averaged parameters from a sample of sperm; the averaging being done over the individual sperm cells, and over successive time periods.

An example output achieved using sperm in medium, collected using 'swim-up' is

Parameter		Value	Units	Standard Deviation
Path Velocity	VAP	85.4	μm/s	27.6
Prog. Velocity	VSL	77.3	μm/s	27.8
Track Speed	VCL	122.3	μm/s	46.7
Lateral Amplitude	ALH	4.0	μm	1.9
Beat Frequency	BCF	3.8	Hz	3.3
Straightness	STR	90	%	16
Linearity	LIN	66	%	20
Elongation		66	%	15
Area		4.9	μm^2	1.4

Figure A.1: An example table of data available from the Hamilton Thorne IVOS Casa system.

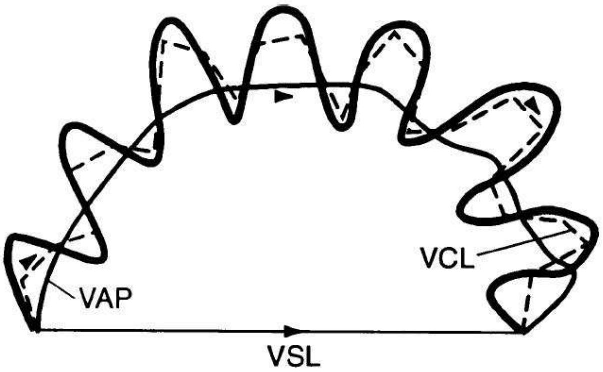

Figure A.2: Sperm motility trajectories showing the average path velocity (VAP), curvilinear velocity (VCL) and straight line velocity (VSL). From Kay and Robertston (1998).

presented in Figure A.1. The output is a series of motility parameters shown in the table as path velocity (VAP), progressive velocity (VSL), curvilinear velocity (VCL), the amplitude of lateral head displacement (ALH) beat cross frequency (BCF), straightness (STR=VSL/VAP) and linearity (LIN=VSL/VCL). The relation between VAP, VCL and VSL are shown if Figure A.2 for a sample trajectory. Elongation is the ratio of head width to head length and is used to distinguish non-motile sperm from other static objects; sperm have a head shape with elongation $< 75\%$, other objects such as bacteria will have larger elongation.

A.3 High speed imaging: acquisition and processing

Using high speed cameras attached to microscopes, Birmingham Women's Hospital also has the ability to collect image data of sperm beat pattern at speed of up to 1000 frames per second. As sperm beat at around 10-20Hz, a complete beat cycle is encompassed in around 50 frames meaning that many subtleties of the beat pattern can be noticed.

Typically, sperm cells prepared using swim-up are then introduced into a Kremer tube; a Kremer tube is a glass tube with rectangular cross section. Typically the tube may have a depth and width of 0.4mm and a length of 50mm. By considering sperm at different lengths along the Kremer we are able to reduce the concentration as to make detailed analysis of a single sperm swimming possible. Figure A.3 illustrates some example photographs taken using a Photron Super 10K High Speed digital camera

Once the photographs have been recorded we need to obtain quantitative data about the position of the head and flagellum. This is done using image processing techniques developed by Dr Eamonn Gaffney (Oxon) using MATLAB's image processing toolbox. Some examples of the initial photographs and the recovered data are shown in Figure A.4.

The outcome of the image processing is a MATLAB file which contains time series data for, amongst other things, the position of the flagellum and the position of the head. The data can then be manipulated in MATLAB; for example, in our case it is necessary to translate each frame to occur in a 'body frame', with the head centered at $(0, 0)$ and the head/flagellar junction parallel to the X axis. Some example data, prior to translation and rotation is presented in Figure A.5.

The advantage of high speed imaging and acquisition over CASA type analysis is that we can track the motility of individual sperm cells in great detail, rather than comparing mean parameters determined from a number of sperm cells. The high speed imaging also allows careful tracking and analysis of the motion of the head and flagellum of a single cell. Advances in image acquisition are providing an understanding of free-swimming motile

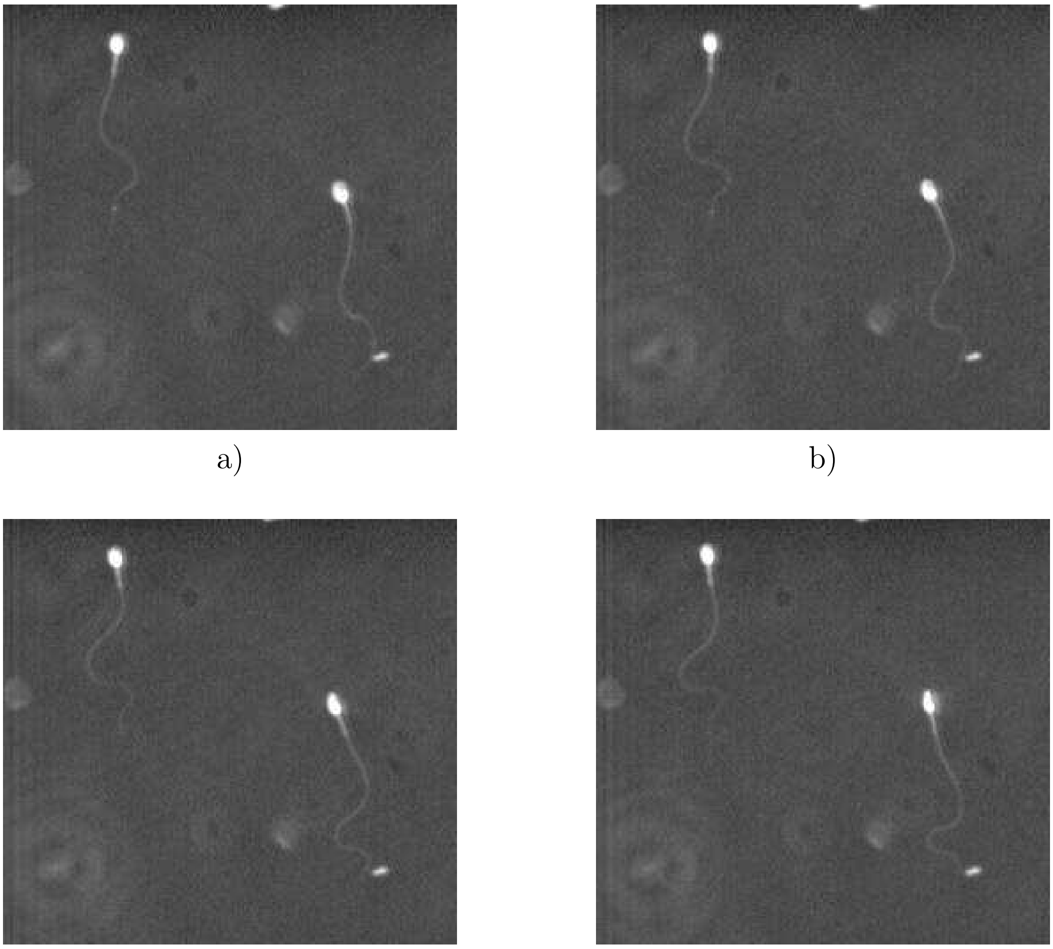

a)

b)

c)

d)

Figure A.3: Example images taken using Photron Super 10K High Speed Digital Camera; the width of each frame is approximately 150μm. The human sperm are imaged swimming in a Kremer tube (50 mm length, 4mm width, 0.4mm depth) loaded with hyaluronic acid, which is a polymer which is used as a cervical mucus analogue. The interval between successive photographs is 10ms. (Personal Communications: Kirkman-Brown and Smith)

sperm that were previously only available in fixed sperm.

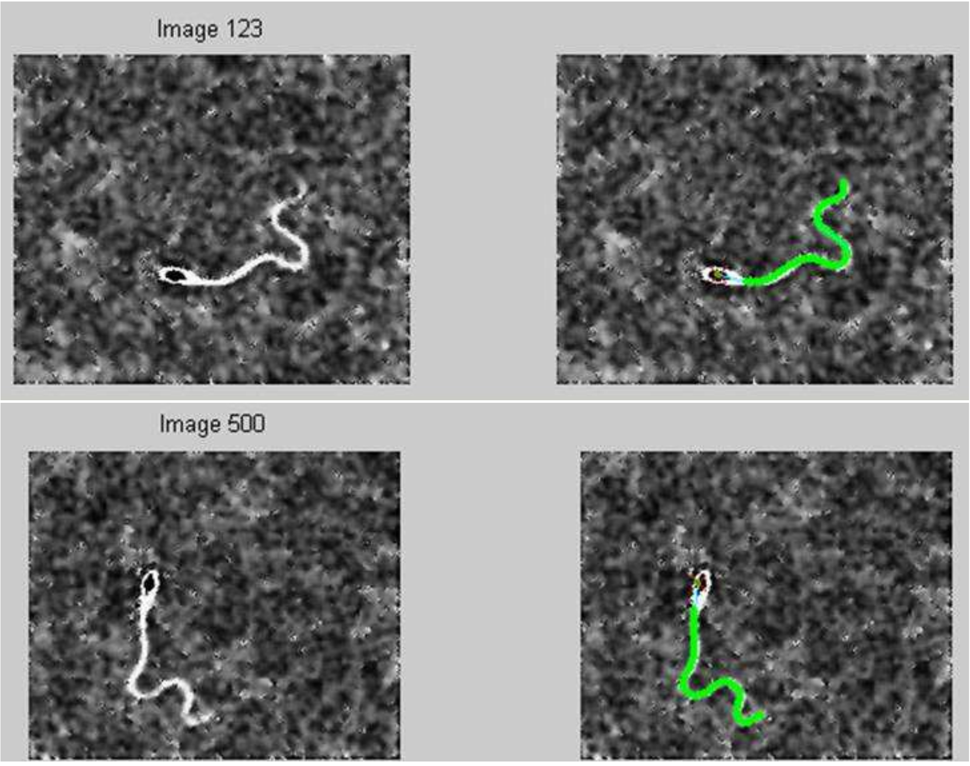

Figure A.4: Example data for a single human sperm in Methylcellulose 4000cps at 2%. The original photographs are shown on the left; the right hand pictures illustrate the recovered position of the tail (green) and the centroid of the head (red cross – very faint). The ‘halo’ around the sperm’s head causes some problems obtaining an accurate fix on the head’s location.

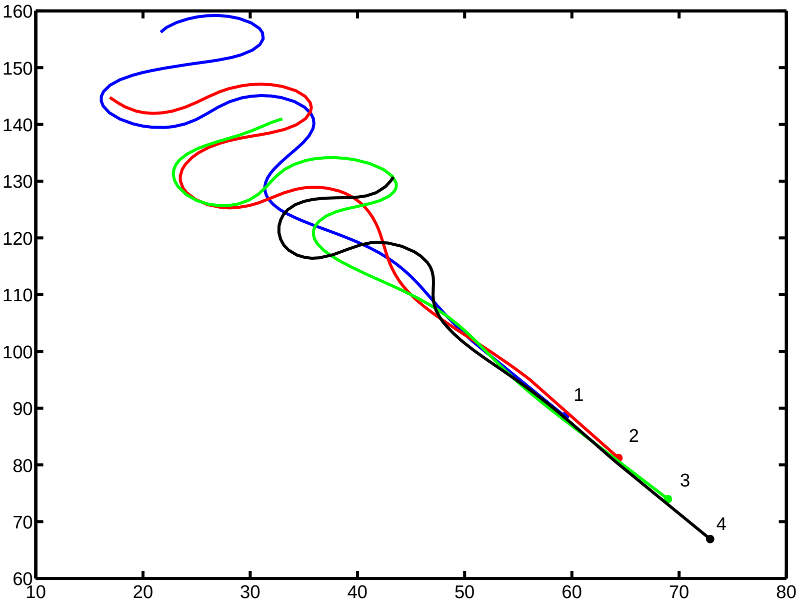

Figure A.5: Example experimental data captured from high speed photographs, processed using MATLAB. The four 'snap-shots' are from data taken 30 frames apart at approximately 400 frames per second, so each snap-shop is approximately 75ms from the previous one.

APPENDIX B

DERIVATION OF THE STOKESLET

Green's functions are an important mathematical technique for solving inhomogeneous differential equations. The Stokeslet is the Green's function for Stokes flow with a point force as the only body force $\boldsymbol{F}(\boldsymbol{x}) = \boldsymbol{f}\delta(\boldsymbol{x})$ ($\boldsymbol{f} \in \mathbb{R}^3$) at the point $\boldsymbol{x} = \boldsymbol{0}$. The governing Stokes equations are (we have used the standard notation $\Delta \equiv \nabla^2$ in this section for clarity),

$$0 = -\nabla p + \mu\Delta\boldsymbol{u} + \boldsymbol{F}, \qquad \nabla \cdot \boldsymbol{u} = 0, \tag{B.1}$$

where $\boldsymbol{u} \in \mathbb{R}^3$ and $p \in \mathbb{R}$, with the far-field conditions $|\boldsymbol{u}| \to 0$ as $|\boldsymbol{x}| \to 0$.

We cast the Stokes equations in $\mathbb{R}^3$ as

$$\mathcal{L}\boldsymbol{u} = \boldsymbol{F}, \tag{B.2}$$

where $\boldsymbol{u} = (u, v, w, p)$ and the operator is

$$\mathcal{L} = \begin{pmatrix} -\mu\Delta & 0 & 0 & \partial/\partial x \\ 0 & -\mu\Delta & 0 & \partial/\partial y \\ 0 & 0 & -\mu\Delta & \partial/\partial z \\ \partial/\partial x & \partial/\partial y & \partial/\partial z & 0 \end{pmatrix}.$$

To calculate the fundamental solution tensor $\mathcal{G}$ for $\mathcal{L}$ we consider the integral representation of the solution in the whole space

$$\boldsymbol{u}(\boldsymbol{x}) = \int_{\mathbb{R}^3} \mathcal{G}(\boldsymbol{x} - \boldsymbol{y}) \boldsymbol{F}(\boldsymbol{y}) \, \mathrm{d}\boldsymbol{y}. \tag{B.3}$$

The Fourier space representation of Equation (B.2) is

$$\widehat{\mathcal{L}\boldsymbol{u}} = \widehat{\mathcal{L}} \widehat{\boldsymbol{u}} = \widehat{\boldsymbol{F}}$$

where

$$\widehat{\mathcal{L}} = \begin{pmatrix} \mu k^2 & 0 & 0 & -\mathrm{i}k_1 \\ 0 & \mu k^2 & 0 & -\mathrm{i}k_2 \\ 0 & 0 & \mu k^2 & -\mathrm{i}k_3 \\ -\mathrm{i}k_1 & -\mathrm{i}k_2 & -\mathrm{i}k_3 & 0 \end{pmatrix}$$

with $\boldsymbol{k} = (k_1, k_2, k_3)$ and $k^2 = \boldsymbol{k} \cdot \boldsymbol{k}$.

Therefore

$$\begin{aligned} \boldsymbol{u}(\boldsymbol{x}) &= \int_{\mathbb{R}^3} \widehat{\mathcal{L}}^{-1} \widehat{\boldsymbol{F}}(\boldsymbol{k}) \mathrm{e}^{\mathrm{i}\boldsymbol{k}\cdot\boldsymbol{x}} \, \mathrm{d}\boldsymbol{k} \\ &= \frac{1}{2\pi} \int_{\mathbb{R}^3} \int_{\mathbb{R}^3} \widehat{\mathcal{L}}^{-1} \boldsymbol{F}(\boldsymbol{y}) \mathrm{e}^{\mathrm{i}\boldsymbol{k}\cdot(\boldsymbol{x}-\boldsymbol{y})} \, \mathrm{d}\boldsymbol{k} \, \mathrm{d}\boldsymbol{y} \end{aligned}$$

Comparing this to Equation (B.3) we deduce that $\widehat{\mathcal{L}}^{-1}(\boldsymbol{k})$ is related to $\widehat{\mathcal{G}}(\boldsymbol{k})$ as

$$\widehat{\mathcal{G}}(\boldsymbol{k}) = \frac{1}{2\pi} \widehat{\mathcal{L}}^{-1}(\boldsymbol{k}) = \frac{1}{2\pi k^2 \alpha(\boldsymbol{k})} \begin{pmatrix} k_2^2 + k_3^2 & -k_1 k_2 & -k_1 k_3 & \mathrm{i}k_1 \alpha(\boldsymbol{k}) \\ -k_1 k_2 & k_1^2 + k_3^2 & -k_2 k_3 & \mathrm{i}k_2 \alpha(\boldsymbol{k}) \\ -k_1 k_3 & -k_2 k_3 & k_1^2 + k_2^2 & \mathrm{i}k_3 \alpha(\boldsymbol{k}) \\ -\mathrm{i}k_1 \alpha(\boldsymbol{k}) & \mathrm{i}k_2 \alpha(\boldsymbol{k}) & \mathrm{i}k_3 \alpha(\boldsymbol{k}) & \alpha(\boldsymbol{k})^2 \end{pmatrix}$$

where $\alpha(\boldsymbol{k}) = \mu k^2$

Hence using the properties of the Fourier transform, we find that in $\mathbb{R}^3$

$$\mathcal{G} = \begin{pmatrix} -\left(\frac{\partial^2}{\partial y^2}+\frac{\partial^2}{\partial z^2}\right)\mathcal{G}_Q & \frac{\partial^2}{\partial x \partial y}\mathcal{G}_Q & \frac{\partial^2}{\partial x \partial z}\mathcal{G}_Q & -\frac{\partial}{\partial x}\mathcal{G}_\Delta \\ \frac{\partial^2}{\partial x \partial y}\mathcal{G}_Q & -\left(\frac{\partial^2}{\partial x^2}+\frac{\partial^2}{\partial z^2}\right)\mathcal{G}_Q & \frac{\partial^2}{\partial y \partial z}\mathcal{G}_Q & -\frac{\partial}{\partial y}\mathcal{G}_\Delta \\ \frac{\partial^2}{\partial x \partial z}\mathcal{G}_Q & \frac{\partial^2}{\partial y \partial z}\mathcal{G}_Q & -\left(\frac{\partial^2}{\partial x^2}+\frac{\partial^2}{\partial y^2}\right)\mathcal{G}_Q & -\frac{\partial}{\partial z}\mathcal{G}_\Delta \\ -\frac{\partial}{\partial x}\mathcal{G}_\Delta & -\frac{\partial}{\partial y}\mathcal{G}_\Delta & -\frac{\partial}{\partial z}\mathcal{G}_\Delta & -\mu\Delta\mathcal{G}_\Delta \end{pmatrix}$$

$\mathcal{G}_\Delta$ is the fundamental solution for the negative Laplacian and $\mathcal{G}_Q$ is the fundamental solution for the operator $\mathcal{Q} = -\Delta(-\mu\Delta) = \mu\Delta^2$; namely

$$\mathcal{G}_\Delta = -\frac{1}{4\pi|\boldsymbol{x}|}, \qquad \mathcal{G}_Q = -\frac{|\boldsymbol{x}|}{8\pi\mu}. \tag{B.4}$$

Therefore, given our form for $\mathcal{G}$, using the convolution (B.3), together with our form of the force as $\boldsymbol{F} = \boldsymbol{f}\delta(\boldsymbol{x})$, we easily recover the equations for (u_j, p) as such

$$u_j(\boldsymbol{x}) = \frac{f_k}{8\pi\mu}\left(\frac{\delta_{jk}}{|\boldsymbol{x}|}+\frac{x_j x_k}{|\boldsymbol{x}|^3}\right), \tag{B.5}$$

$$p(\boldsymbol{x}) = -\frac{f_k x_k}{4\pi|\boldsymbol{x}|}$$

The *Kronecker delta* is defined as δ_{ij} such that if $i = j$ then $\delta_{ij} = 1$, and if $i \neq j$ then $\delta_{ij} = 0$.

The equation for u_j (Equation B.5) is often written as $u_j = S_{jk}f_k$, where S_{jk} is the fundamental solution of the Stokes Equations, known as the *Stokeslet*

$$S_{jk}(\boldsymbol{x}) = \frac{1}{8\pi\mu}\left(\frac{\delta_{jk}}{|\boldsymbol{x}|}+\frac{x_j x_k}{|\boldsymbol{x}|^3}\right).$$

APPENDIX C

COMPUTATIONAL IMPLEMENTATION AND PSEUDO-CODE

In this appendix, we briefly outline the computational method in the slender-body theory problems in chapters 2-5, the finite difference scheme used in calculating the derivatives for the optimisation routines (chapters 3-5) and in determining the Lyapunov exponents used in Chapter 6

C.1 Slender-body theory code

This section outlines the algorithm used for constructing the solution to the Higdon problem.

Mathematically, we have $3N+6$ unknowns $f_k(s_n)$, U_{0k}, Ω_{0k}, $k=1,2,3$, $n=1,..,N$, and $3N+6$ equations; $3N$ equations from applying the boundary condition at N collocation points on the flagellum (Equation C.1), 3 equations from evaluating the 'force' balance (Equation C.2) and 3 equations from evaluating the moment balance (Equation C.3).

$$\begin{aligned} U_{0j} + \varepsilon_{jkl}\Omega_{0k}x_l + \varepsilon_{jkl}[(-\omega,0,0)]_k x_l \\ = \frac{3}{4}A\left(S_{jk}(\boldsymbol{x},0) - \frac{A^2}{3}D_{jk}(\boldsymbol{x},0)\right)U_{0_k} + \frac{A^3}{|\boldsymbol{x}|^3}\varepsilon_{jkl}x_l\Omega_{0_k} \\ + \sum_{n=1}^{N}\int_{s_n-\delta s_n}^{s_n+\delta s_n}\mathcal{K}_{jk}(\boldsymbol{x},\boldsymbol{X}(s))f_k(s_n)\,\mathrm{d}s. \quad \text{(C.1a)} \end{aligned}$$

with

$$\begin{aligned}&\mathcal{K}_{jk}(\boldsymbol{x}, \boldsymbol{X}(s_n)) \\ &\quad = \frac{1}{8\pi\mu}\left[S_{jk}(\boldsymbol{x}, \boldsymbol{X}(s)) + S^{\star}_{jk}(\boldsymbol{x}, \boldsymbol{X}(s)) - D_{jl}(\boldsymbol{x}, \boldsymbol{X}(s))\frac{a^2}{2}\left(\delta_{lk} - t_l(s_n)t_k(s_n)\right)\right] \quad \text{(C.1b)}\end{aligned}$$

$$\sum_{n=1}^{N}\left\{\left[(1 + C_T(s_n))\delta_{jk} + \left(\frac{X_j(s_n)X_k(s_n)}{|\boldsymbol{X}(s_n)|^2}\right)(C_R(s_n) - C_T(s_n))\right] f_j(s_n) 2\delta s_n\right\} + 6\pi\mu A U_{0_k} = 0 \quad \text{(C.2)}$$

$$\sum_{n=1}^{N}\left\{\varepsilon_{kji}X_j(s_n)f_i(s_n)\left(1 - \frac{A^3}{|\boldsymbol{X}(s_n)|^3}\right)2\delta s_n\right\} + 8\pi\mu A^3\Omega_{0_k} = 0 \quad \text{(C.3)}$$

These $3N + 6$ equations essentially form a matrix system of the form $\mathsf{A}\boldsymbol{x} = \boldsymbol{b}$, the construction of which we shall discuss in some detail.

C.1.1 The kernel $\mathcal{K}_{jk}$

We pay particular attention to the kernel $\mathcal{K}_{jk}$; computationally construction of this is the most time consuming part of the problem. Written crudely there will be many nested `for` loops, however, we can investigate the properties of the Kernel further, and then construct a MATLAB routine which harnesses the matrix handling capabilities of MATLAB.

Considering the last term in Equation (C.1a) (which calculates a velocity, which to avoid ambiguity we call $\boldsymbol{u}^{\star}$), we see that for each point $\{\boldsymbol{x}_m\}_{1\leqslant m\leqslant N} \in \mathbb{R}^3$, we have

$$u^{\star}_j(\boldsymbol{x}_m) = \sum_{n=1}^{N}\int_{s_n-\delta s_n}^{s_n+\delta s_n}\mathcal{K}_{jk}(\boldsymbol{x}_m, \boldsymbol{X}(s))f_k(s_n)\,\mathrm{d}s = \sum_{k=1}^{3}\left(\sum_{n=1}^{N}\int_{s_n-\delta s_n}^{s_n+\delta s_n}\mathcal{K}_{jk}(\boldsymbol{x}_m, \boldsymbol{X}(s))\,\mathrm{d}s\right)f_k(s_n). \quad \text{(C.4)}$$

This is equivalent to the block system

$$\begin{pmatrix} \boldsymbol{u}_1^\star \\ \boldsymbol{u}_2^\star \\ \boldsymbol{u}_3^\star \end{pmatrix} = \begin{pmatrix} K_{11} & K_{12} & K_{13} \\ K_{21} & K_{22} & K_{23} \\ K_{31} & K_{32} & K_{33} \end{pmatrix} \begin{pmatrix} \boldsymbol{f}_1 \\ \boldsymbol{f}_2 \\ \boldsymbol{f}_3 \end{pmatrix}, \tag{C.5}$$

where $\boldsymbol{u}_j^\star, \boldsymbol{f}_k \in \mathbb{R}^N$ and $K_{ij} \in \mathbb{R}^{N\times N}$, and $(\boldsymbol{f}_k)_n = f_k(s_n)$ and

$$(K_{jk})_{mn} = \int_{s_n-\delta s_n}^{s_n+\delta s_n} \mathcal{K}_{jk}(\boldsymbol{x}_m, \boldsymbol{X}(s))\,\mathrm{d}s \tag{C.6}$$

$$= \delta s_n \int_{-1}^{1} \mathcal{K}_{jk}(\boldsymbol{x}_m, \boldsymbol{X}(s + t\delta s_n))\,\mathrm{d}t \tag{C.7}$$

$$= \delta s_n \sum_{l=1}^{n_l} w_l \mathcal{K}_{jk}(\boldsymbol{x}_m, \boldsymbol{X}(s + \xi_l \delta s_n)) \tag{C.8}$$

where (w_l, ξ_l) defines a Gauss-Legendre quadrature rule on $[-1, 1]$ with n_l points.

C.1.2 Assembling the matrix

Section C.1.1 demonstrates how to calculate the coefficients of the force components due to the boundary conditions. The overall structure of the matrix ($\in \mathbb{R}^{(3N+6)\times(3N+6)}$), is as follows

$$\left(\begin{array}{ccc|c} K_{11} & K_{12} & K_{13} & \\ K_{21} & K_{22} & K_{23} & 3N \times 6 \text{ from boundary conditions} \\ K_{31} & K_{32} & K_{33} & \\ \hline \multicolumn{4}{c}{3 \times (3N+6) \text{ rows from } \textit{force} \text{ balance}} \\ \hline \multicolumn{4}{c}{3 \times (3N+6) \text{ rows from } \textit{moment} \text{ balance}} \end{array}\right) \begin{pmatrix} \boldsymbol{f}_1 \\ \boldsymbol{f}_2 \\ \boldsymbol{f}_3 \\ \boldsymbol{U}_0 \\ \boldsymbol{\Omega}_0 \end{pmatrix} = \boldsymbol{b} \tag{C.9}$$

where $\boldsymbol{f}_k \in \mathbb{R}^N$ with $(\boldsymbol{f}_k)_n = f_k(s_n)$ as before, and $\boldsymbol{U}_0, \boldsymbol{\Omega}_0 \in \mathbb{R}^3$.

This resultant system can then be inverted to yield the quantities of interest $f_k(s_n), U_{0j}$ and Ω_{0j}.

C.1.3 Schematic of the MATLAB code

Presented below is an outline of the structure of the MATLAB code used to solve this single sperm swimming problem.

- Setup all global parameters,
- Calculate the weights and node (w_l, ξ_l) for Gauss-Legendre quadrature; typically $n_l = 10$,
- Ensure the arc-length of the flagellum, adjusting any derived quantities as appropriate,
- Calculate the position of the flagellum, to give N midpoints `X`,
- Calculate the arc-length between successive midpoint; the δs_n's,
- Calculate the Tangent and Normal vectors at each midpoint,
- Calculate the N collocation point `XB` by projecting a distance a along the normal vector from each midpoint,
- Construct the Kernel $\mathcal{K}_{jk}$,
- Construct the coefficients of $\boldsymbol{U}_0$ and $\boldsymbol{\Omega}_0$ due to the boundary condition (utilising `for` loops),
- Construct the coefficients of $\boldsymbol{f}_k(s_n)$, $\boldsymbol{U}_0$ and $\boldsymbol{\Omega}_0$ due to the force and moment rows (using `for` loops),
- Solve the system $Ax = b$ as `x=A\b`, to find the desired values,
- Calculate quantities of interest, such as power P, inverse efficiency η^{-1}, average swimming speed $\bar{U}$ and bending moment densities.

C.2 Calculating the Hessian matrix with finite difference

For a particular function f, such as inverse efficiency (being an output of the slender-body theory code), we will not necessarily have an analytic form for the partial derivatives required to construct the Hessian (3.5), and it will be necessary to construct these using numerical methods, in particular finite differences. A standard approach is to use the central difference formulae which are second order accurate. For example, in two dimensions (x, y), with grid spacing $(\Delta x, \Delta y)$ we find the central difference finite difference approximations to the first and second derivatives as follows

$$\left(\frac{\partial f}{\partial x}\right)_{i,j} = \frac{f_{i+1,j} - f_{i-1,j}}{2\Delta x} + \mathrm{O}((\Delta x)^2), \tag{C.10a}$$

$$\left(\frac{\partial^2 f}{\partial x^2}\right)_{i,j} = \frac{f_{i+1,j} - 2f_{i,j} + f_{i-1,j}}{(\Delta x)^2} + \mathrm{O}((\Delta x)^2), \tag{C.10b}$$

$$\left(\frac{\partial^2 f}{\partial x \partial y}\right)_{i,j} = \frac{f_{i+1,j+1} - f_{i+1,j-1} - f_{i-1,j+1} + f_{i-1,j-1}}{4\Delta x \Delta y} + \mathrm{O}((\Delta x)^2) + \mathrm{O}((\Delta y)^2). \tag{C.10c}$$

The calculation of the finite difference derivatives, requires the evaluation of the function in 2-dimensions at $3^2 = 9$ places in a grid as shown in Figure C.1(a); in n-dimensions this figure is 3^n function evaluations. This can often be computationally intensive, so a reduction in the number of function evaluations required would be beneficial.

The formulae given in Equation (C.10) are second-order accurate, however, as we have a choice over the values of Δx and Δy (the grid spacing) we can utilise the first-order accurate forward difference formulae, and by making the grid spacing arbitrarily small maintain similar accuracy. However, this may be a poor trade-off if we inadvertently increase the number of iterations and hence matrix assemblies required, and hence the overall computational time.

Calculating the forward difference second derivative with respect to one variable, requires 3 function evaluations; thus there is no saving to be made adopting forward difference solution for the non-mixed second derivatives. As the calculation of either the forward or central difference first derivatives requires the use of two out of the three points which have to be used in order to calculate the non-mixed second derivative we can make no computational saving here either.

We can however, make a saving by modifying the scheme to calculate the mixed partial derivatives. From Figure C.1(a), we can see that the four points utilised to calculate the second derivative in the central difference scheme are used solely for this purpose. By adopting a forward difference approach, we move to Figure C.1(b), where we need only calculate one additional function value above those used to calculate the non-mixed derivatives. The particular form of the mixed partial derivative then becomes

$$\left(\frac{\partial^2 f}{\partial x \partial y}\right)_{i,j} = \frac{f_{i+1,j+1} - f_{i+1,j} - f_{i,j+1} + f_{i,j}}{\Delta x \Delta y} + \mathrm{O}(\Delta x) + \mathrm{O}(\Delta y). \tag{C.11}$$

This modification results in three fewer function evaluations in the two-dimensional case. Thus the total number of points required to evaluate the function and construct the Hessian under this hybrid scheme is now $3^2 - 3 = 6$, or in m-dimensions, $2^m + m$.

Alone this saving in the number of function evaluations appears promising; for example in 3-dimensions, the naive central difference approach requires 27 function evaluations, whereas the hybrid method requires only 11. However, this must come with the caveat that we have made a reduction in accuracy from a second order method to a first order method, and we may have a trade-off in terms of requiring more iterations to converge sufficiently to the correct solution.

C.3 Local Lyapunov Exponents

Recall that the definition of the Local Lyapunov Exponent at a point $\boldsymbol{x}_0$ at time t, is

$$\lambda_{LLE}(\boldsymbol{x}_0, t) = \frac{1}{t} \log\left(\frac{||\delta\boldsymbol{x}(t)||}{||\delta\boldsymbol{x}(0)||}\right). \tag{C.12}$$

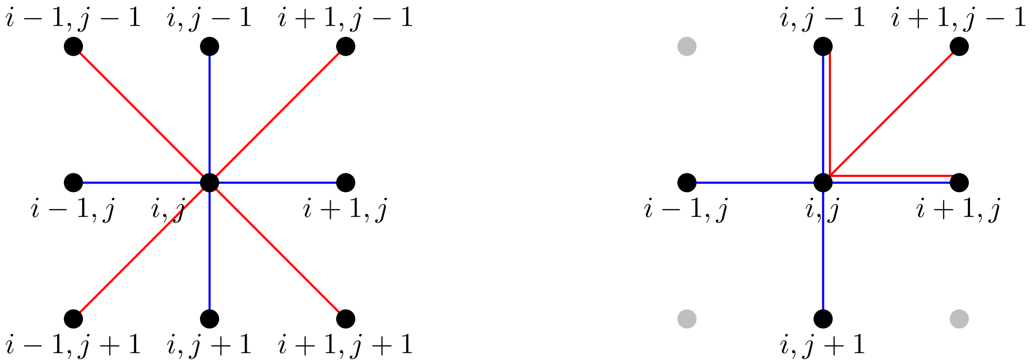

(a) Central difference scheme

(b) Hybrid scheme

Figure C.1: A comparison of the number of points required to calculate the derivatives using (a) central and (b) forward finite difference. The blue line represents the first and second derivatives with respect to the same co-ordinate and are taken as central difference in each case, and the red lines the points required for the calculation of the mixed partial derivatives – the off-diagonal elements of the Hessian.

The algorithm used to construct the Local Lyapunov Exponents is as follows

```
Setup the $x$ and $y$ spatial ranges and the $t$ temporal range; $x$ and $y$ need to form a meshgrid.

for each point $(x, y)$
    Construct the initial separation $\delta\boldsymbol{x}(0)$, eg $(0, -10^{-4})$
    Set $X_1 = (x, y)$ and $X_2 = (x, y) + \delta\boldsymbol{x}(0)$.

    for each time period $[t_i, t_{i+1})$
        Evolve forward the points $X_1$ (to $X_1^\star$) and $X_2$ (to $X_2^\star$) using RK4 routine
        Calculate the distance between $X_1^\star$ and $X_2^\star$, to give $||\delta\boldsymbol{x}(t_{i+1})||$
        Calculate the logarithm of the ratio $||\delta\boldsymbol{x}(t_i)||/||\delta\boldsymbol{x}(0)||$
        Store $\frac{1}{t_{i+1}} \log ||\delta\boldsymbol{x}(t_i)||/||\delta\boldsymbol{x}(0)||$, against original $(x, y)$
```

```
                Set $X_1 = X_1^\star$ and $X_2 = X_2^\star$
            end
        end
```

C.3.1 ODE solvers

In this section we consider two numerical methods for solving the general system of differential equations

$$\frac{\mathrm{d}\boldsymbol{y}}{\mathrm{d}t} = \boldsymbol{f}(t, \boldsymbol{y}), \quad \text{subject to} \quad \boldsymbol{y}(0) = \boldsymbol{y}_0 \tag{C.13}$$

Improved Euler – 'Heun' Scheme

The Heun method is a second order, improved Euler Scheme. The mathematical statement of this method is as follows

$$\boldsymbol{y}_{n+1} = \boldsymbol{y}_n + \frac{h}{2}\left(\boldsymbol{K}_1 + \boldsymbol{K}_2\right) \tag{C.14a}$$

where

$$\boldsymbol{K}_1 = \boldsymbol{f}(t, \boldsymbol{y}_n) \tag{C.14b}$$

$$\boldsymbol{K}_2 = \boldsymbol{f}(t + h, \boldsymbol{y}_n + h\boldsymbol{K}_1) \tag{C.14c}$$

The Heun method is second order accurate. The pseudo-code required to implement this computationally is

```
for each time $t_j$
    Calculate $\boldsymbol{K}_1 = \boldsymbol{f}(t_j, \boldsymbol{y}_n)$
    Calculate $\boldsymbol{K}_2 = \boldsymbol{f}(t_j + h, \boldsymbol{y}_n + h\boldsymbol{K}_1)$
    Calculate $\boldsymbol{y}_{n+1} = \boldsymbol{y}_n + \frac{h}{2}\left(\boldsymbol{K}_1 + \boldsymbol{K}_2\right)$
```

```
end
```

Runge-Kutta Fourth Order Scheme - 'RK4'

The Runge-Kutta fourth order scheme, often abbreviated to RK4, is the most commonly used solver for the form of differential equations given in Equation (C.13). The reason are the high level of accuracy (RK4 is accurate to $\mathrm{O}(h^4)$) combined with the straightforward computation. RK4 is available in MATLAB as the built-in function `ode45`.

The mathematical statement of the RK4 method is as follows

$$\boldsymbol{y}_{n+1} = \boldsymbol{y}_n + \frac{h}{6}\left(\boldsymbol{K}_1 + 2\boldsymbol{K}_2 + 2\boldsymbol{K}_3 + \boldsymbol{K}_4\right) \tag{C.15a}$$

where

$$\boldsymbol{K}_1 = \boldsymbol{f}\left(\boldsymbol{x}_i, t\right) \tag{C.15b}$$

$$\boldsymbol{K}_2 = \boldsymbol{f}\left(\boldsymbol{x}_i + \frac{h}{2}\boldsymbol{K}_1, t + \frac{h}{2}\right) \tag{C.15c}$$

$$\boldsymbol{K}_3 = \boldsymbol{f}\left(\boldsymbol{x}_i + \frac{h}{2}\boldsymbol{K}_2, t + \frac{h}{2}\right) \tag{C.15d}$$

$$\boldsymbol{K}_4 = \boldsymbol{f}\left(\boldsymbol{x}_i + h\boldsymbol{K}_3, t + h\right) \tag{C.15e}$$

The pseudo-code required to implement this computationally is

```
for each time $t_j$
    Calculate $\boldsymbol{K}_1 = \boldsymbol{f}(\boldsymbol{x}_i, t_j)$
    Calculate $\boldsymbol{K}_2 = \boldsymbol{f}\left(\boldsymbol{x}_i + \frac{h}{2}\boldsymbol{K}_1, t_j + \frac{h}{2}\right)$
    Calculate $\boldsymbol{K}_3 = \boldsymbol{f}\left(\boldsymbol{x}_i + \frac{h}{2}\boldsymbol{K}_2, t_j + \frac{h}{2}\right)$
    Calculate $\boldsymbol{K}_4 = \boldsymbol{f}\left(\boldsymbol{x}_i + h\boldsymbol{K}_3, t_j + h\right)$
    Calculate $\boldsymbol{y}_{n+1} = \boldsymbol{y}_n + \frac{h}{6}\left(\boldsymbol{K}_1 + 2\boldsymbol{K}_2 + 2\boldsymbol{K}_3 + \boldsymbol{K}_4\right)$
end
```

APPENDIX D

THE S-TRANSFORM AND SLENDER-BODY THEORY IN STOKES FLOW

This appendix represents a study which has been cowritten with JR Blake and EO Tuck regarding the S-transform, its properties and use in slender-body theory in Stokes flow.

Originally it was planned to use the S-transform to transform integrals to linear equations, however, it was later decided that the numerical approach described earlier is more robust.

Abstract: The Slender-body transform, known in abbreviated form as the S–transform, arises naturally from the asymptotic analysis of very viscous flow around slender bodies. This paper considers some of the properties of the S–transform as well as exploiting the special properties associated with Legendre polynomials to generate a range of slender-body shapes with fixed drag. The viable parameter space for these examples is also presented.

D.1 Introduction

The S–transform arises naturally from the asymptotic analysis of very viscous flow around slender bodies. It is defined as follows

$$\mathcal{S}f(x) = \frac{1}{2}\int_{-1}^{1} \frac{f(x) - f(t)}{|x - t|}\,\mathrm{d}t, \qquad |x| < 1, \tag{D.1}$$

where $f(x)$ is differentiable on $(-1,1)$. Tuck (1964), discovered that for Legendre polynomials $P_n(x)$, it has the elegant relationship

$$\mathcal{S}P_n(x) = \sigma_n P_n(x), \tag{D.2}$$

where $\sigma_0 = 0$ and $\sigma_n = 1 + \frac{1}{2} + \cdots + \frac{1}{n}$, for $n \geqslant 1$; so that the operator $\mathcal{S}$ has eigenvalues σ_n and eigenfunctions P_n. Although this relationship arises from consideration of slender-body theory in two different co-ordinate systems (prolate spheroidal and cylindrical), Tuck proved the relationship independently through the use of recurrence relations and the method of mathematical induction. In the Appendix some further properties of the S–transform are listed for general differentiable functions, polynomials, Legendre and Hermite polynomials.

D.2 Slender-body theory in Stokes flow

Slender-body theory is the study of fluid flow associated with bodies which are characterised by a small slenderness ratio; that is where the width of the body is small in comparison to the length. Examples of slender bodies occurs in biological applications; propulsion of microorganisms by flagella (Higdon, 1979a) or cilia (Blake, 1972), and in industrial applications such as the extrusion of polymers in the petrochemical industry, where slender fibres move near to a free surface.

Stokes flow is fluid flow that is characterised as being viscosity dominated; that is a flow in which the Reynolds number, which is the ratio of inertial to viscous forces, is very small. In this case we take the zero Reynolds number limit of the Navier-Stokes equations and arrive at the Stokes flow equations,

$$\nabla p = \mu \nabla^2 u, \qquad \nabla \cdot \boldsymbol{u} = 0. \tag{D.3}$$

The Stokes flow equations provide a balance between the viscous forces with the pressure gradient.

A general solution for the motion of a slender-body moving in a quiescent fluid can be found in terms of a distribution of Stokeslets and higher order singularities along the axis of symmetry of the body.

D.2.1 Singularities of Stokes flow

The fundamental singularity of Stokes flow is the *Stokeslet* which is the solution of the Stokes flow equations with a point force acting at the point $\boldsymbol{X}$,

$$\nabla p = \mu \nabla^2 \boldsymbol{u} + \boldsymbol{F}\delta(\boldsymbol{x} - \boldsymbol{X}), \quad \nabla \cdot \boldsymbol{u} = 0. \tag{D.4}$$

The solution is of the form

$$u_i(\boldsymbol{x}) = \frac{F_j}{8\pi\mu}\left[\frac{\delta_{ij}}{|\boldsymbol{x} - \boldsymbol{X}|} + \frac{(x_i - X_i)(x_j - X_j)}{|\boldsymbol{x} - \boldsymbol{X}|^3}\right], \tag{D.5a}$$

$$p(\boldsymbol{x}) = \frac{F_j(x_j - X_j)}{4\pi|\boldsymbol{x} - \boldsymbol{X}|^3}. \tag{D.5b}$$

We observe the velocity decays inversely with distance and the induced axial velocity at an equal distance from the point force on the axis is twice that an equivalent radial position above the point force. The unphysical attributes of infinite flux, infinite kinetic energy and non-uniform validity of the solution in the far-field may create problems when in infinite domains.

D.2.2 Flow around a slender-body: zeroth order approximation

Consider a slender-body of length 2ℓ and radius $r_0(x)$ $|x| \leqslant \ell$, so that the major axis of the body is aligned with the x-axis of the cylindrical co-ordinate system. The approximate solution for flow around this body can be written down as an integral along the x-axis of

Stokeslets and potential source-doublets (or dipoles). The solution has the form

$$\begin{aligned} u_i(\boldsymbol{x}) = \frac{1}{8\pi\mu}\int_{-\ell}^{\ell} F_j(\boldsymbol{\xi})\left[\frac{\delta_{ij}}{|\boldsymbol{x}-\boldsymbol{\xi}|} + \frac{(x_i-\xi_i)(x_j-\xi_j)}{|\boldsymbol{x}-\boldsymbol{\xi}|^3}\right] \\ + D_j(\boldsymbol{\xi})\left[-\frac{\delta_{ij}}{|\boldsymbol{x}-\boldsymbol{\xi}|^3} + \frac{3(x_i-\xi_i)(x_j-\xi_j)}{|\boldsymbol{x}-\boldsymbol{\xi}|^5}\right]\mathrm{d}\xi. \quad \text{(D.6)} \end{aligned}$$

The force and dipole strength per unit length are F_j and D_j respectively, and $\boldsymbol{\xi} = (\xi, 0, 0)$ is the 'dummy variable' of integration along the x-axis. Indeed an exact solution exists for a prolate spheroid with a constant Stokeslet distribution and a parabolic source doublet distribution between the two foci (Chwang and Wu, 1975).

We can make some initial progress by supposing that F_j and D_j do not vary along the length of the slender-body, and thus treating them as constant, Equation (D.6) becomes;

$$\begin{aligned} u_i(\boldsymbol{x}) = \frac{F_j(\boldsymbol{x})}{8\pi\mu}\int_{-\ell}^{\ell}\left[\frac{\delta_{ij}}{|\boldsymbol{x}-\boldsymbol{\xi}|} + \frac{(x_i-\xi_i)(x_j-\xi_j)}{|\boldsymbol{x}-\boldsymbol{\xi}|^3}\right]\mathrm{d}\xi \\ + \frac{D_j(\boldsymbol{x})}{8\pi\mu}\int_{-\ell}^{\ell}\left[-\frac{\delta_{ij}}{|\boldsymbol{x}-\boldsymbol{\xi}|^3} + \frac{3(x_i-\xi_i)(x_j-\xi_j)}{|\boldsymbol{x}-\boldsymbol{\xi}|^5}\right]\mathrm{d}\xi. \quad \text{(D.7)} \end{aligned}$$

D.2.3 Longitudinal motion

We shall consider flow around the slender-body in the direction parallel to the x-axis, in particular the resulting velocity will be of the form $\boldsymbol{U} = (U_1, 0, 0)$.

Along the slender-body we shall have that

$$|\boldsymbol{x}-\boldsymbol{\xi}| = \sqrt{(x-\xi)^2 + r_0^2}.$$

This allows us to reduce Equation (D.7) to the following form

$$u_i(\boldsymbol{x}) = \frac{F_j(\boldsymbol{x})}{8\pi\mu}\int_{-\ell}^{\ell}\left[\frac{\delta_{ij}}{\left((x-\xi)^2+r_0^2\right)^{\frac{1}{2}}} + \frac{(x_i-\xi_i)(x_j-\xi_j)}{\left((x-\xi)^2+r_0^2\right)^{\frac{3}{2}}}\right]\mathrm{d}\xi \\ + \frac{D_j(\boldsymbol{x})}{8\pi\mu}\int_{-\ell}^{\ell}\left[-\frac{\delta_{ij}}{\left((x-\xi)^2+r_0^2\right)^{\frac{3}{2}}} + \frac{3(x_i-\xi_i)(x_j-\xi_j)}{\left((x-\xi)^2+r_0^2\right)^{\frac{5}{2}}}\right]\mathrm{d}\xi. \quad \text{(D.8)}$$

We are able to make some progress here by remembering that as we are dealing with slender bodies, that $r_0 \ll \ell$, or more precisely that r_0/ℓ is a small parameter.

By defining

$$I_{ij} = \int_{-\ell}^{\ell}\left[\frac{\delta_{ij}}{\left((x-\xi)^2+r_0^2\right)^{\frac{1}{2}}} + \frac{(x_i-\xi_i)(x_j-\xi_j)}{\left((x-\xi)^2+r_0^2\right)^{\frac{3}{2}}}\right]\mathrm{d}\xi, \quad \text{(D.9a)}$$

$$J_{ij} = \int_{-\ell}^{\ell}\left[-\frac{\delta_{ij}}{\left((x-\xi)^2+r_0^2\right)^{\frac{3}{2}}} + \frac{3(x_i-\xi_i)(x_j-\xi_j)}{\left((x-\xi)^2+r_0^2\right)^{\frac{5}{2}}}\right]\mathrm{d}\xi, \quad \text{(D.9b)}$$

we find the following values for the slender-body approximation for I_{ij}

$$\begin{pmatrix} 2\ln\left(4(\ell^2-x^2)/r_0^2\right)-2 & 0 & 0 \\ 0 & \ln\left(4(\ell^2-x^2)/r_0^2\right)+2\cos^2\theta & \sin 2\theta \\ 0 & \sin 2\theta & \ln\left(4(\ell^2-x^2)/r_0^2\right)+2\sin^2\theta \end{pmatrix}$$

and for J_{ij}

$$\begin{pmatrix} 0 & 0 & 0 \\ 0 & \frac{1}{r_0^2}-\frac{2}{r_0^2}\cos^2\theta & -\frac{\sin 2\theta}{r_0^2} \\ 0 & -\frac{\sin 2\theta}{r_0^2} & \frac{1}{r_0^2}-\frac{2}{r_0^2}\sin^2\theta \end{pmatrix}.$$

For the longitudinal motion we obtain

$$U_1 = \frac{F_1}{8\pi\mu}\left(2\ln\left(\frac{4(\ell^2-x^2)}{r_0^2}\right)-2\right), \quad \text{(D.10)}$$

which can be rearranged to yield the following expression for the force distribution

$$F_1(x) = \frac{4\pi\mu U_1}{\ln\left(\frac{4(\ell^2-x^2)}{r_0^2}\right) - 1} = \frac{4\pi\mu U_1}{2\ln\frac{2\ell}{r_0^\star} - 1 + 2\ln\left(\left(1-\frac{x^2}{\ell^2}\right)^{\frac{1}{2}} \Big/ r_0/r_0^\star\right)}, \tag{D.11a}$$

$$\sim \frac{2\pi\mu U_1}{\ln\frac{2\ell}{r_0^\star} - \frac{1}{2}}, \tag{D.11b}$$

where $2\ell/r_0^\star$ is twice the ratio of the major to minor axis.

A good estimate for the total axial drag is therefore

$$D_1 = \frac{4\pi\mu U_1\ell}{\ln\frac{2\ell}{r_0^\star} - \frac{1}{2}}. \tag{D.12}$$

Indeed we could get closer to an exact solution by considering a prolate spheroid given by $r = r_0^\star\,(1 - x^2/\ell^2)^{\frac{1}{2}}$.

D.2.4 Transverse motion

In the case where the flow is perpendicular to the flow to the major axis of the slender-body, we have a velocity profile of the form $\boldsymbol{U} = (0, U_2, 0)$, and we obtain

$$U_2 = \frac{F_2}{8\pi\mu}\left(\ln\left(\frac{4(\ell^2-x^2)}{r_0^2}\right) + 2\cos^2\theta\right) + \frac{D_2}{8\pi\mu}\left(\frac{1}{r_0^2} - \frac{2\cos^2\theta}{r_0^2}\right). \tag{D.13}$$

If we remove the θ dependence by choosing $D_2(x) = r_0^2 F_2(x)$, then we have

$$U_2 = \frac{F_2}{8\pi\mu}\left(\ln\left(\frac{4(\ell^2-x^2)}{r_0^2}\right) + 1\right), \tag{D.14}$$

which gives the expression for the force as

$$F_2(x) = \frac{8\pi\mu U_2}{\ln\left(\frac{4(\ell^2-x^2)}{r_0^2}\right)+1} = \frac{8\pi\mu U_2}{2\ln\frac{2\ell}{r_0^\star}+1+2\ln\left(\left(1-\frac{x^2}{\ell^2}\right)^{\frac{1}{2}}\Big/\, r_o/r_0^\star\right)}, \tag{D.15a}$$

$$\sim \frac{4\pi\mu U_2}{\ln\frac{2\ell}{r_0^\star}+\frac{1}{2}}. \tag{D.15b}$$

The transverse drag approximation is

$$D_{2,3} = \frac{8\pi\mu U_{2,3}\ell}{\ln\frac{2\ell}{r_0^\star}+\frac{1}{2}}, \tag{D.16}$$

where for convenience we have also include the component for the x_3-direction.

Contrasting equations (D.15a), the force strength for longitudinal motion, and (D.11a), the force strength for transverse motion; we observe, for $r_0/\ell \ll 1$ – the slender-body approximation, we have that F_2 is almost twice F_1. Therefore a slender-body falling under the action of gravity, in a viscous fluid, falls nearly twice as quickly longitudinally than transversely. As noted earlier, this is a direct consequence of the tensorial nature of the Stokeslet and the resulting induced velocities in the axial and equi-distant radial position.

D.3 Higher order approximation for axial motion: streamfunction

There are advantages in using the streamfunction formulation for considering axial motion in Stokes flow. We write the streamfunction for a slender-body in a constant stream U as follows (Tuck, 1968),

$$\psi(x,r) = \frac{1}{2}Ur^2 - \frac{1}{2}r^2\int_{-\ell}^{\ell}\frac{F_1(\xi)\,\mathrm{d}\xi}{[(x-\xi)^2+r^2]^{\frac{1}{2}}} - \frac{1}{2}\int_{-\ell}^{\ell}\frac{(x-\xi)D_1'(\xi)\,\mathrm{d}\xi}{[(x-\xi)^2+r^2]^{\frac{1}{2}}}. \tag{D.17}$$

For convenience we have chosen to integrate the source-doublet term by term to yield a source distribution, hence the derivative $D_1'(\xi)$ in the second integral of (D.17). Thus (D.17) consists of terms representing the free stream, a Stokeslet distribution and a source distribution. The boundary conditions on the slender-body are the no-slip condition

$$\frac{1}{r}\frac{\partial \psi}{\partial r} = \frac{1}{r}\frac{\partial \psi}{\partial x} = 0 \quad \text{on} \quad r = r_0(x). \tag{D.18}$$

The second condition can be replaced with $\psi = 0$ without loss of generality.

Applying the boundary conditions leads to

$$0 = \frac{1}{2}Ur_0^2 - \frac{1}{2}r_0^2 \int_{-\ell}^{\ell} \frac{F_1(\xi)\,\mathrm{d}\xi}{[(x-\xi)^2 + r_0^2]^{\frac{1}{2}}} - \frac{1}{2}\int_{-\ell}^{\ell} \frac{(x-\xi)D_1'(\xi)\,\mathrm{d}(\xi)}{[(x-\xi)^2 + r_0^2]^{\frac{1}{2}}}, \tag{D.19a}$$

$$0 = U + \int_{-\ell}^{\ell} \frac{F_1(\xi)\left[(x-\xi)^2 + \frac{1}{2}r_0^2\right]\,\mathrm{d}\xi}{[(x-\xi)^2 + r_0^2]^{\frac{3}{2}}} + \frac{1}{2}\int_{-\ell}^{\ell} \frac{(x-\xi)D_1'(\xi)\,\mathrm{d}(\xi)}{[(x-\xi)^2 + r_0^2]^{\frac{3}{2}}}. \tag{D.19b}$$

We impose the conditions

$$F_1(\pm\ell) = 0 \quad \text{and} \quad D_1'(\pm\ell) = 0. \tag{D.20}$$

The detailed asymptotic analysis of Tuck (1964, 1968), leads to the following expression for the streamfunction,

$$\psi(x,r) = \frac{1}{2}Ur^2 + D_1(x) + \left(F_1(x) + \frac{1}{2}D_1''\right)r^2\log r + \left[b_2 + \frac{b_1'}{2} - \frac{D_1''}{4}\right]r^2 + E, \tag{D.21a}$$

where

$$b_1 = -D_1'(x)\log 2(\ell^2 - x^2)^{\frac{1}{2}} + \frac{1}{2}\int_{-\ell}^{\ell} \frac{D_1'(x) - D_1'(\xi)}{|x-\xi|}\,\mathrm{d}\xi, \tag{D.21b}$$

$$b_2 = -F_1(x)\log 2(\ell^2 - x^2)^{\frac{1}{2}} + \frac{1}{2}\int_{-\ell}^{\ell} \frac{F_1(x) - F_1(\xi)}{|x-\xi|}\,\mathrm{d}\xi. \tag{D.21c}$$

and E is $\mathrm{o}(r^2\log r)$.

The importance of the integral terms in (D.21b) and (D.21c) is associated with the 'non-local' effects due to the change of source and stokeslet strength along the axis, especially near the ends $x = \pm\ell$. Tuck (2004), in a review paper, discusses the importance of 'non-local' factors in a range of applications from classical potential slender-body theory through to compressible, viscous and elastic problems.

Other studies have concentrated on particular aspects of slender-body theory, both analytical and computational developments. For example, Johnson (1980) investigated the asymptotic and end effects, Lighthill (1996) and Gueron and Liron (1992, 1993) developed techniques for de-singularising the integral equations while Higdon (1979a), Liron and Mochon (1976) and Smith et al. (2007c) adapted the theory to facilitate more accurate calculations.

On applying the boundary condition $\psi = 0$, it is immediately clear that $D_1 = \mathrm{O}(r_0^2)$. The second boundary condition yields

$$0 = U + 2F_1 \log r_0 + F_1 + 2b_2. \tag{D.22}$$

This may be written as an inverse problem, where the radius of the slender-body is a function of the force distribution $F_1(x)$. Thus,

$$r_0(x) = 2\sqrt{\ell^2 - x^2}\exp\left(-\left[F_1 + \int_{-\ell}^{\ell} \frac{F_1(x) - F_1(\xi)}{|x - \xi|}\,\mathrm{d}\xi + U\right]\Big/ 2F_1\right), \tag{D.23}$$

with a drag given by

$$D = 4\pi\mu \int_{-\ell}^{\ell} F_1(x)\,\mathrm{d}\xi. \tag{D.24}$$

If we non-dimensionalise with respect to ℓ and U, we obtain the following form for the dimensionless slender-body radius $R(x)$ ($|x| \leqslant 1$), given by,

$$R(x) = 2\sqrt{1 - x^2}\exp\left(-\frac{A + 2\mathcal{S}A + 1}{2A}\right), \tag{D.25}$$

in terms of the dimensionless force A, noting the drag D is given by,

$$D = 4\pi\mu U\ell \int_{-1}^{1} A(\xi)\,\mathrm{d}\xi. \tag{D.26}$$

D.4 The inverse problem: slender-body shapes

With the argument for the radius containing the S–transform, it is of interest to represent the force distribution as a finite sum of Legendre polynomials. Thus we represents $A(x)$ by

$$A(x) = \sum_{n=0}^{N} A_n P_n(x), \tag{D.27}$$

yielding

$$R(x) = 2\sqrt{1-x^2}\exp\left(-\frac{\sum_{n=0}^{N} C_n Pn(x)}{\sum_{n=0}^{N} A_n P_n(x)}\right), \tag{D.28}$$

where $C_0 = \frac{1}{2} + \frac{1}{2}A_0$ and $C_n = (\sigma_n + \frac{1}{2})A_n$ for $n \geqslant 1$.

The drag is given by the first term as follows,

$$D = 8\pi\mu U\ell A_0. \tag{D.29}$$

We consider three special cases – (i) the prolate spheroid, $A_0 \neq 0$, $A_n = 0$ $n \geqslant 1$, (ii) A_0, A_1, $A_2 \neq 0$, all other $A_n = 0$ and (iii) A_0, A_2, $A_4 \neq 0$, all other $A_n = 0$. While these choices represent only a small subset of possible slender-body shapes with the same drag, they do reveal a range of different body shapes with varying volumes.

(i) Prolate Spheroid ($A_0 \neq 0$, $A_n = 0$ for $n \geqslant 1$)

The drag is given by Equation (D.29) and the radius by

$$R(x) = 2\sqrt{1-x^2}\exp\left[-\frac{A_0+1}{2A_0}\right]. \tag{D.30}$$

The slenderness ratio ε is defined by,

$$\varepsilon = \max_{|x|\leqslant 1} R(x) = 2\exp\left[-\frac{A_0+1}{2A_0}\right], \tag{D.31}$$

which yields a drag

$$D = \frac{4\pi\mu U\ell}{\log\frac{2}{\varepsilon} - \frac{1}{2}}, \tag{D.32}$$

which provides the same result as the earlier zeroth order solution. Payne and Pell (1960) give the exact solution as,

$$D = \frac{8\pi\mu U\ell}{(1+\zeta^2)\coth^{-1}\zeta - \zeta}, \tag{D.33}$$

where $\ell\zeta$ and $\ell(\zeta^2-1)^{\frac{1}{2}}$ are the semi-axes of the meridional ellipse, thus yielding $\varepsilon = \sqrt{\zeta^2-1}/\zeta$, and thence leading to the formula,

$$D = \frac{8\pi\mu U\ell(1-\varepsilon^2)}{(2-\varepsilon^2)\coth^{-1}(1-\varepsilon)^{-\frac{1}{2}} - (1-\varepsilon^2)}. \tag{D.34}$$

For small ε this leads to the leading order term given by Equation (D.32). Although outside the range of discussion for a slender-body $\varepsilon = 0.52$ yields a spheroid with drag 5% less than that of a sphere of the same volume.

(ii) Slender-body with A_0, A_1, $A_2 \neq 0$, all other $A_n = 0$.

In this case the radius of the slender-body is given by

$$R(x) = 2\sqrt{1-x^2}\exp\left(-\frac{C_0P_0 + C_1P_1 + C_2P_2}{A_0P_0 + A_1P_1 + A_2P_2}\right), \tag{D.35}$$

where $C_0 = \frac{1}{2} + \frac{1}{2}A_0$, $C_1 = \frac{3}{2}A_1$, $C_2 = 2A_2$.

We require $A_0 + A_1P_1 + A_2P_2 > 0$ for $|x| < 1$, but since $A_0 > 0$, this reduces to the parameter space (a, b) given by,

$$1 + aP_1 + bP_2 > 0 \qquad |x| < 1.$$

Minima can occur at four point 0, ± 1 and $-\frac{a}{3b}$. This immediately defines the (a, b) parameter space by

$$\begin{aligned} &\text{(i)} && 1 + a + b > 0, \\ &\text{(ii)} && 1 - a + b > 0, \\ &\text{(iii)} && \frac{1}{3b}(a^2 + 3(b-1)^2 - 3) < 0. \end{aligned}$$

The parameter space is depicted in Figure D.1.

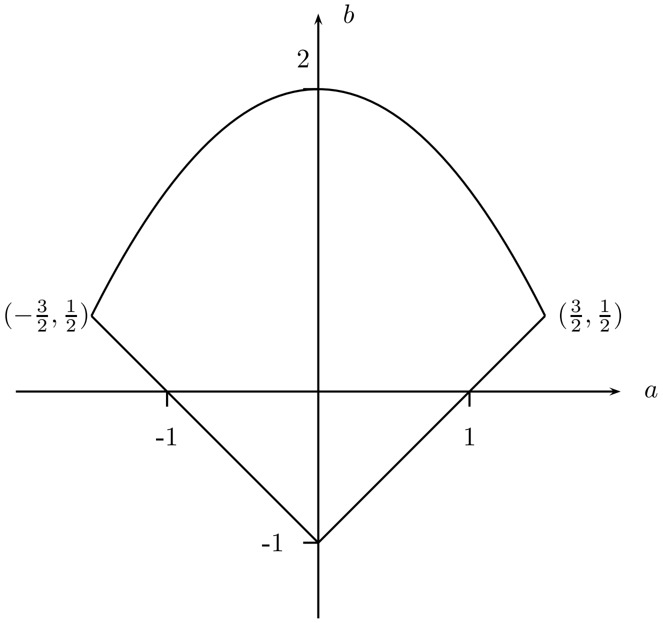

Figure D.1: The viable parameter space for case (ii).

Examples of slender-body shapes for $(\pm 1.5, 0.5)$, $(1, 0)$ and $(0, 0)$ are illustrated in Figure D.2. It is noted that (a, b) and $(-a, b)$ yield the same shape but orientated in the opposite direction, expected on reversibility grounds. The volume calculations are also revealing, as they have the same drag to this order. If we choose $A_0 = 0.2$ and take the spheroid as a basis for comparison we obtain the volume ratios given in Table D.1.

$(A_1/A_0, A_2/A_0)$	Volume ratio
$(0,0)$ – spheroid	1.00
$(1,0)$	1.29
$(-1,0)$	1.29
$(1.5,0.5)$	1.38
$(-1.5,0.5)$	1.38
$(0.7,0.3)$	1.02
$(-0.7,0.3)$	1.02

Table D.1: Volume ratios for case (ii) with $A_0 = 0.2$ and the spheroid is taken to have volume 1 for comparison.

(iii) Slender-body with A_0, A_2, $A_4 \neq 0$, all other $A_n = 0$

In this case we obtain the following expression for the radius $R(x)$,

$$R(x) = 2\sqrt{1-x^2}\exp\left(-\frac{C_0P_0 + C_2P_2 + C_4P_4}{A_0P_0 + A_2P_2 + A_4P_4}\right), \tag{D.36}$$

where $C_0 = \frac{1}{2} + \frac{1}{2}A_0$, $C_2 = 2A_2$, $C_4 = 2\frac{7}{12}A_4$.

In this case the parameter space for $a = A_2/A_0$ and $b = A_4/A_0$ requires

$$1 + aP_2 + bP_4 > 0 \qquad |x| \leqslant 1.$$

It has minima at $\left(0, \pm 1, \pm\sqrt{\frac{15b-6a}{35b}}\right)$, yielding the following constraints

$$\begin{aligned} &\text{(i)} && 1 + a + b > 0, \\ &\text{(ii)} && 1 - \frac{1}{2}a + \frac{3}{8}b > 0, \\ &\text{(iii)} && \frac{1}{b}(280b + 40ab - 36a^3 - 120b^2) > 0. \end{aligned}$$

The parameter space for (a, b) is shown in Figure D.3

As for the previous example a range of shapes are obtained covering ‘dumb-bell’ shapes through to a highly cusped shape, interestingly with the largest volume ratio compared to the spheroid. Examples are shown in Figure D.4. Some volumes are presented in Table D.2

Body	$(A_2/A_0, A_4/A_0)$	Volume
Spheroid	$(0, 0)$	1.00
Near–cylinder	$(\frac{5}{7}, 1)$	0.72
Pinched cylinder	$(\frac{5}{7}, \frac{12}{7})$	0.71
Dumb–bell	$(\frac{20}{7}, \frac{8}{7})$	0.54
Max. Volume	$(-\frac{10}{7}, \frac{3}{7})$	1.53

Table D.2: Volume ratios for case (iii) with the spheroid taken to have volume 1 for comparison.

The maximum volume case has some interesting implications, possibly in a biological context when organisms are seeking to maximise cellular volume for a fixed drag. It would also be interesting to see if considering a larger parameter space of A_n would lead to further improvement.

D.5 Conclusion

In this paper we have presented a range of results for the S–transform when applied to polynomial functions including the Legendre and Hermite special functions. In the case of Legendre functions, they are the eigenfunction of

$$\mathcal{S}f(x) = \lambda f(x),$$

where $\lambda = \sigma_n = 1 + \frac{1}{2} + \cdots + \frac{1}{n}$.

The S–transform is exploited to generate a range of special slender-body shapes with fixed drag which may prove useful in a range of biological and engineering problems.

D.6 Appendix: Further properties of the S–transform

The S–transform is again defined as follows

$$\mathcal{S}f(x) = \frac{1}{2}\int_{-1}^{1} \frac{f(x) - f(t)}{|x - t|}\,\mathrm{d}t, \qquad |x| < 1, \tag{D.37}$$

where $f(x)$ is differentiable on $(-1, 1)$. From the definition of $\mathcal{S}f(x)$ it is clearly linear, i.e.,

$$\mathcal{S}(af(x) + bg(x)) = a\mathcal{S}f(x) + b\mathcal{S}g(x), \tag{D.38}$$

where a and b are constants. It is also clear that the integrand is discontinuous at $t = x$,

$$\lim_{t\to x^-} \frac{f(x) - f(t)}{|x - t|} = f'(x), \tag{D.39a}$$

$$\lim_{t\to x^+} \frac{f(x) - f(t)}{|x - t|} = -f'(x), \tag{D.39b}$$

provided that $f'(x) \neq 0$. The integral may also be written in terms of the sgn function

$$\mathcal{S}f(x) = \frac{1}{2}\int_{-1}^{1} \operatorname{sgn}(x - t)\frac{f(x) - f(t)}{x - t}\,\mathrm{d}t, \tag{D.40a}$$

or by splitting the integrals

$$\mathcal{S}f(x) = \frac{1}{2}\int_{-1}^{x} \frac{f(x) - f(t)}{x - t}\,\mathrm{d}t - \frac{1}{2}\int_{x}^{1} \frac{f(x) - f(t)}{x - t}\,\mathrm{d}t. \tag{D.40b}$$

The linearity of the S–transform enables the common recurrence relations for special functions to be immediately written down. For example, the recurrence relations and properties for Legendre polynomials $P_n(x)$,

$$(n+1)P_{n+1}(x) + nP_{n-1}(x) = (2n+1)xP_n(x), \qquad P_n(1) = 1,$$
$$(2n+1)P_n(x) = P'_{n+1}(x) - P'_{n-1}(x), \qquad P_n(-1) = (-1)^n, \tag{D.41a}$$

yield

$$(n+1)\mathcal{S}P_{n+1}(x) + n\mathcal{S}P_{n-1}(x) = (2n+1)x\mathcal{S}P_n(x) + P_{n+1}(x) - P_{n-1}(x). \tag{D.41b}$$

Whereas for Hermite polynomials, the recurrence relations

$$H_n(x) = 2xH_{n-1}(x) - 2nH_{n-2}(x), \quad 2nH_{n-1}(x) = H'_n(x), \tag{D.42a}$$

yield

$$\mathcal{S}H_n(x) + 2n\mathcal{S}H_{n-2}(x) = 2x\mathcal{S}H_{n-1}(x) + \frac{1}{2n}\left(2H_n(x) - H_n(1) - H_n(-1)\right). \tag{D.42b}$$

It is noted that both these recurrence relations (D.41b) and (D.42b) are non-homogenous

It has already been shown by Tuck (1964) that the relation

$$\mathcal{S}P_n(x) = \sigma_n P_n(x), \tag{D.43}$$

where $\sigma_n = 1 + \frac{1}{2} + \cdots + \frac{1}{n}$ holds. In proving this relationship by induction the relation for $\mathcal{S}x^n$ was required for $n = 1$ and 2. More generally, the relationship is given by,

$$\mathcal{S}x^n = \sigma_n x^n - \frac{1}{2}\sum_{m=1}^{n}\left(1 + (-1)^m\right)\frac{x^{n-m}}{m}. \tag{D.44}$$

It may also be shown that the inner product is symmetric, i.e.,

$$\int_{-1}^{1} G(x)\mathcal{S}F(x)\,\mathrm{d}x = \int_{-1}^{1} F(x)\mathcal{S}G(x)\,\mathrm{d}x, \tag{D.45}$$

where both $F(x)$ and $G(x)$ are continuously differentiable on $(-1, 1)$. The position of the inverse operators may need further analysis. We note that if

$$\mathcal{S}^{-1}\mathcal{S}A(x) = A(x), \tag{D.46}$$

and we let

$$\mathcal{S}A(x) = B(x) = \sum_{n=0}^{\infty} B_n P_n(x), \tag{D.47}$$

then

$$A(x) = A_0 + \sum_{n=1}^{\infty} \frac{B_n}{\sigma_n} P_n(x), \tag{D.48}$$

where A_0 remains arbitrary.

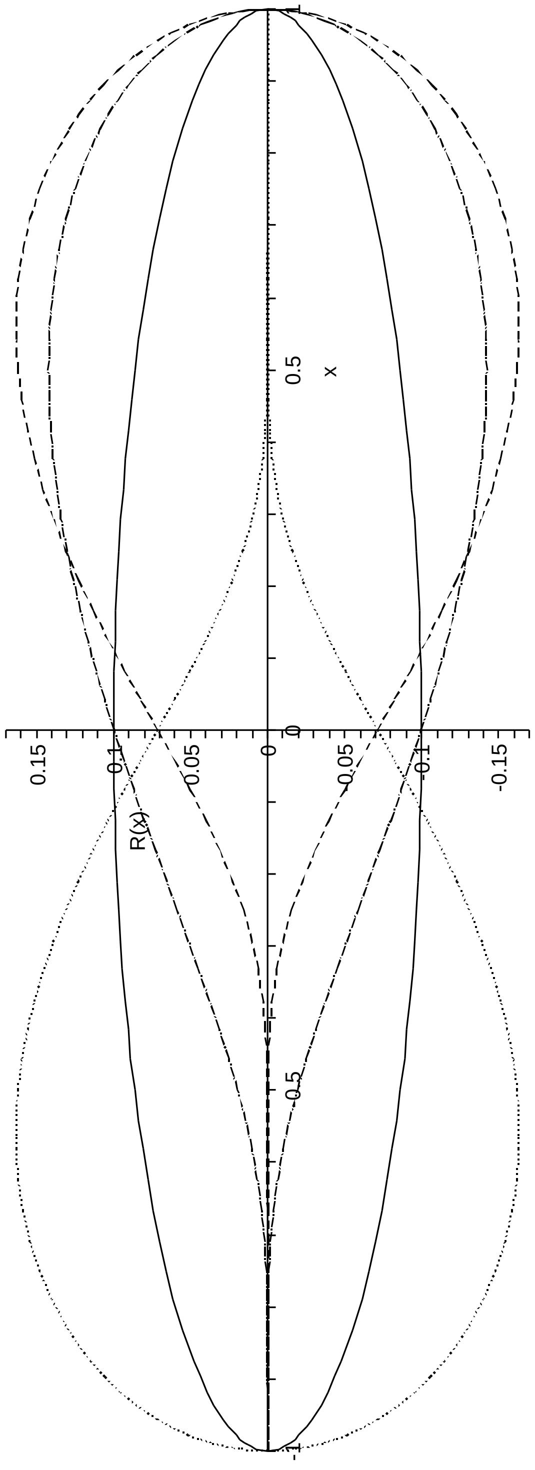

Figure D.2: Plots of $R(x)$ for a variety of slender bodies with A_0, A_1, $A_2 \neq 0$ and all other $A_n = 0$. For all cases $A_0 = 0.2$ and

Solid line	-	$A_1/A_0 = 0$	$A_2/A_0 = 0$;
Dotted line	-	$A_1/A_0 = 1$,	$A_2/A_0 = 0$;
Dashed line	-	$A_1/A_0 = 1.5$,	$A_2/A_0 = 0.5$;
Dot-Dashed line	-	$A_1/A_0 = -1.5$,	$A_2/A_0 = 0.5$.

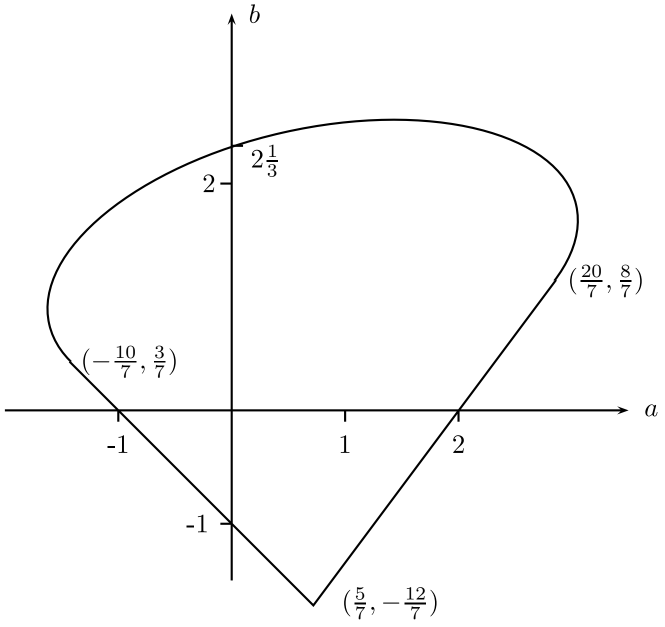

Figure D.3: The viable parameter space for case (iii).

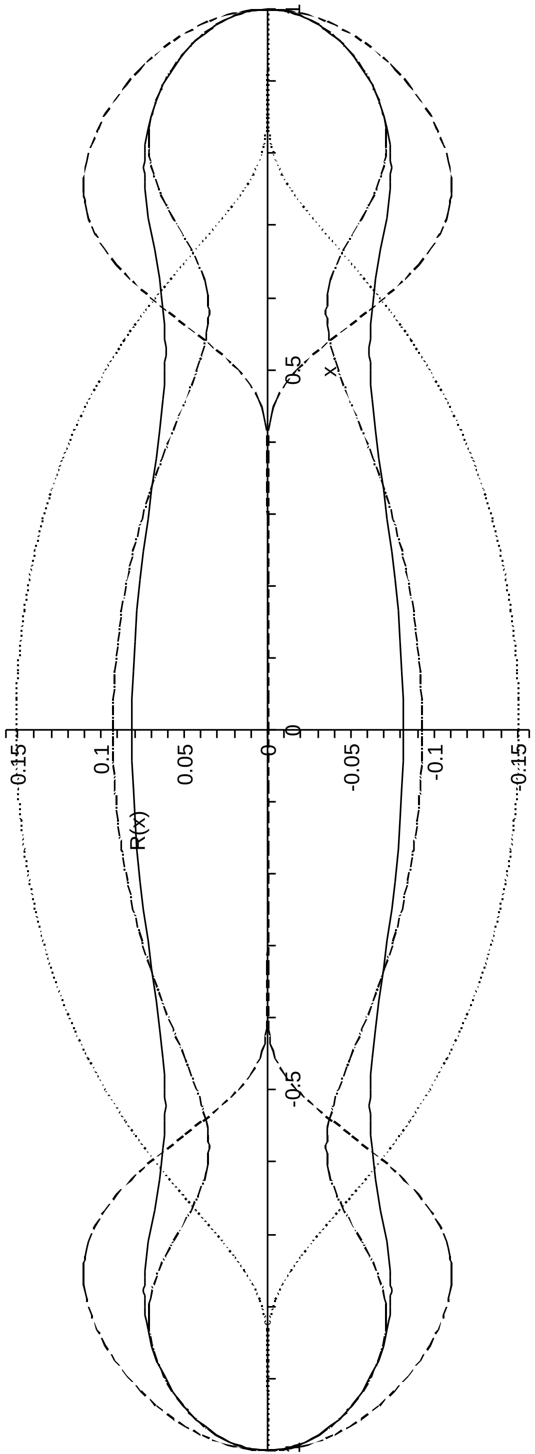

Figure D.4: Plots of $R(x)$ for a variety of slender bodies with A_0, A_2, $A_4 \neq 0$ and all other $A_n = 0$. For all cases $A_0 = 0.2$ and

Solid line - $A_2/A_0 = 5/7$, $A_4/A_0 = 1$;
Dotted line - $A_2/A_0 = 5/7$, $A_4/A_0 = 12/7$;
Dashed line - $A_2/A_0 = 20/7$, $A_4/A_0 = 8/7$;
Dot-Dashed line - $A_2/A_0 = -10/7$, $A_4/A_0 = 3/7$.

LIST OF REFERENCES

S Anand and SK Guhal. Mechanics of transport of the ovum in the oviduct. *Medical and Biological Engineering and Computing*, 16:256–261, 1978.

A Bahat and M Eisenbach. Sperm thermotaxis. *Molecular and Cellular Endocrinology*, 252:115–119, 2006.

J Baltz, DF Katz, and R Cone. The mechanics of sperm egg interaction at the zona pellucida. *Biophysics Journal*, 54:643–654, 1988.

GK Batchelor. *An Introduction to Fluid Dynamics.* Cambridge Mathematical Library. Cambridge University Press, 1967.

GK Batchelor. Slender-body theory for particles of arbitrary cross-section in Stokes flow. *Journal of Fluid Mechanics*, 44:419–440, 1970.

GS Beavers and DD Joseph. Boundary conditions at a naturally permeable wall. *Journal of Fluid Mechanics*, 30:197–207, 1967.

JR Blake. Infinite model for ciliary propulsion. *Journal of Fluid Mechanics*, 49:209–222, 1971.

JR Blake. A model for the micro-structure in ciliated organisms. *Journal of Fluid Mechanics*, 55:1–23, 1972.

JR Blake and AT Chwang. Fundamental singularities of viscous flow. *Journal of Engineering Mathematics*, 8:23–29, 1974.

JR Blake and MA Sleigh. Mechanics of ciliary locomotion. *Biological Review*, 49:85–125, 1974.

JR Blake, PG Vann, and H Winet. A model for ovum transport. *Journal of Theoretical Biology*, 102:145–166, 1982.

G Böhme and R Friedrich. Peristaltic flow of viscoelastic liquids. *Journal of Fluid Mechanics*, 128:109–122, 1983.

JG Brasseur, S Corrsin, and NQ Lu. The influence of a peripheral layer of different viscosity on peristaltic pumping with Newtonian fluids. *Journal of Fluid Mechanics*, 174:495–519, 1987.

CJ Brokaw. Bending moments in free-swimming flagella. *Journal of Experimental Biology*, 53:445–464, 1970.

CJ Brokaw. Bend propogration by a sliding filament model for flagella. *Journal of Experimental Biology*, 55:289–304, 1971.

CJ Brokaw. Simulating the effects of fluid viscosity on the behaviour of sperm flagella. *Mathematical Methods in the Applied Sciences*, 24:1351–1366, 2001.

CJ Brokaw. Computer simulation of flagellar movement VIII: Coordination of dynein by local curvature control can generate helical bending waves. *Cell Motility and the Cytoskeleton*, 53:103–124, 2002.

JC Burns and T Parkes. Peristaltic motion. *Journal of Fluid Mechanics*, 29:731–743, 1967.

F Ceric, D Silva, and P Vigil. Ultrastructure of the human periovulatory cervical mucus. *Journal of Electron Microscopy*, 54:479–484, 2005.

Z Chen, R Hauser, AM Trbovich, JL Shifren, DJ Dorer, L Godfrey-Bailey, and NP Singh. The relationship between human semen characteristics and sperm apoptosis: a pilot study. *Journal of Andrology*, 27:112–120, 2006.

AT Chwang and TY Wu. A note on the helical movement of micro-organisms. *Proceedings of the Royal Society B*, 178:327–346, 1971.

AT Chwang and TY Wu. Hydrodynamics of low-Reynolds-number flow. Part 2: Singularity method for Stokes flow. *Journal of Fluid Mechanics*, 67:787–815, 1975.

J Cohen and DJ Werrett. Antibodies and sperm survival in the female tract of the mouse and rabbit. *Journal of Reproduction and Fertility*, 42:301–310, 1975.

A Cohen-Dayag, I Tur-Kaspa, J Dor, S Mashiach, and M Eisenbach. Sperm capacitation in humans is transient and correlates with chemotactic responsiveness to follicular factors. *Proceedings of the National Academy of Sciences*, 92:11039–11043, 1995.

RG Cox. The motion of long slender bodies in a viscous fluid. Part 1: General theory. *Journal of Fluid Mechanics*, 44:791–810, 1970.

RG Cox. The motion of long slender bodies in a viscous fluid. Part 2: Shear flow. *Journal of Fluid Mechanics*, 45:625–657, 1971.

M Debuse. *Endocrine and reproductive systems.* Mosby, 1998.

RH Dillion, LJ Fauci, and X Yang. Sperm motility and multiciliary beating: An integrative mechanical model. *Computers and Mathematics with Applications*, 52:749–758, 2006.

RH Dillon, L Fauci, C Omoto, and X Yang. Fluid dynamic models of flagellar and ciliary beating. *Annals of the New York Academy of Sciences*, 1101:494–505, 2007.

WR DiLuzio, L Turner, M Mayer, P Garstecki, DB Weibel, HC Berg, and GM Whitesides. *Escherichia coli* swim on the right-hand side. *Nature*, 435:1271–1274, 2005.

RD Dresdner and DF Katz. Relationships of mammalian sperm motility and morphology to hydrodynamic aspects of cell function. *Biology of Reproduction*, 25:920–930, 1981.

RD Dresdner, DF Katz, and SA Berger. The propulsion by large amplitude waves of uniflagellar micro-organisms of finite length. *Journal of Fluid Mechanics*, 97:591–621, 1980.

EZ Drobnis, Al Yudin, GN Cherr, and DE Katz. Hamster sperm penetration of the zona pellucida: kinematic analysis and mechanical implications. *Developmental Biology*, 130: 311–323, 1988.

B Eckhardt and D Yao. Local Lyapunov exponents in chaotic system. *Physica D*, 65: 100–108, 1993.

M Eisenbach. Sperm chemotaxis. *Reviews of Reproduction*, 4:56–66, 1999.

M Eisenbach. *Chemotaxis*. Imperial College Press and World Scientific, 2004.

O Eytan and D Elad. Analysis of intra-uterine fluid motion induced by uterine contractions. *Bulletin of Mathematical Biology*, 61:221–238, 1999.

O Eytan, AJ Jaffa, J Har-Toov, E Dalach, and D Elad. Dynamics of the intrauterine fluid-wall interface. *Annals of Biomedical Engineering*, 27:372–379, 1999.

O Eytan, F Azem, I Gull, I Wolman, D Elad, and AJ Jaffa. The mechanism of hydrosalpinx in embryo implantation. *Human Reproduction*, 16:2662–2667, 2001a.

O Eytan, I Halevi, J Har-Toov, I Wolman, D Elad, and AJ Jaffa. Characteristics of uterine peristalsis in spontaneous and induced cycles. *Fertility and Sterility*, 76:337–341, 2001b.

O Eytan, AJ Jaffa, and D Elad. Peristaltic flow in a tapered channel: application to embryo transport within the uterine cavity. *Medical Engineering & Physics*, 27:473–482, 2001c.

L Fauci and A McDonald. Sperm motility in the presence of boundaries. *Bulletin of Mathematical Biology*, 57:679–699, 1995.

LJ Fauci and R Dillon. Biofluidmechanics of reproduction. *Annual Review of Fluid Mechanics*, 38:371–394, 2006.

DW Fawcett. The structure of the mammalian spermatozoon. *International Review of Cytology*, 7:195–234, 1958.

GR Fulford, DF Katz, and RL Powell. Swimming of spermatozoa in a linear viscoelastic fluid. *Biorheology*, 35:295–309, 1998.

TC Fung and CS Yih. Peristaltic transport. *Journal of Applied Mechanics*, 35:669, 1968.

J Gray and GJ Hancock. The propulsion of sea-urchin spermatozoa. *Journal of Experimental Biology*, 32:802–814, 1955.

S Gueron and K Levit-Gurevich. The three dimensional motion of slender filaments. *Mathematical Methods in the Applied Sciences*, 24:1577–1603, 2001.

S Gueron and N Liron. Ciliary motion modeling, and dynamics multicilia interactions. *Biophysical Journal*, 63:1045–1058, 1992.

S Gueron and N Liron. Simulations of three-dimensional ciliary beats and cilia interactions. *Biophysical Journal*, 65:499–507, 1993.

GJ Hancock. The self-propulsion of microscopic organisms through liquids. *Proceedings of the Royal Society A*, 217:96–121, 1953.

M Hanin. The flow through a channel due to transversely oscillating walls. *Israel Journal of Technology*, 6:67–71, 1968.

HFEA. The HFEA guide to infertility 2007/08, 2007. URL `http://www.hfea.gov.uk`.

JJL Higdon. A hydrodynamic analysis of flagellar propulsion. *Journal of Fluid Mechanics*, 90:685–771, 1979a.

JJL Higdon. The generation of feeding currents by flagellar motions. *Journal of Fluid Mechanics*, 94:305–330, 1979b.

JJL Higdon. The hydrodynamics of flagellar propulsion: helical waves. *Journal of Fluid Mechanics*, 94:331–351, 1979c.

M Hines and JJ Blum. Bend propogation in flagella: I. Derivation of equations of motion and their simulation. *Biophysical Journal*, 23:41–57, 1978.

H Ho and SS Saurez. Hyperactivation of mammalian spermatozoa: function and regulation. *Reproduction*, 122:519–526, 2001.

MG Hull, CM Glazener, NJ Kelly, DI Conway, PA Foster, RA Hinton, C Coulson, PA Lambert, EM Watt, and KM Desai. Population study of causes, treatment, and outcome of infertility. *British Medical Journal*, 14:1693–1697, 1985.

TK Hung and TD Brown. Solid-particle motion in two-dimensional peristaltic flows. *Journal of Fluid Mechanics*, 73:77–96, 1976.

S Ishijima, S Oshio, and H Mohri. Flagellar movement of human spermatozoa. *Gamete Reserach*, 13:185–197, 1986.

A Ivic, H Onyeaka, A Girling, IA Brewis, B Ola, N Hammadieh, S Papaioannou, and CLR Barratt. Critical evaluation of methylcellulose as an alternative medium in sperm migration tests. *Human Reproduction*, 17:143–149, 2002.

MY Jaffrin and AH Shapiro. Peristaltic pumping. *Annual Review of Fluid Mechanics*, 3: 13–36, 1971.

RPS Jansen. Cyclic changes in the human fallopian tube isthmus and their functional importance. *American Journal of Obstetrics and Gynecology*, 136:292–308, 1980.

RE Johnson. An improved slender body theory for Stokes flow. *Journal of Fluid Mechanics*, 99:411–431, 1980.

CJ de Jonge and CLR Barratt. *The Sperm Cell: Production, Maturation, Fertilization, Regeneration.* Cambridge University Press, 2006.

Z Karni, WZ Polishuk, A Adoni, and Y Diament. Newtonian viscosity of the cervical mucus during the menstrual cycle. *International Journal of Fertility*, 16:185–188, 1971.

D Katz, R Mills, and T. Pritchett. The movement of human spermatazoa in cervical mucus. *Biology of Reproduction*, 25:931–937, 1978.

DF Katz, JR Blake, and SL Paveri-Fontana. On the measurement of slender bodies near plane boundaries at low Reynolds number. *Journal of Fluid Mechanics*, 72:529–540, 1975.

DF Katz, EZ Drobnis, and JW Overstreet. Factors regulating mammalian sperm migration through the female reproductive tract and oocyte vestments. *Gamete Research*, 22:443–469, 1989.

VJ Kay and L Robertston. Hyperactivated motility of human spermatozoa: a review of physiological function and application in assisted reproduction. *Human Reproduction Update*, 4:776–786, 1998.

SR Keller, TY Wu, and C Brennen. *Swimming and Flying in Nature*, chapter 'A traction layer model for ciliary propulsion', pages 253–272. Plenum, 1975.

AC King, J Billingham, and SR Otto. *Differential Equations: Linear, Nonlinear, Ordinary and Partial.* Cambridge University Press, 2003.

TF Kruger, AA Acosta, KF Simmons, RJ Swanson, JF Matta, and S Oehninger. Predictive value of abnormal sperm morphology in vitro fertilization. *Fertility and Sterility*, 49:112–117, 1988.

M Li and JG Brasseur. Non-steady peristaltic transport in finite-length tubes. *Journal of Fluid Mechanics*, 248:129–151, 1993.

J Lighthill. On the squirming motion of nearly spherical deformable bodies through liquids at very small Reynolds numbers. *Communications on Prue and Applied Sciences*, V: 109–118, 1952.

J Lighthill. *Mathematical Biofluiddynamics*. Society for Industrial and Applied Mathematics, 1975.

J Lighthill. Flagellar Hydrodynamics: The John von Neumann Lecture 1975. *SIAM Review*, 18:161–230, 1976.

J Lighthill. Reinterpreting the basic theorem of flagellar hydrodynamics. *Journal of Engineering Mathematics*, 30:25–34, 1996.

CB. Lindemann. The Geometric Clutch as a working hypothesis for future research on cilia and flagella. *Ann NY Acad Sci*, page annals.1389.024, 2007. doi: 10.1196/annals.1389.024.

N Liron and S Mochon. Stokes flow for a Stokeslet between two parallel flat plates. *Journal of Engineering Mathematics*, 10:287–303, 1976.

KE Machin. Wave propagation along flagella. *Journal of Experimental Biology*, 35:796–806, 1958.

KE Machin. The control and synchronistaion of flagellar movement. *Proceedings of the Royal Society B*, 158:88–104, 1963.

M Mishra and A Ramachandra Rao. Peristaltic transport of a Newtonian fluid in an asymmetric channel. *Zeitschrift für Angewandte Mathematik und Physik*, 52:532–550, 2003.

TK Mittra and SN Prasad. Interaction of peristaltic motion with Poiseuille flow. *Bulletin of Mathematical Biology*, 36:127–141, 1974.

D Mortimer. Sperm preparation techniques and iatrogenic failures of in-vitro fertilization. *Human Reproduction*, 7:173–176, 1991.

J Neuwinger, TG Cooper, UA Knuth, and E Nieschlag. Hyaluronic acid as a medium for human sperm migration tests. *Human Reproduction*, 6:396–400, 1991.

MA Nicosia and JG Brasseur. A mathematical model for estimating muscle tension *in vivo* during esophageal bolus transport. *Journal of Theoretical Biology*, 219:235–255, 2002.

L Nilsson. *A child is born*. Doubleday, 1990.

CW Oseen. *Neuere Methoden und Ergebnisse in der Hydrodynamik*. Akademische Verlagsgesellschaft, Leipzig, 1927.

JM Ottino. *The Kinematics of Mixing: Stretching, Chaos, and Transport.* Cambridge University Press, 1989.

SR Otto, AN Yannacopoulos, and JR Blake. Transport and mixing in Stokes flow: the effect of chaotic dynamics on the blinking Stokeslet. *Journal of Fluid Mechanics*, 430: 1–26, 2001.

EF Pate and CJ Brokaw. Movement of spermatozoa in viscous envionments. *Journal of Experimental Biology*, 88:395–397, 1980.

LE Payne and WH Pell. The Stokes flow problem for a class of axially symmetric bodies. *Journal of Fluid Mechanics*, 7:529–549, 1960.

N Phan-Thien, T Tran-Cong, and M Ramia. A boundary element analysis of flagellar propulsion. *Journal of Fluid Mechanics*, 184:533–549, 1987.

O Pironneau and DF Katz. Optimal swimming of flagellated micro-organisms. *Journal of Fluid Mechanics*, 66:391–415, 1974.

C Pozrikidis. A study of peristaltic flows. *Journal of Fluid Mechanics*, 180:515–527, 1987.

C Pozrikidis. *Boundary integral and singularity methods for linearized viscous flow.* Cambridge University Press, 1992.

C Pozrikidis. *A Practical Guide to Boundary Element Methods with the Software Library BEMLIB.* Chapman & Hall/CRC, 2002.

D Quemada. A nonlinear Maxwell model of biofluids - application to normal blood. *Biorheology*, 30:253–256, 1993.

D Ralt, M Manor, A Cohen-Dayag, I Tur-Kaspa, I Ben-Shlomo, A Makler, I Yuli, J Dor, S Blumberg, and S Mashiach. Chemotaxis and chemokinesis of human spermatozoa to follicular factors. *Biology of Reproduction*, 50:774–785, 1994.

M Ramia, DL Tullock, and N Phan-Thien. The role of hydrodynamic interaction in the locomotion of microorganisms. *Biophysical Journal*, 65:755–778, 1993.

A Ramachandra Rao and M Mishra. Nonlinear and curvature effects on peristaltic flow of a viscous fluid in an asymmetric channel. *Acta Mechanica*, 168:35–59, 2004a.

A Ramachandra Rao and M Mishra. Peristaltic transport of a power-law fluid in a porous tube. *Journal of non-Newtonian Fluid Mechanics*, 121:163–174, 2004b.

SM Ross and S Corrsin. Results of an analytical model of mucociliary pumping. *Journal of Applied Physiology*, 37:333–340, 1974.

Lord Rothschild. Non-random distribution of bull spermatozoa in a drop of sperm suspension. *Nature*, 198:1221–1222, 1963.

PG Saffman. On the boundary condition at the surface of a porous medium. *Studies in Applied Mathematics*, 50:93–101, 1971.

KA Schmitz, DL Holcomb-Wygle, DJ Oberski, and CB Lindemann. Measurements of the force produce by an intact bull sperm flagellum in isometric arrest and estimation of the dynein stall force. *Biophysical Journal*, 79:468–478, 2000.

MA Scott. A glimpse at sperm function in vivo: sperm transport and epithelial interaction in the female reproductive tract. *Animal Reproductive Science*, 60:337–348, 2000.

AH Shapiro, MY Jaffrin, and SL Weinberg. Peristaltic pumping with long wavelengths at low Reynolds numbers. *Journal of Fluid Mechanics*, 37:799–825, 1969.

L Sherwood. *Human Physiology: From Cells to Systems.* Brooks Cole, 5th edition, 2003.

ACE Sjösten, H Ellis, and GAB Edelstam. Retrograde migration of glove powder in the human female genital tract. *Human Reproduction*, 19:991–995, 2004.

DJ Smith, JR Blake, and EA Gaffney. A visco-elastic traction layer model of muco-ciliary transport. *Bulletin of Mathematical Biology*, 69:289–327, 2007a.

DJ Smith, JR Blake, and EA Gaffney. A model of tracer transport in airway surface liquid. *Bulletin of Mathematical Biology*, 69:817–836, 2007b.

DJ Smith, EA Gaffney, and JR Blake. Discrete cilia modelling with singularity distributions: Application to the embryonic node and the airway surface liquid. *Journal Bulletin of Mathematical Biology*, 69:1477–1510, 2007c.

DJ Smith, EA Gaffney, JR Blake, and JC Kirkman-Brown. Human sperm accumulation near to surfaces - a simulation study. *In preparation*, 2008a.

DJ Smith, EA Gaffney, H Gadêlha, and JC Kirkman-Brown. Flagellar movement of human sperm: imaging, kinematics and mechanical properties. *In preparation*, 2008b.

DJ Smith, EA Gaffney, N Kapur, and JC Kirkman-Brown. The effect of viscosity on sperm motility. *In preparation*, 2008c.

M Spehr, G Gisselmann, A Poplawski, JA Riffell, CH Wetzel, RK Zimmer, and H Hatt. Identification of a testicular odorant receptor mediating human sperm chemotaxis. *Science*, 299:2054–2058, 2003.

LM Srivastava and VP Srivastava. Peristaltic transport of a non-Newtonian fluid: applications to the vas deferens and small intestine. *Annals of Biomedical Engineering*, 13: 137–153, 1985.

GG Stokes. On the effect of the internal friction of fluids on the motion of pendulums. *Transactions of the Cambridge Philosophical Society*, 9:8–106, 1851.

A Strandell, U Waldenstrom, L Nilsson, and L Hamberger. Hydrosalpinx reduces *in-vitro* fertilization/embryo transfer pregnancy rates. *Human Reproduction*, 9:861–863, 1994.

A Strandell, A Lindhard, U Waldenstrom, J Thorburn, PO Janson, and L Hamberger. Hydrosalpinx and IVF outcome: a prospective, randomized multicentre trial in Scandinavia on salpingectomy prior to IVF. *Human Reproduction*, 14:2762–2769, 1999.

A Strandell, A Lindhard, U Waldenstrom, J Thorburn, PO Janson, and L Hamberger. Hydrosalpinx and IVF outcome: cumulative results after salpingectomy in a randomised controlled trial. *Human Reproduction*, 16:2403–2410, 2001.

AH Stroud and D Secrest. *Gaussian Quadrature Formulas*. Prentice-Hall, 1966.

SS Suarez and AA Pacey. Sperm transport in the female reproductive tract. *Human Reproduction Update*, 12:23–37, 2006.

SS Suarez, DF Katz, DH Owen, JB Andrew, and RI Powell. Evidence for the function of hyperactivated motility in sperm. *Biology of Reproduction*, 44:375–381, 1991.

E Süli and DF Mayer. *An Introduction to Numerical Analysis*. Cambridge University Press, 2003.

GI Taylor. Analysis of the swimming of microscopic organisms. *Proceedings of the Royal Society of London, Series A*, 209:447–461, 1951.

GI Taylor. The action of waving cylindrical tails in propelling microscopic organisms. *Proceedings of the Royal Society A*, 211:225–239, 1952.

A Templeton, C Fraser, and B Thompson. The epidemiology of infertility in Aberdeen. *British Medical Journal*, 301:148–152, 1990.

EO Tuck. Some methods for flows past blunt slender bodies. *Journal of Fluid Mechanics*, 18:619–635, 1964.

EO Tuck. Toward the calculation and minimization of Stokes drag on bodies of arbitrary shape. In *3rd Australasian Conference on Hydraulics and Fluid Mechanics, Sydney*, pages 29–32, 1968.

EO Tuck. On thin or slender bodies, Lighthill Lecture, British Applied Mathematics Colloquium, Norwich, 2004.

University of Kansas Medical Center. The JayDoc HistoWeb, 2006. URL `http://www.kumc.edu/instruction/medicine/anatomy/histoweb/`.

PG Vann and JR Blake. Mechanics of ovum transport in the oviduct. *Cell Motility and the Cytoskeleton*, 2:53–57, 1982.

H Winet, GS Berstein, and J Head. Observations of the response of human spermatozoa to gravity, boundaries and fluid shear. *Journal of Reproduction and Fertility*, 70:511–523, 1984.

DP Wolf, L Blasco, MA Khan, and Litt MA. Human cervical mucus. I. Rheologic characteristics. *Fertility and Sterility*, pages 41–46, 1977a.

DP Wolf, L Blasco, MA Khan, and Litt MA. Human cervical mucus. II. Changes in viscoelasticity during the ovulatory menstrual cycle. *Fertility and Sterility*, pages 47–52, 1977b.

DM Woolley and GG Vernon. A study of helical and planar waves on sea urchin sperm flagella, with a theory of how they are generated. *Journal of Experimental Biology*, 204: 1333–1345, 2001.

World Health Organisation. *WHO laboratory manual for the examination of human semen and sperm-cervical mucus interaction.* Cambridge University Press, 4th edition, 1999.

S Yaniv, D Elad, AJ Jaffa, and O Eytan. Biofluid aspects of embryo transfer. *Annals of Biomedical Engineering*, 31:1255–1262, 2003.

FCP Yin and YC Fung. Comparison of theory and experiment in peristaltic transport. *Journal of Fluid Mechanics*, 47:93–112, 1971.

LJD Zaneveld, CJ De Jonge, RA Anderson, and SR Mack. Human sperm capacitation and the acrosome reaction. *Human Reproduction*, 6:1265–1274, 1991.

TF Zien and S Ostrach. A long wave approximation to peristaltic motion. *Journal of Biomechanics*, 3:63–75, 1970.